The effect of high pressure on crystal structures, polymorphism, and intermolecular interactions in the simplest aliphatic hydrocarbons and their derivatives

Wpływ wysokiego ciśnienia na struktury krystaliczne, polimorfizm i oddziaływania międzycząsteczkowe w najprostszych węglowodorach alifatycznych i ich pochodnych

Natalia Sacharczuk

A thesis submitted to
The Faculty of Chemistry, Adam Mickiewicz University, Poznań
in fulfilment of requirements for the degree of
Doctor of Philosophy in Chemistry

Supervised by Prof. UAM dr hab. Marcin Podsiadło

and co-supervisor: Prof. UAM dr hab. Anna Olejniczak

Poznań, 2026

The research presented in the thesis was funded by the National Science Center as part of the project: **OPUS 19** (2020/37/B/ST4/00982)

NATIONAL SCIENCE CENTRE
POLAND

This research was also partly supported by ID-UB.

Acknowledgements

Niniejsza praca stanowi podsumowanie moich ostatnich pięciu lat życia. Jestem dumna, że dotarłam do tego etapu, choć byłoby to niemożliwe bez wsparcia i obecności wielu osób, którym chciałabym podziękować.

Przede wszystkim chciałabym serdecznie podziękować mojemu promotorowi, Profesorowi Marcinowi Podsiadło, oraz mojej promotorce pomocniczej, Profesor Annie Olejniczak, za wprowadzenie mnie w świat badań wysokociśnieniowych i towarzyszenie mi na kolejnych etapach pracy doktorskiej. Dziękuję za przekazaną wiedzę, cierpliwość, opiekę naukową, liczne rozmowy oraz wskazówki, które pomagały mi rozwijać się jako badaczce. Jestem wdzięczna za okazane zaufanie, wsparcie merytoryczne oraz możliwość samodzielnego mierzenia się z wyzwaniami badawczymi. Chciałabym również podziękować Profesorowi Andrzejowi Katrusiakowi za poświęcony czas, cierpliwość oraz gotowość do tłumaczenia wielu zagadnień związanych z krystalografią wysokociśnieniową. Dziękuję za cenne rozmowy, wskazówki i dzielenie się doświadczeniem, które pomogły mi lepiej zrozumieć tę dziedzinę i rozwijać się naukowo.

Chciałabym także serdecznie podziękować całemu Zakładowi Chemii Materiałów za życzliwą, pomocną i przyjazną atmosferę pracy. Szczególne podziękowania kieruję do Idy — za rozmowy, które rozwijały mój mózg nie tylko naukowo, ale i życiowo; za pokazywanie mi innych perspektyw i za odważne, trochę szalone podejście do życia. Paulince dziękuję za wspólne dziesięć lat bycia *lab partners*, za obecność i dzielenie ze mną wielu codziennych momentów. Kindze i Michalinie dziękuję za pomoc w rozwiązywaniu małych i dużych problemów, bez was wiele rzeczy byłoby o wiele trudniejsze. Ewie — za zrozumienie, obiektywność i za ciepłe, budujące rozmowy wtedy, gdy najbardziej ich potrzebowałam. Shiva, thank you for all the afternoon chatting, without judgement, with a lot of laugh and fun. Szymonowi dziękuję za to, że pomógł mi na nowo dostrzec w sobie naukowczynię i przypomniał mi, że nauka może znów sprawiać frajdę. Dziękuję za motywowanie mnie do szukania rozwiązań, mierzenia się z problemami oraz stawiania sobie nowych wyzwań. Jestem wdzięczna za wszystkie rozmowy, wsparcie i wiarę w moje możliwości, szczególnie wtedy, gdy sama na chwilę ją traciłam.

Bartkowi dziękuję za przyjaźń, szczerość, poczucie humoru i za to, że w chwilach największego zmęczenia zawsze potrafił zaproponować najprostsze rozwiązanie: rzucić to wszystko i odzyskać święty spokój. Dziękuję, że mimo tych kuszących propozycji byłeś obok i pomagałeś mi dotrwać do końca.

Szczególne podziękowania kieruję do moich Rodziców i Babci, którym zawdzięczam znacznie więcej, niż potrafię wyrazić słowami. Dziękuję za stworzenie mi możliwości uczenia się i rozwoju, za wspieranie moich wyborów oraz za kibicowanie mi na każdym etapie tej drogi. Bez Waszej miłości, cierpliwości i wiary we mnie nie byłoby mnie dziś w miejscu, w którym jestem.

Filipowi dziękuję z całego serca za to, że był przy mnie przez wszystkie lata tej drogi. To Ty widziałeś najwięcej — wszystkie momenty radości, zwątpienia, zmęczenia i walki o to, by iść dalej. Dziękuję Ci za to wszystko. Bez Twojej obecności, miłości i nieustannego wsparcia na pewno nie byłoby mnie dziś w tym miejscu.

“A smooth sea never made a skilled sailor.”

Franklin D. Roosevelt

Table of Contents

The list of abbreviations used

DAC – Diamond Anvil Cell

GPa – Gigapascal

TPa – Terapascal

MPa – Megapascal

DFT – Density Functional Theory

IUPAC – International Union of Pure and Applied Chemistry

HP – High Pressure

LT – Low Temperature

H-bonds – Hydrogen Bonds

NMR – Nuclear Magnetic Resonance

vdW – van der Waals

CSD – Cambridge Structural Database

SI – Supporting Information

SCXRD – Single Crystal X-ray Diffraction

IR – Infrared Spectroscopy

UV – Ultraviolet Spectroscopy

SPA – Simplest Primary Amines

EA, PA, BA, PEA, HA – Ethylamine, Propylamine, Butylamine, Pentylamine, Hexylamine

DME, DEE, DPE – Dimethyl Ether, Diethyl Ether, Dipropyl Ether

B, CB, TB, IB – 1-Butene, Cis-2-butene, Trans-2-butene, Isobutene

Streszczenie w języku polskim

Rozprawa doktorska poświęcona jest badaniu wpływu wysokiego ciśnienia na struktury krystaliczne, polimorfizm oraz oddziaływania międzycząsteczkowe w najprostszych węglowodorach alifatycznych oraz ich pochodnych. Badania koncentrują się na niewielkich cząsteczkach organicznych zbudowanych z lekkich pierwiastków (C, H, N, O), które w warunkach normalnych występują jako ciecze lub gazy i są słabo reprezentowane w strukturalnych bazach danych. Zastosowanie wysokiego ciśnienia umożliwiło ich krystalizację oraz szczegółowe poznanie mechanizmów stabilizacji faz stałych.

Celem pracy było określenie, w jaki sposób kompresja wpływa na organizację cząsteczek w krysztale, prowadząc do przemian strukturalnych, przejść fazowych oraz zmian konformacyjnych, a także określenie roli oddziaływań międzycząsteczkowych, od wiązań wodorowych po oddziaływania dyspersyjne. Badania obejmowały szeregi homologiczne amin alifatycznych, symetryczne etery dialkilowe, izomery butenu oraz izobutan.

Podstawową metodą badawczą była wysokociśnieniowa monokrystaliczna dyfrakcja promieniowania rentgenowskiego prowadzona z wykorzystaniem komory diamentowej. Uzupełniająco zastosowano obliczenia kwantowo-mechaniczne oraz analizę powierzchni Hirshfelda w celu ilościowego i jakościowego opisu oddziaływań międzycząsteczkowych. Wszystkie kryształy były otrzymywane *in situ* w warunkach wysokiego ciśnienia, bez użycia rozpuszczalników czy mediów hydrostatycznych.

W ramach pracy wyznaczono łącznie 64 nowe struktury krystaliczne oraz odkryto 20 nieznanych wcześniej polimorfów. Wykazano, że podatność na polimorfizm i przemiany strukturalne zależy od subtelnej równowagi pomiędzy geometrią cząsteczki, jej symetrią, elastycznością konformacyjną oraz charakterem dominujących oddziaływań międzycząsteczkowych.

Uzyskane wyniki pokazują, że wysokie ciśnienie stanowi skuteczne narzędzie do badania i modyfikowania krajobrazu strukturalnego prostych cząsteczek organicznych. Praca wnosi istotny wkład w rozwój krystalografii wysokociśnieniowej oraz pogłębia zrozumienie roli słabych oddziaływań międzycząsteczkowych w stabilizacji faz stałych, dostarczając dane i modele istotne zarówno dla chemii fizycznej, jak i nauk o materiałach oraz chemii strukturalnej.

Summary in English

The doctoral dissertation investigates the effects of high pressure on crystal structures, polymorphism, and intermolecular interactions in the simplest aliphatic hydrocarbons and their derivatives. The research focuses on small organic molecules composed of light elements (C, H, N, O) that, under ambient conditions, exist as liquids or gases and are therefore poorly represented in structural databases. The application of high pressure facilitated their crystallization and contributed to a detailed understanding of the mechanisms stabilizing their solid phases.

The aim of the study was to determine how compression influences molecular organization in crystals, leading to structural transformations, phase transitions, and conformational changes, and to assess the role of intermolecular interactions, ranging from hydrogen bonding to dispersion forces. The investigations covered homologous series of aliphatic amines, symmetric dialkyl ethers, butene isomers, and isobutane.

The primary experimental technique employed was high-pressure single-crystal X-ray diffraction using a diamond anvil cell. Complementary quantum-mechanical calculations and Hirshfeld surface analysis were applied to provide both quantitative and qualitative descriptions of intermolecular interactions. All crystals were obtained *in situ* under high-pressure conditions, without the use of solvents or hydrostatic media.

In total, 64 new crystal structures were determined, and 20 previously unknown polymorphs were discovered. It was demonstrated that the susceptibility to polymorphism and structural transformations depends on a subtle balance between molecular geometry, symmetry, conformational flexibility, and the nature of the dominant intermolecular interactions.

The results show that high pressure is an effective tool for probing and modifying the structural landscape of simple organic molecules. This work makes a significant contribution to the development of high-pressure crystallography and deepens understanding of the role of weak intermolecular interactions in stabilizing solid phases, providing data and models relevant to physical chemistry, materials science, and structural chemistry.

1. Introduction

1.1 Materials under high pressure

From a thermodynamic perspective, pressure is one of the most fundamental parameters, strongly influencing the physical and chemical behavior of matter. Despite its importance, pressure has historically been less accessible in laboratory studies compared to temperature. The fundamentals of high-pressure science were established by Percy W. Bridgman, whose pioneering work in the early 20th century not only expanded the pressure range achievable in laboratory experiments but also established the foundation for the thermodynamic exploration of materials under various pressures.[1] His contribution, which brought him the Nobel Prize in Physics in 1946, continues to influence high-pressure techniques and theory today.[2] Advances in high-pressure technology, thanks to the development of the diamond-anvil cell (DAC), have allowed reaching pressure levels exceeding 1,000 gigapascals (GPa), broadening the scope of materials chemistry.[3,4]

In chemistry and materials science, pressure offers a unique way to tune and study the atomic and molecular arrangement in condensed matter. While temperature affects kinetic energy and can induce phase transitions by changing atomic vibrations, pressure directly acts on volume, reducing intermolecular distances and promoting new modes of atomic packing.[5] As atoms are forced closer together, their electronic orbitals begin to overlap more significantly, resulting in changes in bonding patterns, molecular geometry, and electronic properties. Pressure strongly alters chemical bonding, reactivity, and phase stability, often leading to novel phases with unique properties, some of which may be recoverable at ambient conditions. These conditions enable the design of materials for energy conversion, storage, and transmission, and extend research into hydrogen-rich compounds for storage and superconductivity.[6–9]

Compression can also cause significant disorder, amorphization, or even create materials in a glassy state, way below their melting points. Many technologically important materials, novel pharmaceuticals,[10,11] superhard

ceramics,[12–14] and framework structures,[15,16] have been discovered or optimized through high-pressure studies.[17]

While pressure at Earth's surface rarely exceeds a few megapascals, deep inside Earth it can reach about 365 GPa and rise into the Terapascal range within giant planets or stars.[18,19] At the Sun's core, pressures are estimated to reach around 24,000,000 GPa (*i.e.*, 24,000 TPa).[20] What we consider "extreme" pressure is, in fact, common beyond our narrow thermodynamic environment near the triple point of water. Understanding how crystal structures behave under pressure is therefore essential, not only in solid-state chemistry but also in geology, planetary science, and astrophysics.[21–23] Notable examples include the formation of diamonds, the structure of dense silica phases like stishovite,[24] and the propagation of seismic waves through the Earth's crust.

Pressure also enables the solidification and structural investigation of compounds that exist as liquids or gases at ambient pressure. Many small molecules, such as hydrocarbons, alcohols, and sulfur- and nitrogen-containing species, can be compressed into condensed phases, where they form crystals, enabling structural studies by X-ray diffraction or spectroscopic methods. This is particularly useful for understanding weak intermolecular interactions, molecular packing, and polymorphism in compounds that are otherwise difficult to study.

In recent decades, high-pressure research has rapidly advanced through the integration of X-ray and synchrotron radiation, *in situ* spectroscopy, and computational modeling.[25–27] These tools enable real-time observation of structural, vibrational, and electronic changes under compression, offering unprecedented insight into the mechanisms driving pressure-induced phenomena. In addition, theoretical approaches, particularly those based on density functional theory (DFT), allow exploration of phase stability, reaction pathways, and electronic structure in systems where experimental data are limited or challenging.[27–29] These general aspects of high-pressure science provide the conceptual framework for understanding how compression can induce crystallization and structural transformations in the small-molecular systems investigated in this work.

1.2. Intermolecular interactions

Intermolecular interactions are fundamental forces that enable the existence of liquids and solids, and they play a key role in determining the properties of gases, condensed phases, and molecular crystals.[30] Even though they are much weaker than covalent or ionic bonds, they affect the equilibrium geometry, lattice energy, and overall stability of crystalline materials.[31] These interactions can be classified based on the distance between the interacting species: short-range repulsive exchange forces (typically below ~2.2 Å), intermediate-range van der Waals attractions (~2.5-3.2 Å), and long-range electrostatic interactions (extending beyond ~4.0 Å), including dipole-dipole, quadrupole-dipole, and induction effects.[30,32,33]

In molecular crystals, the energy of intramolecular (covalent) bonds usually exceeds 100 kJ mol^{-1}, whereas intermolecular attractions are typically at least one order of magnitude weaker. According to Kitaygorodsky,[34] four main categories of intermolecular forces can be distinguished:

1. **Coulombic (electrostatic) interactions** occur between two charged or partially charged molecules. Unlike ionic bonds, the charge is not localized on a single atom but is delocalized across several atoms in each molecule.
2. **Hydrogen bonds** arise when a hydrogen atom with a partial positive charge is shared between two electronegative atoms carrying partial negative charges.
3. **Dipole-dipole interactions** exist between molecules possessing permanent dipole moments. They are weaker than ionic or Coulombic forces because they involve partial charges and are often counterbalanced by repulsive interactions between like-charged regions.
4. **van der Waals forces** result from the attraction between a permanent dipole and an induced dipole, or between two induced dipoles. Though individually weak, these forces are omnipresent and play a decisive role in stabilizing molecular crystals, particularly when stronger directional bonds are absent.

Among these, hydrogen bonds are often particularly important due to their directionality, partial covalency, and role in guiding supramolecular architecture. According to the IUPAC definition, a hydrogen bond is an attractive interaction between a hydrogen atom bound to a more electronegative atom (the donor) and an electron-rich region (the acceptor), typically involving linear geometries and observable spectroscopic or structural signatures.[35] These include bond lengthening, red shifts in vibrational frequencies, and deshielding in NMR signals. However, a complete picture of crystal packing requires consideration of other non-covalent forces, including π–π stacking between aromatic systems, halogen and chalcogen bonds, and even weak hydrogen-hydrogen contacts, which can all critically influence molecular assembly.

All these interactions can be characterized by both geometric parameters (bond lengths and angles) and energetic descriptors, such as the positions, widths, and intensities of vibrational or optical absorption bands.[36] A comparative analysis of multiple structures, rather than a single-point examination, is especially helpful in identifying the relative contributions of different interactions. These comparative cases may include:

1. Pressure-induced structural changes on compression of the atmospheric phase of the compound;
2. studying new solid forms that appear as a result of pressure-induced phase transitions;
3. analyzing polymorphs obtained by crystallizing compounds from solution or melt under non-ambient conditions.

Classical strong O–H···O bonds are characterized by donor-acceptor distances of ~2.6-2.8 Å and nearly linear angles approaching 180°, and they are regarded as one of the most directional and stabilizing structural motifs. Medium-strength contacts, such as O–H···N or N–H···N, are slightly longer, typically in the 2.8-3.1 Å range. Weak hydrogen bonds, such as C–H···O, C–H···S, C–H···π, or C–H···F, are longer (3.2-3.6 Å or more) and often show bent geometries. Individually, these bonds are weak, but when many occur together, they can significantly influence crystal packing and polymorphism. Understanding the

role of weak hydrogen bonds is important for explaining their competition with much weaker dispersive interactions.[37,38]

High-pressure crystallization offers unique insights into how different intermolecular interactions govern nucleation and crystal growth. Since this process is complex, crystallization at high pressure provides a valuable tool for untangling their roles in the appearance of different crystalline forms, especially for compounds that are liquid at ambient conditions.[25,39–41]

Under high-pressure conditions, the conventional hierarchy of intermolecular interactions established at ambient pressure is progressively altered. Compression enforces close molecular packing, reducing intermolecular distances and making weak contacts (*e.g.*, CH···O, CH···N) more structurally important. As a result, geometric constraints imposed by efficient packing increasingly compete with interaction energetics, leading to structural rearrangements, conformational changes, and pressure-induced phase transitions.

A detailed understanding of how intermolecular interactions respond to compression is therefore essential for interpreting the pressure-induced structural rearrangements and phase transitions observed in the studied molecular crystals. More broadly, analyzing the balance between strong, directional hydrogen bonds and weaker dispersive contacts is thus essential for crystal engineering, for predicting and interpreting structural changes, and for the application of molecular crystals as functional materials.[42,43]

1.3. Molecular crystals

Molecular crystals are composed of individual molecules arranged in periodic lattices, stabilized by relatively weak interactions such as hydrogen bonds, van der Waals forces, or dipole-dipole interactions.[44] Because these interactions are often of comparable strength, the molecular aggregation is governed mainly by the size, geometry, and symmetry of the molecules.[45] Even slight changes in the position of molecules may significantly affect solubility, compressibility, conductivity, or optical properties, which explains their importance in pharmaceuticals,[46] construction elements,[47] and electronic devices.[48] Thus, the properties of molecular crystals can be tuned by modifying the molecular structure, enabling their optimization for specific applications.[46,49,50]

An important aspect of molecular crystals is their response to the external environment, especially temperature and pressure.[51] They are considered “softer" than ionic or covalent solids, and they usually exhibit higher compressibility and thermal expansion. Under compression, the lattice adjusts toward intermolecular contacts, which may lead to molecular reorientation, conformational changes, and, in some cases, abrupt phase transitions.[52] High-pressure studies have shown that such transformations may reorganize hydrogen-bond networks, strengthen weak interactions, or, in some cases, even result in polymerization.[53,54] These processes may be reversible, but they can also produce metastable phases that are preserved after decompression, thereby revealing new structural motifs inaccessible under ambient conditions. This dual role of pressure, a probe of intermolecular cohesion forces and a generator of novel crystalline forms, highlights the broader significance of molecular crystals as model systems for exploring structure-property relationships.[55,56]

Small molecular crystals composed of light elements provide useful model systems for rationalizing these effects, due to their structural simplicity and well-defined intermolecular contacts. Under compression, such systems allow subtle packing rearrangements and the emergence of otherwise secondary intermolecular contacts to be observed in a structurally transparent manner.

1.4. Polymorphism

Polymorphism, derived from the Greek words *poly* (many) and *morph* (form), describes the ability of a single compound to crystallize in two or more distinct structural arrangements, each characterized by unique unit-cell parameters. This phenomenon primarily occurs in molecular and ionic organic compounds.[57] The concept of polymorphism was first introduced to crystallography by Mitscherlich in 1822,[58] who observed that certain substances could adopt more than one crystal form. Later, McCrone[59] formalized the term, defining a polymorph as a distinct crystalline phase of a compound existing in at least two distinct molecular arrangements in the solid state. This includes conformational polymorphism, where flexible molecules adopt different conformations, but excludes changes in chemical identity, such as tautomerism.

The interplay of thermodynamic and kinetic factors plays a central role in the stability and formation of polymorphs. Thermodynamics favors the structure with the lowest free energy, while kinetics may lead to the formation of metastable forms that crystallize more rapidly.[60] This balance strongly influences which polymorphic form develops under specific conditions and whether transformations between forms can happen over time.[61] These principles are often visualized as phase diagrams, with water, which includes twenty polymorphic ice phases, some of which are stable only under specific temperature and pressure conditions, being the most prominent example.[62–65] Although the number and variety of known polymorphs continue to increase, understanding the fundamental mechanisms remains a key challenge in solid-state chemistry.[66] Besides structural and energetic distinctions, polymorphism also highlights the complexity of molecular recognition and self-assembly within solids. The formation of a particular polymorph is influenced not only by the interplay of molecular conformations, intermolecular interactions (such as hydrogen bonding, π–π stacking, and van der Waals forces), but also by the choice of solvent and even subtle variations in nucleation conditions.[67–69] Advances in crystallography, computational modeling, and structural databases, such as the Cambridge Structural Database (CSD), have deepened our understanding of these phenomena.[70–72] Nevertheless, reliably predicting or controlling the appearance

of specific polymorphs and their properties remains a significant challenge; however, the modification of the intrinsic properties of different polymorphs, along with their possible application areas, illustrated in Figure 1, indicates that this is an important area of research.[71]

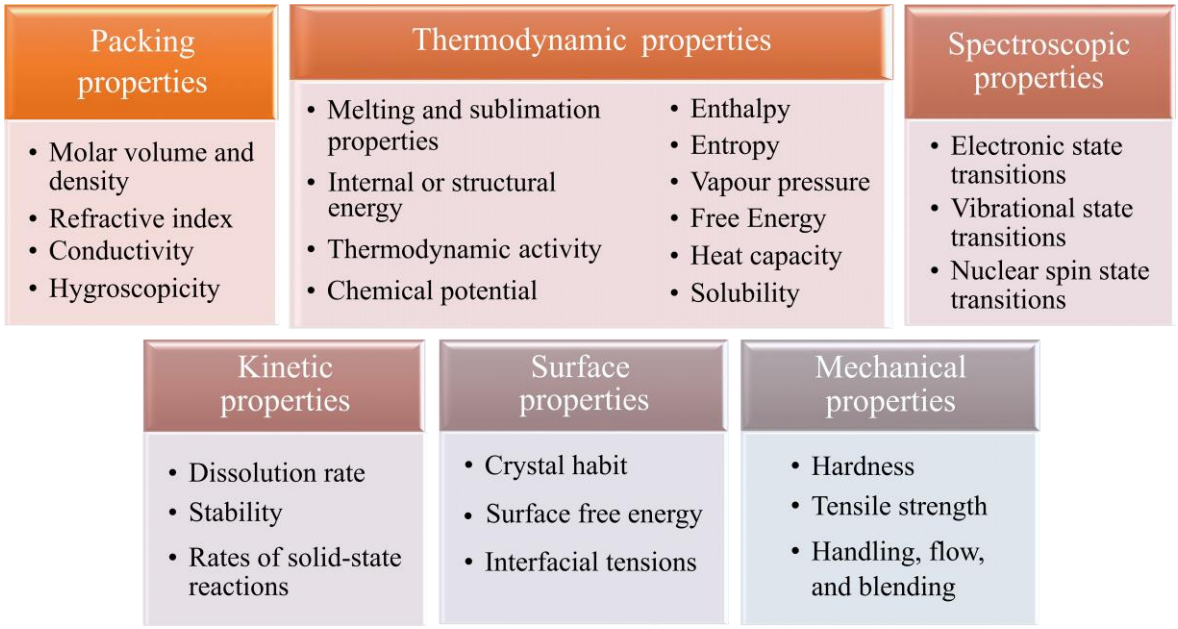

Figure 1. Schematic illustration of the physical properties that differ among polymorphs.

Despite significant progress in understanding polymorphism, it remains highly unpredictable. A comprehensive statistical analysis has shown that approximately half of all screened compounds exhibit polymorphism, including a wide range of salts and cocrystals, with a slightly lower occurrence among solvates and hydrates.[5] McCrone famously noted that "*every compound has different polymorphic forms, and that, in general, the number of forms known for a given compound is proportional to the time and money spent in research on that compound*," highlighting the inherently empirical nature of polymorph screening.[59]

Chiral molecules are less likely to exhibit polymorphism than achiral compounds, and the possibility of forming hydrogen bonds only slightly increases the chance of observing a polymorphic transition.[73] These findings challenge earlier assumptions that molecular rigidity or the presence of functional groups can be directly translated into the polymorphic behavior of a compound. The latest investigation on polymorphic phenomena suggests that the energetic

differences between polymorphs are usually minor, with most differing in lattice energy by less than 4 kJ·mol^{-1}.[67] Moreover, the studies also indicate that the energy difference between polymorphs exhibiting these same or almost identical conformations is even smaller.[73] Ultimately, to this point, it is hard to elucidate universal rules that could be used to determine how many polymorphs a given compound can form, how to obtain them, or what their physical properties might be, all of which underscores the importance of the experimental work in the area of polymorph discovery.[5,72,74–76]

These considerations highlight the relevance of high-pressure studies for exploring polymorphic landscapes and provide the basis for the systematic investigation of pressure-induced phase transitions presented in this work. In this context, high-pressure serves as a controlled external variable that enables access to polymorphic forms and phase transitions that are often inaccessible under ambient conditions.

1.5. Aims and objectives

Despite numerous high-pressure studies on inorganic and complex organic systems, simple aliphatic hydrocarbons and their derivatives remain poorly characterized at the structural level under compression, particularly with respect to polymorphism, conformational response, and intermolecular interactions. Therefore, the main aim of this thesis is to investigate how the simplest aliphatic hydrocarbons and their derivatives, specifically amines, ethers, butene isomers, and isobutane, respond to compression and how their molecular and supramolecular features determine their high-pressure behaviour.

The research focuses on identifying the mechanisms of structural transformations, conformational changes, and pressure-induced polymorphism. Particular attention is given to the hierarchy of intermolecular interactions, including hydrogen bonding, CH···N contacts, van der Waals forces, which contribute to the stabilization of the observed packing motifs. By systematically comparing compounds of increasing molecular size and structural complexity, this work aims to establish general relationships between molecular structure and the stability and flexibility of crystal phases under high pressure.

The investigated amines, ethers, and simple hydrocarbons were selected as representative model systems because they differ in molecular symmetry, conformational flexibility, and dominant intermolecular interactions. This analysis enables the assessment of how these molecular features influence structural behaviour, packing preferences, and polymorphism during compression.

The results of my PhD research have been published in five papers, highlighting my main achievements. These articles are listed below, with copies included in Appendices P1–P5.

Articles described within this thesis:

Paper 1 (P1) Polymorphism, Intermolecular Interactions, and Properties of Primary Amines at High Pressure
Sacharczuk, N.; Olejniczak, A.; Bujak, M.; Podsiadło, M.
Cryst. Growth Des. **2023**, *23*, 7119−7125

Paper 2 (P2) High-Pressure Crystal Structure of *n*-Hexylamine
Kuleczka, B.; **Sacharczuk, N.**; Olejniczak, A.; Podsiadło, M.
Acta Cryst. **2025**, *C81*, 346−350

Paper 3 (P3) Conformation-Aggregation Interplay in The Simplest Aliphatic Ethers Probed Under High Pressure
Sacharczuk, N.; Olejniczak, A.; Bujak, M.; Dziubek, K. F.; Katrusiak, A.; Podsiadło, M.
IUCrJ **2024**, *11*, 57−61

Paper 4 (P4) Molecular Aggregations in Crystals of Butene Isomers Determined at High Pressure
Sacharczuk, N.; Olejniczak, A.; Bujak, M.; Podsiadło, M.
C*ryst. Growth Des.* **2024***, 24,* 9909−9913

Paper 5 (P5) Mechanism of Isostructural Phase Transition in Isobutane
Sacharczuk, N.; Kuleczka, B.; Olejniczak, A.; Katrusiak, A.; Podsiadło, M.
J. Phys. Chem. C **2025**, *129*, 14196−14203

2. Experimental methods

The following sections summarize all conducted experiments and theoretical calculations. Detailed descriptions are available in the individual articles and the Supporting Information (SI).

2.1. High-pressure methods

The diamond-anvil cell (DAC), developed over 70 years ago,[3] remains the most effective device for generating static high pressure. Over the decades, various DAC designs have been introduced. During my PhD, I used a modified Merrill-Bassett DAC;[25] a graphical representation of the DAC is presented in Figure 2. Due to diamonds' high spectral transparency and low X-ray absorption, the DAC can be used for *in-situ* direct observation of a sample and for studying its structure by diffraction methods.

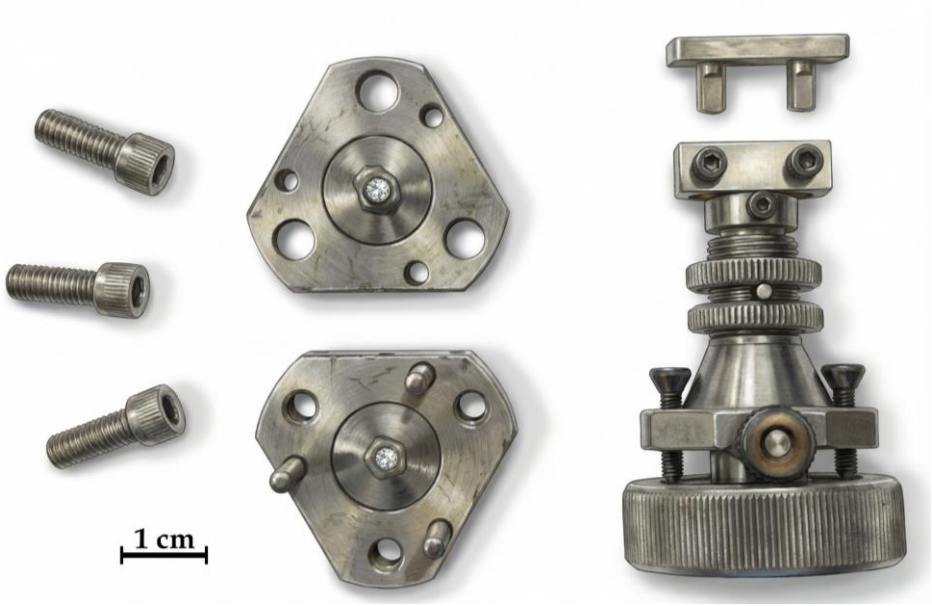

Figure 2. Diamond Anvil Cell used in my research. On the left, the open DAC with screws used to close the DAC; on the right, the DAC goniometer head.

Under ambient conditions, the compounds examined in my doctoral research were either gaseous or low-boiling liquids; consequently, no solvents or hydrostatic media were used. A schematic diagram of the gas-loading procedure is shown in Figure 3.

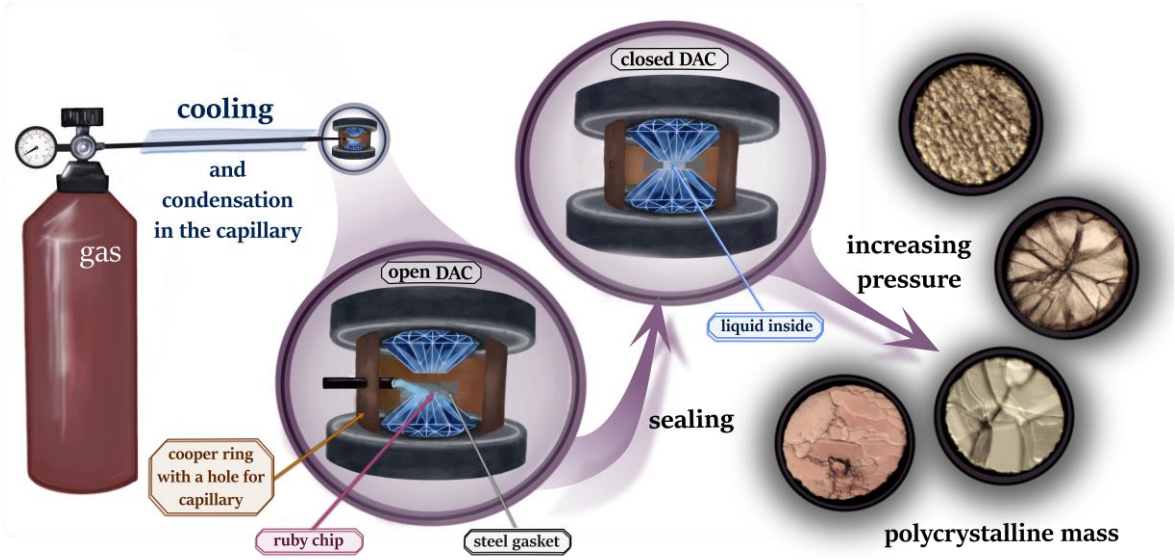

Figure 3. Schematic representation of gas loading to the Diamond Anvil Cell. The figure represents the cross-section of the DAC.

All single crystals were grown *in-situ* under high-pressure conditions, using either isochoric or isothermal methods.[77,78] The process involved obtaining the polycrystalline mass (Figure 4a) and then, depending on the method, either adjusting the temperature or increasing the chamber's volume until the polycrystalline mass was melted down to a single grain (Figure 4c). Then, the DAC was cooled, or its volume was reduced to grow a single crystal. Figure 4 shows an example of this process. The steel gasket used in the DAC had a thickness of 0.3 mm and a central hole with a diameter of ca. 0.4 mm. The diamond culets had diameters of 0.75 mm.

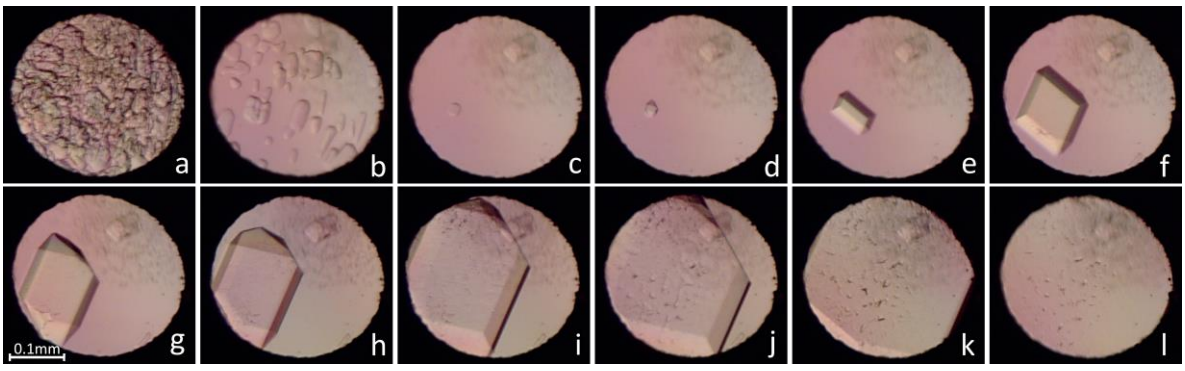

Figure 4. Stages of growing a single crystal inside the DAC chamber.

Pressure inside the DAC was measured with a BETSA spectrometer using the ruby fluorescence method, where the shift of the R1 line is linear with pressure, allowing measurements with an accuracy of 0.02 GPa.[79,80] The

calibrations were performed before and after each X-ray diffraction measurement. Additional compressibility measurements were performed with a piston-cylinder apparatus,[81,82] achieving a pressure resolution of 0.01 GPa.

2.2. Structural studies: high-pressure single crystal X-ray diffraction

Structural measurements were carried out using four-circle single-crystal diffractometers, including Rigaku Xcalibur EOS and Xcalibur ATLAS, and the KUMA KM4-CCD. All of them were equipped with graphite-monochromatic MoKα (λ = 0.71073 Å) radiation. DAC centering was performed using the gasket-shadow method.[83] Data collection, *UB* matrix determination, and integration were carried out using the CrysAlisPro[84] software suite. Programs *OLEX2-1.5*,[85] *SHELX-T,*[86] and *SHELX-L*[87] were used to solve the structures by direct methods, and to the full-matrix least-squares refinement of the models.

2.3 Quantum mechanical calculations

The quantum-mechanical calculations were performed using *GAUSSIAN* 16*W* and *GaussView* software.[88,89] This program is widely used for forecasting spectroscopic data, including infrared (IR), Raman, and ultraviolet (UV) measurements. The software was employed to examine the thermodynamic properties of molecules, conformational variations, and potential energy.

Quantum-mechanical analyses of intermolecular interactions were performed using the program *CrystalExplorer*.[90,91] Hirshfeld surface analysis and interaction energy calculations were performed to assess the nature and strength of intermolecular interactions in the crystals. These tools enabled quantitative evaluation of hydrogen bonding, van der Waals interactions, and other stabilizing forces that influence the molecular packing and cohesion of the studied structures.

3. Results and discussion

The systematic investigation of the C_2-C_6 primary amines: ethylamine (**EA**), propylamine (**PA**), butylamine (**BA**), pentylamine (**PEA**), and hexylamine (**HA**) under high-pressure conditions provides a comprehensive view of how the competition between hydrogen bonding and dispersion interactions governs polymorphic behaviour and structural stability among this homologous series. The chosen amines constitute a good model for studying the subtle interplay between strong, directional NH···N hydrogen bonds and weak, cumulative dispersion forces. Previous research by Maloney et al.,[92] demonstrated that hydrogen bonds primarily govern aggregation in short-chain amines. However, as the alkyl chain becomes larger than 6 carbon atoms, dispersion interaction energy becomes more significant and ultimately dominates the crystal packing of decylamine.[92]

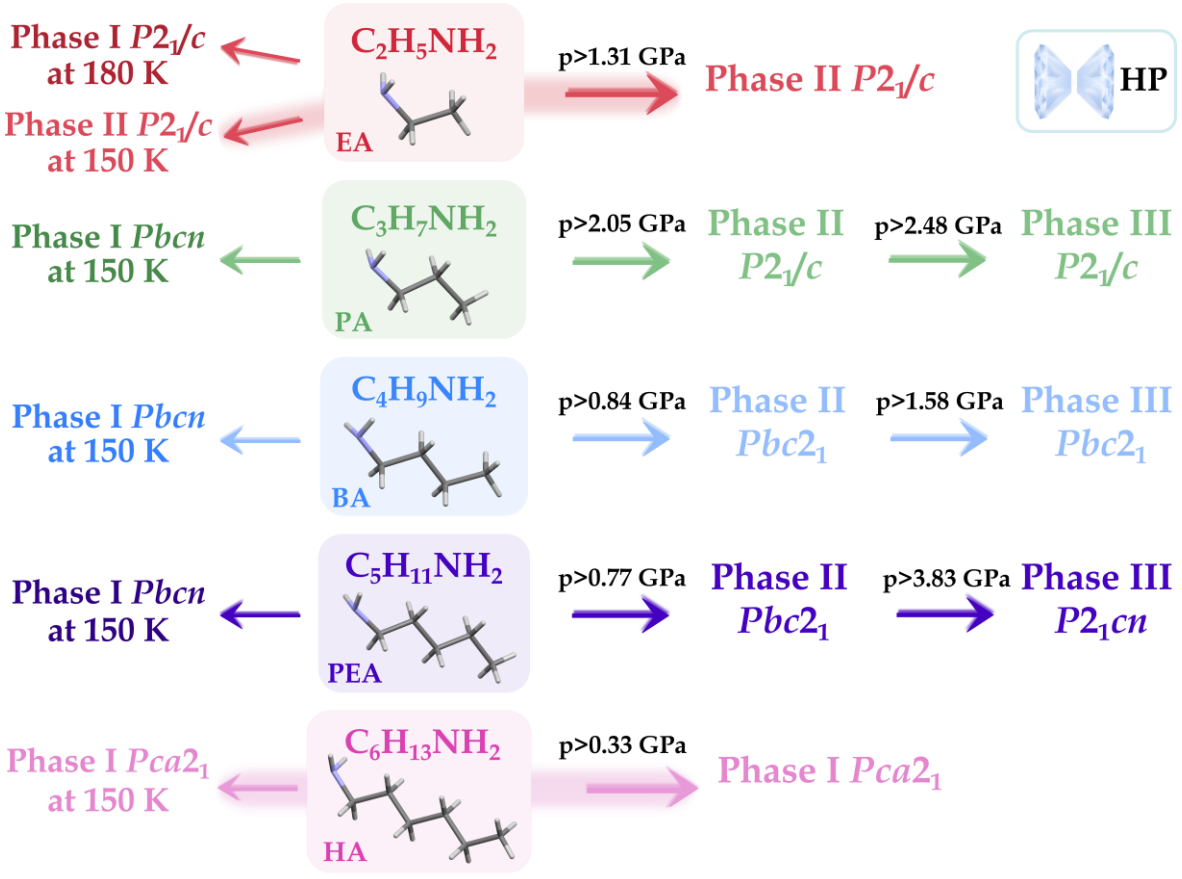

Figure P1.1. Overview of the phase behavior from ethylamine to hexylamine. Low-temperature polymorphs reported previously (left)[92] are compared with the high-pressure phases determined in this study (right). **EA** and **HA** preserve the symmetry of the LT phases upon compression, while **PA**, **BA**, and **PEA** undergo pressure-induced transformations, revealing new phases II and III.

The high-pressure phases of investigated amines, as well as their previously known low-temperature forms, are summarized in Figure P1.1. In total, six new high-pressure polymorphs were identified in **PA**, **BA**, and **PEA**, whereas the high-pressure forms of **EA** and **HA** reveal the same crystal symmetry as their low-temperature forms. Selected crystallographic parameters for the highest-pressure form of each phase are summarized in Table 1, while complete structural details are provided in Tables S1-S4 in SI of P1 and Table 1 of P2.

Table 1. Selected crystal data of all phases of SPA, from the highest investigated pressures (all at 295 K).

	C_2H_7N EA II	C_3H_9N PA II	C_3H_9N PA III	$C_4H_{11}N$ BA II	$C_4H_{11}N$ BA III	$C_5H_{13}N$ PEA II	$C_5H_{13}N$ PEA III	$C_6H_{15}N$ HA I
Pressure (GPa)	5.05(2)	2.45(2)	4.90(2)	1.45(2)	4.00(2)	3.55(2)	4.10(2)	1.40(2)
Space group	$P2_1/c$	$P2_1/c$	$P2_1/c$	$Pbc2_1$	$Pbc2_1$	$Pbc2_1$	$P2_1cn$	$Pca2_1$
Volume (Å^3)	244.0(3)	349.6(3)	314.04(5)	458.83(9)	803.7(4)	971.5(8)	473.6(2)	611.9 (5)
Unit cell dimensions a (Å)	8.310(8)	9.5576(15)	4.7444(2)	12.8348(9)	4.8802(14)	3.7562(6)	3.7101(11)	6.7241 (19)
b (Å)	4.798(4)	5.0525(12)	4.8586(4)	6.5975(11)	7.0738(10)	8.170(4)	4.0956(12)	17.052 (13)
c (Å)	6.775(3)	7.265(6)	13.8145(19)	5.4185(4)	23.282(9)	31.66(2)	31.167(6)	5.3367 (7)
β (°)	115.40(6)	94.82(3)	99.537(8)	90	90	90	90	90
Z, Z'	4, 1	4, 1	4, 1	4, 1	8, 2	8, 2	4, 1	4, 1
R_{int} (all data)	0.0263	0.0307	0.0188	0.0377	0.0397	0.0537	0.035	0.068
D_x (g cm^{-3})	1.227	1.123	1.250	1.059	1.209	1.192	1.222	1.098
R_1 [$F^2 > 2\sigma(F^2)$]	0.0941	0.0661	0.0403	0.0449	0.0596	0.0608	0.0469	0.061

The pressure dependence of molecular volumes for all identified phases is shown in Figure P1.2. All high-pressure phases are denser than their corresponding low-temperature forms. However, the mechanisms of compression differ markedly across the series. **PA**, **BA**, and **PEA** exhibit discontinuities in the molecular volume evolution, while **EA** and **HA** display monotonic compression in the investigated pressure regions.

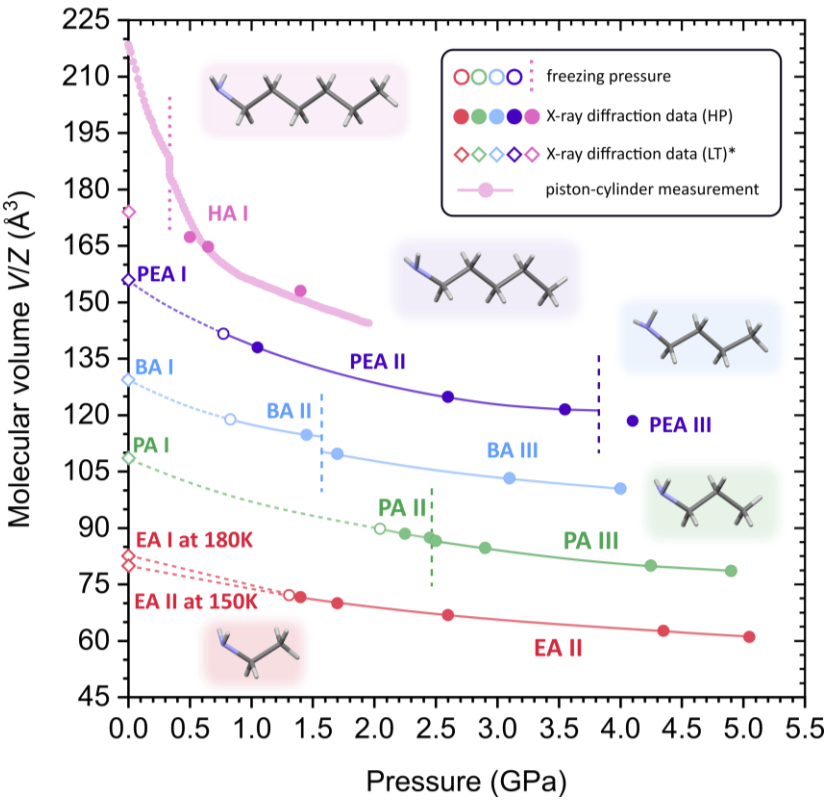

Figure P1.2. Pressure dependence of molecular volumes (Å^3) for C_2-C_6 primary amines. Empty circles and a vertical dotted line (pink) indicate the freezing pressures. Full circles show the volumes measured at high pressure, while those from low temperature (LT)* are represented by empty diamonds.[92] The critical pressures were indicated with vertical dashed lines. The estimated standard deviation (ESD) is smaller than the plotted symbols.

The pressure-volume relations show that differences in the structural response to compression cannot be explained solely by compressibility. This indicates that the distribution of space within the crystal lattice must also be considered. This aspect is examined by analyzing intermolecular voids.

Further structural information is obtained from the void-volume analysis presented in Figure P1.3.a. In **PA**, **BA**, and **PEA** phases II, the amount of free intermolecular space was 9.4%, 14.9%, and 6.2%, respectively.[93] These voids are located in regions that enable local molecular reorientation and provide the structural freedom needed to relieve compression through shortening of CH···N distances and rearrangement of the NH···N chains. All three systems show a reduction in voids during the pressure-induced transition, with free volumes of 2.5% in **PA III**, 4.9% in **BA III**, and 5.3% in **PEA III**, consistent with the formation of more tightly packed structures.

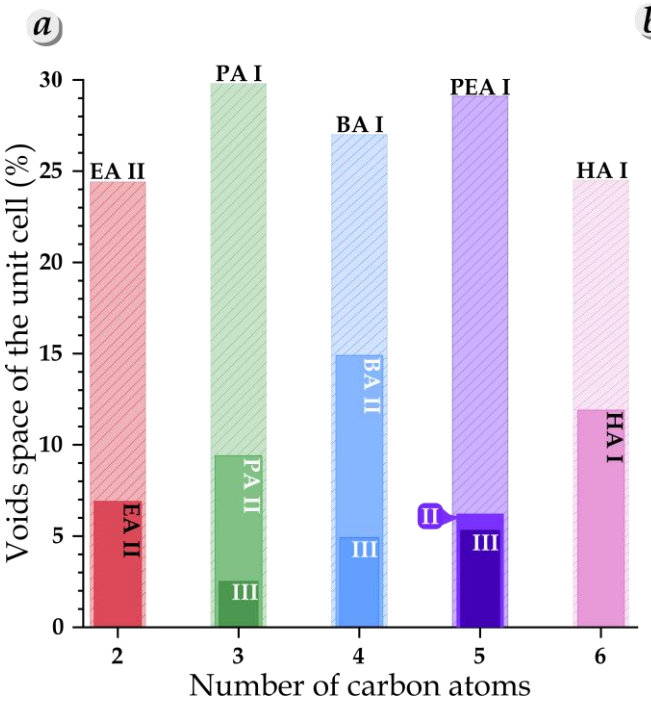

b

Compound	NH···N distance (Å)	N–H···N angle (°)
Ethylamine phase II	2.227(4) 2.596(5)	152.5(3) 154.9(3)
Propylamine phase II	2.366(3) 2.793(3)	157.72(2) 162.06(1)
Propylamine phase III	2.2183(16) 3.3076(16)	161.80(8) 66.73(1)
Butylamine phase II	2.195(3) 2.782(3)	170.39(11) 140.31(14)
Butylamine phase III	2.154(5) 2.156(6)	167.8(6) 167.9(5)
Pentylamine phase II	2.191(7) 2.313(7)	170.3(3) 147.0(9)
Pentylamine phase III	2.232(4) 2.443(4)	168.05(18) 131.82(12)
Hexylamine phase I	2.168(5) 2.811(6)	166.4(2) 142.9(4)

Figure P1.3. (a) Light, striped bars represent LT void volumes, darker bars represent the highest-pressure structures of phase II (**EA**, **PA**, **BA**, **PEA**) and phase I (**HA**). The darkest bars correspond to phase III (**PA**, **BA**, **PEA**). Void volumes were calculated as the intermolecular space accessible to a probe with a radius of 0.3 Å and a grid spacing of 0.2 Å. (b) Two shortest intermolecular H···N distances from NH···N hydrogen bonds from each phase were chosen from the highest pressures of each phase.

In contrast, **EA** and **HA**, despite having moderate free-volume space, 6.9% and 11.9% at 5.05(2) and 1.40(2) GPa, respectively, do not undergo such rearrangements. Crucially, these voids are located around the alkyl chain, which is dominated by stabilizing methyl-methyl dispersion interactions that limit local molecular reorientation. This observation indicates that the mere presence of free volume is insufficient to induce polymorphism; rather, the spatial distribution of voids relative to the hydrogen-bond network determines whether pressure-induced structural transformations can occur.

The structural response to pressure can be described by considering the topology of the hydrogen-bond networks using Etter's graph-set notation.[94] Upon compression, all investigated amines form NH···N hydrogen-bonded infinite chains described by the $C_1^1(2)$ motif, as shown in Figure P1.4., in which each nitrogen atom acts simultaneously as one hydrogen-bond donor and one acceptor; however, pressure induces geometrical rearrangements within the hydrogen-bond network and promotes the formation of additional secondary interactions.

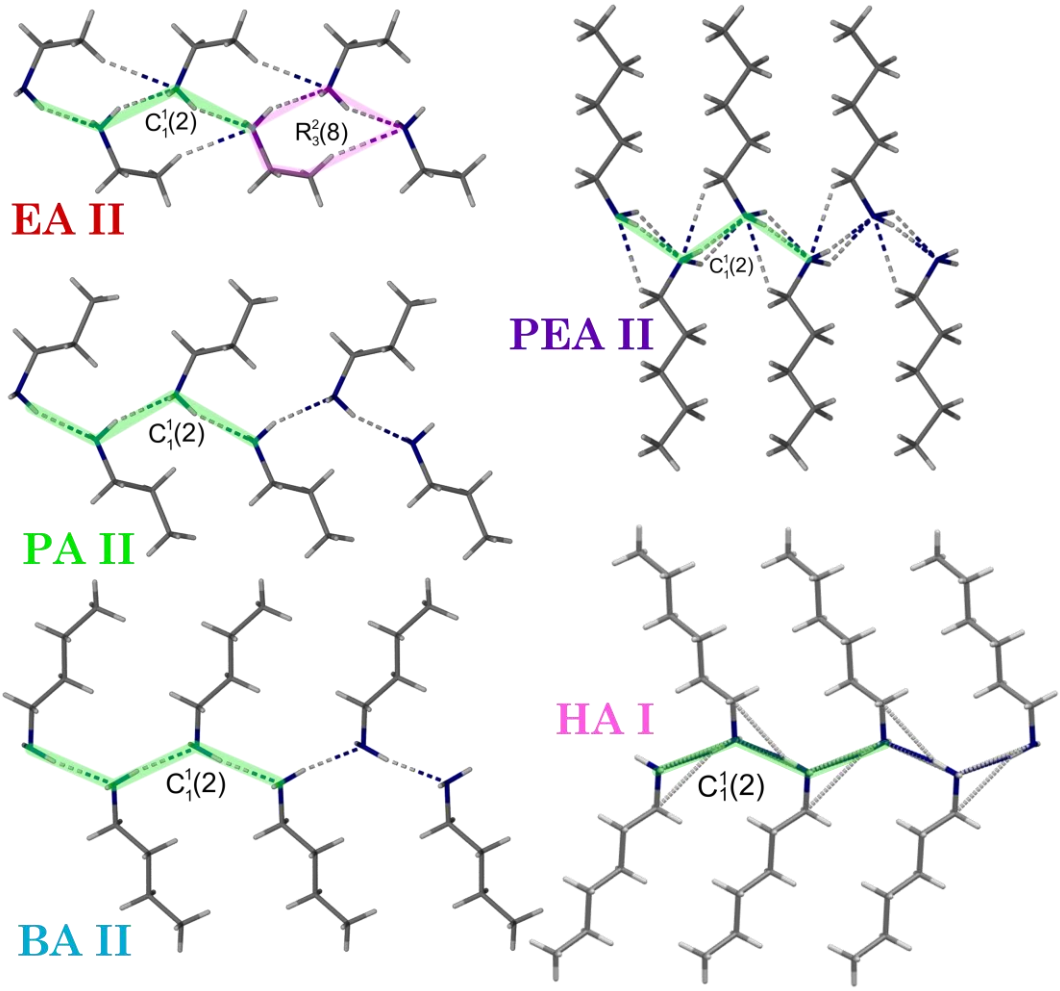

Figure P1.4. Etter's graph notation of hydrogen-bonded motifs observed in phases I and II of SPA: ethylamine (**EA II**), propylamine (**PA II**), butylamine (**BA II**), pentylamine (**PEA II**), and hexylamine (**HA I**). The dominant NH···N hydrogen-bonded chains are highlighted in green.

In **EA**, compression is associated with shortening of intermolecular NH···N distances and with the formation of short CH···N contacts, which in **EA** are observed to be more compressible than the primary NH···N bonds. These contacts lead to the formation of mixed NH···N and CH···N ring motifs of the $R_3^2(8)$ type, while the underlying chain topology remains unchanged.

PA and **PEA** exhibit a more complex evolution of hydrogen-bond motifs. At low temperature, the combination of two independent $C_1^1(2)$ chains leads to the formation of hydrogen-bonded layers containing $R_4^3(8)$ ring motifs. Under high pressure, the $C_1^1(2)$ chains remain the dominant structural element, but pressure induces rearrangements that generate additional $R_3^2(8)$ rings involving both NH···N and CH···N interactions. These changes occur together with the pressure-induced transformations observed in these systems.

BA represents an intermediate case. Although the $C_1^1(2)$ NH···N hydrogen-bonded chains persist across all observed phases, pressure induces successive rearrangements of the surrounding molecular packing, accompanied by the formation of additional short CH···N contacts and changes in ring motifs. This behavior is consistent with the transitional character of BA within the homologous series.

This behavior can be discussed in the context of the odd-even effect previously described for SPA. In their study of low-temperature phases, Maloney et al. showed that the packing of primary amines depends on whether the alkyl chain contains an odd or even number of carbon atoms. In even-numbered amines such as **EA** and HA, the terminal methyl group lies on the opposite side of the molecular axis relative to the NH_2 group, favoring a more regular packing arrangement. In contrast, odd-numbered amines (PA and **PEA**) adopt a different hydrogen-bond arrangement, which provides greater geometrical freedom within the crystal structure.

Butylamine (BA), although formally an even-numbered amine, does not fully follow this trend under high-pressure conditions. Unlike **EA** and HA, BA exhibits two new high-pressure polymorphs. This suggests that, for this chain length, the structural response to compression is not governed solely by the odd-even relation described for the low-temperature series. Instead, BA may be regarded as an intermediate case, in which the balance between NH···N hydrogen bonding, molecular packing, and dispersion interactions remains sensitive to compression.

The odd-even effect is also reflected in the alternation of melting temperatures (Figure P1.5). **PA** and **PEA** exhibit lower melting points, consistent with their more flexible NH···N hydrogen-bond motif, whereas **EA**, **BA**, and **HA** adopt the more rigid motif and therefore melt at higher temperatures. In this respect, the melting behavior follows the expected odd-even alternation. In contrast, the freezing pressures do not follow a strictly alternating trend. While **PA** crystallizes at a higher pressure than **EA**, the freezing pressure of **PEA** is lower than that of **BA**, as shown in Figure P1.5. This suggests that freezing under high-pressure conditions is affected not only by the odd-even relation but also by other structural factors, including molecular packing and the pressure response of intermolecular interactions.

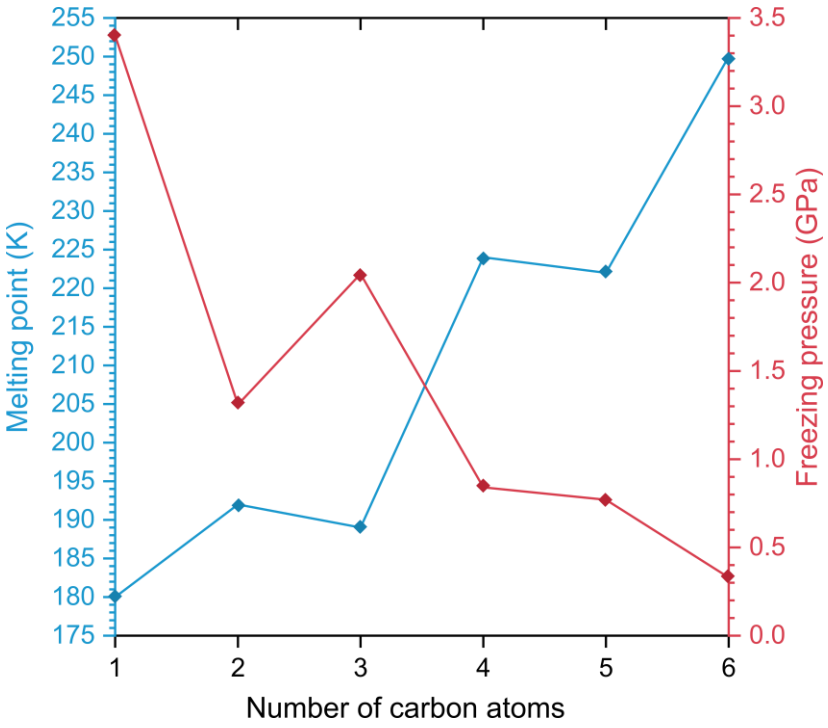

Figure P1.5. Ambient-pressure melting points (K) (blue, left axis) and ambient-temperature freezing pressures (GPa) (red, right axis) of methylamine[95] and the other SPA (**P1**+**P2**).

Overall, the comparison across the SPA series shows that high-pressure polymorphism is favored when two structural conditions occur together: (1) sufficient free volume is present in geometrically accessible regions, and (2) this space is located close to hydrogen-bonded motifs, allowing CH···N and NH···N interactions to participate in packing reorganization.

Understanding the subtle differences in intermolecular interactions arising from molecular size and geometry not only clarifies the mechanisms governing polymorphism in simple organic systems but also provides valuable guidance for interpreting pressure-induced transformations in related hydrogen-bonded materials, including alcohols, amides, and amino acids.[96,97]

P3

The study aimed to understand how high pressure influences the crystal structure, conformational changes, and aggregation patterns of the simplest symmetric dialkyl ethers $(C_nH_{2n+1})_2O$ for n=1−3. In contrast to primary amines, where hydrogen bonding defines the aggregation motif, ethers highlight the role of internal torsional flexibility. Rotation about the C−O bonds directly affects the steric environment of the oxygen atom and, consequently, the balance between CH···O and H···H interactions under compression.

An overview of the phase behaviour of dimethyl ether (**DME**), diethyl ether (**DEE**), and dipropyl ether (**DPE**), including their known low-temperature polymorphs[98,99] and the high-pressure phases identified in this work, is presented in Figure P3.1. While **DEE** and **DPE** have a labile ether oxygen bond, their ability to adapt to pressure strain varies from conformational switching to purely intermolecular reorganization.

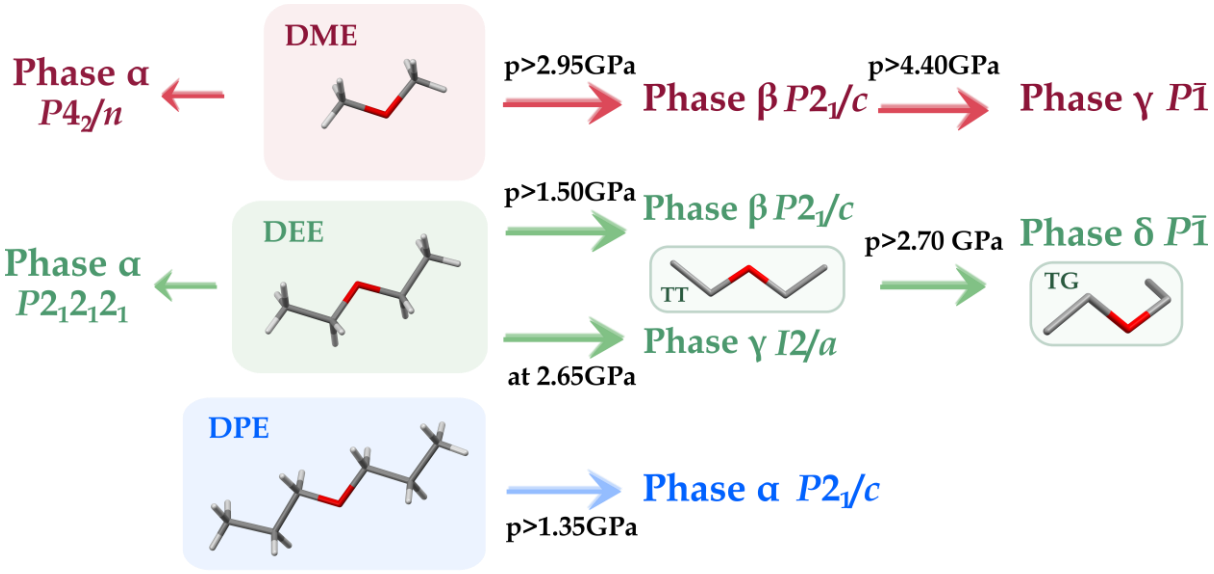

Figure P3.1. Phase behavior of **DME**, **DEE**, and **DPE**. Previously reported low-temperature polymorphs (left)[98,99] are compared with the high-pressure phases determined in this study (right). Under high-pressure conditions, phases β and γ were identified for both **DME** and **DEE**. In **DEE**, phase δ was obtained through pressure-induced transitions from phases β and γ. **DPE** remains in a single monoclinic phase across the entire investigated pressure range.

The conformational flexibility of dialkyl ethers arises from rotation about the C–O bonds and can be described by the dihedral angle τ, as illustrated in Figure P3.2. Among the three ethers, **DEE** shows the most complex high-pressure response. At 295 K, **DEE** crystallizes at 1.50 GPa in phase β, built of *trans-trans* (TT) conformers, and the phase is stable up to 2.70 GPa.

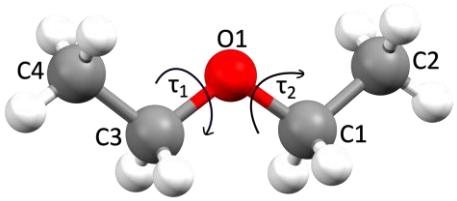

Figure P3.2. Definition of the dihedral angle τ describing the C–O–C torsion in dialkyl ethers. Rotation around the C–O bonds leads to two main conformational families: *trans-trans* (TT), in which both C–O–C–C dihedral angles are close to 180°, and *trans-gauche* (TG), in which one of these angles adopts a gauche orientation ($|\tau| \approx 60°$). These torsional states determine the accessibility of the oxygen atom and the steric environment that governs the formation of short CH···O contacts under pressure.

Phase γ was observed only once, when the sample was quickly compressed from 0.1 MPa directly to 2.65 GPa. This shows that γ is a kinetically accessible polymorph that requires rapid compression for nucleation, while under slow or stepwise compression, the system consistently crystallizes as phase β. Upon further compression, both β and γ phases transform into the triclinic phase δ, where all molecules adopt the *trans-gauche* (TG) conformation. Although the TG conformer has approximately 12.6 kJ mol^{-1} higher potential energy, as indicated by quantum-mechanical calculations in the gas phase, pressure stabilizes it by reducing steric shielding around the oxygen atom. A detailed analysis of the quantum-mechanical calculations is presented in Section 3 of the **P3**. This leads to the formation of additional short CH···O contacts, stabilizing the structure. The reverse δ → β transition on decompression below ~2.70 GPa confirms that the conformational change is fully reversible. **DEE** therefore provides a clear example of a system in which pressure acts as a conformational switch, with the nucleation pathway determining which phase can be accessed. The pressure evolution of the shortest intermolecular H···O and H···H distances observed in the high-pressure structures of **DME**, **DEE**, and **DPE** is summarized in Figure P3.3.

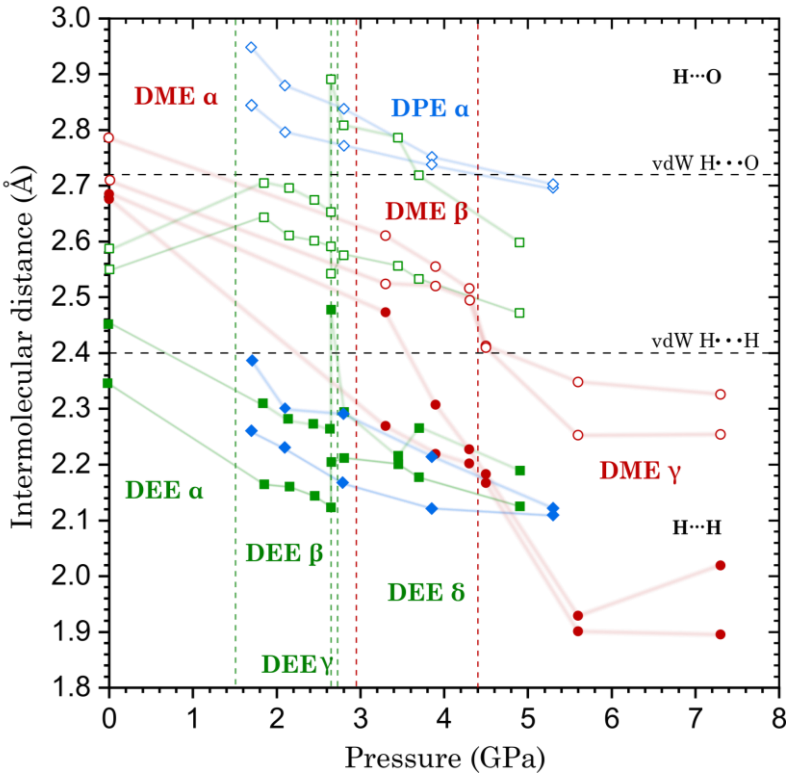

Figure P3.3. Evolution of the selected intermolecular distances of **DME** (**red**), **DEE** (**green**), and **DPE** (**blue**) as a function of pressure. The two shortest distances for the two types of interactions are presented: filled symbols correspond to H···H, while open symbols correspond to H···O distances. Black horizontal lines indicate the sum of the van der Waals radii for H···O (2.72 Å)[100] and H···H (2.40 Å)[100]. Vertical dashed lines mark the pressure stability ranges of the individual crystal phases. Lines connecting data points are guides to the eye only. The estimated standard deviations are smaller than the plotted symbols. Ambient pressure points come from previous works.[98,99]

At ambient pressure and low temperature, **DME** crystallizes in the tetragonal phase α ($P4_2/n$). At 295 K, compression to 3.30 GPa yields a monoclinic phase β ($P2_1/c$), which subsequently transforms into a triclinic phase γ ($P\bar{1}$) at 4.40 GPa. Due to the smaller steric demand of the methyl groups, the oxygen atom in **DME** is already relatively accessible to interact with the surroundings, as shown in Figure S24 in **SI** of **P3**, and the strain of compression is accommodated mainly by tightening and reorganization of existing CH···O and CH···H interactions.

At 295 K, **DPE** crystallizes at 1.70 GPa in a monoclinic phase α ($P2_1/c$). This phase remains stable up to at least 5.30 GPa, and no additional polymorphs of **DPE** were observed in the investigated pressure range. Compression of phase α is mainly reflected in the gradual shortening of intermolecular distances and

small molecular reorientations in the crystal, and is stable across the entire investigated pressure range.

The high-pressure behavior of **DME**, **DEE**, and **DPE** shows that the aggregation of simple aliphatic ethers in the solid state is controlled by the balance between molecular conformation and the formation of CH···O intermolecular contacts. Compression enables the crystallization of several distinct solid phases across the series, revealing different packing motifs accessible under high-pressure conditions. In **DEE**, the occurrence of structures built from TG conformers indicates that pressure can stabilize higher-energy conformations by increasing the accessibility of the oxygen atom and promoting more CH···O contacts. In **DME**, different crystal structures mainly differ in the arrangement of intermolecular interactions. **DPE** retains a single structural motif across the investigated pressure range, with compression accommodated by continuous structural adjustments within the same phase. Taken together, these results demonstrate that even small changes in alkyl chain length lead to different structural responses to pressure, and that weak but directional CH···O interactions play a key role in shaping aggregation patterns in dispersion-bound molecular crystals under high-pressure conditions.

P4

Butene isomers are the simplest unsaturated hydrocarbons and exhibit structural isomerism, making them a useful model system for studying how molecular shape and molecular symmetry affect crystal packing and stability under high pressure. The crystal structures of all four isomers, 1-butene (**B**), cis-2-butene (**CB**), trans-2-butene (**TB**), and isobutene (**IB**), have been determined for the first time by high-pressure single-crystal X-ray diffraction. Under ambient conditions, all four compounds are gases; however, when compressed at room temperature, they crystallize at different pressures. The observed freezing pressures at 295 K follow the sequence: **TB** (0.50 GPa) < **IB** (1.40 GPa) < **CB** (1.55 GPa) < **B** (3.65 GPa). This order indicates significant differences in solidification resistance among the isomers. A schematic representation of the molecular structures of the investigated compounds is shown in Figure P4.1.

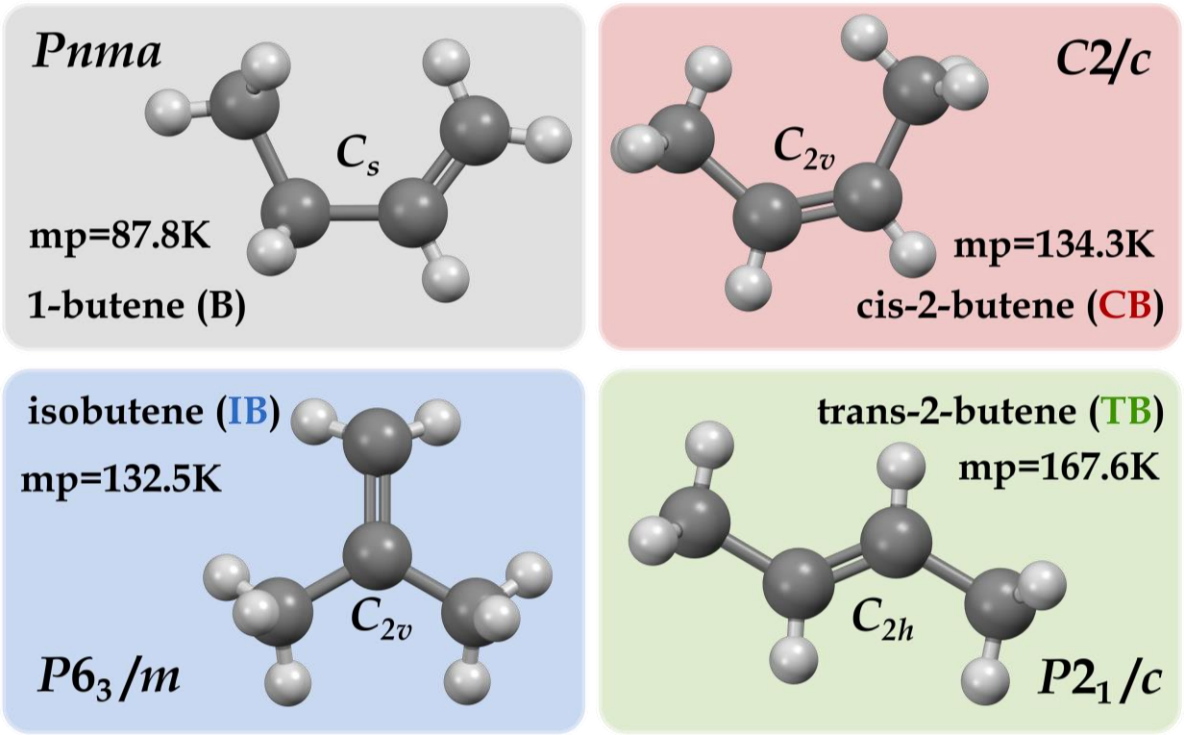

Figure P4.1. Schematic representations of the four investigated butene isomers, their abbreviations, the molecules' symmetries, and melting points are indicated.[101]

Once crystallized, all butene isomers form molecular crystals that remain stable within the investigated pressure ranges. Each isomer adopts a distinct centrosymmetric space group: **B** crystallizes in the orthorhombic space group

Pnma, **CB** and **TB** in monoclinic $C2/c$ and $P2_1/c$, respectively, while **IB** forms a hexagonal structure in $P6_3/m$ with orientationally disordered molecules occupying special positions in the unit cell. Despite having the same molecular formula (C_4H_8), these differences in crystal symmetry and packing reflect variations in molecular geometry and symmetry. (Figure P4.1.)

The four isomers exhibit different molecular symmetries in the isolated state: **B** belongs to the C_s point group, **CB** and **IB** to C_{2v}, and **TB** to C_{2h}. These differences are reflected in their melting points: **B**, with the lowest molecular symmetry, has the lowest melting point (87.8 K); **TB**, the most symmetric isomer, exhibits the highest melting point (167.6 K); **CB** and **IB** display intermediate melting points of 134.3 K and 132.5 K, respectively. (Figure P4.1.)

An inverse relationship is observed between the ambient-pressure melting points and the room-temperature freezing pressures. The isomer with the highest melting point, **TB**, crystallizes at the lowest pressure, while **B**, with the lowest melting point, requires the highest pressure to solidify (*cf.* Figure 2 in **P4**). The densities of the crystal structures determined just above the freezing pressures increase in the order **TB** < **IB** < **CB** < **B**, mirroring the sequence of freezing pressures. These observations indicate that denser molecular packing is associated with higher crystallization pressure in these simple hydrocarbons.

Among the studied compounds, **B** shows the strongest tendency toward pressure- and temperature-assisted polymerization. As a result, its crystal structure could be determined only at 4.40 GPa, where it adopts the orthorhombic *Pnma* structure with four molecules in the unit cell. **IB** also shows a pronounced tendency toward polymerization at elevated temperatures, which limits crystal growth at higher pressures. In both cases, polymerization hindered the preparation of single crystals, as the sample no longer contained a liquid phase suitable for crystal growth, but only solid material together with polymeric products. After opening the DAC, the recovered sample often appeared as a gel-like mass. Although single crystals of **B** and **IB** were obtained in selected experiments, in many cases, crystal growth was disrupted and elongated, and fibrous structures formed instead (Figure P4.2). In contrast, **CB** and **TB** isomers

remain chemically stable and do not polymerize within the investigated pressure and temperature range.

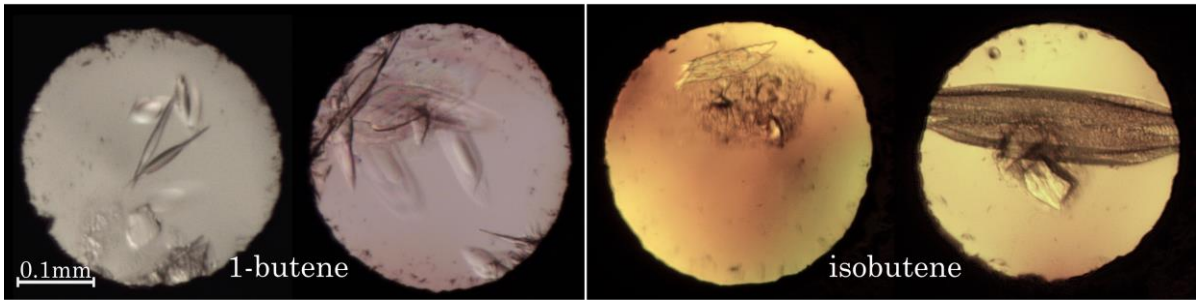

Figure P4.2. Photographs of 1-butene (**B**) and isobutene (**IB**) confined in a DAC after compression and heating at high pressure. Upon cooling, the samples do not resume regular single-crystal growth but retain elongated, fibrous morphologies. This behavior suggests partial polymerization under high-pressure and high-temperature conditions.

To analyze packing efficiency and steric effects, the six shortest intermolecular C···C distances were examined as a function of pressure for each structure, presented in Figure P4.3. In the structure of **B** at 4.40 GPa, all six shortest C···C distances are shorter than the sum of the van der Waals radii of two carbon atoms (3.40 Å), indicating close molecular contacts and significant steric strain. **CB** shows a more gradual evolution: at 2.25 GPa, only two of the shortest distances are below this limit, while above 3 GPa, all six distances become shorter than 3.40 Å. It should be emphasized that the presence of short intermolecular C···C distances reflects increased packing strain under compression but does not, by itself, imply chemical reactivity; the tendency toward polymerization is primarily governed by the intrinsic reactivity and accessibility of the C=C bond.

In contrast, all intermolecular C···C distances in **TB** and **IB** remain longer than the van der Waals threshold throughout the investigated pressure ranges. This observation implies looser packing and reduced steric strain, consistent with the greater structural stability and lack of phase transitions observed for these isomers. Detailed analysis of these contacts, including Hirshfeld surface analysis, is presented in Figures S14-S18 in the Supporting Information.

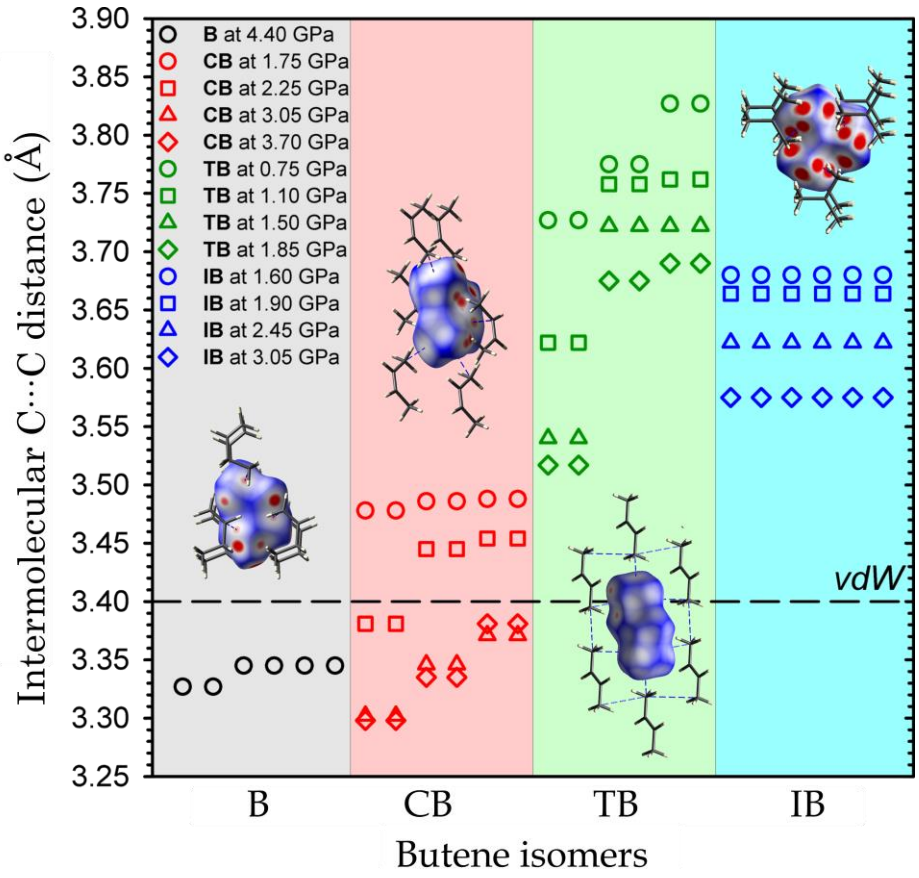

Figure P4.3. Six shortest intermolecular C···C distances (Å) for each high-pressure butene isomer determined at 295 K. The sum of van der Waals radii of two carbon atoms of 3.40 Å is indicated by a horizontal black dashed line. Hirshfeld surfaces for the highest pressures of each isomer are presented, mapped with d_{norm} (from −0.1 to 0.7).[90]

The systematic differences in intermolecular distances provide a structural explanation for the observed variations in stability and polymerization behavior. The presence of short contacts in **B** and **CB** suggests that further compression may promote structural rearrangements or chemical reactions. In contrast, the more loose packing in **TB** and **IB** favors the persistence of the molecular crystal.

The observations made for butene isomers fit into the broader picture of transformation pathways of unsaturated hydrocarbons under extreme thermobaric conditions reported in the literature.[102] Previous experimental studies have shown that for nonaromatic, noncondensed unsaturated hydrocarbons, the dominant pressure-induced transformations are polymerization and, at higher energies, dissociation. It has been shown that increasing pressure lowers the temperature required for polymerization, in some

cases to values below 500 K, and that pressures above approximately 1 GPa can promote the initiation of such reactions.[103–105]

The present results show that polymerization does not occur in every butene isomers subjected to compression. This suggests that, in addition to pressure and temperature, factors such as molecular geometry, the accessibility of the double bond, and constraints imposed by crystal packing also need to be considered when discussing possible pressure-induced reactivity. Overall, the study of butene isomers demonstrates that the response of unsaturated hydrocarbons to compression, including their resistance to polymerization, depends not only on thermodynamic conditions but also on molecular geometry and crystal-packing effects.

P5

Isobutane represents the simplest, branched hydrocarbon in which crystal packing is dominated by dispersion forces.[106] In contrast to linear *n*-butane,[107] the branched molecular shape leads to a different distribution of short intermolecular contacts and steric effects. The present study extends earlier investigations of simple aliphatic hydrocarbons under high pressure, including ethane,[108,109] propane,[107,110] and butane.[111] Under compression, isobutane undergoes an isostructural phase transition between two closely related polymorphs, denoted **α** and **β**, which can be accessed by different nucleation routes (Figure P5.1).

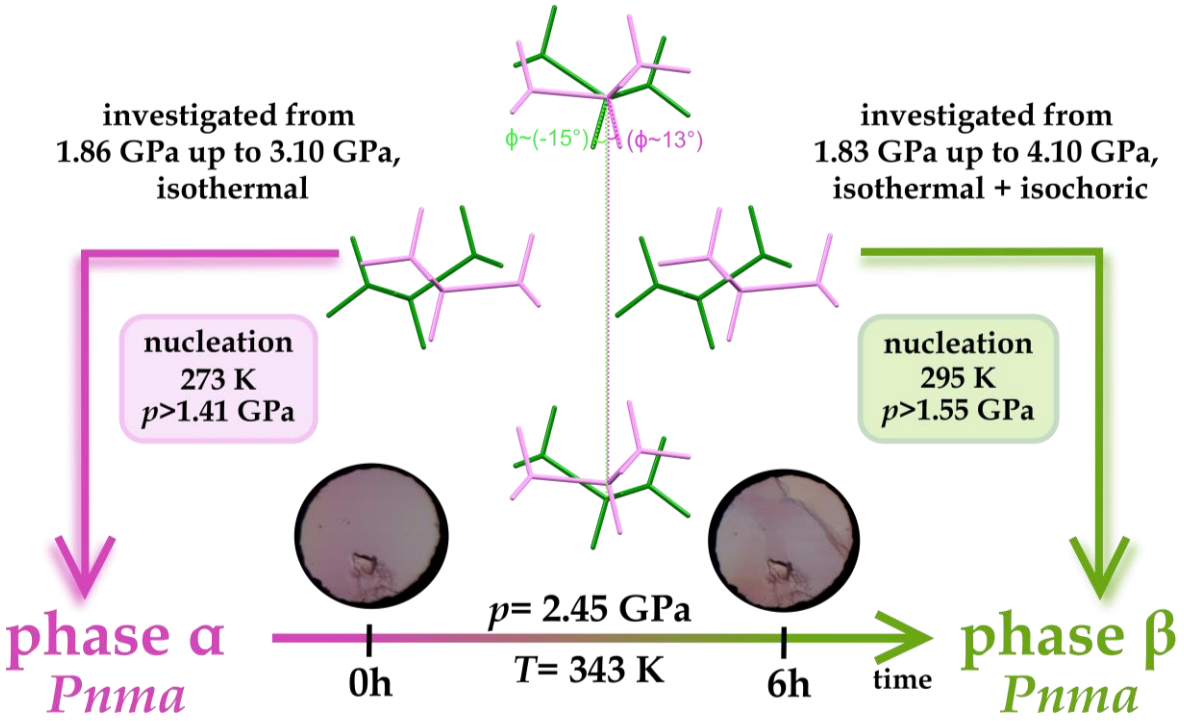

Figure P5.1. Schematic representation of the nucleation process of phases **α** and **β** of isobutane under high pressure, and their thermal phase transition, together with their characteristic molecular tilt angles ($\phi \approx +13°$ for **α** and $\phi \approx -15°$ for **β**).

When the liquid is compressed at room temperature, it crystallizes exclusively as phase **β** at 1.55 GPa. In contrast, phase **α** nucleates only after cooling the sample to 273 K at pressures above 1.41 GPa. To enable a consistent comparison of the crystal packing at the crystallization phase, the molecular volumes of phases **α** and **β**, as well as *n*-butane,[107] were extrapolated to their respective freezing pressures (*cf.* Figure P5.2). According to previous high-pressure

investigations on *n*-butane, it has a much smaller molecular volume and lower void fraction than isobutane (Figure P5.2). The molecular volume at crystallization indicates that phase **α** is slightly more efficiently packed, whereas phase **β** becomes denser at higher pressures. With compression, phase **β** becomes a more energetically favorable phase and ultimately, as indicated by the quantum-mechanical calculations, becomes dominant above 1.64 GPa (*cf.* Figure 5 in **P5**). These observations are further confirmed by the experimental observation that, once formed, phase **α** remains stable at room temperature up to 3.10 GPa; upon heating, it undergoes a phase transition to phase **β**. Details of the experimental procedure are provided in the Experimental Section of **P5**, and the evolution of unit-cell parameters with pressure is shown in Figure S15 of the **SI**.

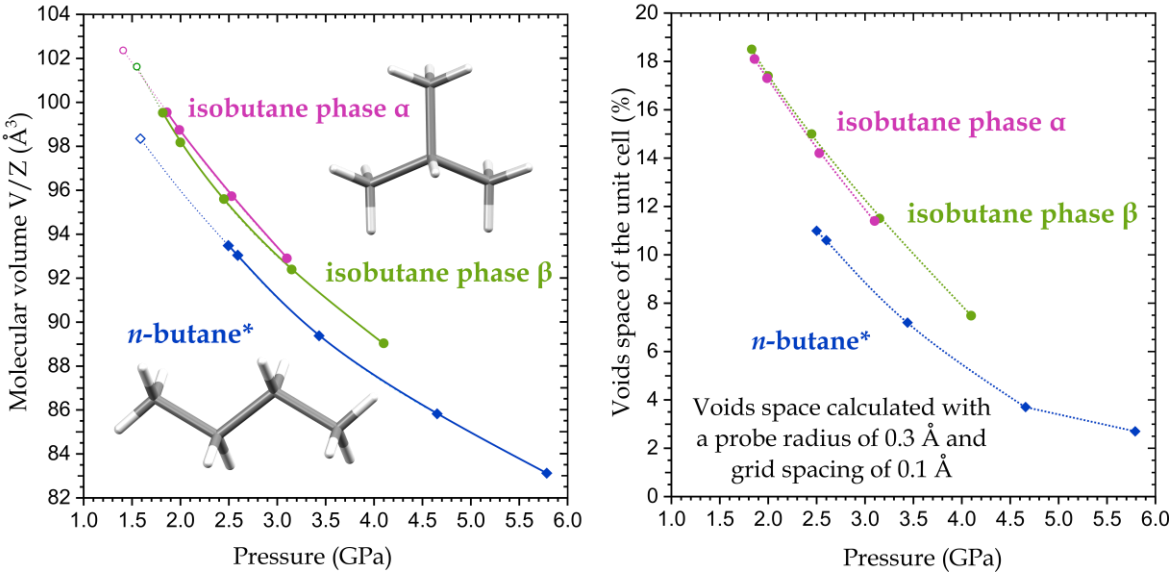

Figure P5.2. Molecular volumes and void space of isobutane phases **α** (**pink**) and **β** (**green**) compared with those of *n*-butane***** (**blue**).[107] Phase **α** is slightly denser near its freezing point, whereas phase **β** becomes the denser isobutane phase at higher pressures. In the entire pressure range, *n*-butane remains more efficiently packed than isobutane, with lower molecular volumes and smaller void fractions.

At this point, it is useful to relate these observations to Carnelley's rule, which states that the more symmetric isomer typically exhibits a higher melting point due to the more efficient crystal packing.[112] The butane isomers are an exception to Carnelley's rule at ambient pressure: the less symmetric *n*-butane melts at 134.9 K, whereas the more symmetric isobutane melts at 113.7 K. Thus, despite

its lower molecular symmetry, *n*-butane packs more efficiently in the solid state than isobutane.[107] Under isothermal compression at 295 K, however, the crystallization behaviour shows the opposite trend. Isobutane freezes at 1.41 GPa into phase α, whereas *n*-butane requires higher pressure to crystallize. Hence, under compression, the higher-symmetric isomer solidifies at lower pressure, in apparent agreement with Carnelley's symmetry argument.

The transformation between phases **α** and **β** is isostructural and displacive: the space-group symmetry and molecular positions in the lattice are preserved, while the unit cell undergoes a pronounced deformation. The structural mechanism of the phase transition involves a reorientation of the isobutane molecules within a crystal lattice. To quantify this reorientation, a molecular tilt angle, ϕ, is defined as the angle between the molecular pseudo-C_3 axis and [*x*] direction (see Figure 4 in **P5)**. In phase **α**, the molecules are tilted by approximately +13°, whereas in phase **β**, the tilt is −15°. This suggests that the transformation between phases **α** and **β** should involve a rotation around the molecular axis through an intermediate position near $\phi \approx -1°$, which marks the barrier between the two free-energy minima. Detailed analysis of the energy barrier is shown in Figure 5 and Table 2 in **P5**.

The molecular reorientation has direct consequences for the macroscopic deformation of the crystal. As illustrated schematically in Figure P5.3, the change in tilt angle from ϕ_α in phase **α** to ϕ_β in phase **β** changes the molecular length L projected onto the crystallographic axes. As a result, the unit cell elongates along the **a** axis while simultaneously contracting along the **c** axis, producing the characteristic anisotropic strain observed experimentally during the **α** → **β** transition. This deformation is fully consistent with the tilt-driven geometric mechanism and does not require changes in molecular identity or symmetry.

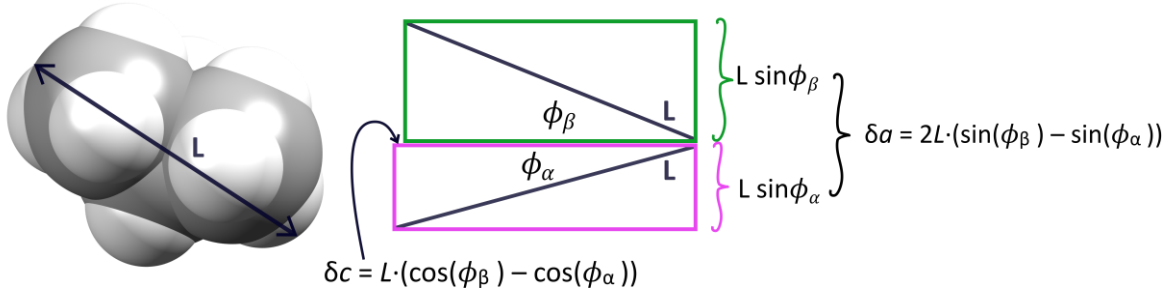

Figure P5.3. Schematic illustration of the geometric mechanism responsible for the anisotropic deformation of the unit cell during the **α** → **β** transition. The change in molecular tilt angle from ϕ_α to ϕ_β affects how the molecular length L aligns with the crystallographic **a** and **c** axes, causing the **a** axis to elongate (by δa) and the **c** axis to shorten (by δc). Values of ϕ_α and ϕ_β are exaggerated for clarity.

With increasing pressure, the tilt-driven rearrangement leads to more efficient packing in phase **β**, in agreement with the evolution of C···H contacts (cf. Figure 7 in **P5**). Taken together, these results show that the **α** → **β** transition in isobutane arises from a subtle interplay between molecular shape, symmetry, and rotational degrees of freedom. Pressure acts here as a driving force that reorganizes dispersion-bound molecular crystals through continuous molecular reorientation rather than reconstructive transformations. Isobutane, therefore, provides a clear and instructive example of how pressure can reshape polymorphic landscapes in simple hydrocarbons by coupling molecular geometry with packing efficiency.

4. Conclusions

This project presents a systematic high-pressure crystallographic investigation of simple organic molecules composed of light elements. Such compounds are strongly underrepresented in structural databases, despite their fundamental importance for understanding molecular packing and intermolecular interactions. Small, single-component organic molecules containing only C, H, O, and N atoms with up to ten carbon atoms account for only about 1% of the Cambridge Structural Database, while very small C H N systems represent less than 0.1%.[113] In this context, the present work addresses a clear gap in experimental crystallography by providing detailed structural data for simple molecular systems under non-ambient conditions.

In total, 64 previously unknown crystal structures were determined and fully characterized for a series of small amines, ethers, hydrocarbons, and their isomers, including ethylamine, propylamine, butylamine, pentylamine, hexylamine, dimethyl ether, diethyl ether, dipropyl ether, butene and its isomers, and isobutane. In addition, 20 new polymorphic forms were discovered across these systems, significantly expanding the known solid-state landscapes of compounds that are often regarded as structurally simple.

Beyond structural determination, the project elucidated the mechanisms of pressure-induced phase transitions in several key systems. These include the isostructural α→β phase transition of isobutane and two distinct phase transitions observed for diethyl ether under high pressure (β→δ and γ→δ). These cases demonstrate that even small, weakly interacting molecules can exhibit complex, non-trivial phase behavior under compression. The results clearly show that pressure acts as an efficient external parameter, capable of driving conformational rearrangements and reorganizing molecular packing without altering chemical composition.

A central outcome of this work is the systematic identification of the role played by weak intermolecular interactions, including N−H···N, C−H···N, C−H···O, O···O, C···C, and H···H contacts, in stabilizing high-pressure and low-temperature phases. The balance between directional interactions and dispersion

forces was shown to control polymorphic stability. These findings provide direct experimental evidence that weak interactions, often considered secondary at ambient conditions, play an important role under compression and govern the structural response of small organic molecules.

The project also substantially extends experimental pressure–temperature phase diagrams for numerous compounds by providing crystallization pressures at room temperature, melting temperatures under high pressure, and thermodynamic conditions of newly discovered phase transitions. These data fill gaps in the experimental literature and offer reliable reference points for future experimental and computational studies.

Overall, the results significantly advance crystallography, physical chemistry, and materials science by deepening the understanding of gas and liquid crystallization under extreme conditions, pressure-driven phase stabilization, conformational flexibility of small molecules, and the structural consequences of weak intermolecular interactions. The structural and mechanistic models developed in this work are expected to be broadly applicable to polymorphism prediction, the design of materials stabilized by weak interactions, and the interpretation of chemical behavior under planetary conditions. In a broader context, the findings are relevant to geochemistry and planetary science, where the investigated pressure range corresponds to conditions present in the interiors of giant planets, as well as to pharmaceutical science and chemical engineering, where understanding pressure-dependent molecular organization is important for solid-state stability, separation processes, and gas storage technologies.

5. References

(1) Bridgman, P. W. Theoretically Interesting Aspects of High Pressure Phenomena. *Rev. Mod. Phys.* **1935**, *7* (1), 1–33. https://doi.org/10.1103/RevModPhys.7.1.

(2) McMillan, P. F. Pressing on: The Legacy of Percy W. Bridgman. *Nat. Mater.* **2005**, *4* (10), 715–718. https://doi.org/10.1038/nmat1488.

(3) Bassett, W. A. Diamond Anvil Cell, 50th Birthday. *High Press. Res.* **2009**, *29* (2), 163–186. https://doi.org/10.1080/08957950802597239.

(4) Dubrovinsky, L.; Dubrovinskaia, N.; Bykova, E.; Bykov, M.; Prakapenka, V.; Prescher, C.; Glazyrin, K.; Liermann, H.-P.; Hanfland, M.; Ekholm, M.; Feng, Q.; Pourovskii, L. V.; Katsnelson, M. I.; Wills, J. M.; Abrikosov, I. A. The Most Incompressible Metal Osmium at Static Pressures above 750 Gigapascals. *Nature* **2015**, *525* (7568), 226–229. https://doi.org/10.1038/nature14681.

(5) Miao, M.; Sun, Y.; Zurek, E.; Lin, H. Chemistry under High Pressure. *Nat. Rev. Chem.* **2020**, *4* (10), 508–527. https://doi.org/10.1038/s41570-020-0213-0.

(6) Struzhkin, V. V. Superconductivity in Compressed Hydrogen-Rich Materials: Pressing on Hydrogen. *Phys. C Supercond. its Appl.* **2015**, *514*, 77–85. https://doi.org/10.1016/j.physc.2015.02.017.

(7) Eremets, M. I.; Trojan, I. A.; Medvedev, S. A.; Tse, J. S.; Yao, Y. Superconductivity in Hydrogen Dominant Materials: Silane. *Science (80-.).* **2008**, *319* (5869), 1506–1509. https://doi.org/10.1126/science.1153282.

(8) Drozdov, A. P.; Eremets, M. I.; Troyan, I. A.; Ksenofontov, V.; Shylin, S. I. Conventional Superconductivity at 203 Kelvin at High Pressures in the Sulfur Hydride System. *Nature* **2015**, *525* (7567), 73–76. https://doi.org/10.1038/nature14964.

(9) Mao, W. L.; Mao, H. Hydrogen Storage in Molecular Compounds. *Proc. Natl. Acad. Sci.* **2004**, *101* (3), 708–710. https://doi.org/10.1073/pnas.0307449100.

(10) Boldyreva, E. V; Shakhtshneider, T. P.; Ahsbahs, H.; Sowa, H.; Uchtmann, H. Effect of High Pressure on the Polymorphs of Paracetamol. *J. Therm. Anal. Calorim.* **2002**, *68* (2), 437–452. https://doi.org/10.1023/A:1016079400592.

(11) Fabbiani, F. P. A.; Pulham, C. R. High-Pressure Studies of Pharmaceutical Compounds and Energetic Materials. *Chem. Soc. Rev.* **2006**, *35* (10), 932–942. https://doi.org/10.1039/b517780b.

(12) Kanyanta, V. Microstructure-Property Correlations for Hard, Superhard, and Ultrahard Materials. *Microstruct. Correl. Hard, Superhard, Ultrahard Mater.* **2016**, 1–239. https://doi.org/10.1007/978-3-319-29291-5.

(13) Wang, Y. X.; Zhang, S. Toward Hard yet Tough Ceramic Coatings. *Surf. Coatings Technol.* **2014**, *258*, 1–16. https://doi.org/10.1016/j.surfcoat.2014.07.007.

(14) Vepřek, S. The Search for Novel, Superhard Materials. *J. Vac. Sci. Technol. A Vacuum, Surfaces, Film.* **1999**, *17* (5), 2401–2420. https://doi.org/10.1116/1.581977.

(15) Collings, I. E.; Goodwin, A. L. Metal-Organic Frameworks under Pressure. *J. Appl. Phys.* **2019**, *126* (18). https://doi.org/10.1063/1.5126911.

(16) Jones, I. M.; Turner, G. F.; Pitts, K.; Powell, R.; Riboldi-Tunnicliffe, A.; Williamson, R.; Boer, S.; Allen, L.; Moggach, S. A. High-Pressure Induced Guest-Mediated Gate Opening Behaviour of the Co-Based Framework ZIF-67. *CrystEngComm* **2023**, *25* (47), 6533–6538. https://doi.org/10.1039/D3CE00979C.

(17) Mao, H.-K.; Chen, X.-J.; Ding, Y.; Li, B.; Wang, L. Solids, Liquids, and Gases under High Pressure. *Rev. Mod.*

Phys. **2018**, *90* (1), 015007. https://doi.org/10.1103/RevModPhys.90.015007.

(18) Lobanov, S. S.; Chen, P.-N.; Chen, X.-J.; Zha, C.-S.; Litasov, K. D.; Mao, H.-K.; Goncharov, A. F. Carbon Precipitation from Heavy Hydrocarbon Fluid in Deep Planetary Interiors. *Nat. Commun.* **2013**, *4* (1), 2446. https://doi.org/10.1038/ncomms3446.

(19) Merlini, M.; Crichton, W. A.; Hanfland, M.; Gemmi, M.; Müller, H.; Kupenko, I.; Dubrovinsky, L. Structures of Dolomite at Ultrahigh Pressure and Their Influence on the Deep Carbon Cycle. *Proc. Natl. Acad. Sci.* **2012**, *109* (34), 13509–13514. https://doi.org/10.1073/pnas.1201336109.

(20) David R. Williams. *Sun Fact Sheet*. NASA. https://nssdc.gsfc.nasa.gov/planetary/factsheet/sunfact.html.

(21) Clark, R. N.; Curchin, J. M.; Barnes, J. W.; Jaumann, R.; Soderblom, L.; Cruikshank, D. P.; Brown, R. H.; Rodriguez, S.; Lunine, J.; Stephan, K.; Hoefen, T. M.; Le Mouélic, S.; Sotin, C.; Baines, K. H.; Buratti, B. J.; Nicholson, P. D. Detection and Mapping of Hydrocarbon Deposits on Titan. *J. Geophys. Res. Planets* **2010**, *115* (E10). https://doi.org/10.1029/2009JE003369.

(22) Fulchignoni, M.; Ferri, F.; Angrilli, F.; Ball, A. J.; Bar-Nun, A.; Barucci, M. A.; Bettanini, C.; Bianchini, G.; Borucki, W.; Colombatti, G.; Coradini, M.; Coustenis, A.; Debei, S.; Falkner, P.; Fanti, G.; Flamini, E.; Gaborit, V.; Grard, R.; Hamelin, M.; Harri, A. M.; Hathi, B.; Jernej, I.; Leese, M. R.; Lehto, A.; Lion Stoppato, P. F.; López-Moreno, J. J.; Mäkinen, T.; McDonnell, J. A. M.; McKay, C. P.; Molina-Cuberos, G.; Neubauer, F. M.; Pirronello, V.; Rodrigo, R.; Saggin, B.; Schwingenschuh, K.; Seiff, A.; Simões, F.; Svedhem, H.; Tokano, T.; Towner, M. C.; Trautner, R.; Withers, P.; Zarnecki, J. C. In Situ Measurements of the Physical Characteristics of Titan's Environment. *Nature* **2005**, *438* (7069), 785–791. https://doi.org/10.1038/nature04314.

(23) Maynard-Casely, H. E.; Cable, M. L.; Malaska, M. J.; Vu, T. H.; Choukroun, M.; Hodyss, R. Prospects for Mineralogy on Titan. *Am. Mineral.* **2018**, *103* (3), 343–349. https://doi.org/10.2138/am-2018-6259.

(24) Brazhkin, V. V.; Lyapin, A. G.; Hemley, R. J. Harder than Diamond: Dreams and Reality. *Philos. Mag. A* **2002**, *82* (2), 231–253. https://doi.org/10.1080/01418610110067743.

(25) Katrusiak, A. High-Pressure Crystallography. *Acta Crystallogr. Sect. A Found. Crystallogr.* **2008**, *64* (1), 135–148. https://doi.org/10.1107/S0108767307061181.

(26) Genoni, A.; Macchi, P. Quantum Crystallography in the Last Decade: Developments and Outlooks. *Crystals* **2020**, *10* (6), 1–20. https://doi.org/10.3390/cryst10060473.

(27) Price, S. L. The Computational Prediction of Pharmaceutical Crystal Structures and Polymorphism. *Adv. Drug Deliv. Rev.* **2004**, *56* (3), 301–319. https://doi.org/10.1016/j.addr.2003.10.006.

(28) Kendrick, J.; Leusen, F. J. J.; Neumann, M. A.; Van De Streek, J. Progress in Crystal Structure Prediction. *Chem. - A Eur. J.* **2011**, *17* (38), 10736–10744. https://doi.org/10.1002/chem.201100689.

(29) Reilly, A. M.; Cooper, R. I.; Adjiman, C. S.; Bhattacharya, S.; Boese, A. D.; Brandenburg, J. G.; Bygrave, P. J.; Bylsma, R.; Campbell, J. E.; Car, R.; Case, D. H.; Chadha, R.; Cole, J. C.; Cosburn, K.; Cuppen, H. M.; Curtis, F.; Day, G. M.; DiStasio, R. A.; Dzyabchenko, A.; Van Eijck, B. P.; Elking, D. M.; Van Den Ende, J. A.; Facelli, J. C.; Ferraro, M. B.; Fusti-Molnar, L.; Gatsiou, C. A.; Gee, T. S.; De Gelder, R.; Ghiringhelli, L. M.; Goto, H.; Grimme, S.; Guo, R.; Hofmann, D. W. M.; Hoja, J.; Hylton, R. K.; Iuzzolino, L.; Jankiewicz, W.; De Jong, D. T.; Kendrick, J.; De Klerk, N. J. J.; Ko, H. Y.; Kuleshova, L. N.; Li, X.; Lohani, S.; Leusen, F. J. J.; Lund, A. M.; Lv, J.; Ma, Y.; Marom, N.; Masunov, A. E.; McCabe, P.; McMahon, D. P.; Meekes, H.; Metz, M. P.; Misquitta, A. J.; Mohamed, S.; Monserrat, B.; Needs, R. J.; Neumann, M. A.; Nyman, J.; Obata, S.; Oberhofer, H.; Oganov, A. R.; Orendt, A. M.; Pagola, G. I.; Pantelides, C. C.; Pickard, C. J.; Podeszwa, R.; Price, L. S.; Price, S. L.; Pulido, A.; Read, M. G.; Reuter, K.; Schneider, E.; Schober, C.; Shields, G. P.; Singh, P.; Sugden, I. J.; Szalewicz, K.; Taylor, C. R.; Tkatchenko, A.; Tuckerman, M. E.; Vacarro, F.; Vasileiadis, M.; Vazquez-Mayagoitia, A.; Vogt, L.; Wang, Y.;

Watson, R. E.; De Wijs, G. A.; Yang, J.; Zhu, Q.; Groom, C. R. Report on the Sixth Blind Test of Organic Crystal Structure Prediction Methods. *Acta Crystallogr. Sect. B Struct. Sci. Cryst. Eng. Mater.* **2016**, *72* (4), 439–459. https://doi.org/10.1107/S2052520616007447.

(30) Steiner, T. The Hydrogen Bond in the Solid State. *Angew. Chemie Int. Ed.* **2002**, *41* (1), 48–76. https://doi.org/10.1002/1521-3773(20020104)41:1<48::AID-ANIE48>3.0.CO;2-U.

(31) Resnati, G.; Boldyreva, E.; Bombicz, P.; Kawano, M. Supramolecular Interactions in the Solid State. *IUCrJ* **2015**, *2* (6), 675–690. https://doi.org/10.1107/S2052252515014608.

(32) Desiraju, G. R. Hydrogen Bridges in Crystal Engineering: Interactions without Borders. *Acc. Chem. Res.* **2002**, *35* (7), 565–573. https://doi.org/10.1021/ar010054t.

(33) Dunitz, J. D.; Gavezzotti, A. Molecular Recognition in Organic Crystals: Directed Intermolecular Bonds or Nonlocalized Bonding? *Angew. Chemie - Int. Ed.* **2005**, *44* (12), 1766–1787. https://doi.org/10.1002/anie.200460157.

(34) Kitaigorodsky, A. I. *Molecular Crystals and Molecules*; New York ; London : Academic Press, 1973.

(35) Arunan, E.; Desiraju, G. R.; Klein, R. A.; Sadlej, J.; Scheiner, S.; Alkorta, I.; Clary, D. C.; Crabtree, R. H.; Dannenberg, J. J.; Hobza, P.; Kjaergaard, H. G.; Legon, A. C.; Mennucci, B.; Nesbitt, D. J. Definition of the Hydrogen Bond (IUPAC Recommendations 2011). *Pure Appl. Chem.* **2011**, *83* (8), 1637–1641. https://doi.org/10.1351/PAC-REC-10-01-02.

(36) Pramanik, S.; Chopra, D. Unravelling the Importance of H Bonds, σ–Hole and π–Hole-Directed Intermolecular Interactions in Nature. *J. Indian Inst. Sci.* **2020**, *100* (1), 43–59. https://doi.org/10.1007/s41745-019-00144-6.

(37) Dereka, B.; Yu, Q.; Lewis, N. H. C.; Carpenter, W. B.; Bowman, J. M.; Tokmakoff, A. Crossover from Hydrogen to Chemical Bonding. *Science (80-.).* **2021**, *371* (6525), 160–164. https://doi.org/10.1126/science.abe1951.

(38) Matta, C. F.; Hernández-Trujillo, J.; Tang, T. H.; Bader, R. F. W. Hydrogen - Hydrogen Bonding: A Stabilizing Interaction in Molecules and Crystals. *Chem. - A Eur. J.* **2003**, *9* (9), 1940–1951. https://doi.org/10.1002/chem.200204626.

(39) Katrusiak, A. General Description of Hydrogen-Bonded Solids at Varied Pressures and Temperatures. In *High-Pressure Crystallography*; Springer Netherlands: Dordrecht, 2004; pp 513–520. https://doi.org/10.1007/978-1-4020-2102-2_31.

(40) Katrusiak, A. Macroscopic and Structural Effects of Hydrogen-Bond Transformations. *Crystallogr. Rev.* **1996**, *5* (2), 133–175. https://doi.org/10.1080/08893119608035390.

(41) Katrusiak, A. Hydrogen-Bonded Solids at Varied Pressures and Temperatures. *High-Pressure Crystallogr. - Lect. Notes, 34th Erice Course* **2003**, 459–464.

(42) Dunitz, J. D.; Gavezzotti, A. How Molecules Stick Together in Organic Crystals: Weak Intermolecular Interactions. *Chem. Soc. Rev.* **2009**, *38* (9), 2622–2633. https://doi.org/10.1039/b822963p.

(43) Ho, P. C.; Wang, J. Z.; Meloni, F.; Vargas-Baca, I. Chalcogen Bonding in Materials Chemistry. *Coord. Chem. Rev.* **2020**, *422*, 213464. https://doi.org/10.1016/j.ccr.2020.213464.

(44) Wright, J. D. *Molecular Crystals*, 1st ed.; Molecular Crystals; Cambridge University Press: Cambridge, 1995.

(45) Fahlman, B. D. *Materials Chemistry*, 1st ed.; Springer Netherlands: Dordrecht, 2007. https://doi.org/10.1007/978-1-4020-6120-2.

(46) Shefter, E.; Higuchi, T. Dissolution Behavior of Crystalline Solvated and Nonsolvated Forms of Some Pharmaceuticals. *J. Pharm. Sci.* **1963**, *52* (8), 781–791. https://doi.org/10.1002/jps.2600520815.

(47) Naumov, P.; Chizhik, S.; Panda, M. K.; Nath, N. K.; Boldyreva, E. Mechanically Responsive Molecular Crystals. *Chem. Rev.* **2015**, *115* (22), 12440–12490. https://doi.org/10.1021/acs.chemrev.5b00398.

(48) Awad, W. M.; Davies, D. W.; Kitagawa, D.; Mahmoud Halabi, J.; Al-Handawi, M. B.; Tahir, I.; Tong, F.; Campillo-Alvarado, G.; Shtukenberg, A. G.; Alkhidir, T.; Hagiwara, Y.; Almehairbi, M.; Lan, L.; Hasebe, S.; Karothu, D. P.; Mohamed, S.; Koshima, H.; Kobatake, S.; Diao, Y.; Chandrasekar, R.; Zhang, H.; Sun, C. C.; Bardeen, C.; Al-Kaysi, R. O.; Kahr, B.; Naumov, P. Mechanical Properties and Peculiarities of Molecular Crystals. *Chem. Soc. Rev.* **2023**, 3098–3169. https://doi.org/10.1039/d2cs00481j.

(49) Kaupp, G. Solid-State Reactions, Dynamics in Molecular Crystals. *Curr. Opin. Solid State Mater. Sci.* **2002**, *6* (2), 131–138. https://doi.org/10.1016/S1359-0286(02)00041-4.

(50) Safari, F.; Katrusiak, A. High-Pressure Polymorphs Nucleated and Stabilized by Rational Doping under Ambient Conditions. *J. Phys. Chem. C* **2021**, *125* (42), 23501–23509. https://doi.org/10.1021/acs.jpcc.1c07297.

(51) Ahmed, E.; Karothu, D. P.; Naumov, P. Crystal Adaptronics: Mechanically Reconfigurable Elastic and Superelastic Molecular Crystals. *Angew. Chemie - Int. Ed.* **2018**, *57* (29), 8837–8846. https://doi.org/10.1002/anie.201800137.

(52) Dunitz, J. D. Phase Transitions in Molecular Crystals from a Chemical Viewpoint. *Pure Appl. Chem.* **1991**, *63* (2), 177–185. https://doi.org/10.1351/pac199163020177.

(53) Boldyreva, E. V. High-Pressure Diffraction Studies of Molecular Organic Solids. A Personal View. *Acta Crystallogr. Sect. A Found. Crystallogr.* **2008**, *64* (1), 218–231. https://doi.org/10.1107/S0108767307065786.

(54) Hemley, R. J.; Dera, P. Molecular Crystals. *Rev. Mineral. Geochemistry* **2000**, *41* (1), 335–419. https://doi.org/10.2138/rmg.2000.41.12.

(55) Corpinot, M. K.; Bučar, D.-K. A Practical Guide to the Design of Molecular Crystals. *Cryst. Growth Des.* **2019**, *19* (2), 1426–1453. https://doi.org/10.1021/acs.cgd.8b00972.

(56) Moggach, S. A.; Allan, D. R.; Parsons, S.; Sawyer, L.; Warren, J. E. The Effect of Pressure on the Crystal Structure of Hexagonal L-Cystine. *J. Synchrotron Radiat.* **2005**, *12* (5), 598–607. https://doi.org/10.1107/S0909049505019850.

(57) Bernstein, J.; Hagler, A. T. Conformational Polymorphism. The Influence of Crystal Structure on Molecular Conformation. *J. Am. Chem. Soc.* **1978**, *100* (3), 673–681. https://doi.org/10.1021/ja00471a001.

(58) Eilhard Mitscherlich. Sur La Relation Qui Existe Entre La Forme Cristalline et Les Proportions Chimiques. I. Memoire Sur Les Arsenates et Les Phosphates. *Ann. Chim. Phys.* **1822**, *19*, 350–419.

(59) Walter Cox McCrone. Polymorphism. In *Physics and Chemistry of the Organic Solid State*; Fox D, Labes M., W. A., Ed.; Wiley-Interscience: New York, 1965; pp 725–767.

(60) Threlfall, T. Structural and Thermodynamic Explanations of Ostwald's Rule. *Org. Process Res. Dev.* **2003**, *7* (6), 1017–1027. https://doi.org/10.1021/op030026l.

(61) Sun, W.; Ceder, G. Induction Time of a Polymorphic Transformation. *CrystEngComm* **2017**, *19* (31), 4576–4585. https://doi.org/10.1039/C7CE00766C.

(62) Hansen, T. C. The Everlasting Hunt for New Ice Phases. *Nat. Commun.* **2021**, *12* (1), 10–12. https://doi.org/10.1038/s41467-021-23403-6.

(63) Hermann, A.; Ashcroft, N. W.; Hoffmann, R. High Pressure Ices. *Proc. Natl. Acad. Sci. U. S. A.* **2012**, *109* (3), 745–750. https://doi.org/10.1073/pnas.1118694109.

(64) Chou, I.-M.; Blank, J. G.; Goncharov, A. F.; Mao, H.; Hemley, R. J. In Situ Observations of a High-Pressure Phase

of H2O Ice. *Science (80-.).* **1998**, *281* (5378), 809–812. https://doi.org/10.1126/science.281.5378.809.

(65) Kalichevsky, M. T.; Knorr, D.; Lillford, P. J. Potential Food Applications of High-Pressure Effects on Ice-Water Transitions. *Trends Food Sci. Technol.* **1995**, *6* (8), 253–259. https://doi.org/10.1016/S0924-2244(00)89109-8.

(66) Nangia, A. Conformational Polymorphism in Organic Crystals. *Acc. Chem. Res.* **2008**, *41* (5), 595–604. https://doi.org/10.1021/ar700203k.

(67) Cruz-Cabeza, A. J.; Reutzel-Edens, S. M.; Bernstein, J. Facts and Fictions about Polymorphism. *Chem. Soc. Rev.* **2015**, *44* (23), 8619–8635. https://doi.org/10.1039/c5cs00227c.

(68) Bernstein, J. Polymorphism - A Perspective. *Cryst. Growth Des.* **2011**, *11* (3), 632–650. https://doi.org/10.1021/cg1013335.

(69) Bernstein, N.; Hellberg, C. S.; Johannes, M. D.; Mazin, I. I.; Mehl, M. J. What Superconducts in Sulfur Hydrides under Pressure and Why. *Phys. Rev. B - Condens. Matter Mater. Phys.* **2015**, *91* (6), 1–5. https://doi.org/10.1103/PhysRevB.91.060511.

(70) Kuleshova, L. N.; Antipin, M. Y. Cambridge Structural Database as a Tool for Studies of General Structural Features of Organic Molecular Crystals. *Russ. Chem. Rev.* **1999**, *68* (1), 1–18. https://doi.org/10.1070/RC1999v068n01ABEH000453.

(71) Gavezzotti, A. A Solid-State Chemist's View of the Crystal Polymorphism of Organic Compounds. *J. Pharm. Sci.* **2007**, *96* (9), 2232–2241. https://doi.org/10.1002/jps.20870.

(72) Taylor, C. R.; Mulvee, M. T.; Perenyi, D. S.; Probert, M. R.; Day, G. M.; Steed, J. W. Minimizing Polymorphic Risk through Cooperative Computational and Experimental Exploration. *J. Am. Chem. Soc.* **2020**, *142* (39), 16668–16680. https://doi.org/10.1021/jacs.0c06749.

(73) Cruz-Cabeza, A. J.; Bernstein, J. Conformational Polymorphism. *Chem. Rev.* **2014**, *114* (4), 2170–2191. https://doi.org/10.1021/cr400249d.

(74) Price, S. L. Why Don't We Find More Polymorphs? *Acta Crystallogr. Sect. B Struct. Sci. Cryst. Eng. Mater.* **2013**, *69* (4), 313–328. https://doi.org/10.1107/S2052519213018861.

(75) Day, G. M. Current Approaches to Predicting Molecular Organic Crystal Structures. *Crystallogr. Rev.* **2011**, *17* (1), 3–52. https://doi.org/10.1080/0889311X.2010.517526.

(76) Price, S. L. Predicting Crystal Structures of Organic Compounds. *Chem. Soc. Rev.* **2014**, *43* (7), 2098–2111. https://doi.org/10.1039/c3cs60279f.

(77) Boese, R. Special Issue on In Situ Crystallization. *Zeitschrift für Krist. - Cryst. Mater.* **2014**, *229* (9), 595–601. https://doi.org/10.1515/zkri-2014-5003.

(78) Fabbiani, F. P. A.; Allan, D. R.; David, W. I. F.; Moggach, S. A.; Parsons, S.; Pulham, C. R. High-Pressure Recrystallisation - A Route to New Polymorphs and Solvates. *CrystEngComm* **2004**, *6* (82), 504–511. https://doi.org/10.1039/b406631f.

(79) Piermarini, G. J.; Block, S.; Barnett, J. D.; Forman, R. A. Calibration of the Pressure Dependence of the R1 Ruby Fluorescence Line to 195 Kbar. *J. Appl. Phys.* **1975**, *46* (6), 2774–2780. https://doi.org/10.1063/1.321957.

(80) Mao, H. K.; Xu, J.; Bell, P. M. Calibration of the Ruby Pressure Gauge to 800 Kbar under Quasi-Hydrostatic Conditions. *J. Geophys. Res.* **1986**, *91* (B5), 4673. https://doi.org/10.1029/jb091ib05p04673.

(81) B. Baranowski, A. M. Isothermic Freezing Pressures Of Organic Liquids At High-Pressure Conditions. 2. The System Benzene Thiophene Within The Temperature-Range From (-) 30-Degrees-C To (+) 100-Degrees-C. *Pol. J. Chem.* **1982**, *56* (2), 379–391.

(82) Dziubek; Katrusiak. Complementing Diffraction Data with Volumetric Measurements. *Zeitschrift für Krist. – Cryst. Mater.* **2014**, *229* (2), 129–134. https://doi.org/10.1515/zkri-2013-1677.

(83) Katrusiak, A. Shadowing and Absorption Corrections of High-Pressure Powder Diffraction Data: Toward Accurate Electron-Density Determinations. *Acta Crystallogr. Sect. A Found. Crystallogr.* **2004**, *60* (5), 409–417. https://doi.org/10.1107/S0108767304018902.

(84) CrysAlisPro Software System, Rigaku Oxford Diffraction. Oxford Diffraction Ltd. 2019.

(85) Dolomanov, O. V.; Bourhis, L. J.; Gildea, R. J.; Howard, J. A. K.; Puschmann, H. OLEX2: A Complete Structure Solution, Refinement and Analysis Program. *J. Appl. Crystallogr.* **2009**, *42* (2), 339–341. https://doi.org/10.1107/S0021889808042726.

(86) Sheldrick, G. M. SHELXT - Integrated Space-Group and Crystal-Structure Determination. *Acta Crystallogr. Sect. A Found. Crystallogr.* **2015**, *71* (1), 3–8. https://doi.org/10.1107/S2053273314026370.

(87) Sheldrick, G. M. Crystal Structure Refinement with SHELXL. *Acta Crystallogr. Sect. C Struct. Chem.* **2015**, *71* (Md), 3–8. https://doi.org/10.1107/S2053229614024218.

(88) Frisch, M. J.; Trucks, G. W.; Schlegel, H. B.; Scuseria, G. E.; Robb, M. A.; Cheeseman, J. R.; Scalmani, G.; Barone, V.; Petersson, G. A.; Nakatsuji, H.; Li, X.; Caricato, M.; Marenich, A. V.; Bloino, J.; Janesko, B. G.; Gomperts, R.; Mennucci, B.; Hratch, D. J. Gaussian 16, Revision C.01. Gaussian, Inc.: Wallingford CT 2016.

(89) Dennington, Roy; Keith, Todd A.; Millam, J. M. GaussView. Semichem Inc.: Shawnee Mission KS 2019.

(90) Spackman, P. R.; Turner, M. J.; McKinnon, J. J.; Wolff, S. K.; Grimwood, D. J.; Jayatilaka, D.; Spackman, M. A. CrystalExplorer: A Program for Hirshfeld Surface Analysis, Visualization and Quantitative Analysis of Molecular Crystals. *J. Appl. Crystallogr.* **2021**, *54*, 1006–1011. https://doi.org/10.1107/S1600576721002910.

(91) Spackman, M. A.; Spackman, P. R.; Thomas, S. P. Beyond Hirshfeld Surface Analysis: Interaction Energies, Energy Frameworks and Lattice Energies with CrystalExplorer. *Complement. Bond. Anal.* **2021**, 329–352. https://doi.org/10.1515/9783110660074-013.

(92) Maloney, A. G. P.; Wood, P. A.; Parsons, S. Competition between Hydrogen Bonding and Dispersion Interactions in the Crystal Structures of the Primary Amines. *CrystEngComm* **2014**, *16* (19), 3867–3882. https://doi.org/10.1039/c3ce42639d.

(93) Macrae, C. F.; Sovago, I.; Cottrell, S. J.; Galek, P. T. A.; McCabe, P.; Pidcock, E.; Platings, M.; Shields, G. P.; Stevens, J. S.; Towler, M.; Wood, P. A. Mercury 4.0 : From Visualization to Analysis, Design and Prediction. *J. Appl. Crystallogr.* **2020**, *53* (1), 226–235. https://doi.org/10.1107/S1600576719014092.

(94) Etter, M. C.; MacDonald, J. C.; Bernstein, J. Graph-Set Analysis of Hydrogen-Bond Patterns in Organic Crystals. *Acta Crystallogr. Sect. B Struct. Sci.* **1990**, *46* (2), 256–262. https://doi.org/10.1107/S0108768189012929.

(95) Podsiadło, M.; Olejniczak, A.; Katrusiak, A. Structure-Property Relations and Polymorphism in Compressed Methylamines. *Cryst. Growth Des.* **2017**, *17* (4), 2218–2222. https://doi.org/10.1021/acs.cgd.7b00203.

(96) Jones, D. W.; Katrusiak, A. Introduction: Organic Crystal Chemistry IX. *J. Mol. Struct.* **1996**, *374* (1–3), 1–5. https://doi.org/10.1016/0022-2860(95)09138-6.

(97) Sobczak, S. A New High-Pressure Phase of n-Butanol and Its Structural Relationship with the Low-Temperature Structure. *Sci. Rep.* **2025**, *15* (1), 39921. https://doi.org/10.1038/s41598-025-23729-x.

(98) André, D.; Fourme, R.; Zechmeister, K. Crystal and Molecular Structure of Diethyl Ether at 128°K. *Acta Crystallogr. Sect. B Struct. Crystallogr. Cryst. Chem.* **1972**, *28* (8), 2389–2395. https://doi.org/10.1107/s0567740872006181.

(99) Vojinović, K.; Losehand, U.; Mitzel, N. W. Dichlorosilane–Dimethyl Ether Aggregation: A New Motif in Halosilane Adduct Formation. *Dalt. Trans.* **2004**, No. 16, 2578–2581. https://doi.org/10.1039/B405684A.

(100) Bondi, A. Van Der Waals Volumes and Radii. *J. Phys. Chem.* **1964**, *68* (3), 441–451. https://doi.org/10.1021/j100785a001.

(101) *CRC Handbook of Chemistry and Physics*; Haynes, W. M., Lide, D. R., Bruno, T. J., Eds.; CRC Press, 2016; Vol. 44. https://doi.org/10.1201/9781315380476.

(102) Kolesnikov, A. Y.; Saul, J. M.; Kutcherov, V. G. Chemistry of Hydrocarbons Under Extreme Thermobaric Conditions. *ChemistrySelect* **2017**, *2* (4), 1336–1352. https://doi.org/10.1002/slct.201601123.

(103) Schettino, V.; Bini, R. Constraining Molecules at the Closest Approach: Chemistry at High Pressure. *Chem. Soc. Rev.* **2007**, *36* (6), 869. https://doi.org/10.1039/b515964b.

(104) Schettino, V.; Bini, R. Molecules under Extreme Conditions: Chemical Reactions at High Pressure. *Phys. Chem. Chem. Phys.* **2003**, *5* (10), 1951. https://doi.org/10.1039/b301381b.

(105) Schettino, V.; Bini, R.; Ceppatelli, M.; Citroni, M. Activation and Control of Chemical Reactions at Very High Pressure. *Phys. Scr.* **2008**, *78* (5). https://doi.org/10.1088/0031-8949/78/05/058104.

(106) Wagner, J. P.; Schreiner, P. R. London Dispersion in Molecular Chemistry—Reconsidering Steric Effects. *Angew. Chemie Int. Ed.* **2015**, *54* (42), 12274–12296. https://doi.org/10.1002/anie.201503476.

(107) Podsiadło, M.; Olejniczak, A.; Katrusiak, A. Why Propane? *J. Phys. Chem. C* **2013**, *117* (9), 4759–4763. https://doi.org/10.1021/jp311747m.

(108) Podsiadło, M.; Olejniczak, A.; Katrusiak, A. A New Ethane Polymorph. *Cryst. Growth Des.* **2017**, *17* (1), 228–232. https://doi.org/10.1021/acs.cgd.6b01474.

(109) Shimizu, H.; Shimazaki, I.; Sasaki, S. High-Pressure Raman Study of Liquid and Molecular Crystal Ethane up to 8 Gpa. *Jpn. J. Appl. Phys.* **1989**, *28* (9 R), 1632–1635. https://doi.org/10.1143/JJAP.28.1632.

(110) Kudryavtsev, D.; Serovaiskii, A.; Mukhina, E.; Kolesnikov, A.; Gasharova, B.; Kutcherov, V.; Dubrovinsky, L. Raman and IR Spectroscopy Studies on Propane at Pressures of Up to 40 GPa. *J. Phys. Chem. A* **2017**, *121* (32), 6004–6011. https://doi.org/10.1021/acs.jpca.7b05492.

(111) Kudryavtsev, D. A.; Kutcherov, V. G.; Dubrovinsky, L. S. Raman High-Pressure Study of Butane Isomers up to 40 GPa. *AIP Adv.* **2018**, *8* (11), 115104–1. https://doi.org/10.1063/1.5049481.

(112) Carnelley, T. XIII. Chemical Symmetry, or the Influence of Atomic Arrangement on the Physical Properties of Compounds . *London, Edinburgh, Dublin Philos. Mag. J. Sci.* **1882**, *13* (79), 112–130. https://doi.org/10.1080/14786448208627154.

(113) Groom, C. R.; Bruno, I. J.; Lightfoot, M. P.; Ward, S. C. The Cambridge Structural Database. *Acta Crystallogr. Sect. B Struct. Sci. Cryst. Eng. Mater.* **2016**, *72* (2), 171–179. https://doi.org/10.1107/S2052520616003954.

Scientific articles included in this dissertation

Paper P1

Polymorphism, Intermolecular Interactions, and Properties Of Primary Amines At High Pressure

Sacharczuk, N.; Olejniczak, A.; Bujak, M.; Podsiadło, M.

Cryst. Growth Des. **2023**, *23*, 7119−7125

CRYSTAL GROWTH & DESIGN

pubs.acs.org/crystal

Article

Polymorphism, Intermolecular Interactions, and Properties of Primary Amines at High Pressure

Natalia Sacharczuk, Anna Olejniczak, Maciej Bujak, and Marcin Podsiadło*

Cite This: *Cryst. Growth Des.* 2023, 23, 7119−7125

Read Online

ACCESS | Metrics & More | Article Recommendations | Supporting Information

ABSTRACT: A homologous series of the simplest primary amines, ethylamine (EA), propylamine (PA), butylamine (BA), and pentylamine (PEA), has been studied at high pressure by single-crystal X-ray diffraction. The structures of these compounds have been determined, at ambient temperature, from their freezing pressures up to ca. 5 GPa. Ethylamine at high pressure crystallizes in phase II of space group $P2_1/c$, already found at ambient pressure and low temperature. For other amines, six new polymorphs have been found: two of propylamine (phases II and III, both of space group $P2_1/c$), two of butylamine (phases II and III, both of space group $Pbc2_1$), and two of pentylamine (phases II and III, space groups $Pbc2_1$ and $P2_1cn$, respectively). The competition between NH···N and CH···N intermolecular interactions has been studied for the polymorphic forms of all amines. The properties of investigated compounds have been correlated with the number of carbon atoms in their aliphatic chains.

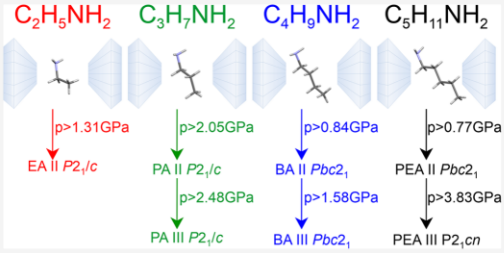

INTRODUCTION

The factors of close packing, symmetry, and interactions are considered to be the most important parameters in the formation of crystals, in particular those of organic compounds. Therefore, understanding the cohesion forces is essential to comprehend the rules that govern molecular aggregation. Intermolecular interactions, such as hydrogen bonds, often have a crucial role in crystals and their polymorphs. Also, due to the relatively weak energy of hydrogen bonds,[1,2] they can relatively easily transform at varied temperature and pressure conditions.[3−8]

Strong NH···N and weak CH···N hydrogen bonds are important forces in biomolecules, self-organizing materials, drugs, and switching molecules.[1,9] The competition and properties of these intermolecular interactions were studied for various amines under different thermodynamic conditions. For instance, the determinations of low-temperature and high-pressure structures of 1,2-diaminoethane revealed five phases and phase transitions, whose existence can be explained in terms of NH_2-group rotations and transformations of the NH···N hydrogen bonds.[10] Moreover, it was also found, in the group of methylamine, dimethylamine, and trimethylamine, that the intermolecular interactions of NH···N bonds and electrostatic forces in their crystals played an essential role in the generation of polymorphic forms, phase transitions, and the macroscopic properties of these compounds, including their melting and boiling behavior with temperature and pressure.[11]

The competition between hydrogen bonds and dispersion interactions in the crystal structures of the primary amines, determined at ambient pressure and low temperature, has been studied for the series from ethylamine to decylamine.[12] The crystal structures of all those primary amines consist of layers with molecules interacting through NH···N hydrogen bonds and also dispersion interactions between alkyl chains. The layers stack with dispersion interactions between the methyl groups in opposing layers. The authors concluded that the intermolecular interactions in even-membered amines are stronger and their crystal packing is more efficient than in the odd-numbered members.[12]

In this study, we have investigated a series of the simplest primary amines (SPA): ethylamine (EA), propylamine (PA), butylamine (BA), and pentylamine (PEA) using single-crystal X-ray diffraction at high pressure. EA is gaseous, while PA, BA, and PEA are liquids at ambient conditions. All of these compounds are widely used in organic chemistry, and their crystal structures have previously only been determined at ambient pressure and low temperature.[12] We have obtained and investigated single crystals of the SPA, in a diamond-anvil cell (DAC), in the range between their freezing pressures at ambient temperature to ca. 5 GPa.

Received: April 14, 2023
Revised: August 16, 2023
Published: August 29, 2023

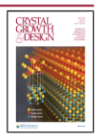

https://doi.org/10.1021/acs.cgd.3c00456
Cryst. Growth Des. 2023, 23, 7119−7125

EXPERIMENTAL SECTION

Ethylamine, EA (97%), propylamine, PA (≥99%), butylamine, BA (99.5%), and pentylamine, PEA (99%, all from Sigma-Aldrich) were in situ crystallized in modified Merrill-Basset DACs.[13] EA with a boiling point of ca. 290 K[14] was loaded into a DAC at cryogenic conditions. In each experiment, the DAC was equipped with a 0.3 mm-thick steel gasket with the hole 0.4 mm in diameter. At 295 K, EA, PA, BA, and PEA froze at 1.31, 2.05, 0.84, and 0.77 GPa, respectively, in the form of polycrystalline mass filling the whole volume of the DAC chamber. Single crystals were obtained at isochoric conditions: the DAC and the polycrystalline mass inside the chamber were heated with a hot-air gun until all but one grain melted. Then the DAC was slowly cooled to room temperature, and the single-crystal samples grew eventually filling the whole volume of the chamber. The temperature inside the DAC was measured using the infrared laser thermometer. Most of the obtained crystals showed high sensitivity to temperature changes. The single crystals were grown in situ over and over again at each pressure point. The pressure was determined by the ruby fluorescence method[15,16] using a Photon Control spectrometer with an accuracy of 0.02 GPa. The measurements were performed before and after each X-ray diffraction data-collection experiment. The experimental details and progress in growing the single crystals are shown in Figures 1 and S1−S19 (in the Supporting Information).

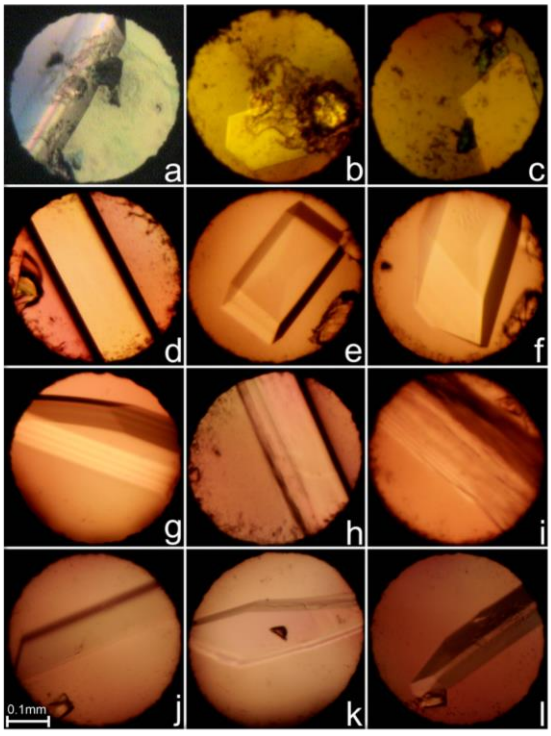

Figure 1. Single crystals of EA, PA, BA, and PEA grown in situ in the DAC chamber: (a) EA phase II at 1.40 GPa/348 K, (b) EA phase II at 2.60 GPa/438 K, (c) EA phase II at 4.35 GPa/454 K, (d) PA phase II at 2.45 GPa/336 K, (e) PA phase III at 2.90 GPa/394 K, (f) PA phase III at 4.25 GPa/437 K, (g) BA phase II at 1.45 GPa/351 K, (h) BA phase III at 1.70 GPa/375 K, (i) BA phase III at 3.10 GPa/433 K, (j) PEA phase II at 2.60 GPa/443 K, (k) PEA phase II at 3.55 GPa/468 K, and (l) PEA phase III at 4.10 GPa/479 K.

Diffractometers Xcalibur EOS and KUMA KM4-CCD were used for high-pressure studies. The DAC was centered by the gasket-shadow method.[17] The *CrysAlisPro* program suite was used for data collections, determination of the *UB*-matrices, and data reductions.[18] All data were accounted for the Lorentz, polarization, and absorption effects. Programs *OLEX2−1.5*,[19] *SHELXT*,[20] and *SHELXL*[21] were used to solve the structures by direct methods and then to the full-matrix least-squares refinement. Anisotropic displacement parameters were applied for nonhydrogen atoms, but the isotropic displacement parameters were occasionally retained for the atoms with unreasonable anisotropic parameters or in the case of the lower completeness/quality data. The H-atoms of methylene and methyl groups were located based on the molecular geometry, with C-H distances equal to 0.97 or 0.96 Å and their U_{iso} factors constrained to 1.2 or 1.5 times U_{eq} of their carriers. The H-atoms of the amine ($-NH_2$) group were located based on the molecular geometry, assuming the geometrical parameters for the analogous structures retrieved from the Cambridge Structural Database.[22,23] The completeness of the data obtained in this study varies from 16% for EA at 1.70 GPa to 60% for BA at 1.45 GPa (Tables 1 and S1−S4 in the Supporting Information). The crystal data and refinement details are summarized in Tables 1 and S1−S4.

RESULTS AND DISCUSSION

The single crystals of investigated SPA have been obtained at the lowest possible pressure (about 0.2 GPa above the freezing pressure to ensure the stability of the crystal during the X-ray diffraction data-collection experiments). The maximum pressure was the result of reaching the thermal limit of the DAC, corresponding to a temperature of ca. 500 K inside the high-pressure chamber, during the procedure of obtaining single crystals. The crystals obtained at high pressure are more dense compared to those crystallized at ambient pressure and low temperature. All the unit-cell parameters of the investigated SPA crystals decrease with increasing pressure. The molecular volume of SPA as a function of pressure is plotted in Figure 2.

Ethylamine. At ambient pressure, on cooling to 150 K, EA undergoes a slow reconstructive phase transition.[12] The crystal structure of EA I has been determined by the single-crystal X-ray diffraction method at 180 K, while that of EA II by powder diffraction at 150 K.[12] EA I and II at 0.1 MPa crystallizes in centrosymmetric space group $P2_1/c$. In both phases, the molecules are arranged into NH···N bonded chains showing a different orientation of the molecules with respect to the chain direction. These NH···N bonded chains can be described by symbol $C_1^1(2)$ according to the graph notation of H-bonds.[24] Within the chains, each N atom serves as one donor and one acceptor of the H atom. This interaction can be considered as the main cohesion force in the ambient pressure/low temperature obtained crystals and is characterized by the H···N intermolecular distances shorter by ca. 0.35 Å than the sum of the van der Waals radii of H and N atoms[25] (Figure 3). These distances are even shorter at 1.40 GPa/295 K when EA freezes into phase II. It is characteristic that the shortest CH···N contacts are much more compressible than the main NH···N contacts with increasing pressure (Figure 3). Furthermore, during the squeezing of the EA phase II, additional short CH···N contacts appear and the $R_3^2(8)$ rings of NH···N and CH···N interacting molecules are formed (Figure 3).

Propylamine. PA at 0.1 MPa/150 K crystallizes in centrosymmetric phase I of the orthorhombic space group *Pbcn* with the amine molecules forming two independent NH···N infinite $C_1^1(2)$ chains.[12] The combination of these

https://doi.org/10.1021/acs.cgd.3c00456
Cryst. Growth Des. 2023, 23, 7119−7125

Table 1. Selected Crystal Data of EA Phase II, PA Phases II and III, BA Phases II and III, and PEA Phases II and III, All at 295 K

	EA phase II	PA phase II	PA phase III	BA phase II	BA phase III	PEA phase II	PEA phase III
p (GPa)	1.40(2)	2.25(2)	2.50(2)	1.45(2)	1.70(2)	1.05(2)	4.10(2)
crystal system	monoclinic	monoclinic	monoclinic	orthorhombic	orthorhombic	orthorhombic	orthorhombic
space group	$P2_1/c$	$P2_1/c$	$P2_1/c$	$Pbc2_1$	$Pbc2_1$	$Pbc2_1$	$P2_1cn$
a (Å)	8.80(6)	9.5676(11)	4.8983(3)	12.8348(9)	5.020(5)	3.9646(14)	3.7101(11)
b (Å)	4.9804(10)	5.0810(16)	4.9746(3)	6.5975(11)	7.337(4)	8.682(4)	4.0956(12)
c (Å)	7.130(17)	7.303(3)	14.451(3)	5.4185(4)	23.823(5)	32.055(5)	31.167(6)
β (°)	113.5(5)	94.589(18)	100.758(11)	90	90	90	90
V (Å^3)	286(2)	353.9(2)	345.94(8)	458.83(9)	877.4(11)	1103.4(6)	473.6(2)
Z, Z'	4, 1	4, 1	4, 1	4, 1	8, 2	8, 2	4, 1
D_x (g cm^{-3})	1.046	1.109	1.135	1.059	1.107	1.049	1.222
completeness (%)	17	33	34	60	35	54	55
R_1 ($F^2 > 2\sigma(F^2)$)	0.0552	0.0399	0.0367	0.0449	0.0891	0.0665	0.0469
R_1 (all data)	0.0822	0.0495	0.0388	0.0631	0.1331	0.1200	0.0710

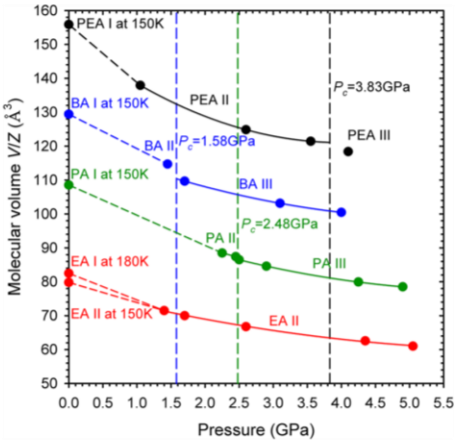

Figure 2. Molecular volume (V/Z) of investigated primary amines plotted as a function of pressure. The dashed lines joining the points of different phases are for guiding the eye only. The dashed vertical lines indicate the transformation pressure (P_c) between the high-pressure polymorphs. The estimated standard deviations are smaller than the plotted symbols.

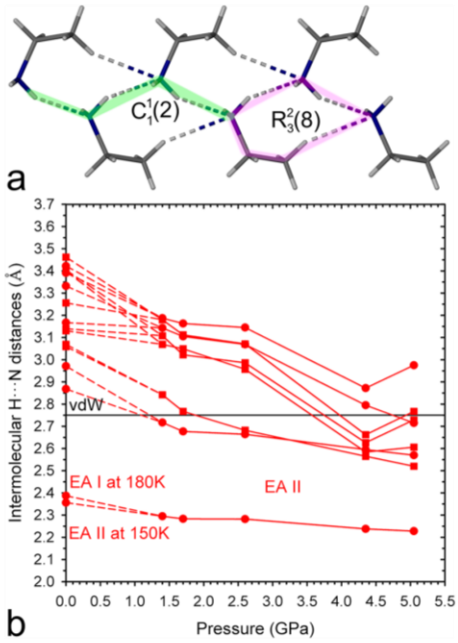

Figure 3. H-bond patterns observed in EA: (a) the H-bonded chain and ring in EA II at 5.05 GPa; (b) intermolecular H···N distances plotted as a function of pressure. Four shortest distances for two types of interactions are presented: circles represent NH···N and squares depict the CH···N hydrogen···acceptor distances. The black horizontal line shows the sum of van der Waals radii of H and N of 2.75 Å.[25] The estimated standard deviations are smaller than the plotted symbols.

two chains leads to the formation of NH···N bonded layers with $R_4^3(8)$ rings of NH···N interacting molecules. In contrast, at high pressure of 2.05 GPa/295 K PA crystallizes in centrosymmetric phase II of space group $P2_1/c$ and then, with increasing pressure, at 2.48 GPa it transforms to phase III (space group $P2_1/c$). The lattice vectors of PA II and PA III are related through the following matrix equation:

$$\begin{pmatrix} a_{\mathrm{PAII}} \\ b_{\mathrm{PAII}} \\ c_{\mathrm{PAII}} \end{pmatrix} = \begin{pmatrix} 2 & 0 & 0 \\ 0 & 1 & 0 \\ 0 & 0 & 0.5 \end{pmatrix} \begin{pmatrix} a_{\mathrm{PAIII}} \\ b_{\mathrm{PAIII}} \\ c_{\mathrm{PAIII}} \end{pmatrix}$$

In both high-pressure polymorphs, the main cohesion forces are NH···N infinite $C_1^1(2)$ chains (Figure 4). Within the chains, each N atom is simultaneously a one donor and one acceptor of the H atom. In PA III, the distances between H and N atoms involved in NH···N chains are shorter compared to PA I and II. In addition, the $R_3^2(8)$ rings of NH···N and CH···N hydrogen-bonded molecules are formed (Figure 4). Both these interactions join molecules into layers, which are further stabilized by another short CH···N intermolecular contacts.

Butylamine. BA at 0.1 MPa/150 K crystallizes in the centrosymmetric phase I of space group *Pbcn* with the molecules forming independent NH···N infinite $C_1^1(2)$ chains.[12] Within the chains, each N atom is both a one donor and one acceptor of the H atom. These chains persist at high pressure when at 0.84 GPa/295 K BA crystallize in the noncentrosymmetric space group $Pbc2_1$ (BA II, Figure 5). Further increasing pressure, at 1.58 GPa, leads to trans-

https://doi.org/10.1021/acs.cgd.3c00456
Cryst. Growth Des. 2023, 23, 7119−7125

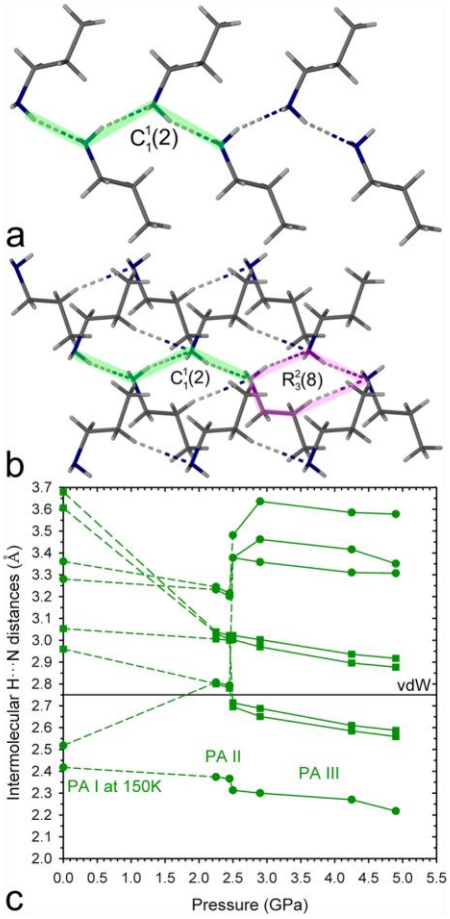

Figure 4. H-bond patterns in PA: (a) NH···N bonded chain in PA II at 2.45 GPa; (b) H-bonded chain and ring in PA III at 4.90 GPa; (c) intermolecular H···N distances plotted as a function of pressure. Four shortest distances are presented from two possible types of interactions: circles and squares represent NH···N and CH···N contacts, respectively. The black horizontal line shows the sum of van der Waals radii of H and N of 2.75 Å.[25] The estimated standard deviations are smaller than the plotted symbols.

formation to BA III characterized by the same space group $Pbc2_1$, but the number of symmetry-independent molecules increases from 1 to 2. The lattice vectors of BA II and BA III are connected through the matrix equation:

$$\begin{pmatrix} a_{\mathrm{BAII}} \\ b_{\mathrm{BAII}} \\ c_{\mathrm{BAII}} \end{pmatrix} = \begin{pmatrix} 0 & 0 & 1 \\ 0 & 1 & 0 \\ 0.5 & 0 & 0 \end{pmatrix} \begin{pmatrix} a_{\mathrm{BAIII}} \\ b_{\mathrm{BAIII}} \\ c_{\mathrm{BAIII}} \end{pmatrix}$$

In the more dense phase III, the BA molecules are arranged into NH···N bonded layers. Within the layers, the NH···N and CH···N bonded network is formed. Pressure enhances the role of CH···N intermolecular interactions, as the CH···N distances in phases I and II are longer than the sum of van der Waals radii (Figure 5).

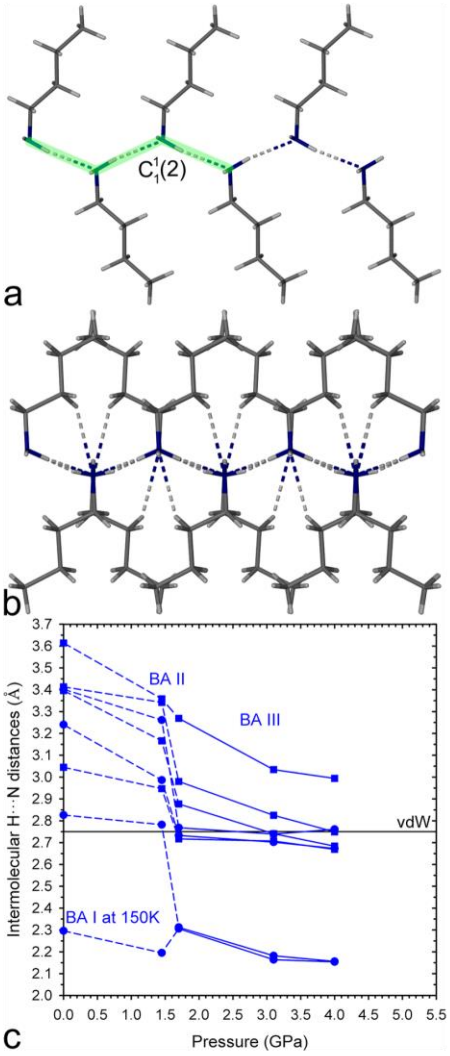

Figure 5. H-bond patterns in BA: (a) NH···N bonded chain in BA II at 1.45 GPa; (b) H-bonded interacting molecules in BA III at 4.00 GPa; (c) intermolecular H···N distances plotted as a function of pressure. Four shortest distances are presented for two possible types of interactions: circles represent NH···N and squares CH···N contacts, respectively. The black horizontal line shows the sum of van der Waals radii of H and N of 2.75 Å.[25] The estimated standard deviations are smaller than the plotted symbols.

Pentylamine. PEA at 0.1 MPa/150 K crystallizes in the centrosymmetric phase I of space group *Pbcn* with the molecules forming two independent NH···N infinite $C_1^1(2)$ chains.[12] The combination of these two chains leads to the formation of NH···N bonded layers with $R_4^3(8)$ rings of the NH···N hydrogen-bonded molecules. At 0.77 GPa/295 K, PEA crystallizes in the noncentrosymmetric phase II of space group $Pbc2_1$ with two symmetry-independent molecules. With increasing pressure to 3.83 GPa, it transforms to phase III (space group $P2_1cn$) comprising one symmetry-independent molecule in the unit cell. We have used the nonstandard

https://doi.org/10.1021/acs.cgd.3c00456
Cryst. Growth Des. 2023, 23, 7119−7125

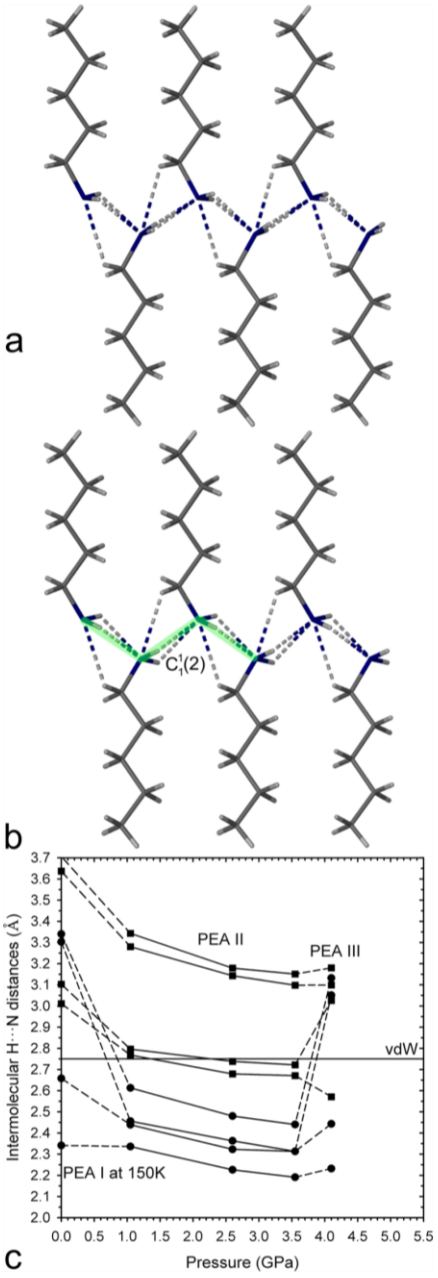

Figure 6. H-bond patterns in PEA: (a) PEA II at 3.55 GPa, and (b) PEA III at 4.10 GPa; (c) intermolecular H···N distances plotted as a function of pressure. Four shortest distances are presented for two possible types of interactions: circles represent NH···N, whereas squares are for CH···N contacts. The black horizontal line shows the sum of van der Waals radii of H and N of 2.75 Å.[25] The estimated standard deviations are smaller than the plotted symbols.

space group setting for PEA III to show the relation to PEA II. The lattice vectors of PEA II and PEA III are related to the following equation:

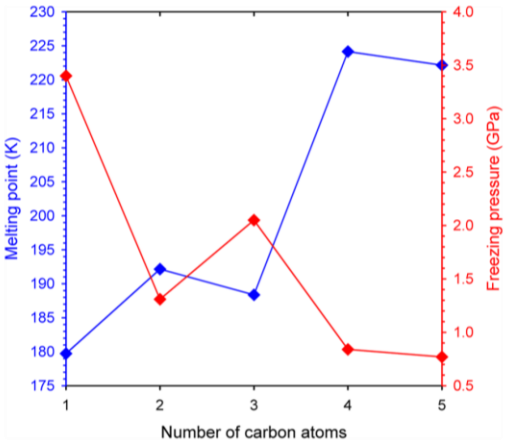

Figure 7. Ambient pressure melting points (K)[14] and ambient temperature freezing pressures (GPa) of methylamine[11] and the other SPA (this work).

$$\begin{pmatrix} a_{\mathrm{PEAII}} \\ b_{\mathrm{PEAII}} \\ c_{\mathrm{PEAII}} \end{pmatrix} = \begin{pmatrix} 1 & 0 & 0 \\ 0 & 2 & 0 \\ 0 & 0 & 1 \end{pmatrix} \begin{pmatrix} a_{\mathrm{PEAIII}} \\ b_{\mathrm{PEAIII}} \\ c_{\mathrm{PEAIII}} \end{pmatrix}$$

The molecules in PEA II are arranged in NH···N bonded layers. Within the layers, the NH···N bonded network is formed. Each N atom also plays a role of acceptor of the CH···N hydrogen bond (Figure 6). In PEA III, pressure enhances the role of CH···N intermolecular interactions. The number of NH···N short contacts is reduced to two independent NH···N infinite $C_1^1(2)$ chains. The shortest H···N intermolecular distances of NH···N bonds in PEA III at 4.10 GPa are slightly longer than those in PEA II at 3.55 GPa. At the same time, the shortest of H···N intermolecular distances of CH···N bonds decrease in comparison to the PEA phases II and III (Figure 6).

Melting Points and Freezing Pressures of Amines. The characteristic 'zig-zag' in the melting point diagram has been noted for the homologous series of *n*-alkanes, C_iH_{2i+2}, by Baeyer in 1877.[26] This is associated with the systematically lower melting points of *n*-alkanes with odd *i* compared to those with *i* even numbers. Over 120 years later, this phenomenon was explained by the molecular shape unsuitable for the dense packing in crystals.[27,28] The melting point and density in a series of primary monoamines have been studied for a sequence from ethylamine to decylamine.[12] It was noticed that the melting points of those amines are alternated, with odd members of the series having lower melting points than the even members (Figure 7). It is also worth mentioning that each even primary amine has an odd number chain length (for example PA has a four-membered chain containing 3C and 1N). This reverse dependence, compared to Boese's concept, reveals the influence and importance of hydrogen bonding, modifying the crystal packing of the alkyl chains. The freezing pressures of SPA determined at ambient temperature together with the freezing pressure of methylamine[11] as a function of the length of the alkyl chain are depicted in Figure 7. In the series from methylamine to butylamine, the reverse dependence of melting point and freezing pressure is observed: lower

https://doi.org/10.1021/acs.cgd.3c00456
Cryst. Growth Des. 2023, 23, 7119−7125

melting point and higher freezing pressure values are observed for odd i numbers of carbon atoms and higher melting point and lower freezing pressure values are characteristic of even i members. PEA fits to the trend of the series of melting point; however, the freezing pressure of PEA of 0.77(2) GPa is lower compared to the freezing pressure of BA of 0.84(2) GPa.

CONCLUSIONS

In the series of primary amines from EA to PEA, only EA undergoes a phase transition at ambient pressure and low temperature, while crystals of other amines do not exhibit any structural transformations.[12] However, at high pressure, the situation is reversed. EA crystallizes in the low-temperature phase II, which is stable up to ca. 5 GPa, while the other amines exhibit polymorphism. For each amine, two new structural forms, different from the low-temperature ones, have been reported in this study. In all of the investigated SPA, the main cohesion force is the NH···N intermolecular interaction. Also, despite considerable structural differences between the polymorphs, the molecular arrangements based on the NH···N hydrogen bond pattern are preserved. In the PA, BA, and PEA phases III, high pressure enhances the role of the CH···N intermolecular interactions.

ASSOCIATED CONTENT

Data Availability Statement

The crystal structures have been deposited in the CIFs form as supplementary publications in the Cambridge Crystallographic Database Centre (deposition numbers 2255822-2255840).

Supporting Information

The Supporting Information is available free of charge at https://pubs.acs.org/doi/10.1021/acs.cgd.3c00456.

Detailed experiment and structures description (PDF)

AUTHOR INFORMATION

Corresponding Author

Marcin Podsiadło − *Faculty of Chemistry, Adam Mickiewicz University, Poznań 61-614, Poland;* orcid.org/0000-0001-6702-1875; Email: marcinp@amu.edu.pl

Authors

Natalia Sacharczuk − *Faculty of Chemistry, Adam Mickiewicz University, Poznań 61-614, Poland;* orcid.org/0000-0001-6931-1059

Anna Olejniczak − *Faculty of Chemistry, Adam Mickiewicz University, Poznań 61-614, Poland;* orcid.org/0000-0002-4460-4362

Maciej Bujak − *Faculty of Chemistry, University of Opole, Opole 45-052, Poland;* orcid.org/0000-0003-2504-1119

Complete contact information is available at: https://pubs.acs.org/10.1021/acs.cgd.3c00456

Author Contributions

The manuscript was written through contributions of all authors. All authors have given approval to the final version of the manuscript.

Notes

The authors declare no competing financial interest.

ACKNOWLEDGMENTS

This study was supported by the National Science Centre, Grant No. 2020/37/B/ST4/00982.

ABBREVIATIONS

SPA, simplest primary amines; EA, ethylamine; PA, propylamine; BA, butylamine; PEA, pentylamine

REFERENCES

(1) Desiraju, G. R.; Steiner, T. *The Weak Hydrogen Bond In Structural Chemistry and Biology; International Union of Crystallography: Monographs on Crystallography*; Oxford University Press, 2001.

(2) Gilli, G.; Gilli, P. *The Nature of the Hydrogen Bond, Outline of a Comprehensive Hydrogen Bond Theory; International Union of Crystallography: Monographs on Crystallography*; Oxford University Press, 2009.

(3) Bordallo, H. N.; Boldyreva, E. V.; Buchsteiner, A.; Koza, M. M.; Landsgesell, S. Structure-Property Relationships in the Crystals of the Smallest Amino Acid: An Incoherent Inelastic Neutron Scattering Study of the Glycine Polymorphs. *J. Phys. Chem. B.* **2008**, *112*, 8748−8759.

(4) Katrusiak, A. Stereochemistry and transformations of NH···N hydrogen bonds Part I. Structural preferences for the hydrogen site. *J. Mol. Struct.* **1999**, *474*, 125−133.

(5) Moggach, S. A.; Parsons, S.; Wood, P. A. High-pressure polymorphism in amino acids. *Crystallogr. Rev.* **2008**, *14*, 143−184.

(6) Olejniczak, A.; Ostrowska, K.; Katrusiak, A. H-Bond Breaking in High-Pressure Urea. *J. Phys. Chem. C* **2009**, *113*, 15761−15767.

(7) Oswald, I. D. H.; Chataigner, I.; Elphick, S.; Fabbiani, F. P. A.; Lennie, A. R.; Maddaluno, J.; Marshall, W. G.; Prior, T. J.; Pulham, C. R.; Smith, R. I. Putting pressure on elusive polymorphs and solvates. *CrystEngComm* **2009**, *11*, 359−366.

(8) Patyk, E.; Katrusiak, A. Transformable H-bonds and conformation in compressed glucose. *Chem. Sci.* **2015**, *6*, 1991−1995.

(9) Jeffrey, G. A.; Saenger, W. *Hydrogen Bonding in Biological Structures*; Springer-Verlag: Berlin Heidelberg, 1994.

(10) Budzianowski, A.; Olejniczak, A.; Katrusiak, A. Competing hydrogen-bonding patterns and phase transitions of 1,2-diaminoethane at varied temperature and pressure. *Acta Crystallogr. B Struct. Sci.* **2006**, *62*, 1078−1089.

(11) Podsiadło, M.; Olejniczak, A.; Katrusiak, A. Structure−Property Relations and Polymorphism in Compressed Methylamines. *Cryst. Growth Des.* **2017**, *17*, 2218−2222.

(12) Maloney, A. G. P.; Wood, P. A.; Parsons, S. Competition between hydrogen bonding and dispersion interactions in the crystal structures of the primary amines. *CrystEngComm* **2014**, *16*, 3867−3882.

(13) Bassett, W. A. Diamond anvil cell, 50th birthday. *High Press. Res.* **2009**, *29*, 163−186.

(14) Haynes, W. M. Editor-in-Chief. *CRC Handbook of Chemistry and Physics*, 95th ed.; Taylor and Francis: Boca Raton, FL, 2014.

(15) Mao, H. K.; Xu, J.; Bell, P. M. Calibration of the ruby pressure gauge to 800 kbar under quasi-hydrostatic conditions. *J. Geophys. Res.* **1986**, *91*, 4673−4676.

(16) Piermarini, G. J.; Block, S.; Barnett, J. D.; Forman, R. A. Calibration of the pressure dependence of the R_1 ruby fluorescence line to 195 kbar. *J. Appl. Phys.* **1975**, *46*, 2774−2780.

(17) Budzianowski, A.; Katrusiak, A. *High-Pressure Crystallography*, Katrusiak, A., McMillan, P. F., Eds.; Kluwer Academic Publishers: Dordrecht, 2004; pp. 101−112.

(18) *CrysAlisPro* Software System. Rigaku Oxford Diffraction, http://www.rigaku.com; version 171.38.46, 2015.

(19) Dolomanov, O. V.; Bourhis, L. J.; Gildea, R. J.; Howard, J. A. K.; Puschmann, H. *OLEX2*: a complete structure solution, refinement and analysis program. *J. Appl. Crystallogr.* **2009**, *42*, 339−341.

(20) Sheldrick, G. M. *SHELXT* − Integrated space-group and crystal-structure determination. *Acta Crystallogr. A Found. Crystallogr.* **2015**, *71*, 3−8.
(21) Sheldrick, G. M. Crystal structure refinement with *SHELXL*. *Acta Crystallogr. C Struct. Chem.* **2015**, *71*, 3−8.
(22) Bruno, I. J.; Cole, J. C.; Edgington, P. R.; Kessler, M.; Macrae, C. F.; McCabe, P.; Pearson, J.; Taylor, R. New software for searching the Cambridge Structural Database and visualizing crystal structures. *Acta Crystallogr. B: Struct. Sci.* **2002**, *58*, 389−397.
(23) Groom, C. R.; Bruno, I. J.; Lightfoot, M. P.; Ward, S. C. The Cambridge Structural Database. *Acta Crystallogr. B: Struct. Sci. Cryst. Eng. Mater.* **2016**, *72*, 171−179.
(24) Etter, M. C.; MacDonald, J. C.; Bernstein, J. Graph-set analysis of hydrogen-bond patterns in organic crystals. *Acta Crystallogr. B Struct. Sci.* **1990**, *46*, 256−262.
(25) Bondi, A. van der Waals Volumes and Radii. *J. Phys. Chem.* **1964**, *68*, 441−451.
(26) Baeyer, A. Ueber Regelmässigkeiten im Schmelzpunkt Homologer Verbindungen. *Ber. Chem. Ges.* **1877**, *10*, 1286−1288.
(27) Boese, R.; Weiss, H.-C.; Bläser, D. The Melting Point Alternation in the Short-Chain *n*-Alkanes: Single-Crystal X-ray Analyses of Propane at 30 K and of *n*-Butane to *n*-Nonane at 90 K. *Angew. Chem., Int. Ed.* **1999**, *38*, 988−992.
(28) Thalladi, V. R.; Boese, R. Why Is the Melting Point of Propane the Lowest Among *n*-Alkanes? *New J. Chem.* **2000**, *24*, 579−581.

https://doi.org/10.1021/acs.cgd.3c00456
Cryst. Growth Des. 2023, 23, 7119−7125

Supporting Information

Polymorphism, intermolecular interactions and properties of primary amines at high pressure

Natalia Sacharczuk[a], Anna Olejniczak[a], Maciej Bujak[b] and Marcin Podsiadło*[a]

[a]*Faculty of Chemistry, Adam Mickiewicz University, Uniwersytetu Poznańskiego 8, Poznań, 61-614, Poland*

[b]*Faculty of Chemistry, University of Opole, Oleska 48, Opole, 45-052, Poland*

*E-mail: marcinp@amu.edu.pl

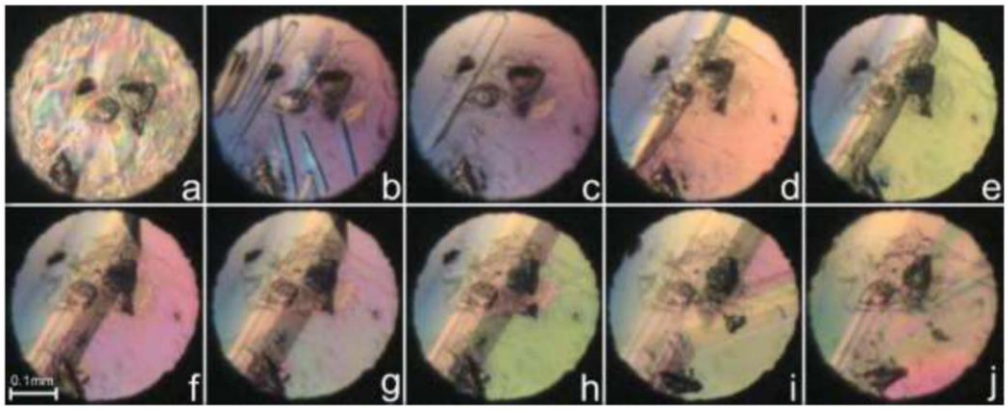

Figure S1. Stages of the ethylamine phase II single-crystal growth inside the DAC chamber (polarized-light mode): (a) polycrystal grown isothermally at 295 K; (b) polycrystal-liquid equilibrium at 358 K; (c) one crystal seed at 358 K; (d-i) the single-crystal cooled to 329 K and (j) filling the DAC chamber at 295 K and 1.40 GPa. The ruby chips for pressure calibration lie in the central and bottom part of the DAC chamber.

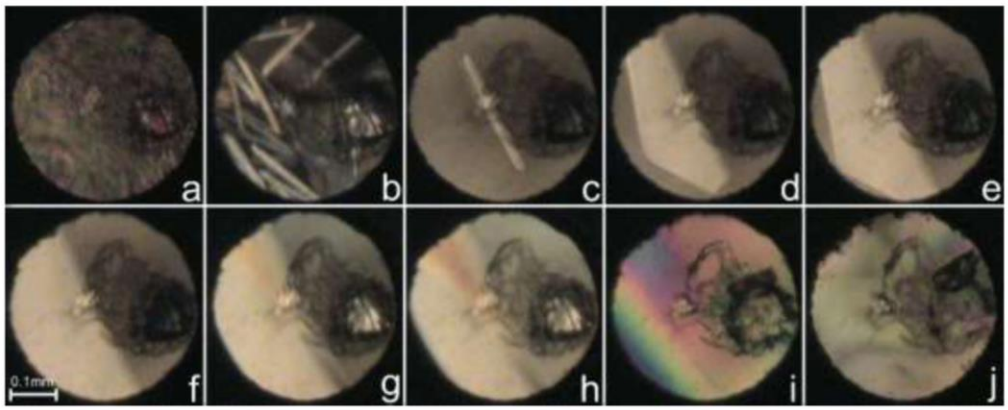

Figure S2. Stages of the ethylamine phase II single-crystal growth inside the DAC chamber (polarized-light mode): (a) polycrystal grown isothermally at 295 K; (b) polycrystal-liquid equilibrium at 386 K; (c) one crystal seed at 387 K; (d-i) the single-crystal cooled to 364 K and (j) filling the DAC chamber at 295 K and 1.70 GPa. The ruby chip for pressure calibration is located in the central part of the DAC chamber.

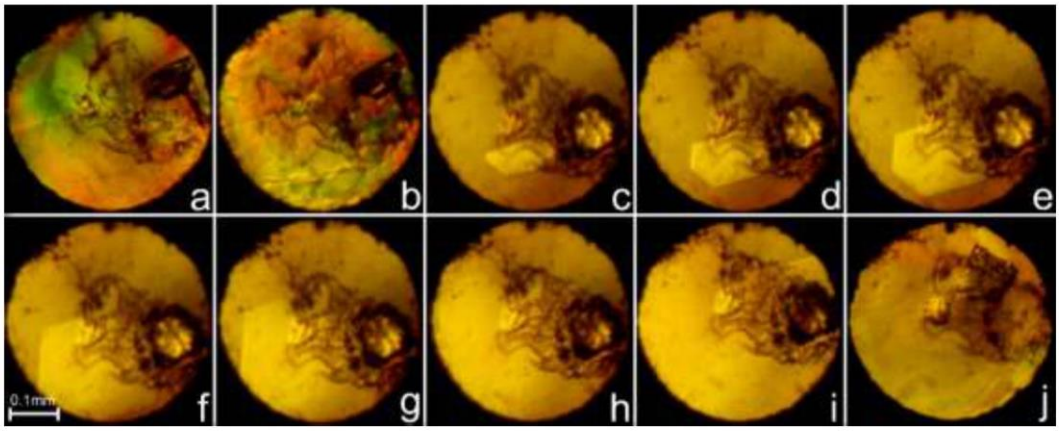

Figure S3. Stages of the ethylamine phase II single-crystal growth inside the DAC chamber (polarized-light mode): (a) polycrystal grown isothermally at 295 K; (b) polycrystal-liquid equilibrium at 433 K; (c) one crystal seed at 438 K; (d-i) the single-crystal cooled to 435 K and (j) filling the DAC chamber at 295 K and 2.60 GPa. The ruby chip for pressure calibration lies in the right part of the DAC chamber.

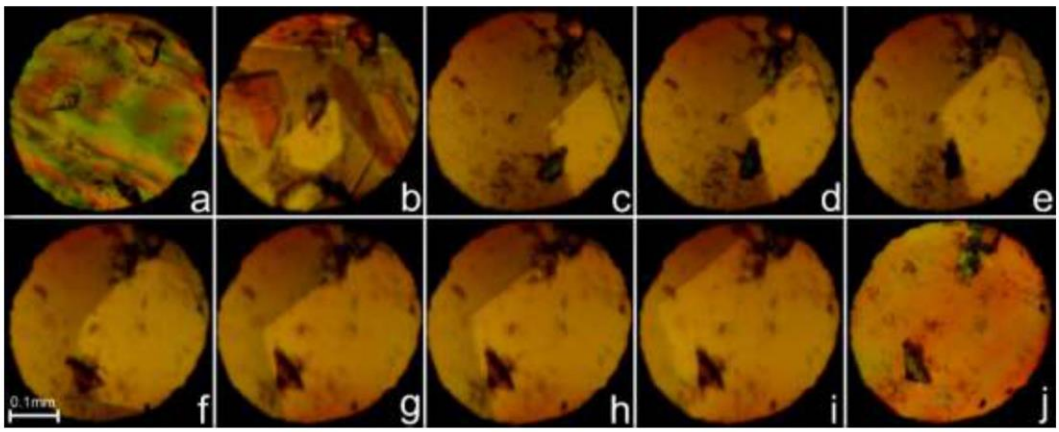

Figure S4. Stages of the ethylamine phase II single-crystal growth inside the DAC chamber (polarized-light mode): (a) polycrystal grown isothermally at 295 K; (b) polycrystal-liquid equilibrium at 453 K; (c) one crystal seed at 454 K; (d-i) the single-crystal cooled to 451 K and (j) filling the DAC chamber at 295 K and 4.35 GPa. Two ruby chips for pressure calibration are situated in the upper and central part of the DAC chamber.

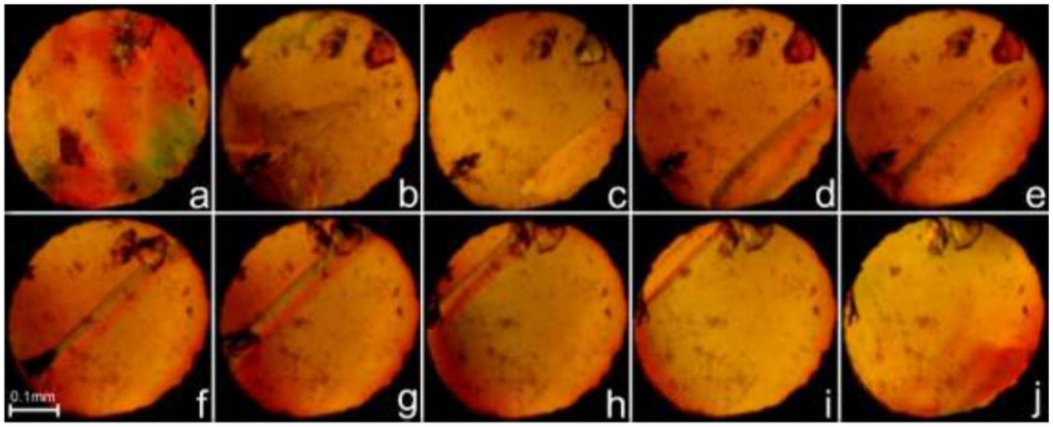

Figure S5. Stages of the ethylamine phase II single-crystal growth inside the DAC chamber (polarized-light mode): (a) polycrystal grown isothermally at 295 K; (b) polycrystal-liquid equilibrium at 455 K; (c) one crystal seed at 455 K; (d-i) the single-crystal cooled to 435 K and (j) filling the DAC chamber at 295 K and 5.05 GPa. Three ruby chips for pressure calibration lie in the upper and left part of the DAC chamber.

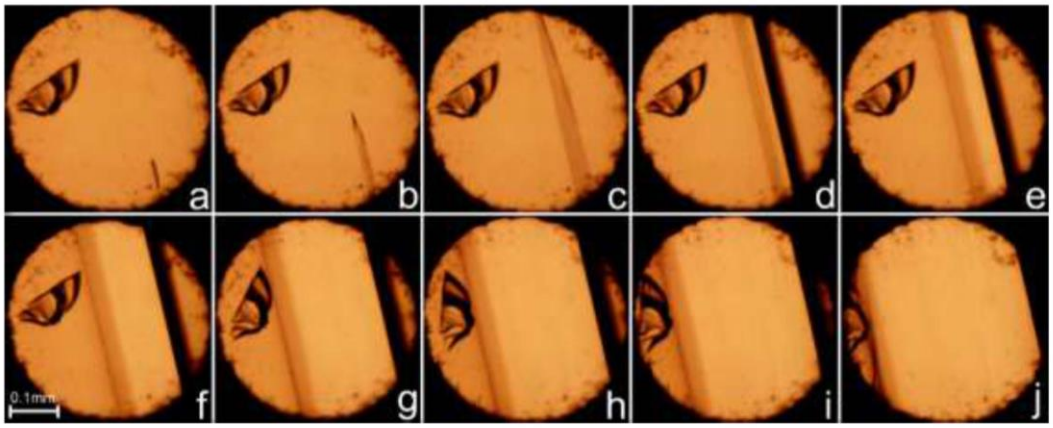

Figure S6. Stages of the propylamine phase II single-crystal growth inside the DAC chamber: (a) one crystal seed at 343 K; (b-i) the single-crystal cooled to 311 K and (j) filling the DAC chamber at 295 K and 2.25 GPa. The ruby chip for pressure calibration is placed in the left part of the DAC chamber.

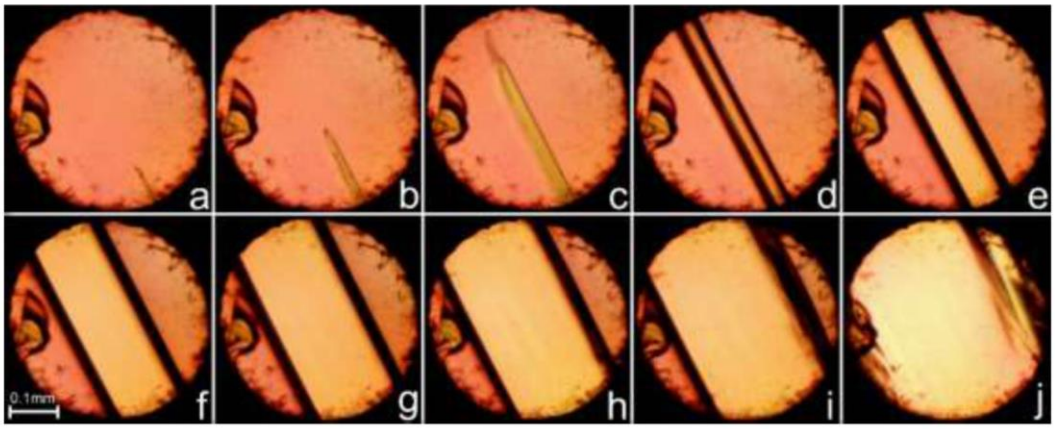

Figure S7. Stages of the propylamine phase II single-crystal growth inside the DAC chamber (polarized-light mode): (a) one crystal seed at 353 K; (b-i) the single-crystal cooled to 323 K and (j) filling the DAC chamber at 295 K and 2.45 GPa. The ruby chip for pressure calibration lies in the left part of the DAC chamber.

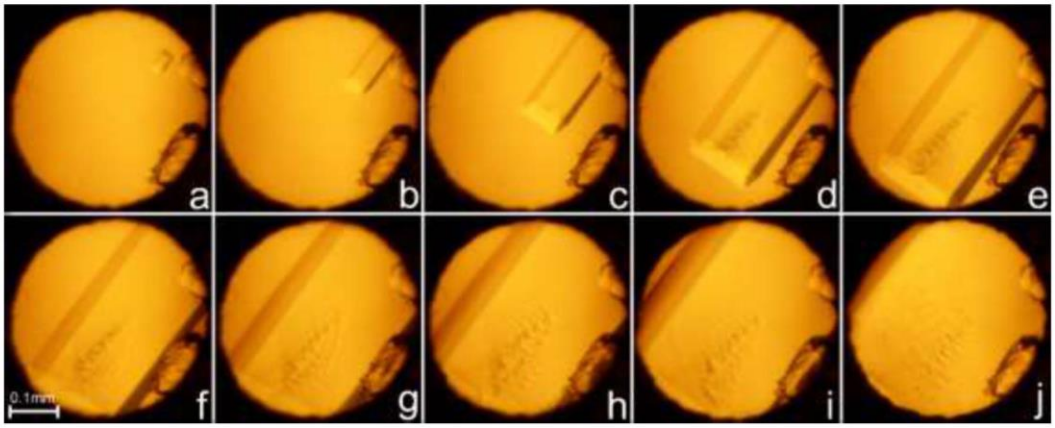

Figure S8. Stages of the propylamine phase III single-crystal growth inside the DAC chamber: (a) one crystal seed at 369 K; (b-i) the single-crystal cooled to 350 K and (j) filling the DAC chamber at 295 K and 2.50 GPa. Two ruby chips for pressure calibration are situated in the right part of the DAC chamber.

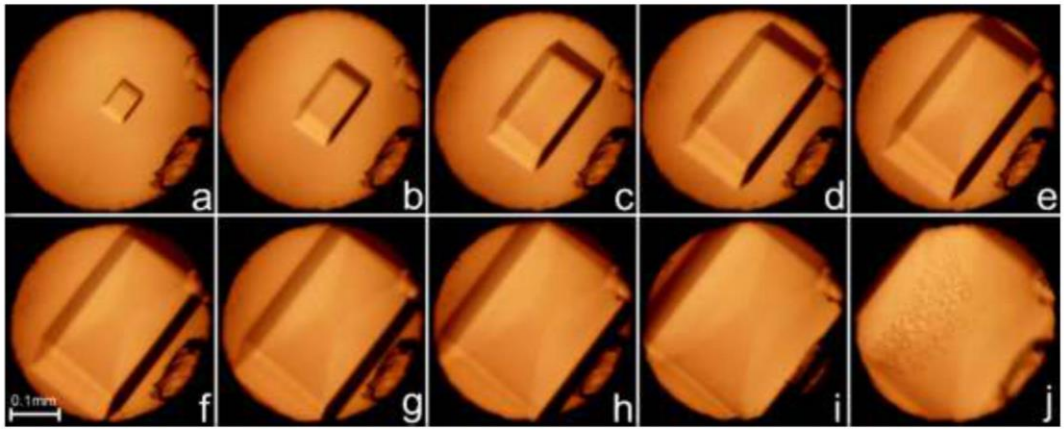

Figure S9. Stages of the propylamine phase III single-crystal growth inside the DAC chamber: (a) one crystal seed at 399 K; (b-i) the single-crystal cooled to 366 K and (j) filling the DAC chamber at 295 K and 2.90 GPa. Two ruby chips for pressure calibration lie in the right part of the DAC chamber.

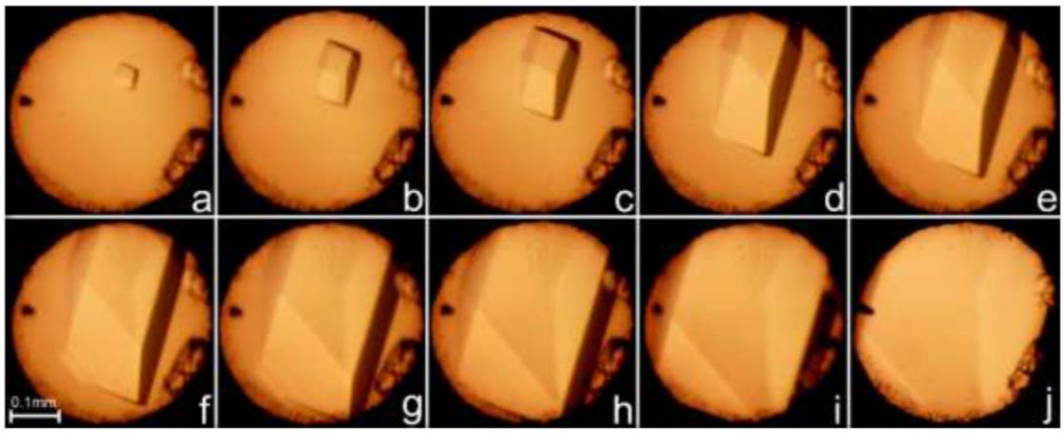

Figure S10. Stages of the propylamine phase III single-crystal growth inside the DAC chamber: (a) one crystal seed at 456 K; (b-i) the single-crystal cooled to 410 K and (j) filling the DAC chamber at 295 K and 4.25 GPa. Two ruby chips for pressure calibration are placed in the right part of the DAC chamber.

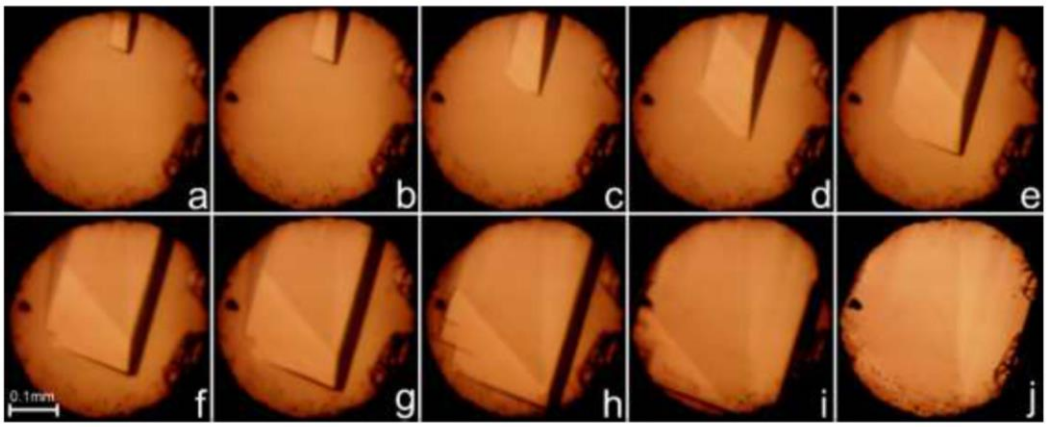

Figure S11. Stages of the propylamine phase III single-crystal growth inside the DAC chamber: (a) one crystal seed at 476 K; (b-i) the single-crystal cooled to 430 K and (j) filling the DAC chamber at 295 K and 4.90 GPa. Two ruby chips for pressure calibration lie in the right part of the DAC chamber.

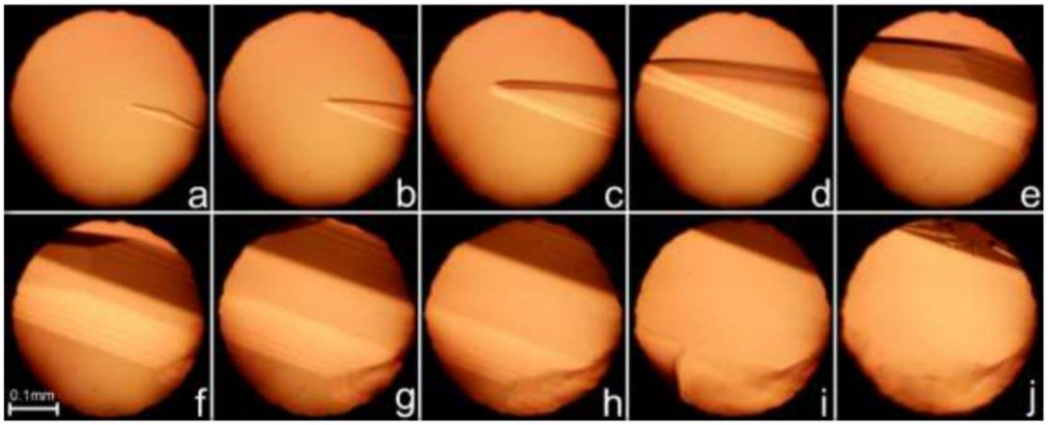

Figure S12. Stages of the butylamine phase II single-crystal growth inside the DAC chamber: (a) one crystal seed at 359 K; (b-i) the single-crystal cooled to 300 K and (j) filling the DAC chamber at 295 K and 1.45 GPa. The ruby chip for pressure calibration is located in the right part of the DAC chamber.

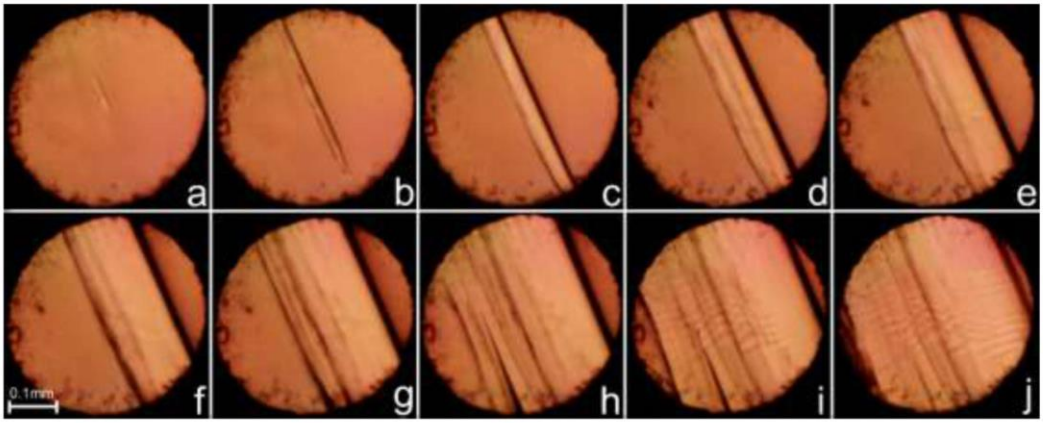

Figure S13. Stages of the butylamine phase III single-crystal growth inside the DAC chamber (polarized-light mode): (a) one crystal seed at 393 K; (b-i) the single-crystal cooled to 351 K and (j) filling the DAC chamber at 295 K and 1.70 GPa. The ruby chip for pressure calibration lies in the left part of the DAC chamber.

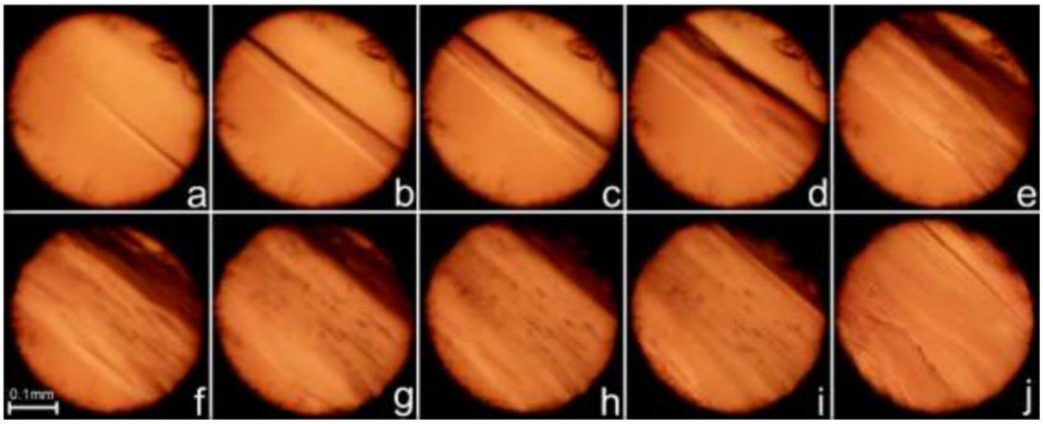

Figure S14. Stages of the butylamine phase III single-crystal growth inside the DAC chamber (polarized-light mode): (a) one crystal seed at 440 K; (b-i) the single-crystal cooled to 413 K and (j) filling the DAC chamber at 295 K and 3.10 GPa. Two ruby chips for pressure calibration are placed in the upper-right part of the DAC chamber.

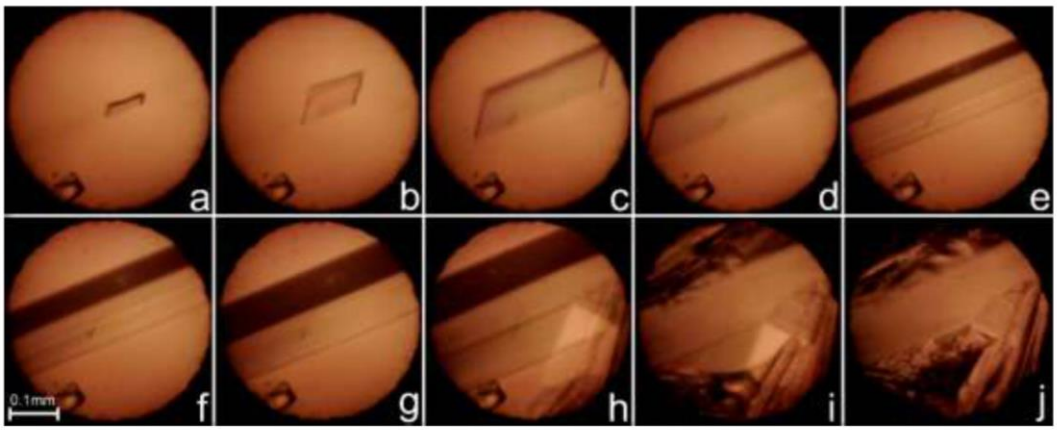

Figure S17. Stages of the pentylamine phase II single-crystal growth inside the DAC chamber: (a) one crystal seed at 450 K; (b-i) the single-crystal cooled to 413 K and (j) filling the DAC chamber at 295 K and 2.60 GPa. The ruby chip for pressure calibration lies in the left-bottom part of the DAC chamber.

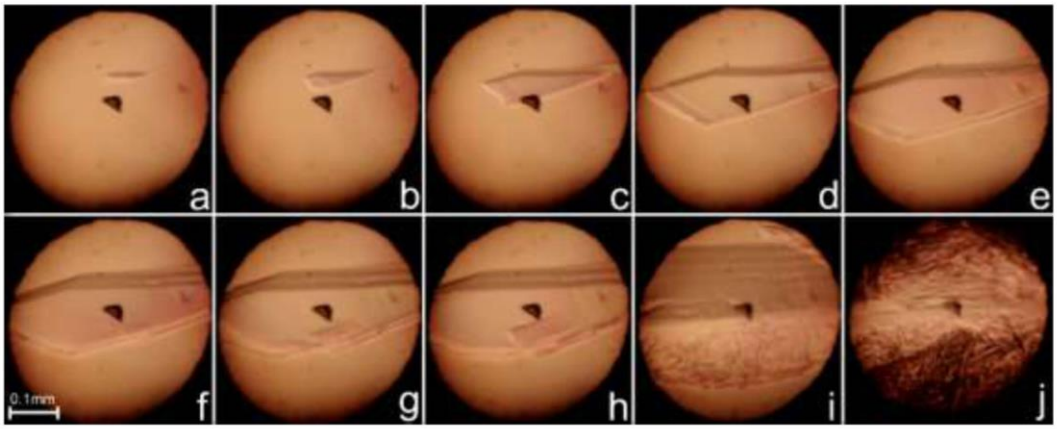

Figure S18. Stages of the pentylamine phase II single-crystal growth inside the DAC chamber (polarized-light mode): (a) one crystal seed at 475 K; (b-i) the single-crystal cooled to 453 K and (j) filling the DAC chamber at 295 K and 3.55 GPa. The ruby chip for pressure calibration is situated in the central part of the DAC chamber.

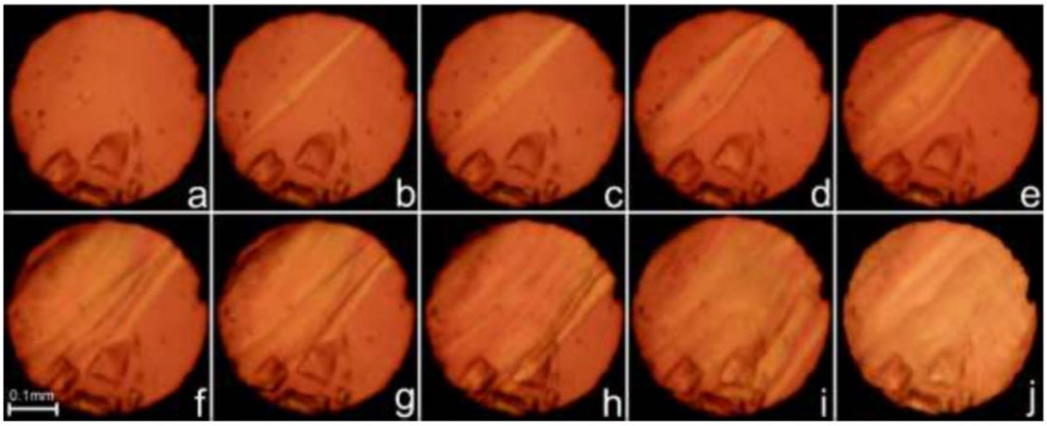

Figure S15. Stages of the butylamine phase III single-crystal growth inside the DAC chamber (polarized-light mode): (a) one crystal seed at 473 K; (b-i) the single-crystal cooled to 457 K and (j) filling the DAC chamber at 295 K and 4.00 GPa. The ruby chips for pressure calibration lie in the bottom part of the DAC chamber.

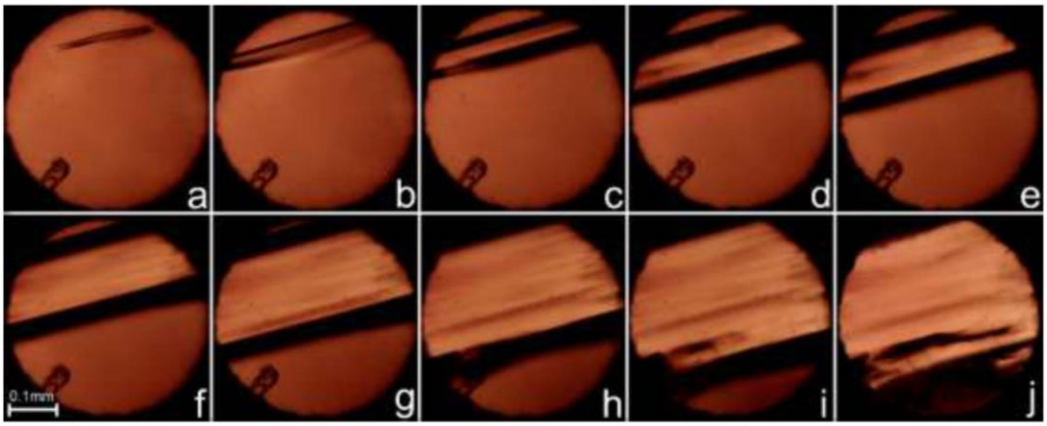

Figure S16. Stages of the pentylamine phase II single-crystal growth inside the DAC chamber: (a) one crystal seed at 366 K; (b-i) the single-crystal cooled to 311 K and (j) filling the DAC chamber at 295 K and 1.05 GPa. The ruby chip for pressure calibration is located in the left-bottom part of the DAC chamber.

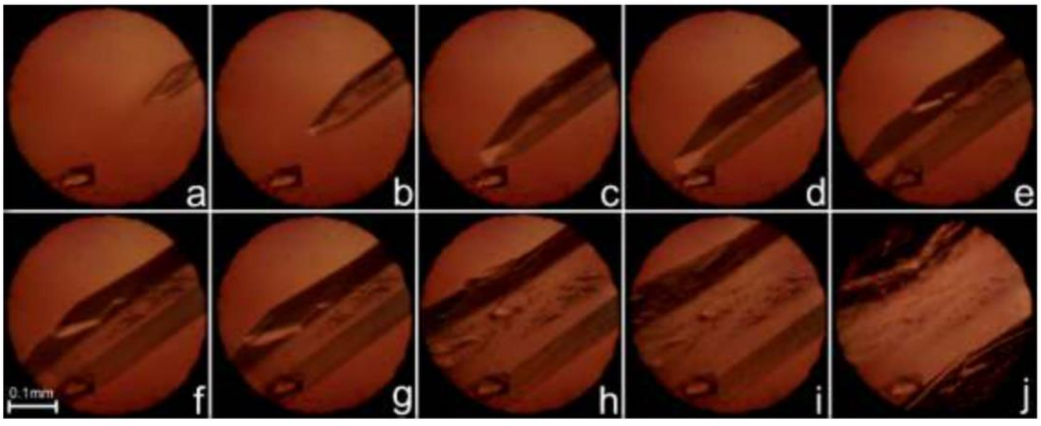

Figure S19. Stages of the pentylamine phase III single-crystal growth inside the DAC chamber (polarized-light mode): (a) one crystal seed at 502 K; (b-i) the single-crystal cooled to 451 K and (j) filling the DAC chamber at 295 K and 4.10 GPa. The ruby chip for pressure calibration lies in the bottom part of the DAC chamber.

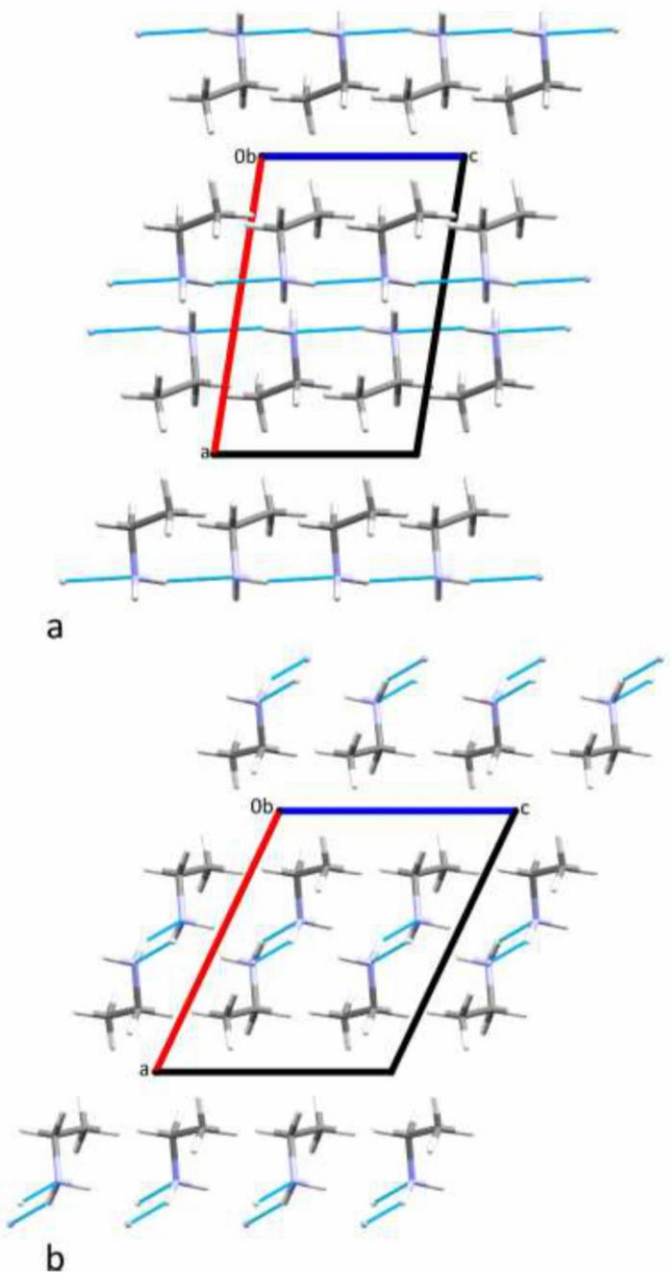

Figure S20. Crystal structures of EA phase I at 0.1 MPa/180 K (a), and EA phase II at 5.05 GPa/295 K (b). The shortest NH···N contacts are indicated with blue dashed lines.

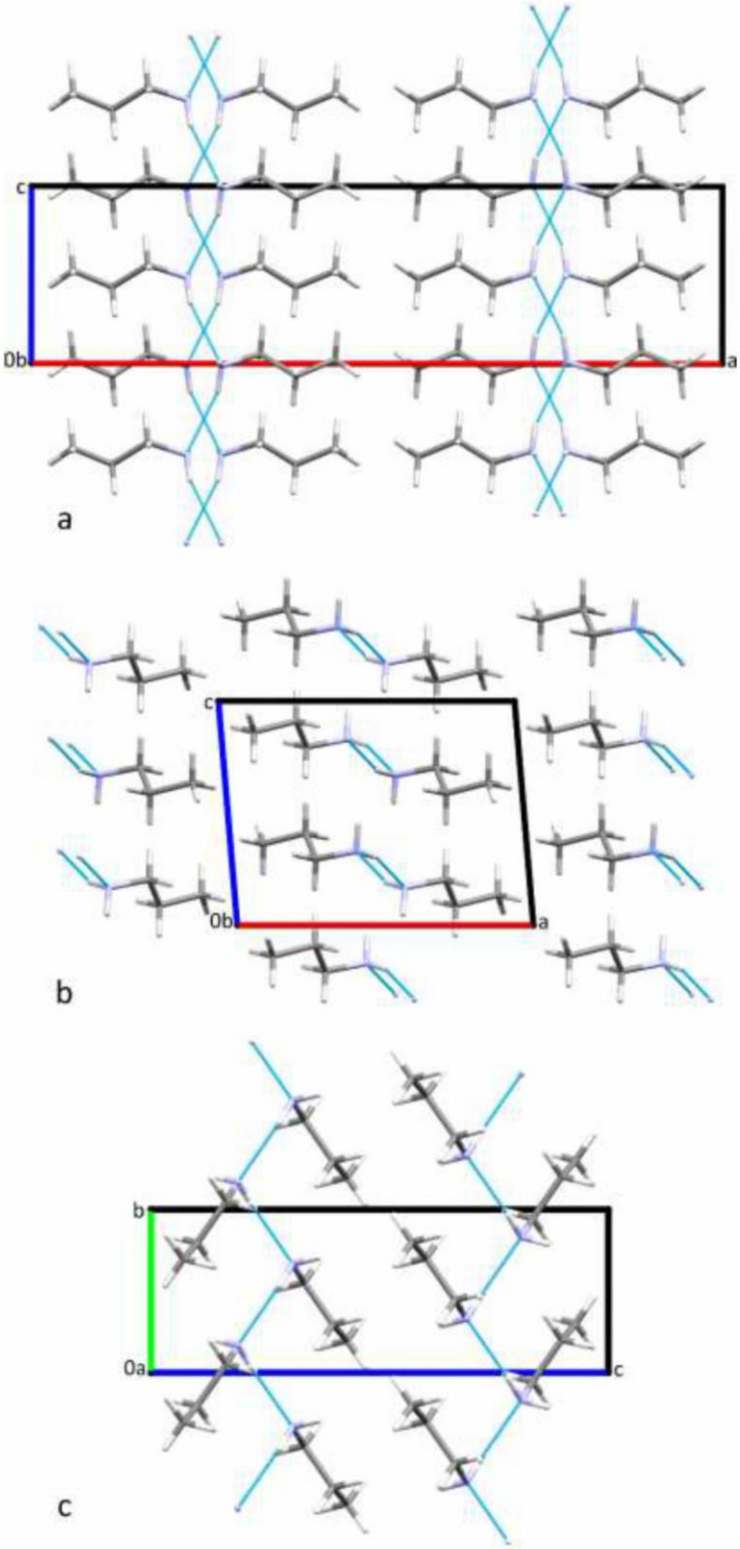

Figure S21. Crystal structures of PA phase I at 0.1 MPa/150 K (a), PA phase II at 2.45 GPa/295 K (b), and PA phase III at 4.90 GPa/295 K (c). The shortest NH···N contacts are indicated with blue dashed lines.

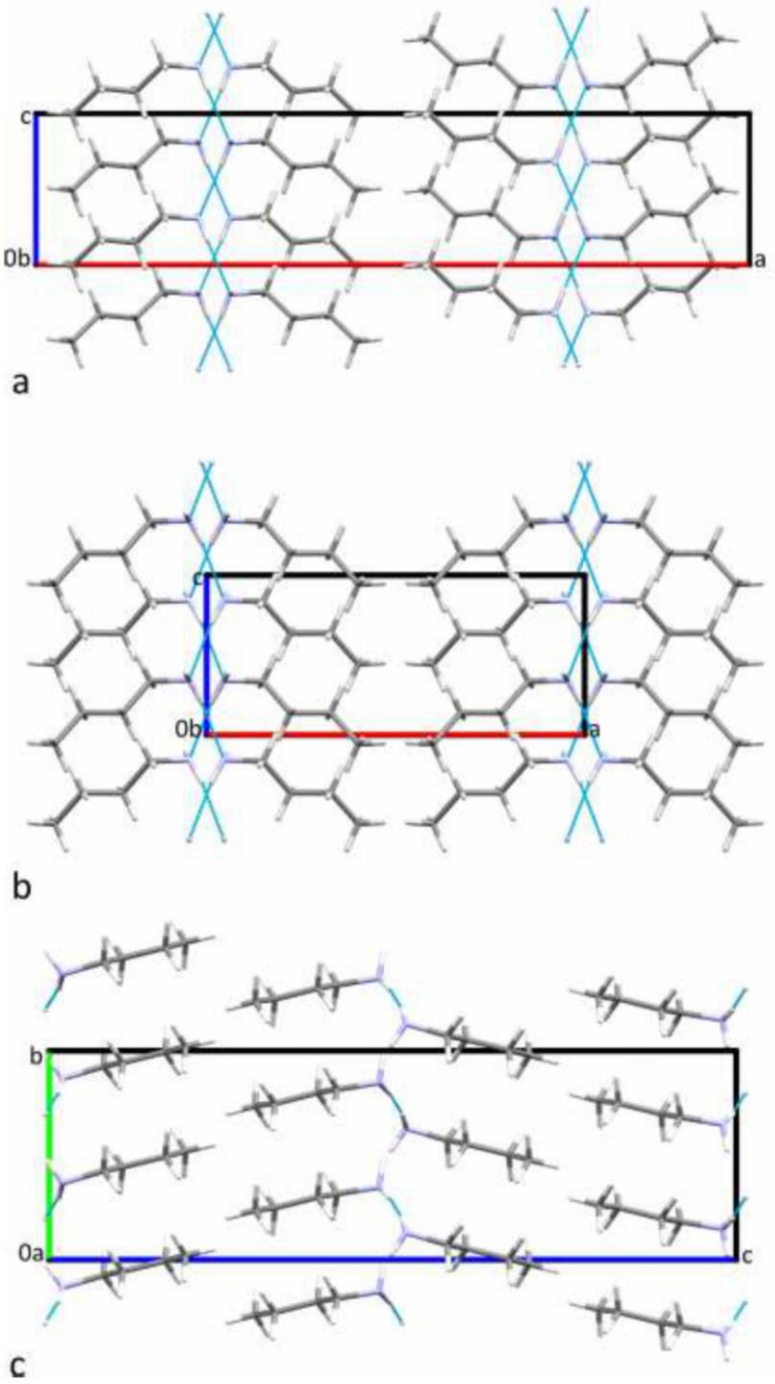

Figure S22. Crystal structures of BA phase I at 0.1 MPa/150 K (a), BA phase II at 1.45 GPa/295 K (b), and BA phase III at 4.00 GPa/295 K (c). The shortest NH···N contacts are indicated with blue dashed lines.

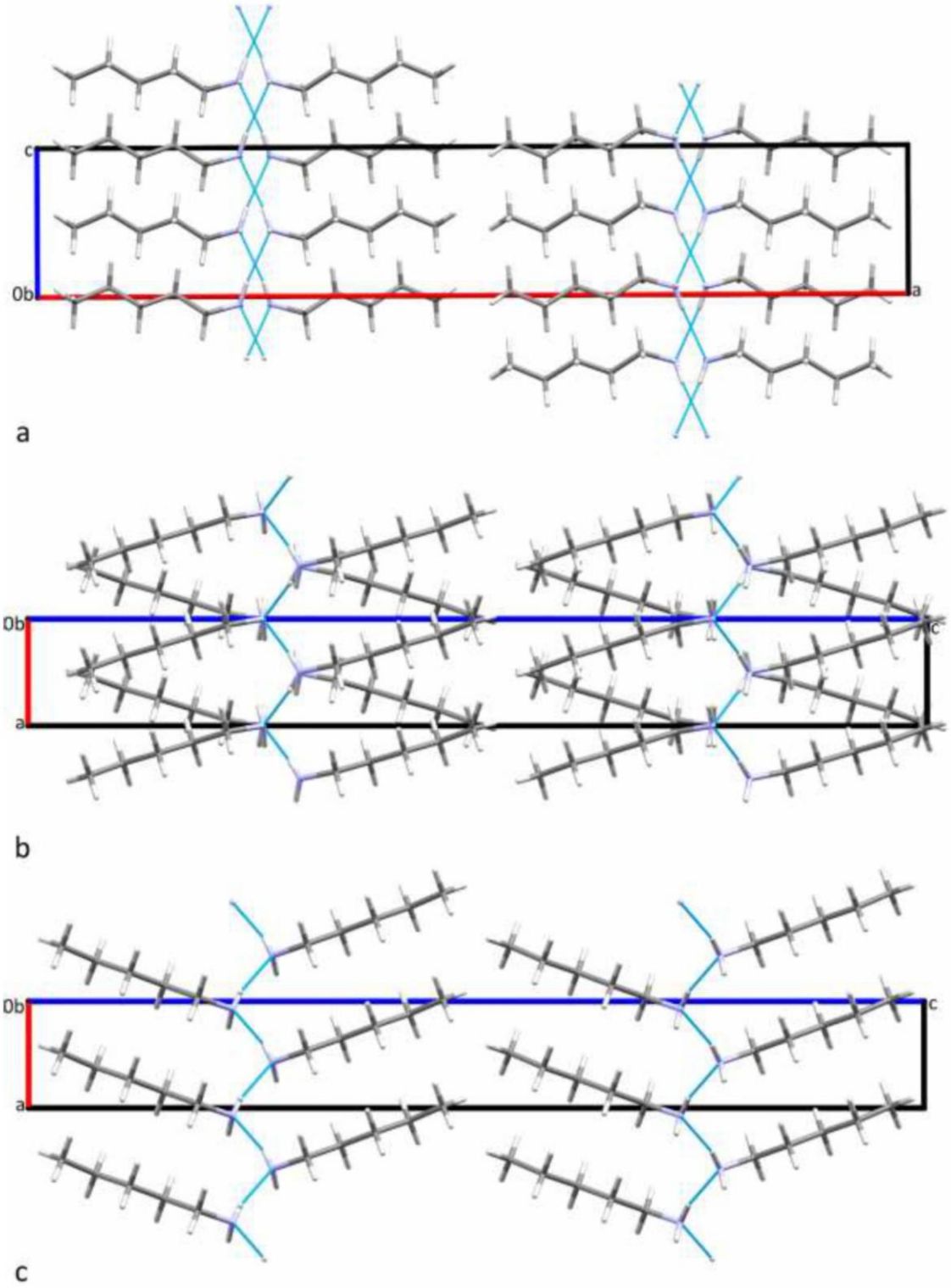

Figure S23. Crystal structures of PEA phase I at 0.1 MPa/150 K (a), PEA phase II at 3.55 GPa/295 K (b), and PEA phase III at 4.10 GPa/295 K (c). The shortest NH···N contacts are indicated with blue dashed lines.

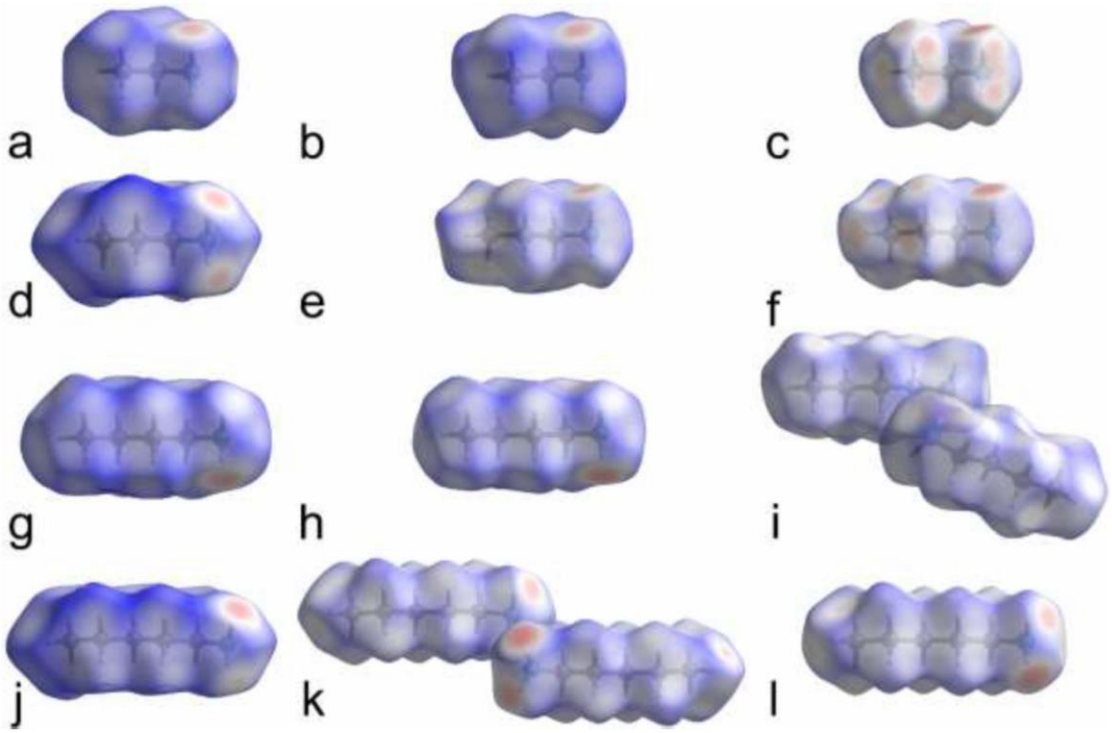

Figure S24. Hirshfeld surfaces (Spackman, P. R.; Turner, M. J.; McKinnon, J. J.; Wolff, S. K.; Grimwood, D. J.; Jayatilaka, D.; Spackman, M. A. *CrystalExplorer21*: a program for Hirshfeld surface analysis, visualization and quantitative analysis of molecular crystals, *J. Appl. Cryst.*, **2021**, *54*, 1006-1011) mapped with d_{norm} (from −1.0500 to 1.3500) of the simplest primary amines molecules: EA phase I at 0.1 MPa/180 K (a), EA phase II at 0.1 MPa/150 K (b), EA phase II at 5.05 GPa/295 K (c), PA phase I at 0.1 MPa/150 K (d), PA phase II at 2.45 GPa/295 K (e), PA phase III at 4.90 GPa/295 K (f), BA phase I at 0.1 MPa/150 K (g), BA phase II at 1.45 GPa/295 K (h), BA phase III at 4.00 GPa/295 K (i), PEA phase I at 0.1 MPa/150 K (j), PEA phase II at 3.55 GPa/295 K (k), and PEA phase III at 4.10 GPa/295 K (l). The white, red and blue colours indicate contacts that are equal, shorter and longer, respectively, than the sums of the van der Waals radii of respective atoms.

Table S1. Crystal data and details of the refinements of ethylamine phase II at 1.40, 1.70 4.35 and 5.05 GPa (all at 295 K).

	C_2H_7N phase II	C_2H_7N phase II	C_2H_7N phase II	C_2H_7N phase II	C_2H_7N phase II
Pressure (GPa)	1.40(2)	1.70(2)	2.60(2)	4.35(2)	5.05(2)
Formula weight	45.09	45.09	45.09	45.09	45.09
Crystal colour	colourless	colourless	colourless	colourless	colourless
Crystal size (mm)	0.34x0.33x0.27	0.33x0.33x0.26	0.34x0.34x0.25	0.37x0.34x0.24	0.39x0.36x0.23
Crystal system	monoclinic	monoclinic	monoclinic	monoclinic	monoclinic
Space group	$P2_1/c$	$P2_1/c$	$P2_1/c$	$P2_1/c$	$P2_1/c$
Unit cell dimensions					
a (Å)	8.80(6)	8.71(7)	8.54(12)	8.382(13)	8.310(8)
b (Å)	4.9804(10)	4.9542(13)	4.895(3)	4.8228(15)	4.798(4)
c (Å)	7.130(17)	7.08(2)	7.00(3)	6.836(5)	6.775(3)
β (°)	113.5(5)	113.6(6)	114.1(11)	115.04(11)	115.40(6)
Volume (Å^3)	286(2)	280(3)	267(5)	250.3(5)	244.0(3)
Z, Z'	4, 1	4, 1	4, 1	4, 1	4, 1
D_x (g·cm^{-3})	1.046	1.070	1.121	1.196	1.227
Wavelength MoKα, λ (Å)	0.71073	0.71073	0.71073	0.71073	0.71073
Absorption coefficient (mm^{-1})	0.066	0.067	0.070	0.075	0.077
F(000) (e)	104	104	104	104	104
2Θ max (°)	54.12	54.53	52.65	52.80	54.12
Min./Max. indices h, k, l	-5/5, -6/6, -8/9	-5/5, -6/6, -8/8	-5/5, -5/6, -8/8	-6/6, -5/5, -8/8	-9/9, -4/4, -7/7
Reflections collected/unique	1014/106	1058/101	884/117	822/147	825/141
R_{int} (all data)	0.0348	0.045	0.0305	0.0353	0.0263
Observed reflections (I>2σ(I))	74	77	79	111	106
Data/restraints/parameters	106/0/13	101/0/13	117/0/13	147/1/13	141/1/13
Completeness (%)	17	16	22	29	26
Goodness of fit on F^2	1.224	1.105	1.257	1.211	1.160
Final R_1 indices (I>2σ(I))	0.0552	0.0436	0.0559	0.0894	0.0941
R_1/wR_2 indices (all data)	0.0822/0.1012	0.0600/0.0802	0.0934/0.1013	0.1301/0.1765	0.1110/0.2635
$\Delta\sigma_{max}$, $\Delta\sigma_{min}$ (e·Å^{-3})	0.08/-0.07	0.05/-0.04	0.10/-0.09	0.20/-0.19	0.21/-0.27
Weighting scheme: x; y[a]	0; 0.34	0.0176; 0.15	0; 0.30	0; 0.98	0.1191; 0.64

[a] $w=1/(\sigma^2(Fo^2)+x^2P^2+yP)$, where $P=(\mathrm{Max}(Fo^2,0)+2Fc^2)/3$

Table S2. Crystal data and details of the refinements of propylamine phase II at 2.25, 2.45 GPa and phase III at 2.50, 2.90, 4.25 and 4.90 GPa (all at 295 K).

	C_3H_9N phase II	C_3H_9N phase II	C_3H_9N phase III	C_3H_9N phase III	C_3H_9N phase III	C_3H_9N phase III
Pressure (GPa)	2.25(2)	2.45(2)	2.50(2)	2.90(2)	4.25(2)	4.90(2)
Formula weight	59.11	59.11	59.11	59.11	59.11	59.11
Crystal colour	colourless	colourless	colourless	colourless	colourless	colourless
Crystal size (mm)	0.37x0.36x0.27	0.38x0.36x0.26	0.31x0.31x0.25	0.33x0.33x0.24	0.37x0.37x0.23	0.47x0.46x0.22
Crystal system	monoclinic	monoclinic	monoclinic	monoclinic	monoclinic	monoclinic
Space group	$P2_1/c$	$P2_1/c$	$P2_1/c$	$P2_1/c$	$P2_1/c$	$P2_1/c$
Unit cell dimensions						
a (Å)	9.5676(11)	9.5576(15)	4.8983(3)	4.8612(2)	4.7754(2)	4.7444(2)
b (Å)	5.0810(16)	5.0525(12)	4.9746(3)	4.9473(2)	4.8803(4)	4.8586(4)
c (Å)	7.303(3)	7.265(6)	14.451(3)	14.308(3)	13.9209(16)	13.8145(19)
β (°)	94.589(18)	94.82(3)	100.758(11)	100.451(8)	99.766(7)	99.537(8)
Volume (Å^3)	353.9(2)	349.6(3)	345.94(8)	338.39(7)	319.73(5)	314.04(5)
Z, Z'	4, 1	4, 1	4, 1	4, 1	4, 1	4, 1
D_x (g·cm^{-3})	1.109	1.123	1.135	1.160	1.228	1.250
Wavelength MoKα, λ (Å)	0.71073	0.71073	0.71073	0.71073	0.71073	0.71073
Absorption coefficient (mm^{-1})	0.067	0.068	0.069	0.071	0.075	0.076
F(000) (e)	136	136	136	136	136	136
2Θ max (°)	53.66	53.90	53.58	53.49	54.00	53.91
Min./Max. indices h, k, l	-12/12, -5/5, -6/6	-12/11, -5/5, -4/4	-6/6, -6/6, -8/8	-6/6, -6/6, -7/7	-5/5, -5/5, -13/13	-5/5, -5/5, -12/12
Reflections collected/unique	1460/251	1392/232	1946/247	1871/196	1753/326	1732/319
R_{int} (all data)	0.0213	0.0307	0.0234	0.0209	0.0181	0.0188
Observed reflections (I>2σ(I))	204	184	231	184	292	278
Data/restraints/parameters	251/0/37	232/0/38	247/0/37	196/0/37	326/0/37	319/0/37
Completeness (%)	33	30	34	27	47	47
Goodness of fit on F^2	1.076	1.169	1.179	1.080	1.084	1.119
Final R_1 indices (I>2σ(I))	0.0399	0.0661	0.0367	0.0353	0.0429	0.0403
R_1/wR_2 indices (all data)	0.0495/0.1162	0.0787/0.2023	0.0388/0.0986	0.0385/0.0980	0.0473/0.1160	0.0453/0.1116
$\Delta\sigma_{max}$, $\Delta\sigma_{min}$ (e·Å^{-3})	0.08/-0.07	0.16/-0.11	0.07/-0.08	0.08/-0.07	0.15/-0.11	0.14/-0.11
Weighting scheme: x; y[a]	0.0690; 0.05	0.1093/0.22	0.0534/0.06	0.0568/0.11	0.0657/0.12	0.0563/0.14

[a] $w=1/(\sigma^2(Fo^2)+x^2P^2+yP)$, where $P=(\mathrm{Max}(Fo^2,0)+2Fc^2)/3$

Table S3. Crystal data and details of the refinements of butylamine phase II at 1.4 phase III at 1.70, 3.10 and 4.00 GPa (all at 295 K).

	$C_4H_{11}N$ phase II	$C_4H_{11}N$ phase III	$C_4H_{11}N$ phase III	$C_4H_{11}N$ phase III
Pressure (GPa)	1.45(2)	1.70(2)	3.10(2)	4.00(2)
Formula weight	73.14	73.14	73.14	73.14
Crystal colour	colourless	colourless	colourless	colourless
Crystal size (mm)	0.38x0.38x0.27	0.39x0.38x0.26	0.30x0.30x0.25	0.33x0.31x0.24
Crystal system	orthorhombic	orthorhombic	orthorhombic	orthorhombic
Space group	$Pbc2_1$	$Pbc2_1$	$Pbc2_1$	$Pbc2_1$
Unit cell dimensions				
a (Å)	12.8348(9)	5.020(5)	4.880(10)	4.8802(14)
b (Å)	6.5975(11)	7.337(4)	7.164(3)	7.0738(10)
c (Å)	5.4185(4)	23.823(5)	23.603(9)	23.282(9)
Volume (Å^3)	458.83(9)	877.4(11)	825.2(17)	803.7(4)
Z, *Z'*	4, 1	8, 2	8, 2	8, 2
D_x (g·cm^{-3})	1.059	1.107	1.177	1.209
Wavelength MoKα, λ (Å)	0.71073	0.71073	0.71073	0.71073
Absorption coefficient (mm^{-1})	0.063	0.066	0.070	0.072
F(000) (e)	168	336	336	336
2Θ max (°)	53.75	52.34	51.47	53.36
Min./Max. indices *h*, *k*, *l*	-15/15, -5/5, -6/6	-3/3, -7/7, -29/29	-3/3, -8/8, -27/27	-5/5, -8/8, -22/21
Reflections collected/unique	2383/597	2627/608	2405/697	4522/889
R_{int} (all data)	0.0377	0.0647	0.0432	0.0397
Observed reflections (I>2σ(I))	470	356	436	733
Data/restraints/parameters	597/1/46	608/1/41	697/2/91	889/7/91
Completeness (%)	60	35	44	54
Goodness of fit on F^2	1.049	1.101	1.074	1.061
Final R_1 indices (I>2σ(I))	0.0449	0.0891	0.0606	0.0596
R_1/wR_2 indices (all data)	0.0631/0.1205	0.1331/0.2512	0.1050/0.1712	0.0738/0.1718
$\Delta\sigma_{max}$, $\Delta\sigma_{min}$ (e·Å^{-3})	0.11/-0.10	0.22/-0.18	0.13/-0.17	0.33/-0.16
Weighting scheme: x; y[a]	0.0689/0.03	0.0971/1.39	0.0900/0	0.0905/0.67

[a] $w=1/(\sigma^2(Fo^2)+x^2P^2+yP)$, where $P=(\mathrm{Max}(Fo^2,0)+2Fc^2)/3$

Table S4. Crystal data and details of the refinements of pentylamine phase II at 1.05, 3.55 GPa, and phase III at 4.10 GPa (all at 295 K).

	$C_5H_{13}N$ phase II	$C_5H_{13}N$ phase II	$C_5H_{13}N$ phase II	$C_5H_{13}N$ phase III
Pressure (GPa)	1.05(2)	2.60(2)	3.55(2)	4.10(2)
Formula weight	87.16	87.16	87.16	87.16
Crystal colour	colourless	colourless	colourless	colourless
Crystal size (mm)	0.39x0.38x0.27	0.41x0.40x0.26	0.40x0.39x0.25	0.39x0.37x0.24
Crystal system	orthorhombic	orthorhombic	orthorhombic	orthorhombic
Space group	$Pbc2_1$	$Pbc2_1$	$Pbc2_1$	$P2_1cn$
Unit cell dimensions				
a (Å)	3.9646(14)	3.8123(16)	3.7562(6)	3.7101(11)
b (Å)	8.682(4)	8.2638(6)	8.170(4)	4.0956(12)
c (Å)	32.055(5)	31.704(3)	31.66(2)	31.167(6)
Volume (Å^3)	1103.4(6)	998.8(4)	971.5(8)	473.6(2)
Z, Z'	8, 2	8, 2	8, 2	4, 1
D_x (g·cm^{-3})	1.049	1.159	1.192	1.222
Wavelength MoKα, λ (Å)	0.71073	0.71073	0.71073	0.71073
Absorption coefficient (mm^{-1})	0.062	0.068	0.070	0.072
F(000) (e)	400	400	400	200
2Θ max (°)	52.86	53.10	53.29	52.93
Min./Max. indices h, k, l	-3/3, -8/8, -39/39	-2/2, -10/10, -37/37	-4/4, -7/7, -31/31	-3/3, -3/3, -36/36
Reflections collected/unique	4831/1209	3951/999	4386/1156	2159/547
R_{int} (all data)	0.0516	0.0331	0.0537	0.0350
Observed reflections (I>2σ(I))	726	696	716	413
Data/restraints/parameters	1209/1/109	999/1/109	1156/1/48	547/1/55
Completeness (%)	54	49	57	55
Goodness of fit on F^2	1.057	1.038	1.014	1.091
Final R_1 indices (I>2σ(I))	0.0665	0.0529	0.0608	0.0469
R_1/wR_2 indices (all data)	0.1200/0.1778	0.0828/0.1315	0.1124/0.1645	0.0710/0.1092
$\Delta\sigma_{max}$, $\Delta\sigma_{min}$ (e·Å^{-3})	0.13/-0.13	0.10/-0.12	0.20/-0.12	0.12/-0.10
Weighting scheme: x; y[a]	0.0616/0.77	0.0545/0.50	0.0688/0.33	0.0407/0.20

[a] $w=1/(\sigma^2(Fo^2)+x^2P^2+yP)$, where $P=(\mathrm{Max}(Fo^2,0)+2Fc^2)/3$

Paper P2

High-Pressure Crystal Structure of *n*-Hexylamine

Kuleczka, B.; **Sacharczuk, N.**; Olejniczak, A.; Podsiadło, M.

Acta Cryst. **2025**, *C81*, 346–350

STRUCTURAL CHEMISTRY
ISSN 2053-2296

High-pressure crystal structure of *n*-hexylamine

Bernadetta Kuleczka, Natalia Sacharczuk, Anna Olejniczak and Marcin Podsiadło*

Faculty of Chemistry, Adam Mickiewicz University, Uniwersytetu Poznańskiego 8, 61-614 Poznań, Poland. *Correspondence e-mail: marcinp@amu.edu.pl

Received 26 March 2025
Accepted 20 May 2025

Edited by I. Oswald, University of Strathclyde, United Kingdom

Keywords: hexylamine; crystal structure; N—H···N hydrogen bonds; aliphatic amines; *in-situ* crystallization; high pressure; compressibility.

CCDC references: 2434096; 2434097; 2434098

Supporting information: this article has supporting information at journals.iucr.org/c

A primary amine, *n*-hexylamine (**HA**, $C_6H_{15}N$), has been studied at high pressure by single-crystal X-ray diffraction. The structure of this compound has been determined, at ambient temperature, from the freezing pressure up to 1.40 GPa. **HA** at high pressure crystallizes in the space group $Pca2_1$, which was already found at ambient pressure and low temperature. The compressibility of the N—H···N hydrogen bonds has been compared with that of the shortest C—H···N and H···H intermolecular distances, revealing that the H···H distances exhibit the highest degree of compressibility among them.

1. Introduction

N—H···N hydrogen bonds often compete with weaker C—H···N hydrogen bonds in crystals (Huang *et al.*, 2013; Leigh *et al.*, 2013; Podsiadło *et al.*, 2017; Sacharczuk *et al.*, 2023; Vega *et al.*, 2005). The role of these interactions, as the main cohesion forces in crystals, has been well documented for biomolecules, self-organizing materials, pharmaceuticals and molecular switches (Desiraju & Steiner, 2001; Jeffrey & Saenger, 1994). The simplest aliphatic amines serve as model compounds for studying the nature of such interactions due to their molecular composition and the minimized effect of the molecular shape on dense packing.

HA
Scheme 1

Structural studies of the simplest *n*-aliphatic amines have been performed at low temperature and ambient pressure for methylamine (Atoji & Lipscomb, 1953), as well as for the series from ethylamine to *n*-decylamine (Maloney *et al.*, 2014). These studies described the role of various types of intermolecular interactions in molecular association. N—H···N hydrogen bonds have been identified as the main cohesion force for the early primary amines; however, the role of dispersive interactions between alkyl chains was also emphasized (for the later compounds, the dispersion interactions dominate over hydrogen bonding). It was also found that dispersive interactions were particularly dominant in the regions between molecular layers linked by N—H···N hydrogen bonds (Maloney *et al.*, 2014).

This study of *n*-hexylamine (**HA**; Scheme 1 and Fig. 1) extends our previous research on the simplest primary amines under high pressure. Recently, we have investigated the series from methylamine to *n*-pentylamine (Podsiadło *et al.*, 2017; Sacharczuk *et al.*, 2023). Only ethylamine crystallizes in the same phase under high pressure (phase II) as found at low temperature. In contrast, seven new polymorphs, different from the low-temperature ones, have been identified at high

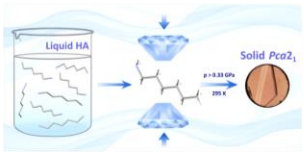

Table 1
Experimental details.

For all determinations: $C_6H_{15}N$, M_r = 101.19, orthorhombic, $Pca2_1$, Z = 4. Experiments were carried out at 295 K with Mo $K\alpha$ radiation. Absorption was corrected for by multi-scan methods (*CrysAlis PRO*; Rigaku OD, 2022). Refinement was on 64 parameters with 1 restraint. H-atom parameters were constrained.

	HA at 0.50 GPa	**HA** at 0.65 GPa	**HA** at 1.40 GPa
Crystal data			
a, b, c (Å)	6.9050 (9), 17.549 (7), 5.5212 (13)	6.8591 (9), 17.494 (5), 5.4892 (4)	6.7241 (19), 17.052 (13), 5.3367 (7)
V (Å^3)	669.1 (3)	658.7 (2)	611.9 (5)
μ (mm^{-1})	0.06	0.06	0.06
Crystal size (mm)	0.28 × 0.28 × 0.27	0.27 × 0.27 × 0.26	0.26 × 0.26 × 0.23
Data collection			
Diffractometer	Rigaku Xcalibur Eos	Rigaku Xcalibur Atlas	Rigaku Xcalibur Atlas
T_{min}, T_{max}	0.573, 1.000	0.600, 1.000	0.447, 1.000
No. of measured, independent and observed [$I > 2\sigma(I)$] reflections	4308, 832, 373	5447, 1085, 527	4114, 852, 401
R_{int}	0.071	0.063	0.068
(sin $\theta/\lambda)_{max}$ (Å^{-1})	0.663	0.732	0.713
Refinement			
$R[F^2 > 2\sigma(F^2)]$, $wR(F^2)$, S	0.054, 0.118, 1.04	0.047, 0.131, 0.98	0.061, 0.194, 1.04
No. of reflections	832	1085	852
$\Delta\rho_{max}$, $\Delta\rho_{min}$ (e Å^{-3})	0.09, −0.09	0.10, −0.10	0.17, −0.20
Absolute structure	Flack x determined using 128 quotients [$(I^+) - (I^-)$]/[$(I^+) + (I^-)$] (Parsons *et al.*, 2013)	Flack x determined using 181 quotients [$(I^+) - (I^-)$]/[$(I^+) + (I^-)$] (Parsons *et al.*, 2013)	Flack x determined using 130 quotients [$(I^+) - (I^-)$]/[$(I^+) + (I^-)$] (Parsons *et al.*, 2013)
Absolute structure parameter	−10.0 (10)	0.7 (10)	3.1 (10)

Computer programs: *CrysAlis PRO* (Rigaku OD, 2022), *SHELXT2018* (Sheldrick, 2015*a*), *SHELXL2018* (Sheldrick, 2015*b*), *Mercury* (Macrae *et al.*, 2020) and *OLEX2* (Dolomanov *et al.*, 2009).

pressure for the remaining amines, *i.e.* one for methylamine (Podsiadło *et al.*, 2017) and two each for propylamine, butylamine and pentylamine (Sacharczuk *et al.*, 2023). In all these polymorphs, molecules interact through N—H···N hydrogen bonds. However, at high pressure, the role of C—H···N hydrogen bonds increases (Sacharczuk *et al.*, 2023).

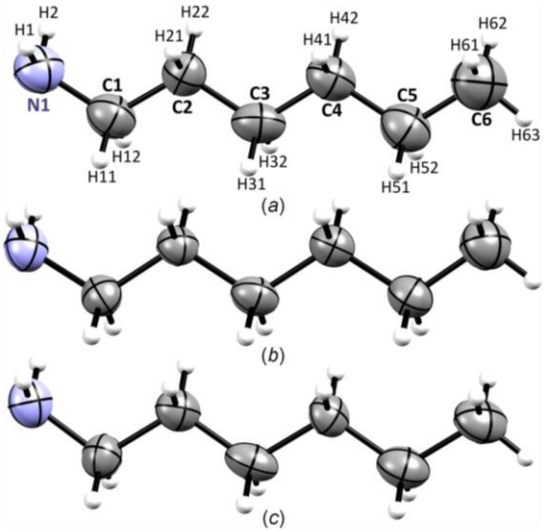

Figure 1
The molecular structures of **HA** at (*a*) 0.50 GPa, (*b*) 0.65 GPa and (*c*) 1.40 GPa (all at 295 K), showing the atomic labelling scheme. Displacement ellipsoids are drawn at the 50% probability level.

In the present study, we have investigated **HA** at high pressure using single-crystal X-ray diffraction. The crystal structure has been determined previously at ambient pressure and low temperature only (Maloney *et al.*, 2014). We have obtained and investigated single crystals of **HA** in a diamond-anvil cell (DAC) in the range between the freezing pressure at ambient temperature of 0.33 GPa up to 1.40 GPa.

2. Experimental

n-Hexylamine, **HA** (99%), from Sigma–Aldrich was crystallized *in situ* in a modified Merrill–Basset diamond-anvil cell (DAC; Bassett, 2009). The DAC was equipped with a 0.3 mm thick steel gasket with a hole of diameter 0.3 mm. At 295 K, **HA** froze at 0.33 GPa, in the form of a polycrystalline mass, filling the whole volume of the DAC chamber. A single crystal of **HA** was obtained under isothermal conditions. The polycrystalline mass was melted, except for one crystallite, by decreasing the pressure slowly. Then, again slowly, the pressure was increased allowing a single crystal of **HA** to grow and eventually fill the entire volume of the chamber (Fig. 2). Afterwards, the pressure was increased by *ca* 0.2 GPa to achieve a stable single crystal required for the X-ray diffraction measurement. Several attempts were made to grow a single crystal under isochoric conditions at pressures above 0.50 GPa; however, all were unsuccessful. The growing single crystals were very sensitive to temperature changes, and each time additional crystallites occurred, even with slow cooling. For this reason, single crystals at pressures of 0.65 and 1.40 GPa were obtained at room temperature by increasing the pressure in the chamber after performing the X-ray

measurements at 0.50 and 0.65 GPa. The pressure was calibrated by the ruby fluorescence method (Mao *et al.*, 1986; Piermarini *et al.*, 1975) using a Photon Control spectrometer with an accuracy of 0.02 GPa. The calibrations were performed before and after each X-ray diffraction experiment. The progress of the growth of the **HA** single crystal is shown in Fig. 2 and Fig. S1 in the supporting information.

Rigaku Xcalibur EOS and Xcalibur ATLAS diffractometers were used for the high-pressure studies. The DAC was centred by the gasket-shadow method (Budzianowski & Katrusiak, 2004).

The room-temperature compressibility measurement was performed up to *ca* 2 GPa in a piston-and-cylinder apparatus (Baranowski & Moroz, 1982; Dziubek & Katrusiak, 2014) with an initial volume of *ca* 8.5 cm^3.

2.1. Refinement

Crystal data, data collection and structure refinement details are summarized in Table 1. The H atoms of the methylene and methyl groups were located based on the molecular geometry, with the C—H distances equal to 0.97 or 0.96 Å and their U_{iso} factors constrained to 1.2 or 1.5 times the U_{eq} value of their carrier. The H atoms of the amine ($-NH_2$) group were located based on the molecular geometry, assuming N—H distances equal to 0.90 Å, and their U_{iso} factors were constrained to 1.2 times the U_{eq} value of their carrier. The crystal data and refinement details are summarized in Tables 1 and 2, and Table S1 in the supporting information.

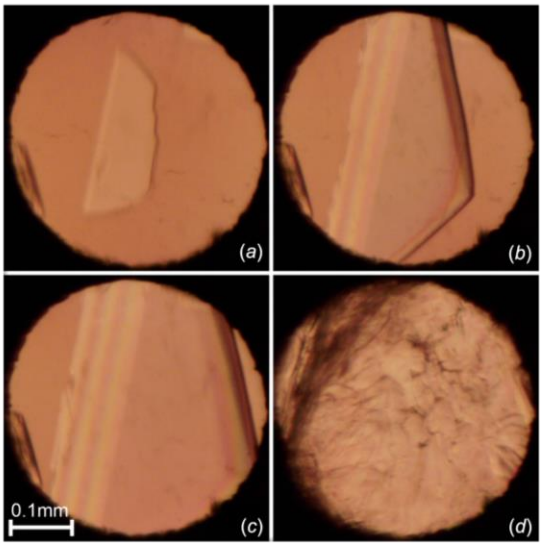

Figure 2
Stages of the **HA** single-crystal growth inside the DAC chamber (polarized-light mode): (*a*) one crystal seed at 295 K and 0.33 GPa, (*b*)/(*c*) the single-crystal growth with increasing pressure and a simultaneous decrease in the volume of the high-pressure chamber, and (*d*) the single crystal filling the DAC chamber at 295 K and 0.50 GPa. The ruby chip, for pressure calibration, is located by the left edge of the DAC.

Table 2
Selected crystal data of **HA** at 0.1 MPa/150 K and 0.50, 0.65 and 1.40 GPa (all at 295 K).

	$C_6H_{15}N^a$	$C_6H_{15}N^b$	$C_6H_{15}N^b$	$C_6H_{15}N^b$
p (GPa)	0.0001	0.50 (2)	0.65 (2)	1.40 (2)
T (K)	150	295 (2)	295 (2)	295 (2)
Crystal system	Orthorhombic	Orthorhombic	Orthorhombic	Orthorhombic
Space group	$Pca2_1$	$Pca2_1$	$Pca2_1$	$Pca2_1$
a (Å)	6.9725 (3)	6.9050 (9)	6.8591 (9)	6.7241 (19)
b (Å)	17.7977 (6)	17.549 (7)	17.494 (5)	17.052 (13)
c (Å)	5.6105 (2)	5.5212 (13)	5.4892 (4)	5.3367 (7)
V ($Å^3$)	696.23 (5)	669.1 (3)	658.7 (2)	611.9 (5)
Z, Z'	4, 1	4, 1	4, 1	4, 1
D_x (g cm^{-3})	0.965	1.005	1.020	1.098
R_1 [$F^2 > 2\sigma(F^2)$]	0.0418	0.0544	0.0472	0.0612
R_1 (all data)	-	0.1726	0.1434	0.1624

References: (*a*) Maloney *et al.* (2014); (*b*) this work.

3. Results and discussion

The single crystal of **HA** was obtained at the lowest possible pressure of 0.50 GPa (*ca* 0.2 GPa above the freezing pressure) to ensure the stability of the crystal during the X-ray diffraction data collection experiment. Two additional measurements were performed on this crystal compressed under isothermal conditions to 0.65 GPa and then to 1.40 GPa. The pressure of 1.40 GPa was the highest, at which the compressive stress on the crystal did not significantly affect the quality of the diffraction data. Above 1.40 GPa, the **HA** single crystal cracked due to mechanical stress. The crystals obtained under high pressure are denser than those crystallized at ambient pressure and low temperature (Table 2). All the unit-cell parameters of the investigated **HA** crystals decrease with increasing pressure, leading to the more dense structures. The molecular volume of **HA** as a function of pressure has been plotted in Fig. 3.

The compression of the molecular volume of **HA** measured at 295 K in a piston-and-cylinder press (Baranowski & Moroz, 1982; Dziubek & Katrusiak, 2014) changes abruptly by 2.6% on freezing the liquid at 0.33 GPa (Fig. 3). After freezing, the solid **HA** is initially strongly compressed until about 0.80 GPa; thereafter, the compression decreases monotonically, and at 1.96 GPa, the volume reaches about 65% of the liquid at 0.1 MPa and 80% of the solid at 0.33 GPa. The molecular volume determined using the piston-and-cylinder press is consistent with that obtained by single-crystal X-ray diffraction (Fig. 3).

HA at 0.1 MPa/150 K crystallizes in the noncentrosymmetric space group $Pca2_1$, adopting a layered arrangement with infinite N—H···N hydrogen-bonded chains running within the layers (Maloney *et al.*, 2014). These N—H···N hydrogen-bonded chains can be described by the symbol $C_1^1(2)$ according to the graph-set notation of hydrogen bonds (Etter *et al.*, 1990). Within the chains, each N atom acts as a donor and an acceptor of an H atom. These chains are retained at high pressure when **HA** crystallizes in the same phase at

Table 3
Hydrogen-bond geometry (Å, °).

N1—H1···N1^{i}	0.50 GPa	0.65 GPa	1.40 GPa
N1—H1	0.900 (7)	0.900 (4)	0.900 (7)
H1···N1^{i}	2.229 (6)	2.230 (3)	2.168 (5)
N1···N1^{i}	3.116 (7)	3.115 (4)	3.050 (8)
N1—H1···N1^{i}	168.2 (2)	167.44 (13)	166.4 (2)

Symmetry code: (i) $-x+1, -y, z-\frac{1}{2}$.

0.33 GPa/295 K (Fig. 4). This structure remains stable up to at least a pressure of 1.40 GPa.

N—H···N hydrogen bonds play a major role in the cohesion force in **HA** crystals at ambient pressure/low temperature and within the investigated pressure range at room temperature. These interactions at ambient pressure/low temperature are characterized by intermolecular H···N distances shorter by *ca* 0.45 Å (Maloney *et al.*, 2014) than the sum of the van der Waals radii of H and N atoms of 2.75 Å (Bondi, 1964) (Figs. 4 and 5). At 0.50 GPa, these distances are 2.229 (6) Å, and they are even shorter at 1.40 GPa, *i.e.* 2.168 (5) Å (Figs. 4 and 5, and Table 3).

It is characteristic that the second shortest intermolecular H···N distances from the N—H···N hydrogen bonding are approximately 0.6 Å longer than the shortest. Within the investigated pressure range, these distances remain longer than the sum of the van der Waals radii (Fig. 5). Such a property was observed for the first time in the high-pressure structures of the simplest primary amines (Podsiadło *et al.*, 2017; Sacharczuk *et al.*, 2023). Furthermore, even in the **HA** structure at 1.40 GPa, no intermolecular H···N distances from C—H···N hydrogen bonds shorter than the sum of the van der Waals radii are observed. **HA** is therefore the first primary *n*-amine in the series from methyl- to hexylamine where, at high pressure, only single N—H···N hydrogen-bonded chains

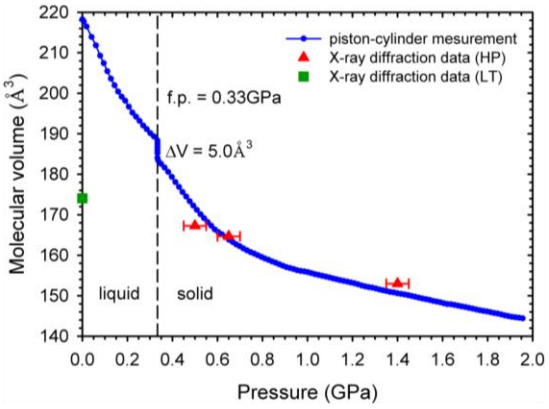

Figure 3
The molecular volume of **HA** at room temperature as a function of pressure measured in the piston-and-cylinder press (blue circles). The volumes measured at high pressure (red triangles) and low temperature (green square; Maloney *et al.*, 2014) by single-crystal X-ray diffraction have been indicated. The freezing pressure (f.p.) of 0.33 GPa is marked with a vertical dashed line.

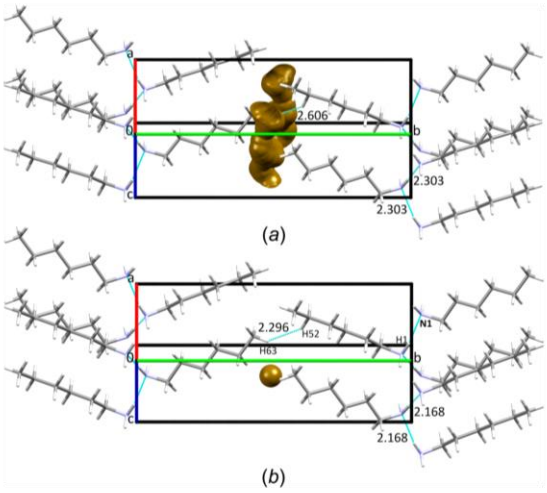

Figure 4
Structures of **HA** at low-temperature (Maloney *et al.*, 2014) and high-pressure conditions: (*a*) 0.1 MPa/150 K and (*b*) 1.40 GPa/295 K. Four hydrogen bonds (N—H···N) and one short intermolecular H···H distance at the end of the carbon chains are marked with dashed lines (distances are indicated). The intermolecular space accessible to a probe with a radius of 0.7 Å and a grid spacing of 0.1 Å (Macrae *et al.*, 2020) is indicated in yellow.

are observed. The C—H···N hydrogen bonds are not formed at all and no phase transition, that would allow molecular rearrangement and the formation of C—H···N interactions, occurred (Podsiadło *et al.*, 2017; Sacharczuk *et al.*, 2023). In the series from methyl- to pentylamine, high pressure does not affect the main cohesive force (N—H···N hydrogen bonds); however, intermolecular C—H···N interactions are observed in the high-pressure polymorphs (Podsiadło *et al.*, 2017; Sacharczuk *et al.*, 2023).

In the **HA** crystals, only at a pressure of 1.40 GPa do the shortest intermolecular H···H distances, at the end of the carbon chains, become shorter than the sum of the van der Waals radii of two H atoms of 2.4 Å (Bondi, 1964) (Figs. 4 and 5, and Fig. S2 in the supporting information). It is characteristic that, with increasing pressure, these shortest intermolecular H···H distances are more compressible than the main N—H···N contacts (Figs. 4 and 5). This is related to the voids observed in the crystals between the ends of the carbon chains (Fig. 4).

In the series from methyl- to hexylamine, **HA** forms the least dense crystals in the structures determined just above their freezing pressure. The crystal density of methylamine determined at 3.65 GPa is 1.165 g cm^{-3} (Podsiadło *et al.*, 2017), ethylamine at 1.40 GPa is 1.046 g cm^{-3} (Sacharczuk *et al.*, 2023), propylamine at 2.25 GPa is 1.109 g cm^{-3} (Sacharczuk *et al.*, 2023), butylamine at 1.45 GPa is 1.059 g cm^{-3} (Sacharczuk *et al.*, 2023) and pentylamine at 1.05 GPa is 1.049 g cm^{-3} (Sacharczuk *et al.*, 2023). The crystal density of **HA**, determined within this study, at 0.50 GPa is 1.005 g cm^{-3}. This correlates with the void volumes in the structures

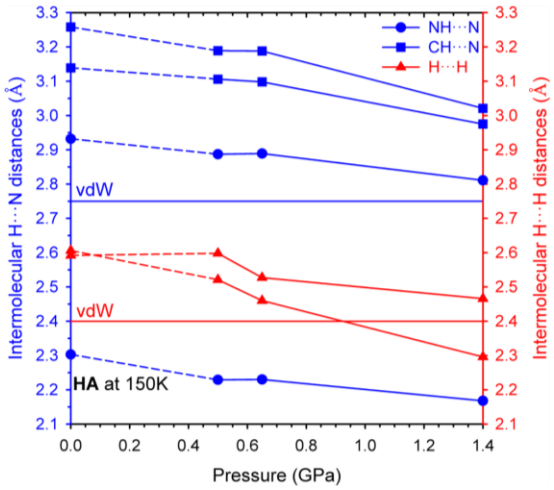

Figure 5
Intermolecular H···N and H···H distances (Å) observed in **HA** structures plotted as a function of pressure. The two shortest distances for each type are presented: blue circles represent the N—H···N and blue squares depict the C—H···N hydrogen–acceptor (H···*A*) distances, while red triangles represent intermolecular H···H distances. Blue and red horizontal lines show the sum of the van der Waals radii of H and N of 2.75 Å, and of two H atoms of 2.40 Å (Bondi, 1964). The estimated standard deviations are smaller than the plotted symbols.

mentioned above, which, in the series from methyl- to hexylamine, are 0, 7.15, 7.86, 12.94, 13.65 and 38.45 Å^3, respectively (the intermolecular space accessible to a probe with a radius of 0.6 Å and a grid spacing of 0.1 Å; the parameters used in the calculations differ from those used in Fig. 4, ensuring distinguishable void volumes across the entire series; Macrae *et al.*, 2020).

4. Conclusions

The high-pressure crystal structure of **HA** is isostructural with the phase determined at low temperature at 0.1 MPa (Maloney *et al.*, 2014). This represents the first example among the series of the simplest aliphatic amines where the crystal symmetry remains unchanged between low-temperature and high-pressure conditions. The space group symmetry of $Pca2_1$ remains stable within the investigated pressure range. Similar to other aliphatic *n*-amines, the main cohesion force in the **HA** crystals involves the N—H···N hydrogen-bonded chains. However, no additional intermolecular distances shorter than the sum of the van der Waals radii are observed. This is unique within the high-pressure studies of the methyl- to pentylamine series, where high pressure enhances the role of intermolecular C—H···N interactions. Only at 1.40 GPa does the first intermolecular H···H distance become shorter than the sum of the van der Waals radii of two H atoms. The compressibility of this distance exceeds that of the intermolecular N—H···N hydrogen bonds. This effect results from the voids surrounding the methyl groups at the ends of the carbon chains. The **HA** crystal obtained just above the freezing pressure is the least dense structure among the high-pressure structures determined in the methyl- to hexylamine series.

Funding information

Funding for this research was provided by: National Science Centre (grant No. 2020/37/B/ST4/00982).

References

Atoji, M. & Lipscomb, W. N. (1953). *Acta Cryst.* **6**, 770–774.
Baranowski, B. & Moroz, A. (1982). *Pol. J. Chem.* **56**, 379–391.
Bassett, W. A. (2009). *High Pressure Res.* **29**, 163–186.
Bondi, A. (1964). *J. Phys. Chem.* **68**, 441–451.
Budzianowski, A. & Katrusiak, A. (2004). *High-Pressure Crystallography*, edited by A. Katrusiak & P. F. McMillan, pp. 101–112. Dordrecht: Kluwer Academic Publishers.
Desiraju, G. R. & Steiner, T. (2001). In *The Weak Hydrogen Bond in Structural Chemistry and Biology*. International Union of Crystallography: Monographs on Crystallography. Oxford University Press.
Dolomanov, O. V., Bourhis, L. J., Gildea, R. J., Howard, J. A. K. & Puschmann, H. (2009). *J. Appl. Cryst.* **42**, 339–341.
Dziubek, K. & Katrusiak, A. (2014). *Z. Kristallogr.* **229**, 129–134.
Etter, M. C., MacDonald, J. C. & Bernstein, J. (1990). *Acta Cryst.* B**46**, 256–262.
Huang, C., LI, Y. & Wang, C. (2013). *Sci. China Chem.* **56**, 238–248.
Jeffrey, G. A. & Saenger, W. (1994). In *Hydrogen Bonding in Biological Structures*. Berlin, Heidelberg: Springer-Verlag.
Leigh, D. A., Robertson, C. C., Slawin, A. M. Z. & Thomson, P. I. T. (2013). *J. Am. Chem. Soc.* **135**, 9939–9943.
Macrae, C. F., Sovago, I., Cottrell, S. J., Galek, P. T. A., McCabe, P., Pidcock, E., Platings, M., Shields, G. P., Stevens, J. S., Towler, M. & Wood, P. A. (2020). *J. Appl. Cryst.* **53**, 226–235.
Maloney, A. G. P., Wood, P. A. & Parsons, S. (2014). *CrystEngComm*, **16**, 3867–3882.
Mao, H. K., Xu, J. & Bell, P. M. (1986). *J. Geophys. Res.* **91**, 4673–4676.
Parsons, S., Flack, H. D. & Wagner, T. (2013). *Acta Cryst.* B**69**, 249–259.
Piermarini, G. J., Block, S., Barnett, J. D. & Forman, R. A. (1975). *J. Appl. Phys.* **46**, 2774–2780.
Podsiadło, M., Olejniczak, A. & Katrusiak, A. (2017). *Cryst. Growth Des.* **17**, 2218–2222.
Rigaku OD (2022). *CrysAlis PRO*. Rigaku Oxford Diffraction Ltd, Yarnton, Oxfordshire, England.
Sacharczuk, N., Olejniczak, A., Bujak, M. & Podsiadło, M. (2023). *Cryst. Growth Des.* **23**, 7119–7125.
Sheldrick, G. M. (2015*a*). *Acta Cryst.* A**71**, 3–8.
Sheldrick, G. M. (2015*b*). *Acta Cryst.* C**71**, 3–8.
Vega, I. E. D., Gale, P. A., Light, M. E. & Loeb, S. J. (2005). *Chem. Commun.* pp. 4913–4915.

supporting information

Acta Cryst. (2025). C**81** [https://doi.org/10.1107/S2053229625004504]

High-pressure crystal structure of *n*-hexylamine

Bernadetta Kuleczka, Natalia Sacharczuk, Anna Olejniczak and Marcin Podsiadło

Computing details

n-Hexylamine (hexylamine_0_50GPa)

Crystal data

$C_6H_{15}N$
$M_r = 101.19$
Orthorhombic, $Pca2_1$
$a = 6.9050$ (9) Å
$b = 17.549$ (7) Å
$c = 5.5212$ (13) Å
$V = 669.1$ (3) Å^3
$Z = 4$
$F(000) = 232$
$D_x = 1.005$ Mg m^{-3}
Mo $K\alpha$ radiation, $\lambda = 0.71073$ Å
Cell parameters from 598 reflections
$\theta = 3.8$–$17.7°$
$\mu = 0.06$ mm^{-1}
$T = 295$ K
Disc, colourless
0.28 × 0.28 × 0.27 mm

Data collection

Rigaku Xcalibur Eos diffractometer
Detector resolution: 16.2413 pixels mm^{-1}
φ– and ω–scans
Absorption correction: multi-scan (CrysAlis PRO; Rigaku OD, 2022)
$T_{min} = 0.573$, $T_{max} = 1.000$
4308 measured reflections
832 independent reflections
373 reflections with $I > 2\sigma(I)$
$R_{int} = 0.071$
$\theta_{max} = 28.1°$, $\theta_{min} = 3.2°$
$h = -9 \rightarrow 9$
$k = -16 \rightarrow 16$
$l = -6 \rightarrow 6$

Refinement

Refinement on F^2
Least-squares matrix: full
$R[F^2 > 2\sigma(F^2)] = 0.054$
$wR(F^2) = 0.118$
$S = 1.04$
832 reflections
64 parameters
1 restraint
Primary atom site location: dual
Hydrogen site location: mixed
H-atom parameters constrained
$w = 1/[\sigma^2(F_o^2) + (0.0376P)^2]$ where $P = (F_o^2 + 2F_c^2)/3$
$(\Delta/\sigma)_{max} < 0.001$
$\Delta\rho_{max} = 0.09$ e Å^{-3}
$\Delta\rho_{min} = -0.09$ e Å^{-3}
Absolute structure: Flack *x* determined using 128 quotients [(I+)-(I-)]/[(I+)+(I-)] (Parsons *et al.*, 2013)
Absolute structure parameter: −10.0 (10)

Special details

Geometry. All esds (except the esd in the dihedral angle between two l.s. planes) are estimated using the full covariance matrix. The cell esds are taken into account individually in the estimation of esds in distances, angles and torsion angles; correlations between esds in cell parameters are only used when they are defined by crystal symmetry. An approximate (isotropic) treatment of cell esds is used for estimating esds involving l.s. planes.

Refinement. Rigaku Xcalibur EOS and Xcalibur ATLAS diffractometers were used for the high-pressure studies. The X-ray wavelength used in all experiments was 0.71073 Å. The DAC was centred by the gasket-shadow method (Budzianowski & Katrusiak, 2004). The *CrysAlis PRO* program suite was used for data collection, determination of the *UB* matrices and data reductions. All data were accounted for the Lorentz, polarization and absorption effects. *OLEX2* (Dolomanov *et al.*, 2009), *SHELXT* (Sheldrick, 2015a) and *SHELXL* (Sheldrick, 2015b) were used to solve the structures by direct methods, and then to the full-matrix least-squares refinement.

Fractional atomic coordinates and isotropic or equivalent isotropic displacement parameters (Å²)

	x	*y*	*z*	U_{iso}*/U_{eq}
N1	0.5556 (7)	0.0349 (4)	0.9147 (10)	0.0687 (19)
H2	0.682796	0.038908	0.947803	0.082*
H1	0.539765	0.010808	0.772063	0.082*
C1	0.4704 (8)	0.1102 (6)	0.9009 (13)	0.063 (3)
H12	0.488877	0.134938	1.056331	0.076*
H11	0.332065	0.104265	0.877298	0.076*
C2	0.5449 (8)	0.1627 (6)	0.7081 (12)	0.055 (3)
H22	0.683900	0.167532	0.728087	0.066*
H21	0.522184	0.138989	0.551947	0.066*
C3	0.4591 (6)	0.2410 (7)	0.7031 (12)	0.062 (3)
H32	0.480115	0.264728	0.859597	0.075*
H31	0.320307	0.236485	0.679769	0.075*
C4	0.5394 (8)	0.2926 (5)	0.5096 (13)	0.061 (3)
H42	0.678221	0.297005	0.532398	0.074*
H41	0.517725	0.269072	0.352958	0.074*
C5	0.4533 (8)	0.3714 (5)	0.5061 (12)	0.070 (3)
H52	0.470541	0.394238	0.664685	0.084*
H51	0.315124	0.367130	0.477184	0.084*
C6	0.5390 (8)	0.4243 (5)	0.3177 (16)	0.088 (3)
H63	0.476617	0.473119	0.327290	0.132*
H62	0.675190	0.430265	0.347089	0.132*
H61	0.519522	0.403112	0.159285	0.132*

Atomic displacement parameters (Å²)

	U^{11}	U^{22}	U^{33}	U^{12}	U^{13}	U^{23}
N1	0.073 (3)	0.079 (7)	0.055 (5)	0.004 (3)	0.001 (4)	0.003 (3)
C1	0.059 (3)	0.076 (10)	0.054 (7)	−0.003 (5)	0.000 (5)	0.003 (5)
C2	0.053 (3)	0.055 (11)	0.057 (7)	−0.001 (5)	−0.007 (5)	−0.002 (5)
C3	0.048 (3)	0.085 (12)	0.054 (7)	0.005 (5)	0.001 (5)	−0.004 (5)
C4	0.056 (3)	0.078 (11)	0.051 (7)	−0.002 (4)	−0.002 (5)	0.004 (4)
C5	0.071 (4)	0.082 (10)	0.057 (7)	−0.004 (5)	0.001 (5)	0.005 (5)
C6	0.088 (4)	0.099 (12)	0.076 (9)	0.008 (5)	−0.005 (6)	0.012 (5)

Geometric parameters (Å, º)

N1—H2	0.9000	C3—C4	1.507 (8)
N1—H1	0.9001	C4—H42	0.9700
N1—C1	1.449 (9)	C4—H41	0.9700

C1—H12	0.9700	C4—C5	1.506 (8)
C1—H11	0.9700	C5—H52	0.9700
C1—C2	1.498 (10)	C5—H51	0.9700
C2—H22	0.9700	C5—C6	1.515 (11)
C2—H21	0.9700	C6—H63	0.9600
C2—C3	1.497 (12)	C6—H62	0.9600
C3—H32	0.9700	C6—H61	0.9600
C3—H31	0.9700		

H2—N1—H1	109.5	C4—C3—H31	108.6
C1—N1—H2	109.6	C3—C4—H42	108.6
C1—N1—H1	109.4	C3—C4—H41	108.6
N1—C1—H12	108.0	H42—C4—H41	107.6
N1—C1—H11	108.0	C5—C4—C3	114.6 (7)
N1—C1—C2	117.3 (7)	C5—C4—H42	108.6
H12—C1—H11	107.2	C5—C4—H41	108.6
C2—C1—H12	108.0	C4—C5—H52	108.6
C2—C1—H11	108.0	C4—C5—H51	108.6
C1—C2—H22	108.2	C4—C5—C6	114.7 (6)
C1—C2—H21	108.2	H52—C5—H51	107.6
H22—C2—H21	107.4	C6—C5—H52	108.6
C3—C2—C1	116.2 (7)	C6—C5—H51	108.6
C3—C2—H22	108.2	C5—C6—H63	109.5
C3—C2—H21	108.2	C5—C6—H62	109.5
C2—C3—H32	108.6	C5—C6—H61	109.5
C2—C3—H31	108.6	H63—C6—H62	109.5
C2—C3—C4	114.8 (6)	H63—C6—H61	109.5
H32—C3—H31	107.5	H62—C6—H61	109.5
C4—C3—H32	108.6		

N1—C1—C2—C3	−178.1 (6)	C2—C3—C4—C5	−179.7 (6)
C1—C2—C3—C4	179.1 (6)	C3—C4—C5—C6	177.9 (6)

n-Hexylamine (hexylamine_0_65GPa)

Crystal data

$C_6H_{15}N$	D_x = 1.020 Mg m^{-3}
M_r = 101.19	Mo $K\alpha$ radiation, λ = 0.71073 Å
Orthorhombic, $Pca2_1$	Cell parameters from 1173 reflections
a = 6.8591 (9) Å	θ = 3.2–23.5°
b = 17.494 (5) Å	μ = 0.06 mm^{-1}
c = 5.4892 (4) Å	T = 295 K
V = 658.7 (2) Å^3	Disc, colourless
Z = 4	0.27 × 0.27 × 0.26 mm
F(000) = 232	

Data collection

Rigaku Xcalibur Atlas diffractometer
Detector resolution: 10.5384 pixels mm^{-1}
φ– and ω–scans
Absorption correction: multi-scan (CrysAlis PRO; Rigaku OD, 2022)
T_{min} = 0.600, T_{max} = 1.000
5447 measured reflections
1085 independent reflections
527 reflections with $I > 2\sigma(I)$
R_{int} = 0.063
θ_{max} = 31.4°, θ_{min} = 3.2°
h = −8→8
k = −15→15
l = −7→7

Refinement

Refinement on F^2
Least-squares matrix: full
$R[F^2 > 2\sigma(F^2)]$ = 0.047
$wR(F^2)$ = 0.131
S = 0.98
1085 reflections
64 parameters
1 restraint
Primary atom site location: dual
Hydrogen site location: mixed
H-atom parameters constrained
$w = 1/[\sigma^2(F_o^2) + (0.0573P)^2]$ where $P = (F_o^2 + 2F_c^2)/3$
$(\Delta/\sigma)_{max} < 0.001$
$\Delta\rho_{max}$ = 0.10 e Å^{-3}
$\Delta\rho_{min}$ = −0.10 e Å^{-3}
Absolute structure: Flack x determined using 181 quotients [(I+)-(I-)]/[(I+)+(I-)] (Parsons *et al.*, 2013)
Absolute structure parameter: 0.7 (10)

Special details

Geometry. All esds (except the esd in the dihedral angle between two l.s. planes) are estimated using the full covariance matrix. The cell esds are taken into account individually in the estimation of esds in distances, angles and torsion angles; correlations between esds in cell parameters are only used when they are defined by crystal symmetry. An approximate (isotropic) treatment of cell esds is used for estimating esds involving l.s. planes.

Refinement. Rigaku Xcalibur EOS and Xcalibur ATLAS diffractometers were used for the high-pressure studies. The X-ray wavelength used in all experiments was 0.71073 Å. The DAC was centred by the gasket-shadow method (Budzianowski & Katrusiak, 2004). The *CrysAlis PRO* program suite was used for data collection, determination of the *UB* matrices and data reductions. All data were accounted for the Lorentz, polarization and absorption effects. *OLEX2* (Dolomanov *et al.*, 2009), *SHELXT* (Sheldrick, 2015a) and *SHELXL* (Sheldrick, 2015b) were used to solve the structures by direct methods, and then to the full-matrix least-squares refinement.

Fractional atomic coordinates and isotropic or equivalent isotropic displacement parameters (Å^2)

	x	y	z	U_{iso}*/U_{eq}
N1	0.5563 (5)	0.0358 (3)	0.9205 (5)	0.0550 (14)
H2	0.684017	0.040646	0.954979	0.066*
H1	0.542127	0.011566	0.777019	0.066*
C1	0.4676 (5)	0.1112 (3)	0.9056 (6)	0.0464 (17)
H12	0.484199	0.136515	1.061406	0.056*
H11	0.328753	0.104832	0.879059	0.056*
C2	0.5472 (5)	0.1630 (3)	0.7083 (6)	0.0442 (17)
H22	0.686689	0.168369	0.731413	0.053*
H21	0.526551	0.138715	0.551522	0.053*
C3	0.4575 (5)	0.2410 (4)	0.7023 (7)	0.0497 (17)
H32	0.475565	0.264744	0.860355	0.060*
H31	0.318406	0.235580	0.675689	0.060*
C4	0.5404 (5)	0.2940 (3)	0.5071 (7)	0.0464 (15)
H42	0.679673	0.299029	0.533055	0.056*
H41	0.521480	0.270362	0.349076	0.056*

C5	0.4517 (5)	0.3729 (4)	0.5013 (6)	0.0539 (16)
H51	0.312578	0.368251	0.473613	0.065*
H52	0.470200	0.396829	0.659017	0.065*
C6	0.5376 (5)	0.4237 (3)	0.3078 (9)	0.0695 (17)
H63	0.475481	0.472863	0.313277	0.104*
H62	0.674870	0.429650	0.336080	0.104*
H61	0.517151	0.401053	0.150563	0.104*

Atomic displacement parameters (Å²)

	U^{11}	U^{22}	U^{33}	U^{12}	U^{13}	U^{23}
N1	0.065 (3)	0.055 (5)	0.0453 (17)	0.0000 (18)	−0.004 (2)	0.004 (2)
C1	0.051 (3)	0.045 (7)	0.043 (2)	−0.003 (2)	0.001 (3)	−0.003 (3)
C2	0.046 (3)	0.049 (7)	0.0372 (19)	0.001 (2)	0.000 (2)	0.001 (2)
C3	0.040 (3)	0.065 (7)	0.044 (2)	0.000 (2)	0.000 (3)	0.002 (2)
C4	0.043 (3)	0.055 (6)	0.041 (2)	−0.002 (2)	−0.003 (3)	0.000 (2)
C5	0.054 (3)	0.059 (6)	0.048 (2)	−0.002 (2)	0.004 (3)	0.001 (2)
C6	0.072 (3)	0.077 (6)	0.060 (3)	0.004 (2)	0.001 (3)	0.008 (3)

Geometric parameters (Å, º)

N1—H2	0.9000	C3—C4	1.528 (6)
N1—H1	0.9000	C4—H42	0.9700
N1—C1	1.454 (6)	C4—H41	0.9700
C1—H12	0.9700	C4—C5	1.508 (6)
C1—H11	0.9700	C5—H51	0.9700
C1—C2	1.514 (6)	C5—H52	0.9700
C2—H22	0.9700	C5—C6	1.505 (6)
C2—H21	0.9700	C6—H63	0.9600
C2—C3	1.496 (6)	C6—H62	0.9600
C3—H32	0.9700	C6—H61	0.9600
C3—H31	0.9700		
H2—N1—H1	109.5	C4—C3—H31	108.6
C1—N1—H2	109.5	C3—C4—H42	108.5
C1—N1—H1	109.4	C3—C4—H41	108.5
N1—C1—H12	108.4	H42—C4—H41	107.5
N1—C1—H11	108.4	C5—C4—C3	114.9 (4)
N1—C1—C2	115.6 (3)	C5—C4—H42	108.5
H12—C1—H11	107.4	C5—C4—H41	108.5
C2—C1—H12	108.4	C4—C5—H51	108.9
C2—C1—H11	108.4	C4—C5—H52	108.9
C1—C2—H22	108.7	H51—C5—H52	107.7
C1—C2—H21	108.7	C6—C5—C4	113.4 (4)
H22—C2—H21	107.6	C6—C5—H51	108.9
C3—C2—C1	114.4 (4)	C6—C5—H52	108.9
C3—C2—H22	108.7	C5—C6—H63	109.5
C3—C2—H21	108.7	C5—C6—H62	109.5

C2—C3—H32	108.6	C5—C6—H61	109.5
C2—C3—H31	108.6	H63—C6—H62	109.5
C2—C3—C4	114.6 (3)	H63—C6—H61	109.5
H32—C3—H31	107.6	H62—C6—H61	109.5
C4—C3—H32	108.6		
N1—C1—C2—C3	−178.2 (4)	C2—C3—C4—C5	−179.6 (4)
C1—C2—C3—C4	178.7 (3)	C3—C4—C5—C6	179.7 (3)

n-Hexylamine (hexylamine_1_40GPa)

Crystal data

$C_6H_{15}N$
M_r = 101.19
Orthorhombic, $Pca2_1$
a = 6.7241 (19) Å
b = 17.052 (13) Å
c = 5.3367 (7) Å
V = 611.9 (5) Å^3
Z = 4
$F(000)$ = 232
D_x = 1.098 Mg m^{-3}
Mo $K\alpha$ radiation, λ = 0.71073 Å
Cell parameters from 794 reflections
θ = 3.8–23.7°
μ = 0.06 mm^{-1}
T = 295 K
Disc, colourless
0.26 × 0.26 × 0.23 mm

Data collection

Rigaku Xcalibur Atlas diffractometer
Detector resolution: 10.5384 pixels mm^{-1}
φ– and ω–scans
Absorption correction: multi-scan (CrysAlis PRO; Rigaku OD, 2022)
T_{min} = 0.447, T_{max} = 1.000
4114 measured reflections
852 independent reflections
401 reflections with $I > 2\sigma(I)$
R_{int} = 0.068
θ_{max} = 30.4°, θ_{min} = 3.3°
h = −8→8
k = −14→13
l = −7→7

Refinement

Refinement on F^2
Least-squares matrix: full
$R[F^2 > 2\sigma(F^2)]$ = 0.061
$wR(F^2)$ = 0.194
S = 1.04
852 reflections
64 parameters
1 restraint
Primary atom site location: dual
Hydrogen site location: mixed
H-atom parameters constrained
$w = 1/[\sigma^2(F_o^2) + (0.0896P)^2]$ where $P = (F_o^2 + 2F_c^2)/3$
$(\Delta/\sigma)_{max} < 0.001$
$\Delta\rho_{max}$ = 0.17 e Å^{-3}
$\Delta\rho_{min}$ = −0.19 e Å^{-3}
Absolute structure: Flack x determined using 130 quotients [(I+)-(I-)]/[(I+)+(I-)] (Parsons *et al.*, 2013)
Absolute structure parameter: 3.1 (10)

Special details

Geometry. All esds (except the esd in the dihedral angle between two l.s. planes) are estimated using the full covariance matrix. The cell esds are taken into account individually in the estimation of esds in distances, angles and torsion angles; correlations between esds in cell parameters are only used when they are defined by crystal symmetry. An approximate (isotropic) treatment of cell esds is used for estimating esds involving l.s. planes.

Refinement. Rigaku Xcalibur EOS and Xcalibur ATLAS diffractometers were used for the high-pressure studies. The X-ray wavelength used in all experiments was 0.71073 Å. The DAC was centred by the gasket-shadow method (Budzianowski & Katrusiak, 2004). The *CrysAlis PRO* program suite was used for data collection, determination of the *UB* matrices and data reductions. All data were accounted for the Lorentz, polarization and absorption effects. *OLEX2* (Dolomanov *et al.*, 2009), *SHELXT* (Sheldrick, 2015a) and *SHELXL* (Sheldrick, 2015b) were used to solve the structures by direct methods, and then to the full-matrix least-squares refinement.

Fractional atomic coordinates and isotropic or equivalent isotropic displacement parameters (Å²)

	x	*y*	*z*	U_{iso}*/U_{eq}
N1	0.5636 (8)	0.0353 (5)	0.9407 (9)	0.058 (2)
H2	0.694796	0.041899	0.966999	0.069*
H1	0.544766	0.009549	0.795479	0.069*
C1	0.4647 (9)	0.1130 (6)	0.9275 (12)	0.053 (3)
H12	0.484791	0.140747	1.084208	0.063*
H11	0.322777	0.105681	0.904622	0.063*
C2	0.5466 (9)	0.1622 (6)	0.7122 (11)	0.050 (3)
H22	0.689124	0.168003	0.733140	0.060*
H21	0.523657	0.134733	0.555654	0.060*
C3	0.4542 (8)	0.2414 (6)	0.6972 (12)	0.056 (3)
H32	0.470772	0.267628	0.857227	0.067*
H31	0.312710	0.235476	0.667628	0.067*
C4	0.5425 (9)	0.2932 (6)	0.4908 (10)	0.047 (3)
H42	0.684285	0.298718	0.519215	0.057*
H41	0.524514	0.267358	0.330484	0.057*
C5	0.4508 (9)	0.3733 (6)	0.4782 (11)	0.063 (3)
H52	0.467165	0.398929	0.639147	0.075*
H51	0.309275	0.367858	0.447405	0.075*
C6	0.5408 (8)	0.4251 (5)	0.2748 (12)	0.069 (3)
H63	0.476291	0.475376	0.275976	0.103*
H62	0.680310	0.431891	0.306105	0.103*
H61	0.522333	0.400803	0.114258	0.103*

Atomic displacement parameters (Å²)

	U^{11}	U^{22}	U^{33}	U^{12}	U^{13}	U^{23}
N1	0.067 (4)	0.064 (9)	0.042 (3)	−0.002 (3)	−0.009 (3)	0.005 (3)
C1	0.059 (5)	0.048 (13)	0.051 (4)	0.002 (4)	−0.002 (4)	0.004 (4)
C2	0.048 (5)	0.064 (12)	0.038 (3)	0.002 (4)	−0.004 (4)	0.002 (4)
C3	0.043 (5)	0.084 (12)	0.041 (3)	−0.007 (4)	0.005 (4)	−0.005 (4)
C4	0.052 (5)	0.055 (11)	0.035 (3)	0.000 (4)	−0.003 (4)	0.006 (4)
C5	0.057 (6)	0.082 (13)	0.049 (4)	−0.002 (4)	0.006 (4)	−0.004 (5)
C6	0.068 (5)	0.095 (12)	0.043 (4)	0.006 (4)	0.006 (5)	0.008 (4)

Geometric parameters (Å, º)

N1—H2	0.9000	C3—C4	1.532 (11)
N1—H1	0.8998	C4—H42	0.9700
N1—C1	1.485 (12)	C4—H41	0.9700

C1—H12	0.9700	C4—C5	1.499 (11)
C1—H11	0.9700	C5—H52	0.9700
C1—C2	1.526 (11)	C5—H51	0.9700
C2—H22	0.9700	C5—C6	1.525 (10)
C2—H21	0.9700	C6—H63	0.9600
C2—C3	1.489 (11)	C6—H62	0.9600
C3—H32	0.9700	C6—H61	0.9600
C3—H31	0.9700		

H2—N1—H1	109.5	C4—C3—H31	108.8
C1—N1—H2	109.5	C3—C4—H42	108.9
C1—N1—H1	109.3	C3—C4—H41	108.9
N1—C1—H12	109.4	H42—C4—H41	107.7
N1—C1—H11	109.4	C5—C4—C3	113.4 (6)
N1—C1—C2	111.4 (6)	C5—C4—H42	108.9
H12—C1—H11	108.0	C5—C4—H41	108.9
C2—C1—H12	109.4	C4—C5—H52	108.9
C2—C1—H11	109.4	C4—C5—H51	108.9
C1—C2—H22	109.0	C4—C5—C6	113.4 (6)
C1—C2—H21	109.0	H52—C5—H51	107.7
H22—C2—H21	107.8	C6—C5—H52	108.9
C3—C2—C1	112.9 (6)	C6—C5—H51	108.9
C3—C2—H22	109.0	C5—C6—H63	109.5
C3—C2—H21	109.0	C5—C6—H62	109.5
C2—C3—H32	108.8	C5—C6—H61	109.5
C2—C3—H31	108.8	H63—C6—H62	109.5
C2—C3—C4	113.6 (5)	H63—C6—H61	109.5
H32—C3—H31	107.7	H62—C6—H61	109.5
C4—C3—H32	108.8		

N1—C1—C2—C3	−178.5 (7)	C2—C3—C4—C5	−179.3 (7)
C1—C2—C3—C4	176.9 (6)	C3—C4—C5—C6	179.2 (5)

Paper P3

Conformation-Aggregation Interplay in The Simplest Aliphatic Ethers Probed Under High Pressure

Sacharczuk, N.; Olejniczak, A.; Bujak, M.; Dziubek, K. F.; Katrusiak, A.; Podsiadło, M.

IUCrJ **2024**, *11*, 57–61

IUCrJ
ISSN 2052-2525
CHEMISTRY | CRYSTENG

Conformation–aggregation interplay in the simplest aliphatic ethers probed under high pressure

Natalia Sacharczuk,[a] Anna Olejniczak,[a] Maciej Bujak,[b] Kamil Filip Dziubek,[c] Andrzej Katrusiak[a] and Marcin Podsiadło[a]*

[a]Faculty of Chemistry, Adam Mickiewicz University, Uniwersytetu Poznanskiego 8, Poznan 61-614, Poland, [b]Faculty of Chemistry, University of Opole, Oleska 48, Opole 45-052, Poland, and [c]Institut für Mineralogie und Kristallographie, Universität Wien, Josef-Holaubek-Platz 2, Wien A-1090, Austria. *Correspondence e-mail: marcinp@amu.edu.pl

Received 21 August 2023
Accepted 16 November 2023

Edited by L. R. MacGillivray, University of Iowa, USA

Keywords: conformation–aggregation interplay; aliphatic ethers; *in situ* crystallization; high pressure.

CCDC references: 2282455; 2282456; 2282457; 2282458; 2282459; 2282460; 2282461; 2282462; 2282463; 2282464; 2282465; 2282466; 2282467; 2282468; 2282469; 2282470; 2282471; 2282472; 2282473; 2282474

Supporting information: this article has supporting information at www.iucrj.org

The structures of the simplest symmetric primary ethers $[(C_nH_{2n+1})_2O, n = 1–3]$ determined under high pressure revealed their conformational preferences and intermolecular interactions. In three new polymorphs of diethyl ether $(C_2H_5)_2O$, high pressure promotes intermolecular CH···O contacts and enforces a conversion from the *trans–trans* conformer present in the α, β and γ phases to the *trans–gauche* conformer, which is higher in energy by 6.4 kJ mol^{-1}, in the δ phase. Two new polymorphs of dimethyl ether $(CH_3)_2O$ display analogous transformations of the CH···O bonds. The crystal structure of di-*n*-propyl ether $(C_3H_7)_2O$, determined for the first time, is remarkably stable over the whole pressure range investigated from 1.70 up to 5.30 GPa.

1. Introduction

Pressure can drastically affect the association of molecules, *i.e.* one of the most essential properties of solvents (Boldyreva, 2008; Fabbiani & Pulham, 2006; Resnati *et al.*, 2015). Ethoxyethane [diethyl ether, $(C_2H_5)_2O$, hereafter DEE] is a solvent commonly used in chemical practice and has also previously been applied as a general anaesthetic. Raman spectroscopy (Taga *et al.*, 2006) was used to demonstrate that, in the gaseous and liquid states, the *trans–trans* (TT) conformer prevails over the *trans–gauche* conformers (TG^+, TG^-), which are less stable by *ca* 6.4 kJ mol^{-1}. For over a century, DEE has been known to freeze as stable and metastable polymorphs, melting at 157 and 150 K, respectively (Timmermans, 1911). The melting temperatures, 156.92 K for the stable form and 149.86 K for the metastable form, and the heats of fusion were precisely determined by Counsell *et al.* (1971). In the stable α phase, determined by André *et al.* (1972) in the space group $P2_12_12_1$ with $Z = 8$, the molecules assume the TT conformation. The crystal structure of the metastable form was not determined, but its vibrational spectra indicated that there are two independent molecules, both in the TT conformation (Durig & Church, 1981). The existence of the metastable modification and the tendency of DEE to vitrify were explained in terms of the fairly loose structure of the α phase, and hence the low value of stabilization energy compared with the amorphous state (André *et al.*, 1972).

In the literature, there is much less information about the structure, interactions and properties of other aliphatic ethers. Dimethyl ether (DME) freezes at 93 K and its crystal structure was determined by Vojinović *et al.* (2004). The crystal structure of di-*n*-propyl ether (DPE) had not been determined. It was established that in the structure of tetrahydrofuran, a

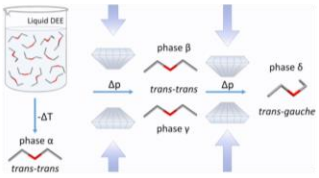

cyclic analogue of DEE, molecular aggregation is stabilized by CH···O interactions, which are strongly enhanced under high pressure (Dziubek *et al.*, 2010; Chang *et al.*, 2005). Such CH···O contacts are sterically hindered in the TT conformers, present in the structure of the α phase of DEE. Therefore, acyclic ethers such as DEE and higher ones are expected to change their TT conformations under high pressure. In the simplest ether DME, the molecular structure can be modified owing to the C—O—C angle and the methyl group rotations, whereas the intermolecular interactions can be changed by a rearrangements of molecules. Here, we describe the effect of high pressure on the crystal structure of DEE, and we also studied DME and DPE in order to obtain more general information about the role of molecular structure with respect to the interactions and aggregation for this class of compounds.

2. Experimental

DME (≥99.9%), DEE (≥99%) and DPE (≥99%), all purchased from Merck, were used as delivered. All three ethers were crystallized *in situ* in a modified Merrill–Bassett diamond-anvil cell (DAC) (Bassett, 2009). In each experiment, the DAC was equipped with a 0.3 mm-thick steel gasket with a hole 0.4 mm in diameter. At 295 K, DME, DEE and DPE froze at 2.95, 1.50 and 1.35 GPa, respectively, in the form of polycrystalline masses filling the volume of the DAC chamber. Single crystals were obtained under isochoric conditions (Fig. 1): the DAC containing the squeezed polycrystalline mass of the ether sample was heated with a hot-air gun until all but one grain melted. Then the DAC was slowly cooled to room temperature and the single crystal grew to eventually fill the whole chamber. The temperature inside the DAC was measured using an infrared thermometer. The pressure was calibrated by the ruby fluorescence method (Mao *et al.*, 1986) before and after the X-ray diffraction measurements using a Photon Control spectrometer with an accuracy of 0.02 GPa. The experimental details and progress in growing the single crystals are shown in Figs. S1–S18 of the supporting information.

The KUMA KM4-CCD diffractometer was used for the high-pressure X-ray diffraction studies. The DAC was centred by the gasket-shadow method (Budzianowski & Katrusiak, 2004). The *CrysAlisPro* suite was used for data collection, determination of the **UB** matrices and unit-cell parameters, and data reductions (Rigaku Oxford Diffraction, 2019). For all data, we accounted for the Lorentz, polarization and absorption effects. The programs *SHELXT* (Sheldrick, 2015*a*) and *SHELXL* (Sheldrick, 2015*b*) within the *OLEX2* (Dolomanov *et al.*, 2009) GUI were used to solve the structures by direct methods and refine the models by full-matrix least-squares on F^2. Anisotropic displacement parameters were applied for non-hydrogen atoms, but the isotropic thermal parameters were occasionally retained for atoms with unreasonable anisotropic factors or for lower-quality datasets. Hydrogen atoms were located from the molecular geometry, with the C—H distances equal to 0.97 Å (–CH_2–) or 0.96 Å (–CH_3) and their U_{iso} factors constrained to 1.2 or 1.5 times that of U_{eq} of the carriers. The crystal and experimental data are summarized in Table 1 and Tables S1–S4 of the supporting information.

A conformational analysis of the isolated DEE molecule in the gas phase was performed with the *ab initio* approach of the density functional theory (DFT) with the B3LYP/6–311++g(2d,2p) method using *GAUSSIAN 16W* (Frisch *et al.*, 2016). The potential energy E_p map has been created as a function of the torsion angles C2—C1—O1—C3 and C4—C3—O1—C1 with a step of 30° (Dennington *et al.*, 2016). The methyl hydrogen atoms (constraint AFIX 137) deviate by up to *ca* 8° in the H—C—C—O torsion angles for DEE compared with those obtained from the geometry optimization for the isolated molecule by *GAUSSIAN 16W*. The structure of DEE in the γ phase best agrees with the calculations, and the largest difference was observed for the δ phase.

3. Results and discussion

The lowest pressure for investigating the structure of the simplest primary ethers was chosen, about 0.3 GPa above their freezing pressure points, to ensure the stability of the single-crystal samples during the X-ray diffraction data collection experiments. The maximum pressure was the result of reaching the mechanical or thermal limitation of the DAC during the procedure to obtain the single crystals. The

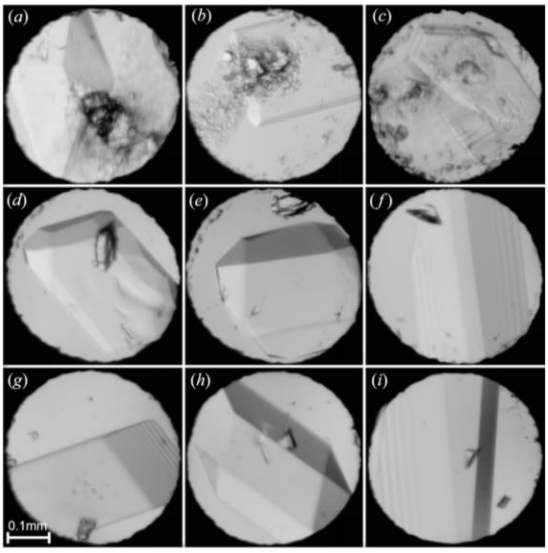

Figure 1
Single crystals grown *in situ* in the DAC. (*a*) β-DME at 3.90 GPa and 349 K, (*b*) γ-DME at 4.50 GPa and 359 K, (*c*) γ-DME at 5.60 GPa and 372 K, (*d*) β-DEE at 1.85 GPa and 327 K, (*e*) β-DEE at 2.45 GPa and 349 K, (*f*) γ-DEE at 2.65 GPa and 340 K, (*g*) δ-DEE at 2.80 GPa and 377 K, (*h*) δ-DEE at 3.45 GPa and 413 K, and (*i*) α-DPE at 2.10 GPa and 344 K.

Table 1
Selected crystal data of high-pressure phases of DME, DEE and DPE at 295 K (*cf* detailed data of all 20 determinations in Tables S1–S4).

	β DME	γ DME	β DEE	γ DEE	δ DEE	α DPE
P (GPa)	3.30 (2)	4.50 (2)	1.85 (2)	2.65 (2)	2.80 (2)	1.70 (2)
Space group	$P2_1/c$	$P\bar{1}$	$P2_1/c$	$I2/a$	$P\bar{1}$	$P2_1/c$
a (Å)	5.5541 (4)	4.3394 (12)	6.8268 (3)	7.7073 (12)	5.1196 (4)	9.416 (4)
b (Å)	6.6179 (11)	8.414 (2)	8.1428 (17)	4.0885 (4)	5.6659 (10)	4.1817 (3)
c (Å)	6.964 (3)	12.821 (6)	7.7731 (3)	13.233 (2)	7.2999 (4)	15.579 (7)
α (°)	90	90.55 (4)	90	90	97.275 (8)	90
β (°)	103.84 (2)	93.89 (6)	93.443 (4)	93.793 (16)	102.728 (6)	101.23 (5)
γ (°)	90	90.83 (2)	90	90	96.747 (10)	90
V (Å^3)	248.56 (12)	467.0 (3)	431.32 (9)	416.07 (10)	202.56 (4)	601.7 (4)
Z, Z'	4, 1	8, 4	4, 1	4, 0.5	2, 1	4, 1
D_x (g cm^{-3})	1.231	1.311	1.141	1.183	1.215	1.128
R_1 [$F^2 > 2\sigma(F^2)$]	0.0708	0.0554	0.0353	0.0371	0.0388	0.0455

molecular volumes of the ethers studied as a function of pressure are plotted in Fig. 2.

We have established that DEE freezes at 1.50 GPa when isothermally compressed at 295 K. Therefore, the single crystal was grown under isochoric conditions from the liquid in a DAC at 1.85 GPa (Fig. 1). The new β phase, built of TT conformers, is stable up to 2.65 GPa, when the γ phase, also built of the TT conformers, is formed. At even higher pressure, the DEE molecules adopt the TG conformation and the δ phase is formed, investigated between 2.80 and 4.90 GPa (Fig. 2). In the TG conformers, the reduced steric hindrance around the oxygen atom facilitates the formation of a larger number of CH···O contacts. When releasing pressure, the δ phase transforms to the β phase below 2.70 GPa.

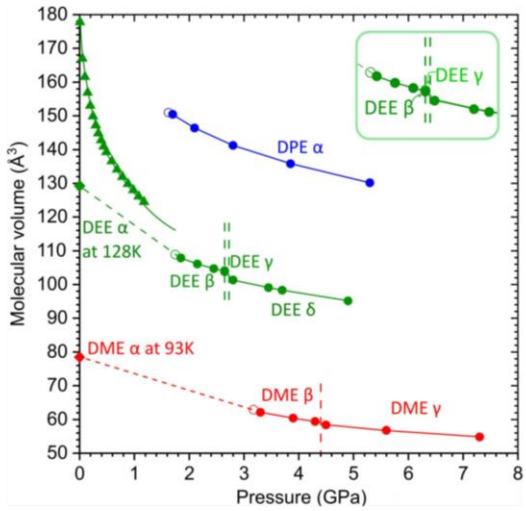

Figure 2
Molecular volume (V/Z) of DME, DEE and DPE plotted as a function of pressure: solid high-pressure (circles, this work) and low-temperature [diamonds (André *et al.*, 1972; Vojinović *et al.*, 2004)] phases as well as liquid DEE [triangles (Bridgman, 1913)]. Open circles indicate the V_m values estimated at the freezing-pressure points. The vertical dashed lines mark the solid–solid transition pressure points (this work). The ambient- and high-pressure points at 295 K are joined by dashed lines. The solid lines between points are guides for the eye only. The estimated standard deviations are smaller than the plotted symbols.

In DME, the steric hindrance around the oxygen atom is smaller and the number of H···O contacts increases without conformational transformations. At 0.1 MPa and 93 K, DME crystallizes in the centrosymmetric α phase of the tetragonal space group $P4_2/n$ (Vojinović *et al.*, 2004). At 3.30 GPa and 295 K, DME forms the centrosymmetric β phase in the space group $P2_1/c$, and then, with increasing pressure, to 4.40 GPa, it transforms to the γ phase of the space-group symmetry $P\bar{1}$ (Fig. 2). In DPE, the conformation is important for the molecular aggregation. The crystal structure of DPE at 0.1 MPa and low temperature has not yet been reported. At high pressure and 295 K, DPE crystallizes in the centrosymmetric space group $P2_1/c$. It was found that this phase (α phase) is stable from 1.70 to 5.30 GPa at least.

Our quantum-mechanical computations performed with *Gaussian* (Frisch *et al.*, 2019) show that the idealized TT conformer ($\tau_1 = \tau_2 = 180°$) is 8.72 kJ mol^{-1} more stable than the idealized TG conformers ($\tau_1 = 180°$, $\tau_2 = \pm 60°$). This E_p difference is somewhat larger than that previously determined by the B3LYP/6–311+G** method (Taga *et al.*, 2006). Owing to the crystal-field effects, the E_p difference calculated by us between the TT and TG conformers present in the β ($\tau_1 = 172.47°$, $\tau_2 = 179.45°$) and δ ($\tau_1 = 177.70°$, $\tau_2 = -77.55°$) DEE phases is 6.43 kJ mol^{-1} and between the γ ($\tau_1 = \tau_2 = 168.53°$) and δ phases it is 5.12 kJ mol^{-1}. Therefore, the volume reductions of 2.54 and 2.74 Å^3 for the β–δ and γ–δ phase transitions, respectively, at 2.70 GPa, associated with the work component of the Gibbs free energies equal to 4.13 and 4.45 kJ mol^{-1}, is consistent with the energy gain of the system for a transition involving conformational changes. When assuming the initial density of the liquid at 293 K (0.7134 g cm^{-3}), the work performed on the sample to 2.70 GPa amounts to about 59 kJ mol^{-1}, which is commensurate with the energy of the E_p barrier equal to about 11.3 kJ mol^{-1} in the E_p map in Fig. 3.

According to intermolecular distances, the cohesion forces in DME, DEE and DPE crystals are dominated by CH···O bonds (Figs. 4, 5 and S19–S26). The approaching hydrogen atoms are roughly (within about 30°) grouped about the directions of the lone-electron pairs of oxygen atoms. For the

β and γ phases of DEE, only the methyl hydrogen atoms participate in the hydrogen bonds, whereas in the α and δ phases of DEE, there are both methyl and methylene hydrogen donors. The CH···O bonds aggregate the molecules into different and characteristic architectures of rings (α DME), chains (α DEE, γ DEE, α DPE), ribbons (δ DEE), sheets (β DME, β DEE) and a three-dimensional pattern (γ DME). In DME, the number of CH···O contacts that are shorter than the sum of the van der Waals radii (Bondi, 1964) increases with pressure, hence the three-dimensional aggregation patterns are promoted. This relation does not apply for the DEE polymorphs.

The four phases of DEE clearly reveal the systematic transformation of patterns of intermolecular interactions at high pressure. The initial compression of H···H contacts and the small compression of H···O contacts between the α, β and γ phases are reversed in the δ phase, where the conformational change increases the access to the oxygen atom (Fig. S20). It promotes the formation of CH···O contacts at high pressure. The CH···O bonded molecules in the β, γ and δ phases are attracted with intermolecular interaction energies of about −12.0, −11.4 and −9.9 kJ mol^{-1}, respectively compared with about −4 kJ mol^{-1} for the molecules with H···H contacts only (Gavezzotti, 1994; Gavezzotti & Filippini, 1994).

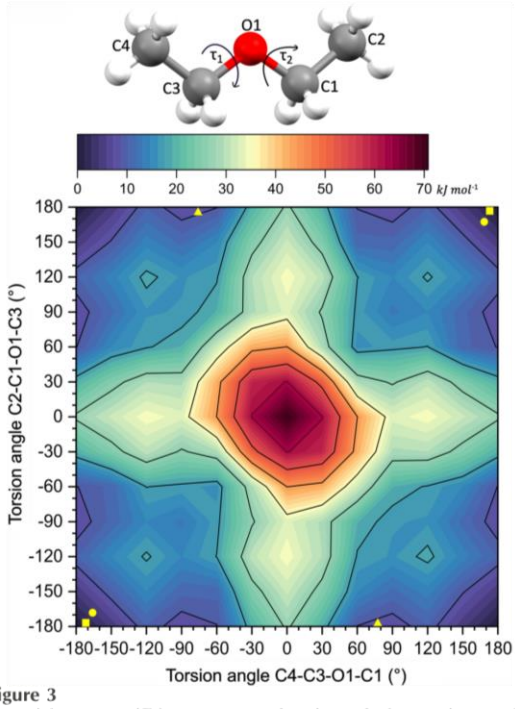

Figure 3
Potential energy (E_p) map as a function of the torsion angles C4—C3—O1—C1 (τ_1) and C2—C1—O1—C3 (τ_2) for the isolated DEE molecule, with $E_p = 0$ for the TT conformer. The conformers present in the crystalline state for β DEE (square), γ DEE (circle) and δ DEE (triangle) are indicated in yellow.

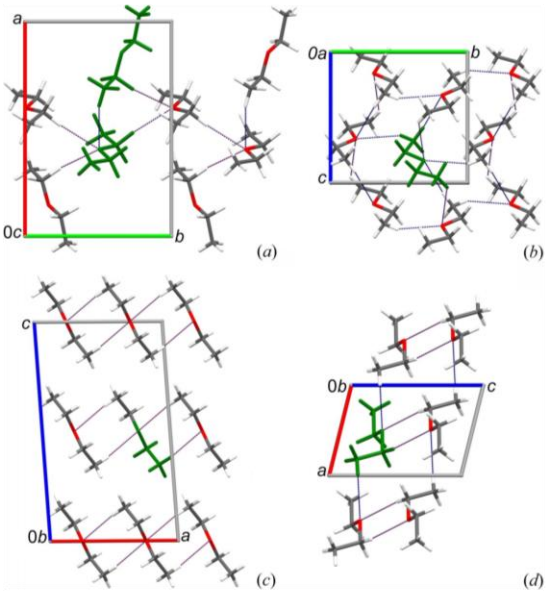

Figure 4
Patterns of the CH···O bonds (dotted lines) in the structures of the DEE polymorphs (*a*) α, (*b*) β, (*c*) γ and (*d*) δ. The symmetry-independent structural units (0.5, 1 and 2 molecules) are indicated in green.

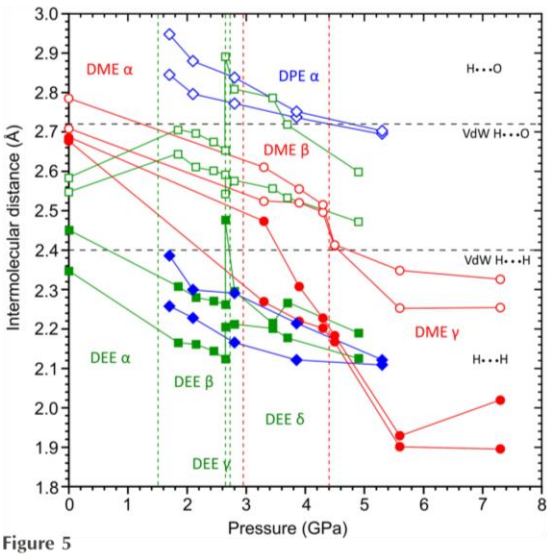

Figure 5
Evolution of the intermolecular distances for the different phases of DME (red), DEE (green) and DPE (blue) with pressure. The two shortest distances for the two types of interactions are presented: full shapes represent H···H and empty shapes represent H···O distances. The black horizontal lines show the sum of the van der Waals radii (Bondi, 1964) of hydrogen and oxygen (2.72 Å) and of hydrogen and hydrogen (2.4 Å); the vertical dashed lines mark the limits of the pressure stability ranges of individual crystal phases. The estimated standard deviations are smaller than the plotted symbols.

4. Conclusions

The interplay of preferences for the CH···O bond and low-E_p conformation govern the aggregation in solid phases of simple aliphatic ethers. We have found six new polymorphs: the β and γ phases of DME; the β, γ and δ phases of DEE; and the α phase of DPE. The conformational conversions can regulate access to the oxygen atom, and in this way can increase the number of stronger CH···O bonds and reduce the number of weak H···H contacts. Consequently, we observed a higher compressibility of CH···O distances in δ DEE compared with the compressibility of H···H within this phase. Though high pressure has proved to be a useful tool for inducing conformational changes in simple molecular compounds, it also shows the energetic landscape of thermally activated conformational conversions in liquids. Cohesion forces, molecular conformations and aggregation in the crystal structures of simple ethers still require further studies by theoretical methods. There are also asymmetric ethers, which can provide additional information about the structure–property relations of ethers, however their applications and availability are limited.

Funding information

This study was supported by the National Science Centre, Poland (grant No. 2020/37/B/ST4/00982).

References

André, D., Fourme, R. & Zechmeister, K. (1972). *Acta Cryst.* B**28**, 2389–2395.
Bassett, W. A. (2009). *High. Press. Res.* **29**, 163–186.
Boldyreva, E. V. (2008). *Acta Cryst.* A**64**, 218–231.
Bondi, A. (1964). *J. Phys. Chem.* **68**, 441–451.
Bridgman, P. W. (1913). *Proc. Am. Acad. Arts Sci.* **49**, 3–114.
Budzianowski, A. & Katrusiak, A. (2004). *High-Pressure Crystallography*, edited by A. Katrusiak & P. F. McMillan, pp. 101–112. Dordrecht: Kluwer Academic Publishers.
Chang, H.-C., Jiang, J.-C., Chuang, C.-W., Lin, J.-S., Lai, W.-W., Yang, Y.-C. & Lin, S. H. (2005). *Chem. Phys. Lett.* **410**, 42–48.
Counsell, J. F., Lee, D. A. & Martin, J. F. (1971). *J. Chem. Soc. A*, pp. 313.
Dennington, R., Keith, T. & Millam, J. (2016). *GaussView*. Version 6.1. Semichem Inc., Shawnee Mission, KS, USA.
Dolomanov, O. V., Bourhis, L. J., Gildea, R. J., Howard, J. A. K. & Puschmann, H. (2009). *J. Appl. Cryst.* **42**, 339–341.
Durig, J. R. & Church, J. S. (1981). *Mol. Cryst. Liq. Cryst.* **69**, 217–240.
Dziubek, K. F., Jęczmiński, D. & Katrusiak, A. (2010). *J. Phys. Chem. Lett.* **1**, 844–849.
Fabbiani, F. P. A. & Pulham, C. R. (2006). *Chem. Soc. Rev.* **35**, 932–942.
Frisch, M. J., Trucks, G. W., Schlegel, H. B., Scuseria, G. E., Robb, M. A., Cheeseman, J. R., Scalmani, G., Barone, V., Petersson, G. A., Nakatsuji, H., Li, X., Caricato, M., Marenich, A. V., Bloino, J., Janesko, B. G., Gomperts, R., Mennucci, B., Hratchian, H. P., Ortiz, J. V., Izmaylov, A. F., Sonnenberg, J. L., Williams-Young, D., Ding, F., Lipparini, F., Egidi, F., Goings, J., Peng, B., Petrone, A., Henderson, T., Ranasinghe, D., Zakrzewski, V. G., Gao, J., Rega, N., Zheng, G., Liang, W., Hada, M., Ehara, M., Toyota, K., Fukuda, R., Hasegawa, J., Ishida, M., Nakajima, T., Honda, Y., Kitao, O., Nakai, H., Vreven, T., Throssell, K., Montgomery, J. A., Jr., Peralta, J. E., Ogliaro, F., Bearpark, M. J., Heyd, J. J., Brothers, E. N., Kudin, K. N., Staroverov, V. N., Keith, T. A., Kobayashi, R., Normand, J., Raghavachari, K., Rendell, A. P., Burant, J. C., Iyengar, S. S., Tomasi, J., Cossi, M., Millam, J. M., Klene, M., Adamo, C., Cammi, R., Ochterski, J. W., Martin, R. L., Morokuma, K., Farkas, O., Foresman, J. B. & Fox, D. J. (2016). *Gaussian 16W*, Revision C.01, Gaussian, Inc. Wallingford, CT, USA.
Gavezzotti, A. (1994). *Acc. Chem. Res.* **27**, 309–314.
Gavezzotti, A. & Filippini, G. (1994). *J. Phys. Chem.* **98**, 4831–4837.
Mao, H. K., Xu, J. & Bell, P. M. (1986). *J. Geophys. Res.* **91**, 4673–4676.
Resnati, G., Boldyreva, E., Bombicz, P. & Kawano, M. (2015). *IUCrJ*, **2**, 675–690.
Rigaku Oxford Diffraction (2019). *CrysAlisPro*. Rigaku Oxford Diffraction, Yarnton, UK.
Sheldrick, G. M. (2015*a*). *Acta Cryst.* A**71**, 3–8.
Sheldrick, G. M. (2015*b*). *Acta Cryst.* C**71**, 3–8.
Taga, K., Kawasaki, K., Yamamoto, Y., Yoshida, T., Ohno, K. & Matsuura, H. (2006). *J. Mol. Struct.* **788**, 159–175.
Timmermans, J. (1911). *Bull. Soc. Chim. Belg.* **25**, 300–327.
Vojinović, K., Losehand, U. & Mitzel, N. W. (2004). *Dalton Trans.* pp. 2578–2581.

IUCrJ

Volume 11 (2024)

Supporting information for article:

Conformation-aggregation interplay in the simplest aliphatic ethers probed under high pressure

Natalia Sacharczuk, Anna Olejniczak, Maciej Bujak, Kamil Filip Dziubek, Andrzej Katrusiak and Marcin Podsiadło

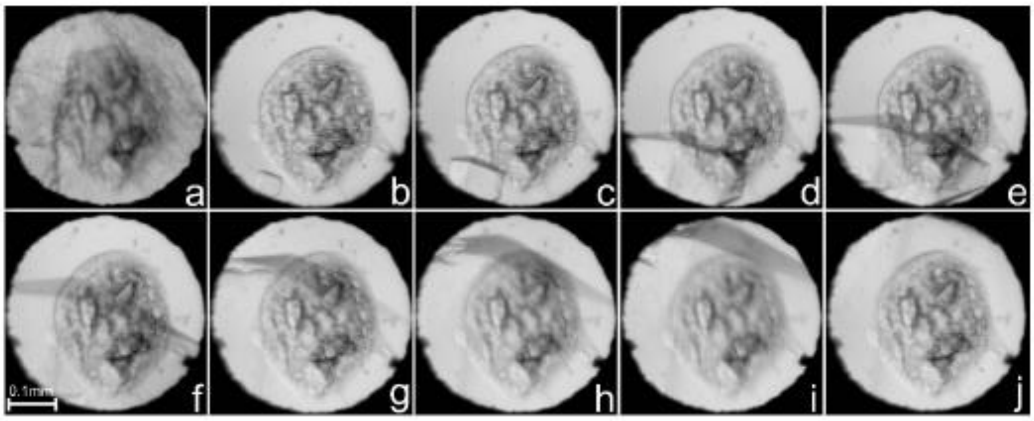

Figure S1. Stages of the dimethyl ether (DME) phase β single-crystal growth inside the DAC chamber: (a) polycrystalline mass grown isothermally at 295 K; (b) one crystal seed at 325 K; (c-i) the single crystal cooled to 311 K and (j) filling the whole volume of the DAC chamber at 295 K and 3.30 GPa. The ruby chips, for pressure calibration, lie in the central part of the DAC.

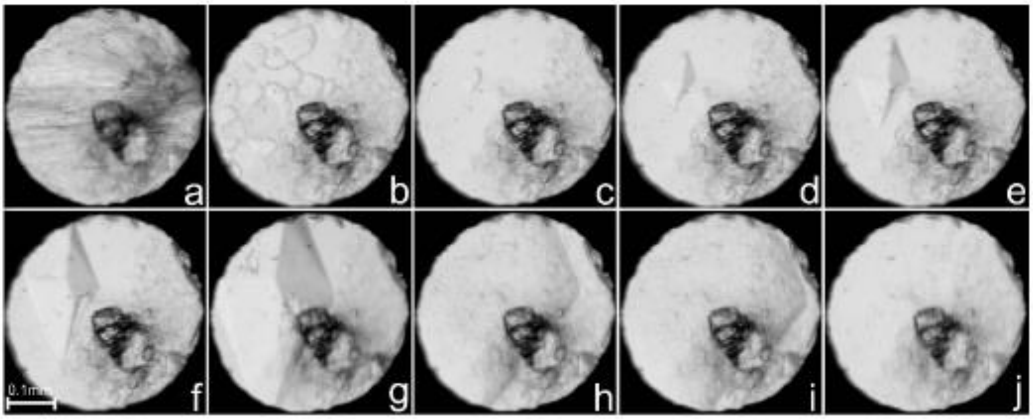

Figure S2. Stages of the DME phase β single-crystal growth inside the DAC chamber: (a) polycrystalline mass grown isothermally at 295 K; (b) polycrystal–liquid equilibrium at 351 K; (c) one crystal seed at 353 K; (d-i) the single crystal cooled to 347 K and (j) filling the DAC chamber at 295 K and 3.90 GPa. The ruby chip, for pressure calibration, is located in the central part of the DAC.

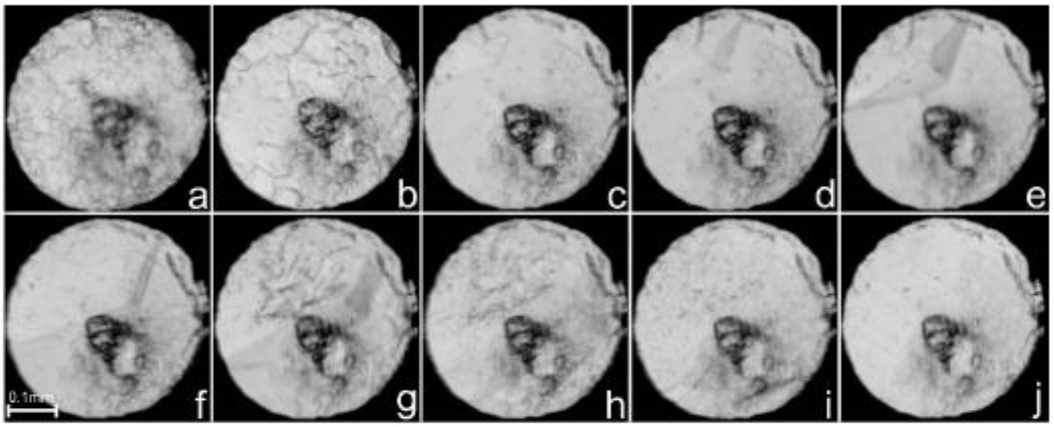

Figure S3. Stages of the DME phase β single-crystal growth inside the DAC chamber: (a) polycrystalline mass grown isothermally at 295 K; (b) polycrystal–liquid equilibrium at 360 K; (c) one crystal seed at 361 K; (d-i) the single crystal cooled to 346 K and (j) filling the whole volume of the DAC chamber at 295 K and 4.30 GPa. The ruby chip, for pressure calibration, is placed in the central part of the DAC.

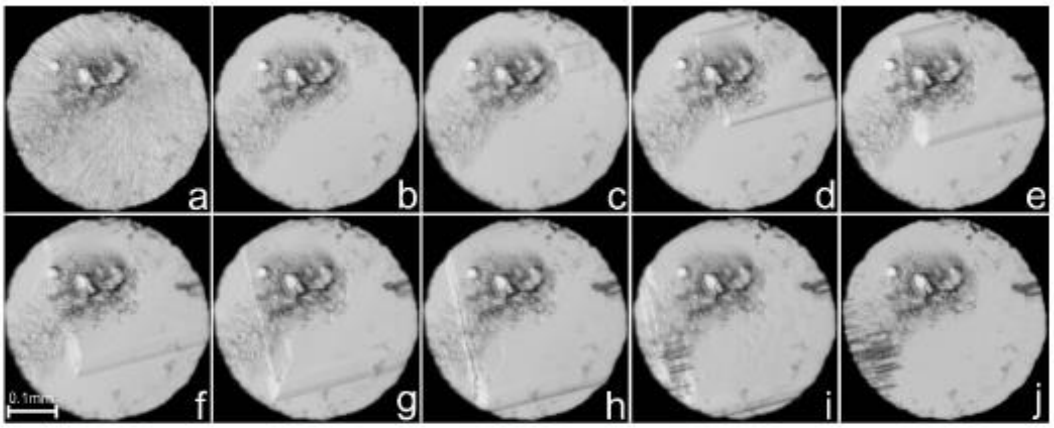

Figure S4. Stages of the DME phase γ single-crystal growth inside the DAC chamber: (a) polycrystal mass grown isothermally at 295 K; (b) one crystal seed at 361 K; (c-i) the single crystal cooled to 351 K and (j) filling the DAC chamber at 295 K and 4.50 GPa. The ruby chips, for pressure calibration, lie in the upper part of the DAC.

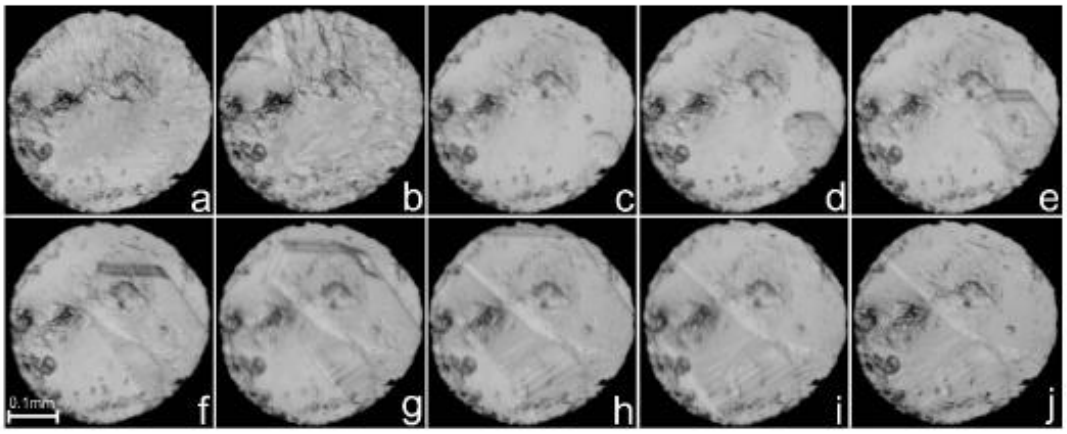

Figure S5. Stages of the DME phase γ single-crystal growth inside the DAC chamber: (a) polycrystalline mass grown isothermally at 295 K; (b) polycrystal–liquid equilibrium at 372 K; (c) one crystal seed at 374 K; (d-i) the single crystal cooled to 369 K and (j) filling the whole volume DAC chamber at 295 K and 5.60 GPa. The ruby chips, for pressure calibration, are placed in the central and left part of the DAC.

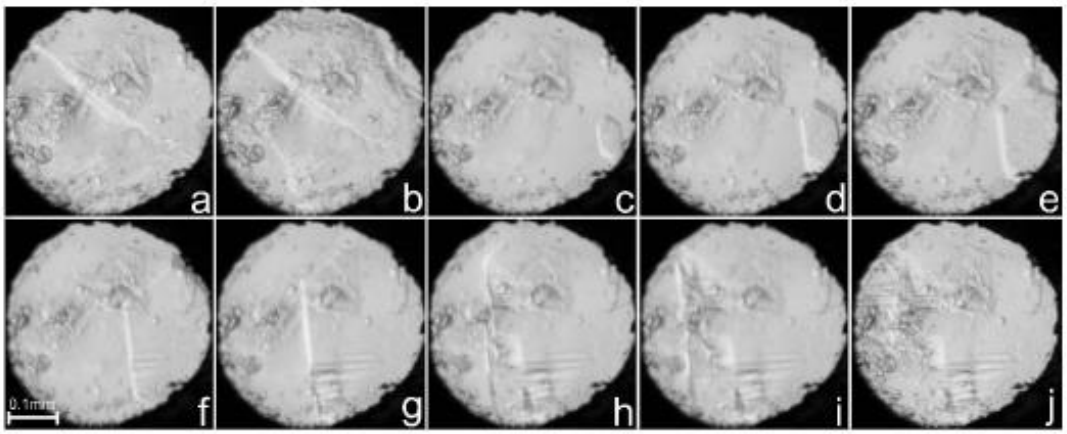

Figure S6. Stages of the DME phase γ single-crystal growth inside the DAC chamber: (a) polycrystalline mass grown isothermally at 295 K; (b) polycrystal–liquid equilibrium at 396 K; (c) one crystal seed at 399 K; (d-i) the single crystal cooled to 394 K and (j) filling the whole volume DAC chamber at 295 K and 7.30 GPa. The ruby chips, for pressure calibration, lie in the central and left part of the DAC.

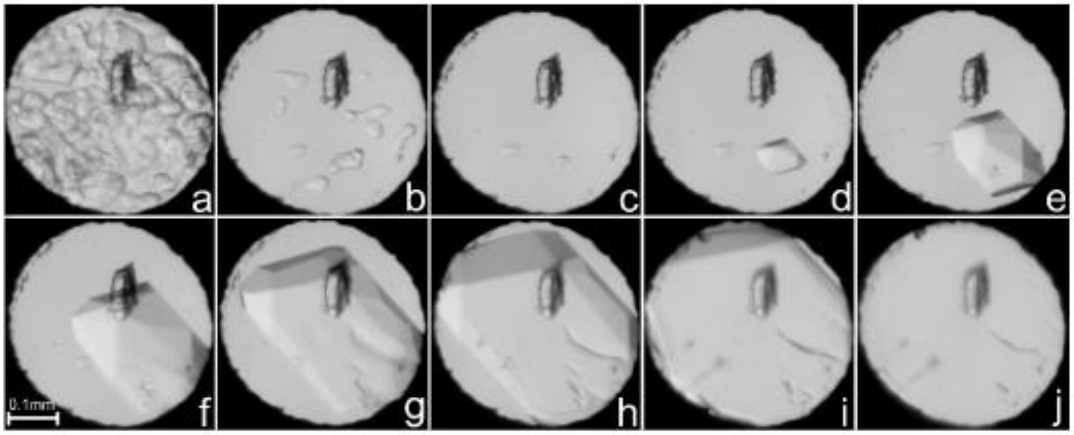

Figure S7. Stages of the diethyl ether (DEE) phase β single-crystal growth inside the DAC chamber: (a) polycrystalline mass grown isothermally at 295 K; (b) polycrystal–liquid equilibrium at 344 K; (c) one crystal seed at 345 K; (d-i) the single crystal cooled to 317 K and (j) filling the whole volume of DAC chamber at 295 K and 1.85 GPa. The ruby chip, for pressure calibration, is placed in the central part of the DAC chamber.

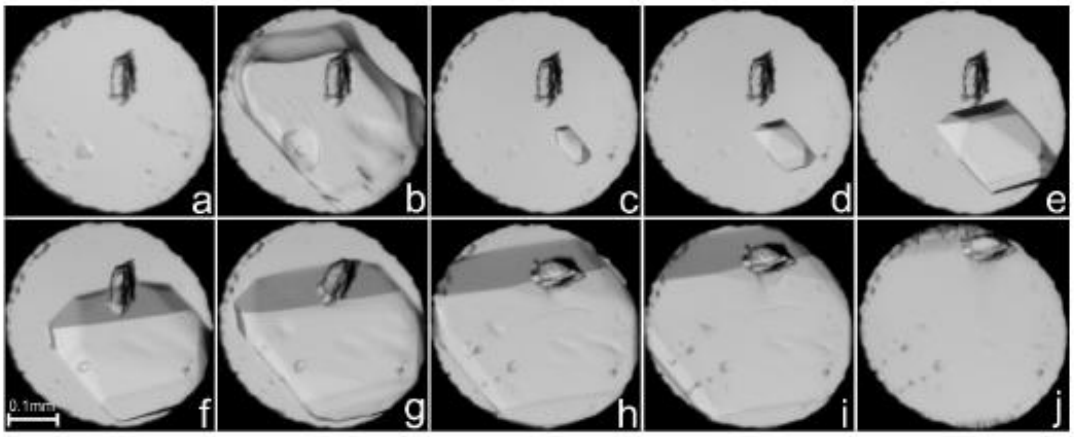

Figure S8. Stages of the DEE phase β single-crystal growth inside the DAC chamber: (a) single-crystal–liquid equilibrium at 308 K; (b) single-crystal–liquid equilibrium at 348 K; (c) one crystal seed at 352 K; (d-i) the single crystal cooled to 331 K and (j) filling the DAC chamber at 295 K and 2.15 GPa. The ruby chip, for pressure calibration, lie in the central part (a-f) and then it is moved to the upper part (g-j) of the DAC.

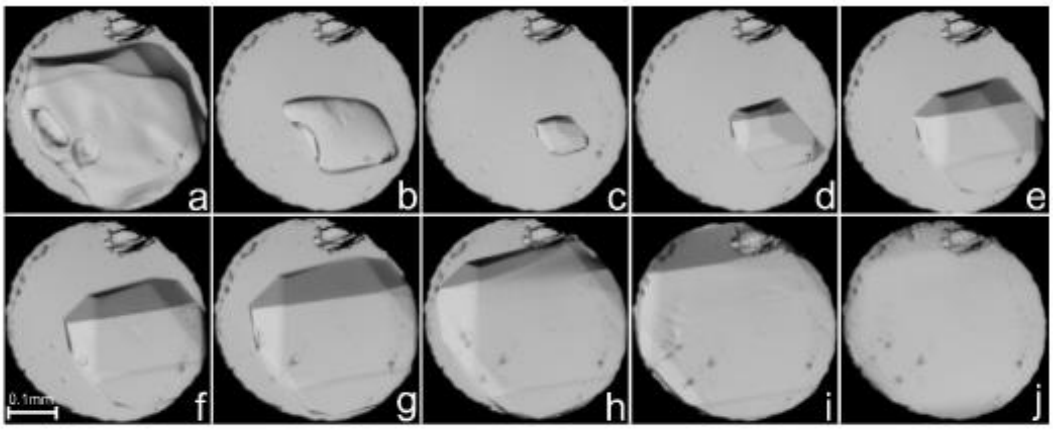

Figure S9. Stages of the DEE phase β single-crystal growth inside the DAC chamber: (a) single-crystal–liquid equilibrium at 360 K; (b) single-crystal–liquid equilibrium at 361 K; (c) one crystal seed at 362 K; (d-i) the single crystal cooled to 338 K and (j) filling the whole volume of DAC chamber at 295 K and 2.45 GPa. The ruby chip for pressure calibration is located in the upper part of the DAC.

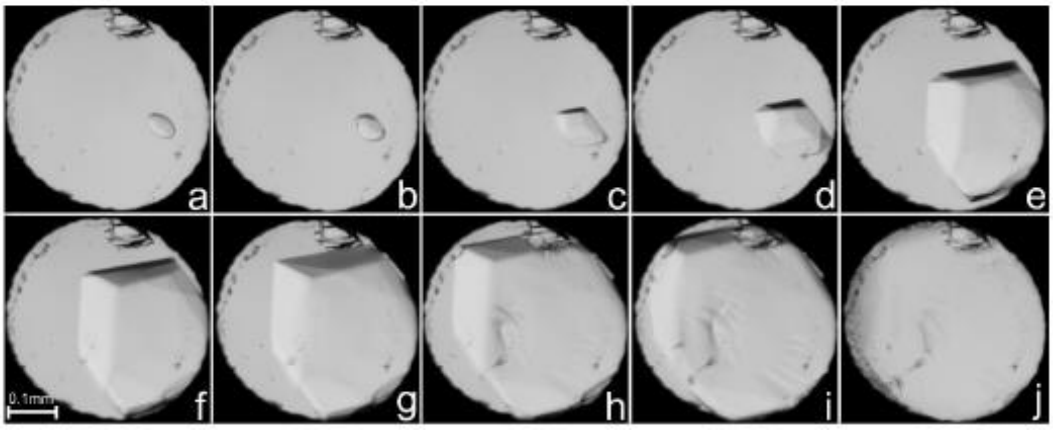

Figure S10. Stages of the DEE phase β single-crystal growth inside the DAC chamber: (a) one crystal seed at 368 K; (b-i) the single crystal cooled to 345 K and (j) filling the DAC chamber at 295 K and 2.65 GPa. The ruby chip, for pressure calibration, lies in the upper part of the DAC.

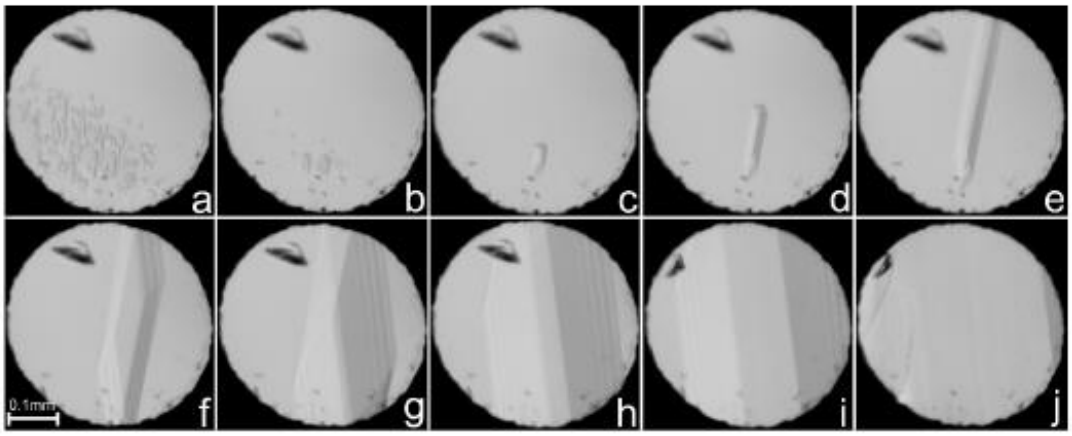

Figure S11. Stages of the DEE phase γ single-crystal growth inside the DAC chamber: (a) polycrystal–liquid equilibrium at 361 K; (b) polycrystal–liquid equilibrium at 363 K; (c) one crystal seed at 359 K; (d-i) the single crystal cooled to 331 K and (j) filling the whole volume of DAC chamber at 295 K and 2.65 GPa. The ruby chip, for pressure calibration, lies in the upper part of the DAC.

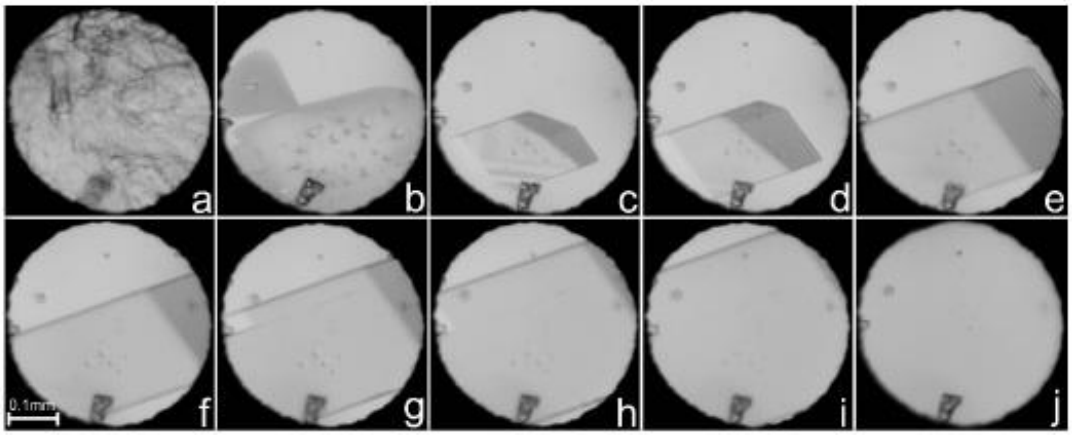

Figure S12. Stages of the DEE phase δ single-crystal growth inside the DAC chamber: (a) polycrystalline mass grown isothermally at 295 K; (b) three single-crystals–liquid equilibrium at 405 K; (c) one crystal seed at 391 K; (d-i) the single crystal cooled to 341 K and (j) filling the DAC chamber at 295 K and 2.80 GPa. The ruby chip, for pressure calibration, lies in the bottom part of the DAC.

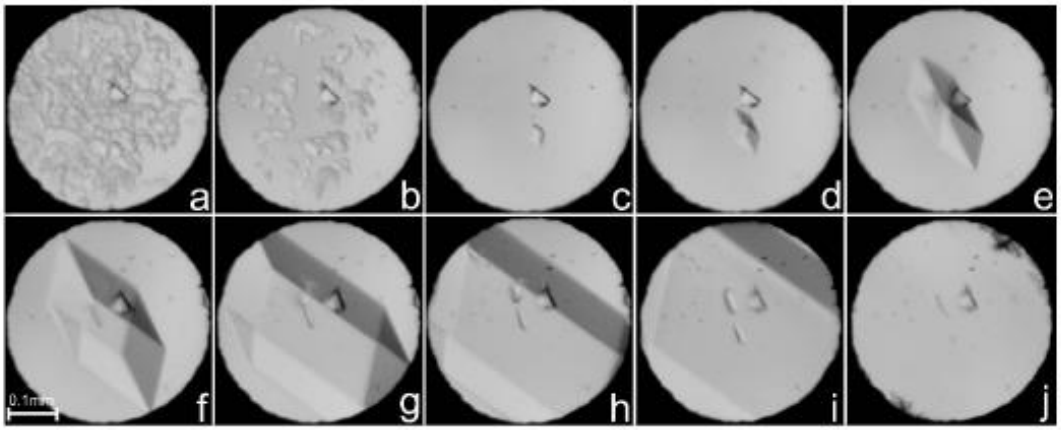

Figure S13. Stages of the DEE phase δ single-crystal growth inside the DAC chamber: (a) polycrystal–liquid equilibrium at 443 K; (b) polycrystal–liquid equilibrium at 444 K; (c) one crystal seed at 445 K; (d-i) the single crystal cooled to 387 K and (j) filling the whole volume of DAC chamber at 295 K and 3.45 GPa. The ruby chip, for pressure calibration, lies in the central part of the DAC.

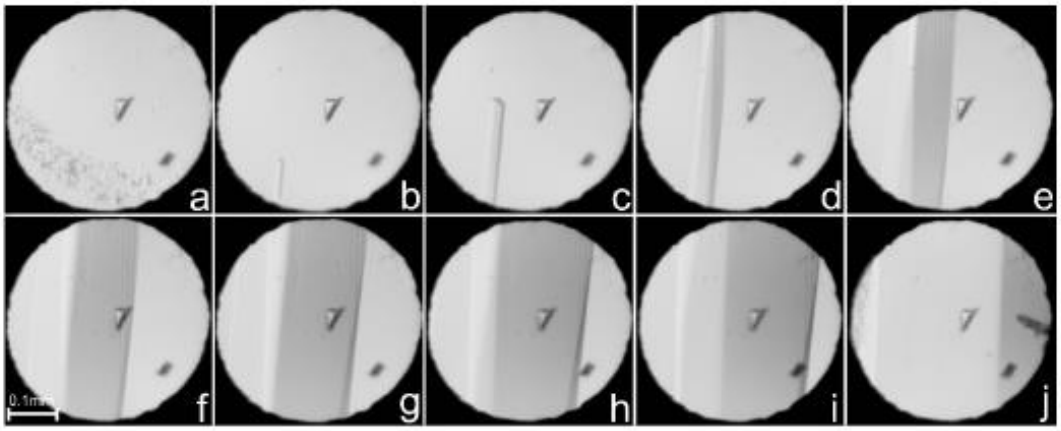

Figure S14. Stages of the dipropyl ether (DPE) phase α single-crystal growth inside the DAC chamber: (a) polycrystal–liquid equilibrium at 334 K; (b) one crystal seed at 334 K; (c-i) the single crystal cooled to 306 K and (j) filling the DAC chamber at 295 K and 1.70 GPa. The ruby chip, for pressure calibration, lies in the central part of the DAC.

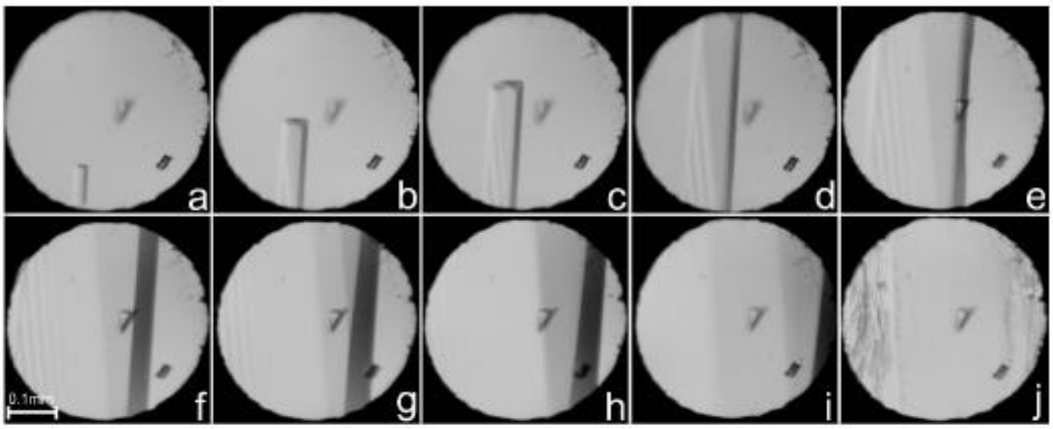

Figure S15. Stages of the DPE phase α single-crystal growth inside the DAC chamber: (a) one crystal seed at 356 K; (b-i) the single crystal cooled to 318 K and (j) filling the whole volume of DAC chamber at 295 K and 2.10 GPa. The ruby chip, for pressure calibration, lies in the central part of the DAC.

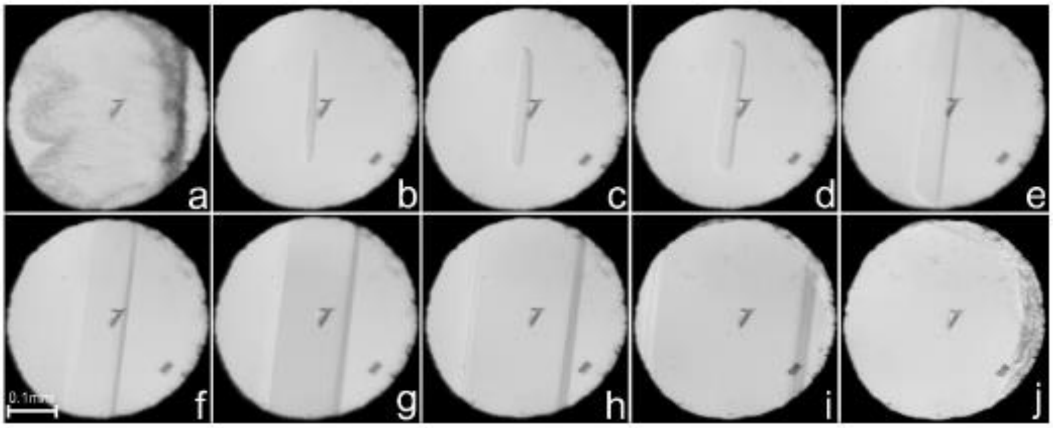

Figure S16. Stages of the DPE phase α single-crystal growth inside the DAC chamber: (a) polycrystal–liquid equilibrium at 393 K; (b) one crystal seed at 396 K; (c-i) the single crystal cooled to 356 K and (j) filling the DAC chamber at 295 K and 2.80 GPa. The ruby chip for pressure calibration lies in the central part of the DAC.

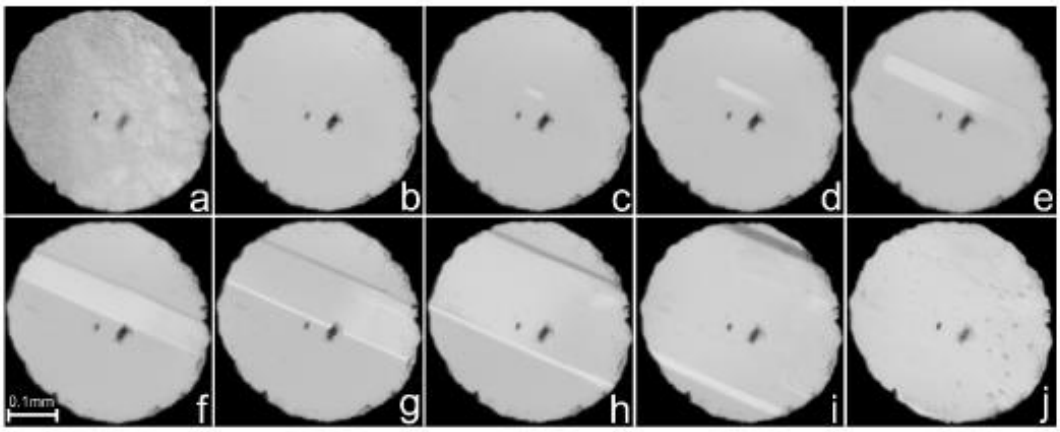

Figure S17. Stages of the DPE phase α single-crystal growth inside the DAC chamber: (a) polycrystal–liquid equilibrium at 295 K; (b) polycrystal–liquid equilibrium at 437 K; (c) one crystal seed at 433 K; (d-i) the single crystal cooled to 401 K and (j) filling the whole volume of DAC chamber at 295 K and 3.85 GPa. The ruby chip, for pressure calibration, lies in the central part of the DAC.

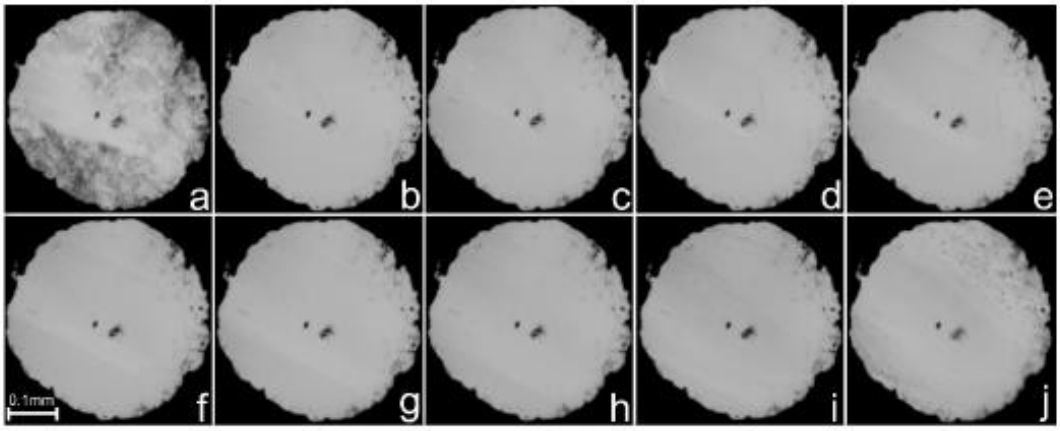

Figure S18. Stages of the DPE phase α single-crystal growth inside the DAC chamber: (a) polycrystal–liquid equilibrium at 295 K; (b) one crystal seed at 483 K; (c-i) the single crystal cooled to 424 K and (j) filling the DAC chamber at 295 K and 5.30 GPa. The ruby chip, for pressure calibration, lies in the central part of the DAC.

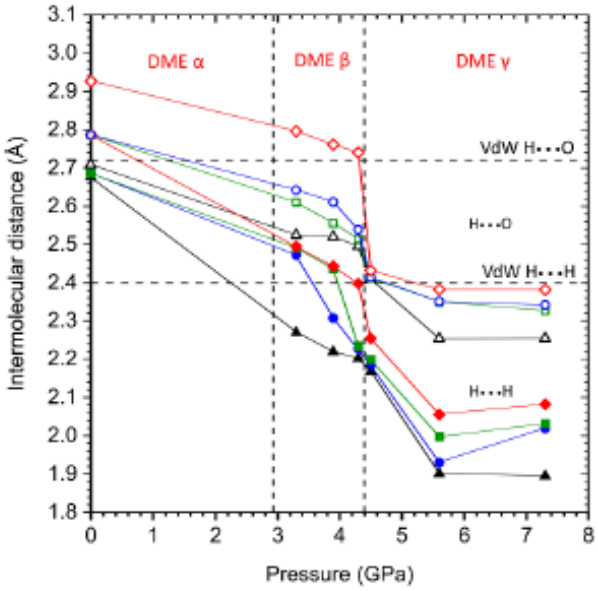

Figure S19. Intermolecular distances plotted as a function of pressure in DME. Four shortest distances for two types of interactions are presented: full shapes represent H···H whereas empty shapes depict the H···O distances. The black horizontal lines show the sum of the van der Waals radii of H and O of 2.72 Å, of H and H of 2.4 Å. The estimated standard deviations are smaller than the plotted symbols.

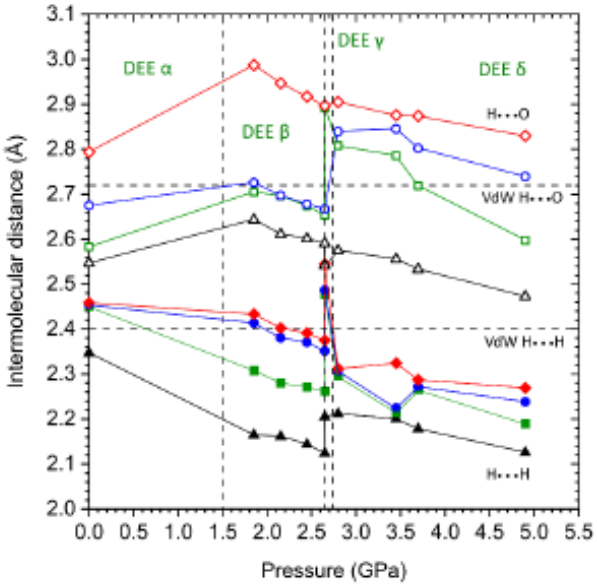

Figure S20. Intermolecular distances plotted as a function of pressure in DEE. Four shortest distances for two types of interactions are presented: full shapes represent H···H whereas empty shapes depict the H···O distances (only two shortest H···O distances for DEE γ are indicated). The black horizontal lines show the sum of the van der Waals radii of H and O of 2.72 Å, and of H and H of 2.4 Å. The estimated standard deviations are smaller than the plotted symbols.

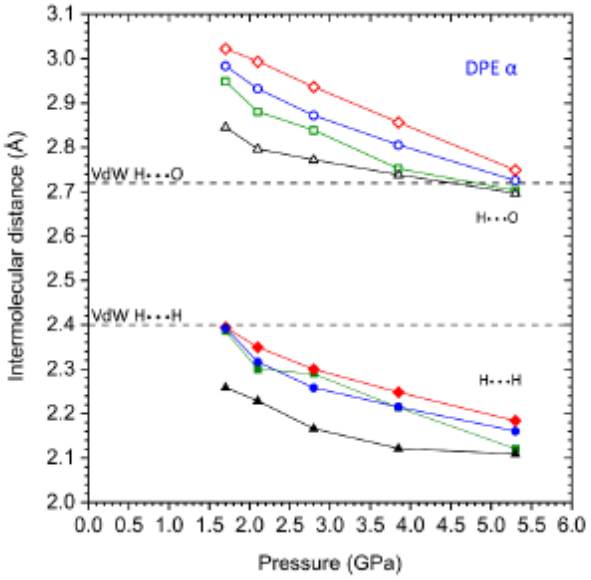

Figure S21. Intermolecular distances plotted as a function of pressure in DPE. Four shortest distances for two types of interactions are presented: full shapes represent H···H whereas empty shapes depict the H···O distances. The black horizontal lines show the sum of the van der Waals radii of H and O of 2.72 Å, and of H and H of 2.4 Å. The estimated standard deviations are smaller than the plotted symbols.

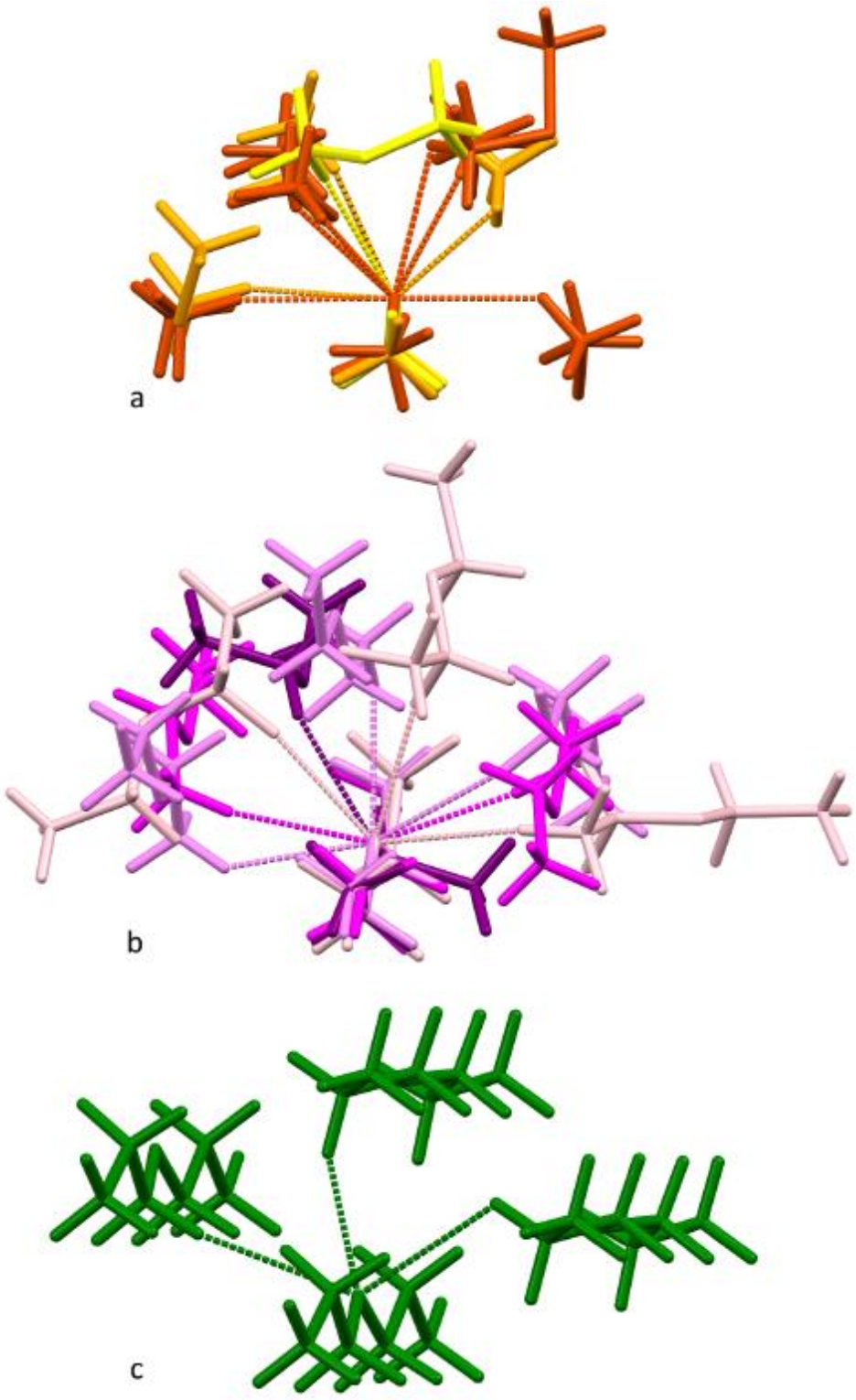

Figure S22. The shortest intermolecular CH···O interactions in: (a) DME phases α (yellow), β (orange) and γ (brown); (b) DEE phases α (pink), β (violet), γ (magenta) and δ (purple) and (c) DPE phase α (green).

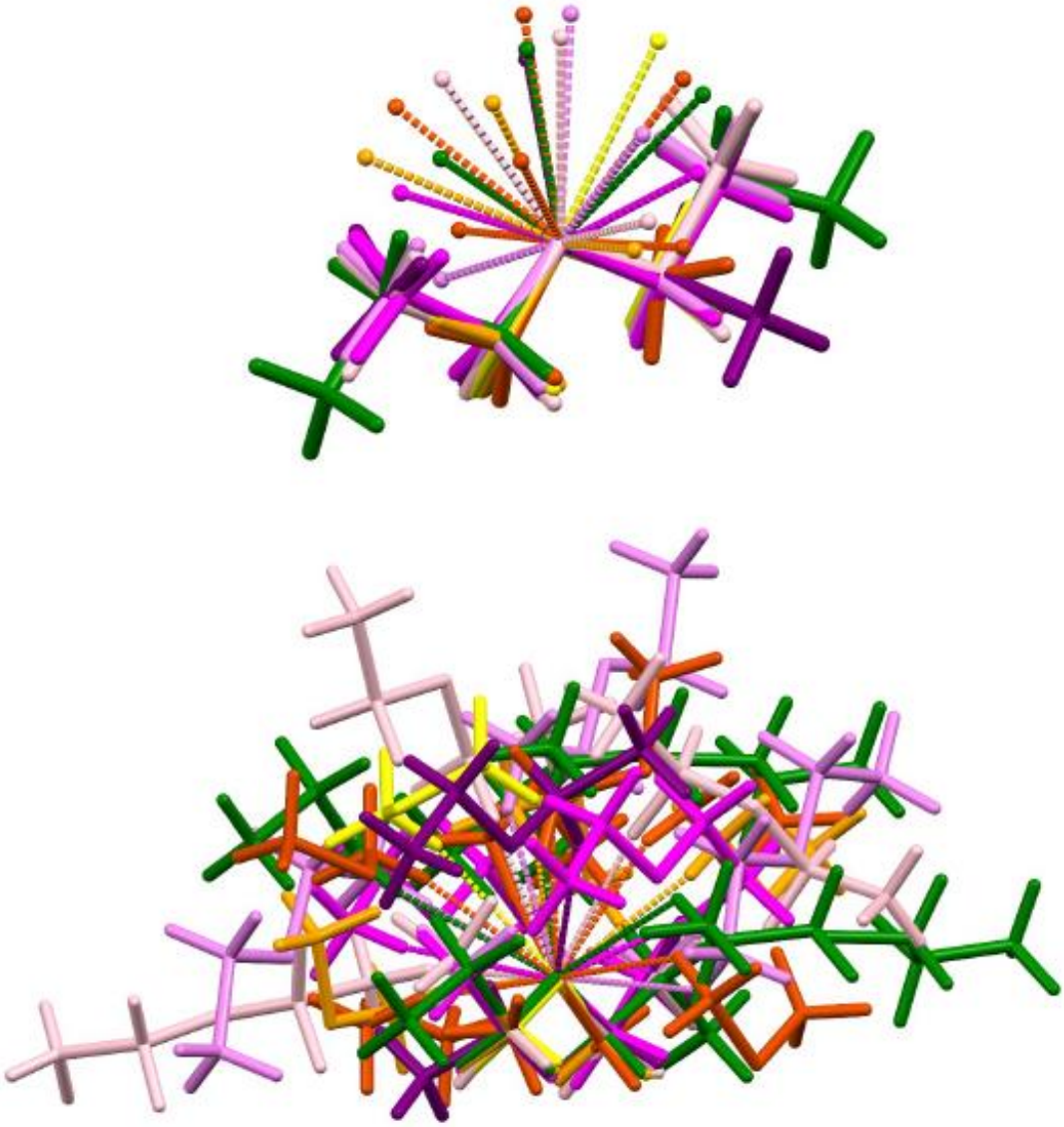

Figure S23. The shortest intermolecular CH···O interactions in the superimposed molecules of DME: phases α (yellow), β (orange), γ (brown); DEE phases α (pink), β (violet), γ (magenta), δ (purple) and DPE phase α (green) (*cf*. Fig. 5).

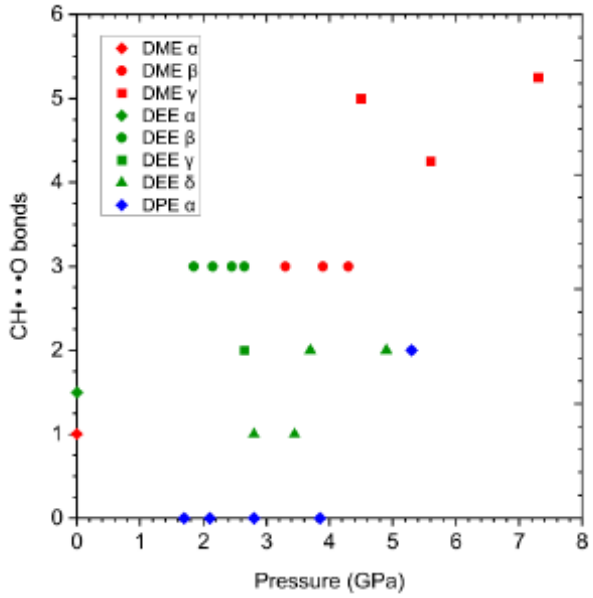

Figure S24. The number of H-donors accepting the O-atoms within the hydrogen bonds CH···O (per one molecule in the unit cell) in different phases of DME, DEE and DPE.

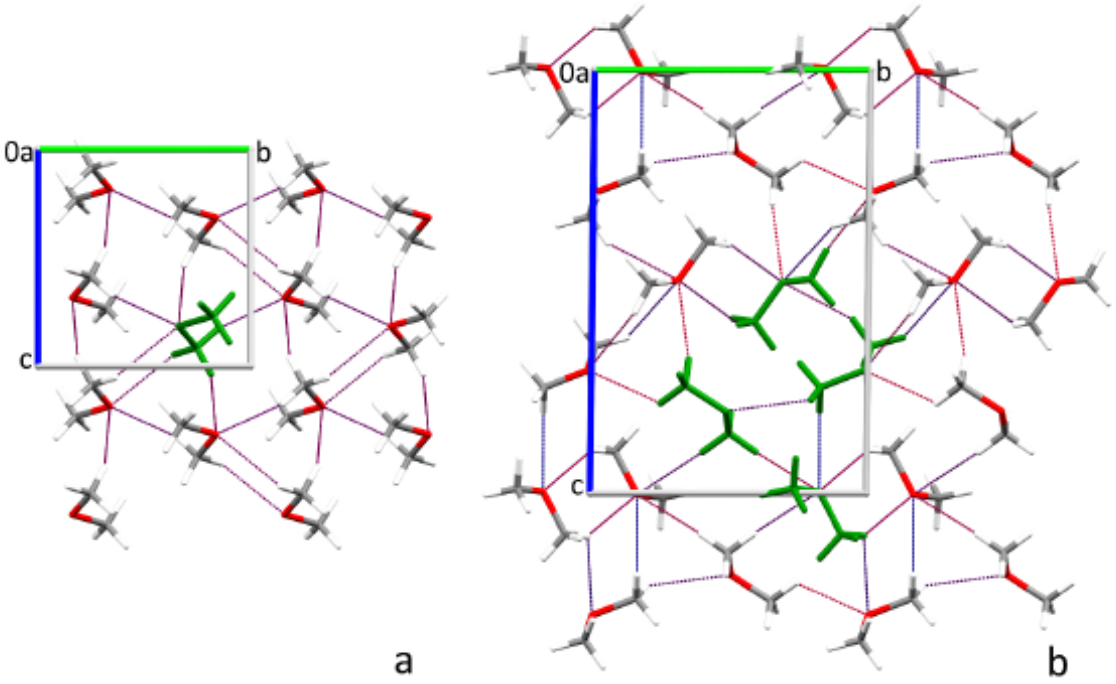

Figure S25. CH···O hydrogen bonding patterns in the crystal structures of DME polymorphs (a) β and (b) γ. The symmetry independent molecules are indicated in green, whereas the CH···O contacts are marked by dotted lines.

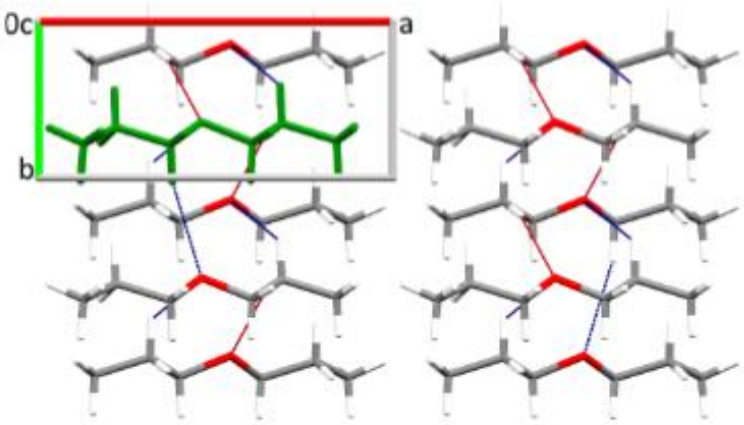

Figure S26. CH···O hydrogen bonding patterns in the high-pressure crystal structure of DPE. The symmetry independent molecule is indicated in green, whereas the CH···O contacts are marked by dotted lines.

Table S1. Crystal data and structure refinement details of DME phase β at 3.30, 3.90, 4.30 GPa and phase γ at 4.50, 5.60, 7.30 GPa (all at 295 K).

	C_2H_6O phase β	C_2H_6O phase β	C_2H_6O phase β	C_2H_6O phase γ	C_2H_6O phase γ	C_2H_6O phase γ
Pressure (GPa)	3.30(2)	3.90(2)	4.30(2)	4.50(2)	5.60(2)	7.30(2)
Temperature (K)	295(2)	295(2)	295(2)	295(2)	295(2)	295(2)
Formula weight	46.07	46.07	46.07	46.07	46.07	46.07
Crystal colour	colourless	colourless	colourless	colourless	colourless	colourless
Crystal size (mm)	0.30x0.29x0.25	0.33x0.33x0.24	0.38x0.38x0.23	0.34x0.32x0.22	0.37x0.35x0.21	0.40x0.38x0.20
Crystal system	monoclinic	monoclinic	monoclinic	triclinic	triclinic	triclinic
Space group	$P2_1/c$	$P2_1/c$	$P2_1/c$	$P\bar{1}$	$P\bar{1}$	$P\bar{1}$
Unit cell dimensions						
a (Å)	5.5541(4)	5.5277(4)	5.5073(4)	4.3394(12)	4.2888(17)	4.250(4)
b (Å)	6.6179(11)	6.527(10)	6.493(5)	8.414(2)	8.3045(18)	8.198(3)
c (Å)	6.964(3)	6.8941(5)	6.8431(8)	12.821(6)	12.7912(13)	12.6105(19)
α (°)	90	90	90	90.55(4)	90.249(12)	90.641(19)
β (°)	103.835(19)	103.869(6)	103.848(8)	93.89(6)	93.92(2)	93.97(3)
γ (°)	90	90	90	90.83(2)	90.14(3)	90.04(5)
Volume (Å^3)	248.56(12)	241.5(4)	237.58(19)	467.0(3)	454.5(2)	438.3(4)
Z, Z'	4, 1	4, 1	4, 1	8, 4	8, 4	8, 4
V/Z	62.14(3)	60.375(1)	59.395(5)	58.375(4)	56.8125(3)	54.7875(5)
D_x (g·cm^{-3})	1.231	1.267	1.288	1.311	1.346	1.396
Wavelength MoKα, λ (Å)	0.71073	0.71073	0.71073	0.71073	0.71073	0.71073
Absorption coefficient (mm^{-1})	0.095	0.098	0.100	0.101	0.104	0.108
F(000) (e)	104	104	104	208	208	208
2Θ max (°)	51.82	51.45	52.24	52.31	52.51	52.24
Min./Max. indices h, k, l	-6/6, -7/7, -4/4	-6/6, -1/1, -8/8	-6/6, -3/3, -7/7	-5/5, -10/10, -5/6	-2/2, -10/9, -15/15	-2/2, -9/9, -15/15
Reflections collected/unique	850/147	634/107	721/129	2659/556	2631/559	2349/523
R_{int} (all data)	0.0646	0.0308	0.0295	0.0338	0.0306	0.0418
Observed reflections ($F^2 > 2\sigma(F^2)$)	132	99	118	481	486	389
Data/restraints/parameters	147/0/31	107/0/15	129/0/31	556/0/117	559/0/58	523/0/118
Goodness of fit on F^2	1.204	1.192	1.181	1.131	1.135	1.055
Final R_1 indices ($F^2 > 2\sigma(F^2)$)	0.0708	0.0690	0.0525	0.0554	0.1173	0.0793
R_1/wR_2 indices (all data)	0.0776/0.1927	0.0728/0.1724	0.0566/0.1399	0.0628/0.1553	0.1296/0.2604	0.1062/0.1868
$\Delta\sigma_{max}$, $\Delta\sigma_{min}$ (eÅ^{-3})	0.19/-0.17	0.17/-0.12	0.14/-0.11	0.15/-0.14	0.23/-0.19	0.15/-0.14
Weighting scheme: x; y[a]	0.1102;0.24	0.1005/0.17	0.1045/0.04	0.0885/0.32	0.0699/2.71	0.0557/1.68

[a] $w=1/(\sigma^2(Fo^2)+x^2P^2+yP)$, where $P=(\mathrm{Max}(Fo^2,0)+2Fc^2)/3$

Table S2. Crystal data and structure refinement details of DEE phase β at 1.85, 2.15, 2.45, 2.65 GPa and phase γ at 2.65 GPa (all at 295 K).

	$C_4H_{10}O$ phase β	$C_4H_{10}O$ phase β	$C_4H_{10}O$ phase β	$C_4H_{10}O$ phase β	$C_4H_{10}O$ phase γ
Pressure (GPa)	1.85(2)	2.15(2)	2.45(2)	2.65(2)	2.65(2)
Temperature (K)	295(2)	295(2)	295(2)	295(2)	295(2)
Formula weight	74.12	74.12	74.12	74.12	74.12
Crystal colour	colourless	colourless	colourless	colourless	colourless
Crystal size (mm)	0.37x0.36x0.27	0.38x0.34x0.26	0.39x0.36x0.25	0.40x0.37x0.24	0.40x0.36x0.24
Crystal system	monoclinic	monoclinic	monoclinic	monoclinic	monoclinic
Space group	$P2_1/c$	$P2_1/c$	$P2_1/c$	$P2_1/c$	$I2/a$
Unit cell dimensions					
a (Å)	6.8268(3)	6.7948(3)	6.7759(3)	6.7612(3)	7.7073(12)
b (Å)	8.1428(17)	8.0952(12)	8.0552(14)	8.0271(15)	4.0885(4)
c (Å)	7.7731(3)	7.7259(2)	7.6873(2)	7.6687(3)	13.233(2)
β (°)	93.443(4)	93.621(3)	93.713(3)	93.784(4)	93.793(16)
Volume (Å^3)	431.32(9)	424.12(7)	418.70(8)	415.29(8)	416.07(10)
Z, Z'	4, 1	4, 1	4, 1	4, 1	4, 0.5
V/Z	107.83(2)	106.03(2)	104.675(2)	103.8225(2)	104.0175(3)
D_x (g·cm^{-3})	1.141	1.161	1.176	1.185	1.183
Wavelength MoKα, λ (Å)	0.71073	0.71073	0.71073	0.71073	0.71073
Absorption coefficient (mm^{-1})	0.079	0.080	0.081	0.082	0.081
F(000) €	168	168	168	168	168
2Θ max (°)	52.79	53.27	52.89	52.79	52.71
Min./Max. indices h, k, l	-8/8, -5/5, -9/9	-8/8, -5/5, -9/9	-8/8, -5/5, -9/9	-8/7, -5/5, -9/9	-7/8, -4/4, -14/14
Reflections collected/unique	2198/386	2208/386	2154/377	2120/375	1160/223
R_{int} (all data)	0.0239	0.0250	0.0245	0.0216	0.0131
Observed reflections ($F^2 > 2\sigma(F^2)$)	352	353	346	342	202
Data/restraints/parameters	386/0/48	386/0/48	377/0/48	375/0/48	223/0/25
Goodness of fit on F^2	1.121	1.168	1.138	1.088	1.130
Final R_1 indices ($F^2 > 2\sigma(F^2)$)	0.0353	0.0327	0.0390	0.0388	0.0371
R_1/wR_2 indices (all data)	0.0403/0.0988	0.0367/0.0928	0.0421/0.1110	0.0423/0.1110	0.0417/0.1085
$\Delta\sigma_{max}$, $\Delta\sigma_{min}$ (eÅ^{-3})	0.10/-0.11	0.09/-0.09	0.12/-0.12	0.14/-0.15	0.09/-0.11
Weighting scheme: x; y[a]	0.0644;0.04	0.0569/0.03	0.0773/0.03	0.0819/0.03	0.0545/0.17

[a] $w=1/(\sigma^2(Fo^2)+x^2P^2+\gamma P)$, where $P=(\mathrm{Max}(Fo^2,0)+2Fc^2)/3$

Table S3. Crystal data and structure refinement details of DEE phase δ at 2.80, 4.90 GPa (all at 295 K).

	$C_4H_{10}O$ phase δ	$C_4H_{10}O$ phase δ	$C_4H_{10}O$ phase δ	$C_4H_{10}O$ phase δ
Pressure (GPa)	2.80(2)	3.45(2)	3.70(2)	4.90(2)
Temperature (K)	295(2)	295(2)	295(2)	295(2)
Formula weight	74.12	74.12	74.12	74.12
Crystal colour	colourless	colourless	colourless	colourless
Crystal size (mm)	0.36x0.36x0.23	0.37x0.37x0.22	0.38x0.38x0.21	0.40x0.40x0.20
Crystal system	triclinic	triclinic	triclinic	triclinic
Space group	$P\bar{1}$	$P\bar{1}$	$P\bar{1}$	$P\bar{1}$
Unit cell dimensions				
a (Å)	5.1196(4)	5.0809(5)	5.072(3)	5.0182(19)
b (Å)	5.6659(10)	5.6329(10)	5.629(2)	5.575(3)
c (Å)	7.2999(4)	7.2451(10)	7.215(5)	7.136(3)
α (°)	97.275(8)	97.382(13)	97.43(5)	97.36(4)
β (°)	102.728(6)	102.749(10)	102.91(6)	102.81(3)
γ (°)	96.747(10)	97.002(11)	97.15(5)	97.72(4)
Volume (Å^3)	202.56(4)	198.13(5)	196.6(2)	190.31(14)
Z, Z'	2, 1	2, 1	2, 1	2, 1
V/Z	101.28(2)	99.065(3)	98.3(1)	95.155(7)
D_x (g·cm^{-3})	1.215	1.242	1.252	1.293
Wavelength MoKα, λ (Å)	0.71073	0.71073	0.71073	0.71073
Absorption coefficient (mm^{-1})	0.084	0.086	0.086	0.089
F(000) (e)	84	84	84	84
2Θ max (°)	52.25	52.25	55.46	55.72
Min./Max. indices h, k, l	-6/6, -4/4, -8/8	-6/6, -5/4, -8/8	-5/5, -7/7, -7/7	-5/5, -6/6, -8/8
Reflections collected/unique	1217/244	1179/243	1025/199	944/195
R_{int} (all data)	0.0138	0.0183	0.0383	0.0950
Observed reflections ($F^2 > 2\sigma(F^2)$)	225	218	177	153
Data/restraints/parameters	244/0/48	243/0/23	199/0/23	195/0/23
Goodness of fit on F^2	1.179	1.788	1.166	1.086
Final R_1 indices ($F^2 > 2\sigma(F^2)$)	0.0388	0.1011	0.0489	0.0610
R_1/wR_2 indices (all data)	0.0419/0.1000	0.1071/0.3608	0.0553/0.1407	0.0739/0.1816
$\Delta\sigma_{max}$, $\Delta\sigma_{min}$ (eÅ^{-3})	0.09/-0.08	0.30/-0.29	0.09/-0.10	0.12/-0.12
Weighting scheme: x; y[a]	0.0403/0.09	0.2000/0	0.0907/0.03	0.1287/0.01

[a] $w=1/(\sigma^2(Fo^2)+x^2P^2+yP)$, where $P=(\mathrm{Max}(Fo^2,0)+2Fc^2)/3$

Table S4. Crystal data and structure refinement details of DPE phase α at 1.70, 2.10, 2.80, 3.85, 5.30 GPa (all at 295 K).

	$C_6H_{14}O$ phase α	$C_6H_{14}O$ phase α	$C_6H_{14}O$ phase α	$C_6H_{14}O$ phase α	$C_6H_{14}O$ phase α
Pressure (GPa)	1.70(2)	2.10(2)	2.80(2)	3.85(2)	5.30(2)
Temperature (K)	295(2)	295(2)	295(2)	295(2)	295(2)
Formula weight	102.18	102.18	102.18	102.18	102.18
Crystal colour	colourless	colourless	colourless	colourless	colourless
Crystal size (mm)	0.39x0.37x0.25	0.39x0.38x0.24	0.46x0.43x0.23	0.38x0.36x0.22	0.44x0.40x0.21
Crystal system	monoclinic	monoclinic	monoclinic	monoclinic	monoclinic
Space group	$P2_1/c$	$P2_1/c$	$P2_1/c$	$P2_1/c$	$P2_1/c$
Unit cell dimensions					
a (Å)	9.416(4)	9.368(8)	9.293(7)	9.198(9)	9.099(12)
b (Å)	4.1817(3)	4.1229(4)	4.0686(2)	4.0064(3)	3.9465(3)
c (Å)	15.579(7)	15.434(4)	15.1855(10)	14.9459(15)	14.649(8)
β (°)	101.23(5)	100.84(6)	100.35(3)	99.54(4)	98.32(10)
Volume (Å^3)	601.7(4)	585.5(6)	564.8(4)	543.1(5)	520.5(7)
Z, Z'	4, 1	4, 1	4, 1	4, 1	4, 1
V/Z	150.425(1)	146.375(1)	141.2(1)	135.775(1)	130.125(2)
D_x (g·cm^{-3})	1.128	1.159	1.202	1.249	1.304
Wavelength MoKα, λ (Å)	0.71073	0.71073	0.71073	0.71073	0.71073
Absorption coefficient (mm^{-1})	0.073	0.075	0.078	0.081	0.085
F(000) (e)	232	232	232	232	232
2Θ max (°)	52.86	53.06	53.10	52.91	52.55
Min./Max. indices h, k, l	-8/8, -5/5, -14/14	-6/6, -5/5, -16/16	-4/4, -5/5, -19/19	-4/4, -5/5, -18/18	-7/7, -4/4, -16/16
Reflections collected/unique	3001/386	2850/383	2881/356	2785/347	2594/310
R_{int} (all data)	0.0254	0.0297	0.0270	0.0297	0.0350
Observed reflections ($F^2 > 2\sigma(F^2)$)	286	287	282	281	232
Data/restraints/parameters	386/0/66	383/0/66	356/0/66	347/0/66	310/6/66
Goodness of fit on F^2	1.077	1.053	1.082	1.111	1.060
Final R_1 indices ($F^2 > 2\sigma(F^2)$)	0.0455	0.0524	0.0456	0.0308	0.0469
R_1/wR_2 indices (all data)	0.0661/0.1513	0.0723/0.1416	0.0591/0.1447	0.0424/0.0900	0.0666/0.1229
$\Delta\sigma_{max}$, $\Delta\sigma_{min}$ (eÅ^{-3})	0.10/-0.09	0.10/-0.10	0.09/-0.12	0.05/-0.06	0.10/-0.08
Weighting scheme: x; y[a]	0.1115/0.01	0.0676/0.31	0.0950/0.11	0.0571/0.02	0.0445/0.34

[a] $w=1/(\sigma^2(Fo^2)+x^2P^2+yP)$, where $P=(\mathrm{Max}(Fo^2,0)+2Fc^2)/3$

Paper P4

Molecular Aggregations in Crystals of Butene Isomers Determined at High Pressure

Sacharczuk, N.; Olejniczak, A.; Bujak, M.; Podsiadło, M.

C*ryst. Growth Des.* **2024***, 24,* 9909−9913

CRYSTAL GROWTH & DESIGN

pubs.acs.org/crystal

Article

Molecular Aggregations in Crystals of Butene Isomers Determined at High Pressure

Natalia Sacharczuk, Anna Olejniczak, Maciej Bujak, and Marcin Podsiadło*

Cite This: *Cryst. Growth Des.* 2024, 24, 9909−9913

Read Online

ACCESS | Metrics & More | Article Recommendations | Supporting Information

ABSTRACT: The crystal structures of all four ambient-condition gaseous butene isomers have been determined, for the first time, by high-pressure single-crystal X-ray diffraction. 1-Butene (but-1-ene, **B**), cis-2-butene ((2*Z*)-but-2-ene, **CB**), trans-2-butene ((2*E*)-but-2-ene, **TB**), and isobutene (2-methylprop-1-ene, **IB**) at high pressure and room temperature froze at 3.65, 1.55, 0.50, and 1.40 GPa, respectively. **B**, **CB**, **TB**, and **IB** crystallize in the centrosymmetric space groups of *Pnma*, *C*2/*c*, $P2_1/c$, and $P6_3/m$, respectively. All of these crystals remain stable within the investigated pressure range. The physical properties of the studied butene isomers have been correlated with their molecular structures, interatomic distances, and molecular packing.

INTRODUCTION

The simplest aliphatic hydrocarbons occur in gaseous forms under normal conditions.[1] However, in nature, e.g., below the Earth's surface, they can appear in a different form as they are exposed to variable extreme pressure and temperature conditions. Structural studies of hydrocarbons under various conditions,[2−4] in particular under high pressure,[5] have significantly advanced in recent years, revealing important insights into intermolecular interactions and phase transitions. These studies have mostly focused on the simplest homologous alkanes such as methane,[6,7] ethane,[8−11] propane,[12−14] and butane.[15] However, those with longer chains have been investigated too.[16−18] Boese et al.[16] reported the crystal structures of *n*-alkanes from propane to nonane and explained the systematically lower melting points of *n*-alkanes with odd *i* numbers compared with those with *i* even numbers.

We recently performed structural studies of ethane at high pressure and room temperature. At these conditions, ethane crystallizes in the tetragonal phase IV with rotationally disordered molecules. The disorder is observed due to thermal activation and a possible reduction of the E_p barrier for molecular rotations by pressure.[8] We have also performed high-pressure structural investigation on the next two higher homologs of propane and butane.[14] In those cases, because of the unfavorable shape, low electrostatic potential on the molecular surface, and electrostatic mismatch between loosely packed molecules, the overall cohesion forces are weaker. As a result, propane is characterized by the lowest melting point of all organic compounds.[14] It was shown that, within the investigated pressure range, ethane, propane, and butane exhibited stable crystal structures.

In this study, we continue our previous structural investigations of simple aliphatic hydrocarbons under high pressure, focusing on butene with the general formula C_4H_8. Butene is the simplest unsaturated aliphatic hydrocarbon existing in four structurally distinct isomers. These can be classified into two main types: linear (straight chain) and branched chain. Three of the four isomers are linear: 1-butene (but-1-ene, **B**) and 2-butene, which has two geometric modifications of cis-2-butene ((2*Z*)-but-2-ene, **CB**) and trans-2-butene ((2*E*)-but-2-ene, **TB**). The fourth isomer, isobutene (2-methylprop-1-ene, **IB**), can be classified as a branched-chain one (Scheme 1). Of note is that all these isomeric compounds have different physical and chemical properties associated with their distinct molecular structures as well as arrangements of atoms and molecules (Scheme 1). In this work, we present, for the first time, the pure crystal structures of all isomers for this well known gas.

EXPERIMENTAL SECTION

Butene isomers, gases at ambient conditions:[1] 1-butene, **B** (99.5%), cis-2-butene, **CB** (99.0%), trans-2-butene, **TB** (99.0%, all from Linde Gaz Polska), and isobutene, **IB** (99.0%, from Sigma-Aldrich) were loaded into modified Merrill-Basset diamond-anvil cells (DACs)[19] at cryogenic

Received: July 16, 2024
Revised: October 31, 2024
Accepted: November 4, 2024
Published: November 15, 2024

https://doi.org/10.1021/acs.cgd.4c00983
Cryst. Growth Des. 2024, 24, 9909−9913

Scheme 1. Butene Isomers: 1-Butene (B), Cis-2-Butene (CB), Trans-2-Butene (TB), and Isobutene (IB)[a]

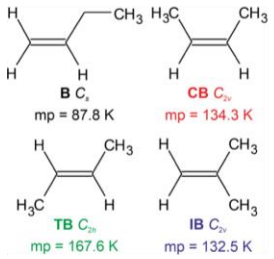

[a]The abbreviations, symmetries of molecules, and the melting points are indicated.[1]

conditions and *in situ* crystallized. The physical opening angle of the DACs used in all experiments ranged from 72 to 80°, while the angle used during data processing in the *CrysAlisPro* program suite[20] varied between 66 and 72°. The size of the diamond culets in the DACs was either 0.7 or 0.8 mm, and they were equipped with cylindrical WC seats. In all the experiments, the DAC was equipped with a 0.3-mm thick steel gasket with a hole 0.4 mm in diameter. At 295 K **B**, **CB**, **TB**, and **IB** froze at 3.65, 1.55, 0.50, and 1.40 GPa, respectively, in the form of polycrystalline mass fully filling the whole volume of the DAC chamber. A single crystal of **B** was obtained under isothermal conditions. The polycrystalline mass was melted except for one crystallite by the slow decreasing pressure. Then, again slowly, the pressure was increased, allowing a single crystal of **B** to grow and eventually fill the entire volume of the chamber. Afterward, the pressure was increased to achieve a stable single crystal required for the X-ray diffraction measurement. Single crystals of **CB**, **TB**, and **IB** were obtained under isochoric conditions: the DAC and polycrystalline mass inside the chamber were heated with a hot air gun until all but one grain melted. Then the DAC was slowly cooled to room temperature, and the single-crystal samples grew, eventually filling the whole volume of the chamber. An infrared laser thermometer was used for measuring the temperature inside the DAC. At each pressure point, the single crystals were grown *in situ*. The pressure was calibrated by the ruby fluorescence method[21,22] using a Photon Control spectrometer with an accuracy of 0.02 GPa. The calibration was performed before and after each X-ray diffraction experiment. The experimental details and progress in growing the single crystals are shown in Figures 1 and S1–S13.

Diffractometers Xcalibur EOS and KUMA KM4-CCD were used for high-pressure studies. The X-ray wavelength used in all experiments was 0.71073 Å. The DAC was centered by the gasket-shadow method.[23] The *CrysAlisPro* program suite was used for data collections, determination of the *UB*-matrices, and data reductions.[20] All data were corrected for the Lorentz, polarization, and absorption effects. Programs *OLEX2–1.5*,[24] *SHELXT*,[25] and *SHELXL*[26] were used to solve the structures by direct methods and then for the full-matrix least-squares refinement of the models. Anisotropic temperature factors were applied for carbon atoms. The H atoms were located based on the molecular geometry, with the C–H distances equal to 0.97, 0.96, and 0.93 Å and their U_{iso} factors constrained to 1.2, 1.5, and 1.2 or 1.5 times, respectively, U_{eq} of their carriers. The crystal data and refinement details are summarized in Tables 1 and S1–S4.

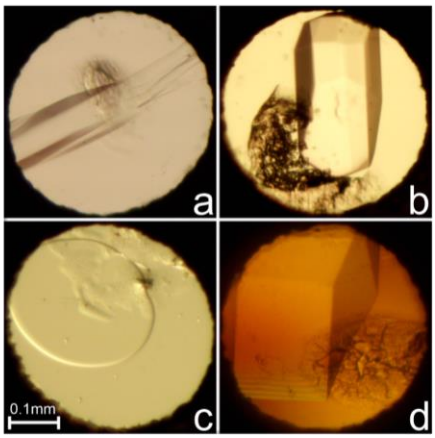

Figure 1. Single crystals of **B**, **CB**, **TB**, and **IB** grown *in situ* in the DAC chamber: (a) **B** at 3.65 GPa/295 K, (b) **CB** at 1.75 GPa/318 K, (c) **TB** at 0.75 GPa/364 K, and (d) **IB** at 1.60 GPa/334 K.

Table 1. Selected Crystal Data of B, CB, TB, and IB, All at 295 K

	B	CB	TB	IB
p (GPa)	4.40(2)	1.75(2)	0.75(2)	1.60(2)
crystal system	orthorhombic	monoclinic	monoclinic	hexagonal
space group	*Pnma*	*C*2/*c*	$P2_1/c$	$P6_3/m$
a (Å)	11.364(4)	3.9161(13)	5.150(6)	5.845(6)
b (Å)	5.9132(10)	9.174(3)	5.0833(4)	5.845(6)
c (Å)	4.8370(7)	10.2411(12)	7.7661(12)	6.344(8)
β (deg)	90	98.87(2)	104.24(5)	90
V (Å^3)	325.04(13)	363.51(18)	197.1(2)	187.7(4)
Z, Z'	4, 1/2	4, 1/2	2, 1/2	2, 1/6
D_x (g·cm^{-3})	1.146	1.025	0.945	0.993
R_1 ($F^2 > 2\sigma(F^2)$)	0.0486	0.0686	0.0773	0.0984
R_1 (all data)	0.0793	0.0733	0.1184	0.1940

RESULTS AND DISCUSSION

The butene isomers, with the formula C_4H_8, exhibit different molecular symmetries: **B**, **CB**, **TB**, and **IB** show C_s, C_{2v}, C_{2h}, and C_{2v} symmetry, respectively. **B**, with the lowest molecular symmetry, also exhibits the lowest melting point of 87.8 K.[1] **CB** and **IB** share the same molecular symmetry with slightly different melting points of 134.3 and 132.5 K, respectively.[1] **TB**, with a molecular symmetry of C_{2h}, is characterized by the highest melting point among all the butene isomers of 167.6 K.[1] The melting points, determined for C_4H_8 isomers,[1] are presented in Figure 2. It is of note that the freezing pressures of the isomers, determined in this study at room temperature (RT), correspond, in an inverse relation, to the melting temperatures (Figure 2). **B** exhibits the highest freezing pressure of 3.65 GPa, and **CB** and **IB** freeze at 1.55 and 1.40 GPa, respectively, while the highest melting solid of **TB** appears at the lowest pressure of 0.50 GPa. The crystal structures of butene isomers, determined just above the

https://doi.org/10.1021/acs.cgd.4c00983
Cryst. Growth Des. 2024, 24, 9909–9913

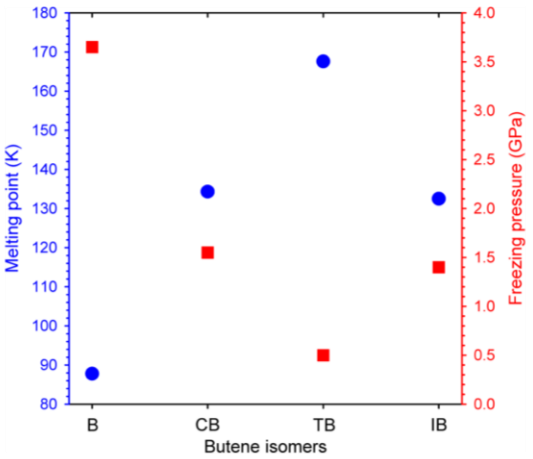

Figure 2. Ambient pressure melting points (blue circles; K)[1] and ambient temperature freezing pressures (red squares; GPa; this work) of butene isomers.

freezing pressure points, exhibit a similar trend in the calculated densities, which increase from **TB** to **B**, with the values of 0.945 (**TB** at 0.75 GPa), 0.993 (**IB** at 1.60 GPa), 1.025 (**CB** at 1.75 GPa), and 1.146 (**B** at 4.40 GPa) g·cm^{-3} (Table 1).

Single crystals of butene isomers were obtained at the lowest possible pressure to ensure the stability of the crystals during the X-ray diffraction data collection experiments (for **CB**, **TB**, and **IB**, this pressure was 0.20, 0.25, and 0.20 GPa higher than their respective freezing pressures). The maximum pressure, under which the diffraction measurement could be performed in this series, was limited by the thermal restriction of the DAC (corresponding to the temperature of approximately 500 K inside the high-pressure chamber) or by the tendency of a given C_4H_8 isomer to polymerize at high temperature and pressure (for **CB**, **TB**, and **IB**, this pressure was 3.70, 1.85, and 3.05 GPa, respectively). The pressure range investigated for the obtained single crystals of **CB**, **TB**, and **IB** was 1.95, 1.10, and 1.45 GPa, respectively. **B** exhibited the highest tendency for polymerization, which was initiated at temperature just above RT. Additionally, **B** has the lowest increase in melting temperature with increasing pressure among all butene isomers. For these reasons, within this study, a single crystal of **B** has been obtained only at a pressure of 4.40 GPa, which is 0.75 GPa higher than the freezing pressure of that isomer.

1-Butene (**B**) crystallizes at 3.65 GPa/295 K. After a single crystal of **B** was obtained under isothermal conditions at the crystallization pressure, the pressure was increased to 4.40 GPa. At this pressure point and 295 K, crystals of **B** are orthorhombic, space group *Pnma*, with four molecules in the unit cell, lying on the mirror planes. The crystal structure of **B** has been determined only at one pressure point due to the sample polymerization observed upon raising the temperature just above the RT. Therefore, *in situ* crystal growth could not be conducted at pressures higher than 4.40 GPa.

Cis-2-butene (**CB**) crystallizes at 1.55 GPa/295 K. The crystal structures of **CB** have been determined at 1.75, 2.25, 3.05, and 3.70 GPa at 295 K. **CB** crystallizes in the monoclinic space group $C2/c$ with four molecules located on the inversion centers. No signs of phase transition were observed over the entire investigated pressure range. Also, no tendency of **CB** to polymerize was observed at an elevated temperature.

Trans-2-butene (**TB**) crystallizes at 0.50 GPa/295 K. It has the lowest freezing pressure in the group of isomeric butenes. The room temperature crystal structures of **TB** were determined at 0.75, 1.10, 1.50, and 1.85 GPa. Among all four isomers, **TB** exhibited the largest increase in the melting temperature with increasing pressure. At high pressure, it crystallizes in the monoclinic space group $P2_1/c$ with two molecules in the unit cell lying on inversion centers. Within the investigated pressure range, there is no sign of phase transition. Similar to **CB**, **TB** has not exhibited any tendency to polymerize. It is characteristic that **TB** crystals, uniquely within the butene isomers, exhibit a spherical morphology (Figures 1 and S6–S9). A similar crystal growth morphology has been observed previously, at high pressure, in the case of benzene,[27] carbon disulfide,[28] diiodomethane,[29] and ethane.[8]

IB crystallizes at 1.40 GPa/295 K. The crystal structures of isobutene have been determined at 1.60, 1.90, 2.45, and 3.05 GPa at 295 K. At this conditions, **IB** crystallizes in the space group $P6_3/m$. In the unit cell, two molecules lie at special positions ($3/m$), showing disorder with three carbon−carbon distances averaged between single and double bonds. This hexagonal symmetry remains stable, with no signs of any phase transition observed within the investigated pressure range. **IB** exhibits a high tendency for polymerization at elevated temperatures that hindered obtaining single crystals at higher pressures. As a result, crystals, upon cooling to room temperature, did not fill the entire volume of the pressure chamber (Figures S12 and S13).

Due to the determination of H atom positions based on the molecular geometry, the packing analysis of butene molecules considered the more reliable intermolecular C···C distances only. The arrangements of isomeric butene molecules in their crystals are shown in Figure 3. This figure also depicts the six shortest intermolecular C···C distances for each crystal structure. The comparison of the shortest C···C distances is plotted in Figure 4.

It is characteristic that all the six shortest intermolecular C···C distances for the **B** structure at 4.40 GPa (the first structure determined above the freezing pressure) are shorter than the sum of the van der Waals radii of two C atoms of 3.40 Å.[31] In the **CB** crystal structure at 2.25 GPa (the second pressure point above freezing), only the first two shortest intermolecular C···C distances are below 3.40 Å, and only in the structures above 3 GPa are all six shortest C···C distances below this limit. In contrast, in all **IB** and **TB** crystal structures, within the investigated pressure range, all of the intermolecular C···C distances are significantly longer than 3.40 Å (Figures 3 and 4). The observation of intermolecular distances in relation to the sum of the van der Waals radii suggested the potential stability of the **IB** and **TB** structures over the investigated pressure range. On the contrary, the **B** and **CB** structures are more likely to transform, at higher pressure, as they become more closely (densely) packed. However, this observation requires further study or implementation of quantum chemical calculations. It is also worth noting that the most compressible are the intermolecular C···C distances in **TB** as they shorten significantly with increasing pressure. The smallest compression is observed in **IB** (Figure 4). In each **IB** structure, the first six shortest intermolecular C···C distances are the same (Figure 4) due to the crystal symmetry of the $P6_3/m$ space group.

https://doi.org/10.1021/acs.cgd.4c00983
Cryst. Growth Des. 2024, 24, 9909−9913

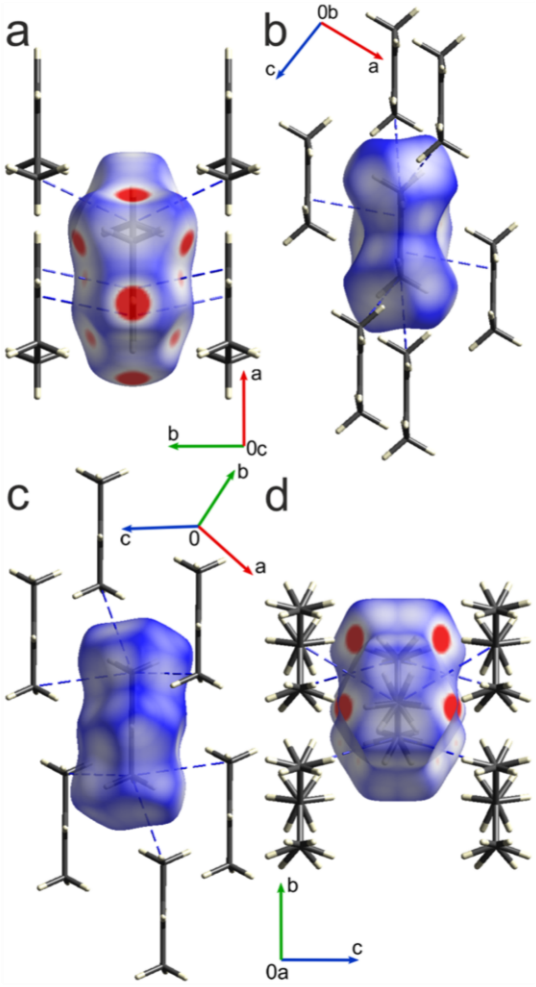

Figure 3. Molecular arrangements of butene isomers with the six shortest intermolecular C···C distances marked by blue dashed lines: (a) **B** at 4.40 GPa/295 K, (b) **CB** at 1.75 GPa/295 K, (c) **TB** at 0.75 GPa/295 K, and (d) **IB** at 1.90 GPa/295 K. Hirshfeld surfaces[30] are mapped with d_{norm} (from −0.1 to 0.7). Colors of white, red, and blue indicate contacts that are equal, shorter, and longer, respectively, than the sum of the van der Waals radii of respective atoms.

■ CONCLUSIONS

We studied the crystal structures of all four butene isomers, determined at high pressure, applying the single-crystal X-ray diffraction method. In this series of unsaturated hydrocarbons, all determined crystal phases remain stable within the investigated pressure range. The freezing pressures of C_4H_8 isomers are inversely related to their freezing temperatures and are associated with their molecular symmetry. Although the isomers have the same molecular formula and weight, they exhibit different behaviors while crystallized. They form monoclinic (**CB** and **TB**), orthorhombic (**B**), or hexagonal (**IB**) centrosymmetric crystals that are related to the symmetry of their molecules. The stability of the obtained forms can be associated with the intermolecular C···C distances, which are

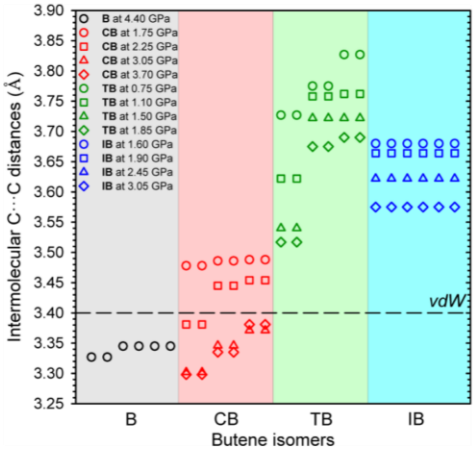

Figure 4. Six shortest intermolecular C···C distances (Å) for each high-pressure butene isomer determined at 295 K. The sum of van der Waals radii of two carbon atoms of 3.40 Å[31] is indicated by a horizontal black dashed line.

significantly longer than the doubled van der Waals radii of the carbon atom in the case of both **TB** and **IB**. These distances are shorter in **B** and **CB**; therefore, they are more likely to transform at higher pressure, however this requires further investigations. Both **B** and **IB**, unlike **CB** and **TB**, show a tendency to polymerize under varying pressure and temperature conditions. The obtained **B** and **IB** polymers are recoverable at ambient conditions, but they do not exhibit crystallinity under either high-pressure or ambient conditions. It can also be noted that the crystal structures of all four butene isomers, gases at ambient conditions, have been determined for the first time.

■ ASSOCIATED CONTENT

Supporting Information

The Supporting Information is available free of charge at https://pubs.acs.org/doi/10.1021/acs.cgd.4c00983.

Detailed experiment and structure description; crystal data of the refinements of **B**, **TB**, **IB**, and **CB** (PDF)

Accession Codes

Deposition Numbers 2370707−2370719 contain the supplementary crystallographic data for this paper. These data can be obtained free of charge via the joint Cambridge Crystallographic Data Centre (CCDC) and Fachinformationszentrum Karlsruhe Access Structures service.

■ AUTHOR INFORMATION

Corresponding Author

Marcin Podsiadło − *Faculty of Chemistry, Adam Mickiewicz University, Poznań 61-614, Poland;* orcid.org/0000-0001-6702-1875; Email: marcinp@amu.edu.pl

Authors

Natalia Sacharczuk − *Faculty of Chemistry, Adam Mickiewicz University, Poznań 61-614, Poland;* orcid.org/0000-0001-6931-1059

Anna Olejniczak − *Faculty of Chemistry, Adam Mickiewicz University, Poznań 61-614, Poland;* orcid.org/0000-0002-4460-4362

Maciej Bujak − *Institute of Chemistry, Faculty of Chemistry and Pharmacy, University of Opole, Opole 45-052, Poland;* orcid.org/0000-0003-2504-1119

Complete contact information is available at: https://pubs.acs.org/10.1021/acs.cgd.4c00983

Author Contributions

The manuscript was written through contributions of all authors. All authors have given approval to the final version of the manuscript.

Notes

The authors declare no competing financial interest.

■ ACKNOWLEDGMENTS

This study was supported by the National Science Centre (grant no. 2020/37/B/ST4/00982).

■ ABBREVIATIONS

B, 1-butene (but-1-ene); **CB**, cis-2-butene ((2*Z*)-but-2-ene); **TB**, trans-2-butene ((2*E*)-but-2-ene); **IB**, isobutene (2-methylprop-1-ene)

■ REFERENCES

(1) Haynes, W. M. *CRC Handbook of Chemistry and Physics*, 95th ed.; Taylor and Francis: Boca Raton, FL, 2014.
(2) Boese, R.; Niederprüm, N.; Bläser, D. Comparative Study by Single Crystal X-ray Structure Determinations of Tetramethylaminoborane and Tetramethylethene at 110 K. *Struct. Chem.* **1992**, *3*, 399−406.
(3) Boese, R.; Roth, W. R.; Bläser, D.; Latz, R.; Bäumen, A. (*E*)-3,4-Diisopropyl-2,5-dimethylhex-3-ene at 125K. *Acta Crystallogr., Sect. C: Cryst. Struct. Commun.* **1998**, *54*, IUC9800055.
(4) Vu, T. H.; Maynard-Casely, H. E.; Cable, M. L.; Choukroun, M.; Malaska, M. J.; Hodyss, R. 1,3-Butadiene on Titan: Crystal Structure, Thermal Expansivity, and Raman Signatures. *ACS Earth Space Chem.* **2022**, *6*, 2274−2281.
(5) Kolesnikov, A. Y.; Saul, J. M.; Kutcherov, V. G. Chemistry of Hydrocarbons Under Extreme Thermobaric Conditions. *Chemistry-Select* **2017**, *2*, 1336−1352.
(6) Stavrou, E.; Maryewski, A. A.; Lobanov, S. S.; Oganov, A. R.; Konôpková, Z.; Prakapenka, V. B.; Goncharov, A. F. Ethane and methane at high pressures: Structure and stability. *J. Chem. Phys.* **2021**, *155*, 184503.
(7) Sun, L.; Yi, W.; Wang, L.; Shu, J.; Sinogeikin, S.; Meng, Y.; Shen, G.; Bai, L.; Li, Y.; Liu, J.; Mao, H.-K.; Mao, W. L. X-ray diffraction studies and equation of state of methane at 202 GPa. *Chem. Phys. Lett.* **2009**, *473*, 72−74.
(8) Podsiadło, M.; Olejniczak, A.; Katrusiak, A. A New Ethane Polymorph. *Cryst. Growth Des.* **2017**, *17*, 228−232.
(9) Read, L. Q.; Spender, J. E.; Proctor, J. E. Raman spectroscopy of ethane (C_2H_6) to 120 GPa at 300 K. *J. Raman Spectrosc.* **2020**, *51*, 2311−2317.
(10) Shimizu, H.; Shimazaki, I.; Sasaki, S. High-Pressure Raman Study of Liquid and Molecular Crystal Ethane Up to 8 GPa. *Jpn. J. Appl. Phys.* **1989**, *28*, 1632−1635.
(11) Toraille, L.; Weck, G.; Geneste, G.; Pépin, C.; Garbarino, G.; Loubeyre, P. Ethane under pressure revisited using x-ray diffraction, Raman spectroscopy, infrared absorption, and *ab initio* calculations up to 150 GPa. *J. Chem. Phys.* **2024**, *160*, 214702.
(12) Kudryavtsev, D.; Serovaiskii, A.; Mukhina, E.; Kolesnikov, A.; Gasharova, B.; Kutcherov, V.; Dubrovinsky, L. Raman and IR Spectroscopy Studies on Propane at Pressures of Up to 40 GPa. *J. Phys. Chem. A* **2017**, *121*, 6004−6011.
(13) Kudryavtsev, D. A.; Fedotenko, T. M.; Koemets, E. G.; Khandarkhaeva, S. E.; Kutcherov, V. G.; Dubrovinsky, L. S. Raman Spectroscopy Study on Chemical Transformations of Propane at High Temperatures and High Pressures. *Sci. Rep.* **2020**, *10* (1), 1483.
(14) Podsiadło, M.; Olejniczak, A.; Katrusiak, A. Why Propane? *J. Phys. Chem. C* **2013**, *117*, 4759−4763.
(15) Kudryavtsev, D. A.; Kutcherov, V. G.; Dubrovinsky, L. S. Raman high-pressure study of butane isomers up to 40 GPa. *AIP Adv.* **2018**, *8*, 115104.
(16) Boese, R.; Weiss, H.-C.; Bläser, D. The Melting Point Alternation in the Short-Chain *n*-Alkanes: Single-Crystal X-ray Analyses of Propane at 30 K and of *n*-Butane to *n*-Nonane at 90 K. *Angew. Chem., Int. Ed.* **1999**, *38*, 988−992.
(17) Poręba, T.; Kicior, I. Pressure-freezing of dodecane: exploring the crystal structures, formation kinetics and phase diagrams for colossal barocaloric effects in *n*-alkanes. *RSC Adv.* **2023**, *13*, 33305−33317.
(18) Takekiyo, T.; Koyama, Y.; Matsuishi, K.; Yoshimura, Y. High-Pressure Raman Study of *n*-Octane up to 15 GPa. *J. Phys. Chem. B* **2020**, *124*, 11189−11196.
(19) Bassett, W. A. Diamond anvil cell, 50th birthday. *High. Press. Res.* **2009**, *29*, 163−186.
(20) *CrysAlisPro Software System*. Rigaku Oxford Diffraction, 2015.
(21) Mao, H. K.; Xu, J.; Bell, P. M. Calibration of the ruby pressure gauge to 800 kbar under quasi-hydrostatic conditions. *J. Geophys. Res.* **1986**, *91*, 4673−4676.
(22) Piermarini, G. J.; Block, S.; Barnett, J. D.; Forman, R. A. Calibration of the pressure dependence of the R_1 ruby fluorescence line to 195 kbar. *J. Appl. Phys.* **1975**, *46*, 2774−2780.
(23) Budzianowski, A.; Katrusiak, A. *High-Pressure Crystallography*; Katrusiak, A.; McMillan, P. eds., Springer: Dordrecht, 2004; pp. 101−112.
(24) Dolomanov, O. V.; Bourhis, L. J.; Gildea, R. J.; Howard, J. A. K.; Puschmann, H. *OLEX2*: a complete structure solution, refinement and analysis program. *J. Appl. Crystallogr.* **2009**, *42*, 339−341.
(25) Sheldrick, G. M. *SHELXT* − Integrated space-group and crystal-structure determination, *Acta Crystallogr. Sect. A: Found. Adv.* **2015**, *71*, 3−8.
(26) Sheldrick, G. M. Crystal structure refinement with *SHELXL*, *Acta Crystallogr. Sect. C: Struct. Chem.* **2015**, *71*, 3−8.
(27) Katrusiak, A.; Podsiadło, M.; Budzianowski, A. Association CH···π and No van der Waals Contacts at the Lowest Limits of Crystalline Benzene I and II Stability Regions. *Cryst. Growth Des.* **2010**, *10*, 3461−3465.
(28) Dziubek, K. F.; Katrusiak, A. Compression of Intermolecular Interactions in CS_2 Crystal. *J. Phys. Chem. B* **2004**, *108*, 19089−19092.
(29) Podsiadło, M.; Katrusiak, A. Competing Patterns of Weak Directional Forces in Pressure-Frozen CH_2ClI and CH_2I_2. *J. Phys. Chem. B* **2008**, *112*, 5355−5362.
(30) Spackman, P. R.; Turner, M. J.; McKinnon, J. J.; Wolff, S. K.; Grimwood, D. J.; Jayatilaka, D.; Spackman, M. A. *CrystalExplorer21*: a program for Hirshfeld surface analysis, visualization and quantitative analysis of molecular crystals. *J. Appl. Crystallogr.* **2021**, *54*, 1006−1011.
(31) Bondi, A. van der Waals Volumes and Radii. *J. Phys. Chem.* **1964**, *68*, 441−451.

Supporting Information

Molecular aggregations in crystals of butene isomers determined at high pressure

Natalia Sacharczuk[a], Anna Olejniczak[a], Maciej Bujak[b] and Marcin Podsiadło*[a]

[a]*Faculty of Chemistry, Adam Mickiewicz University, Uniwersytetu Poznańskiego 8, Poznań, 61-614, Poland*

[b]*Institute of Chemistry, Faculty of Chemistry and Pharmacy, University of Opole, Oleska 48, Opole, 45-052, Poland*

*E-mail: marcinp@amu.edu.pl

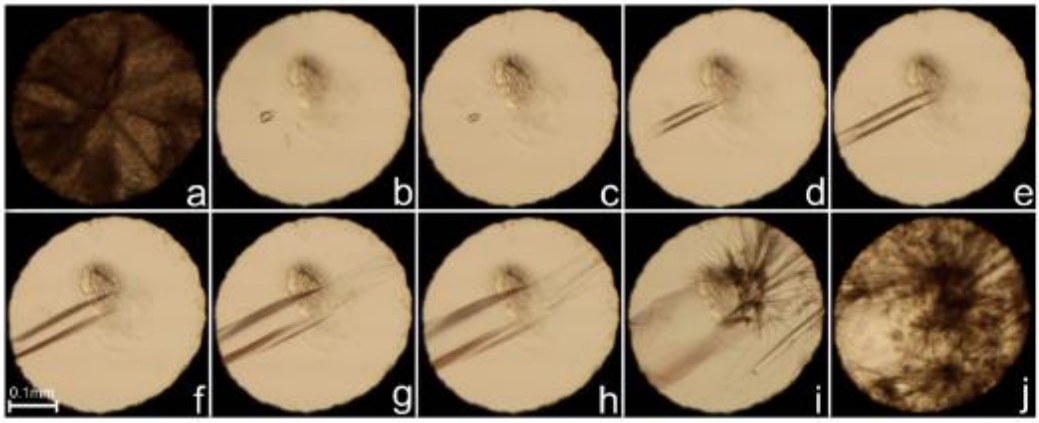

Figure S1. Stages of the **B** single-crystal growth inside the DAC chamber: (a) polycrystalline mass grown isothermally at 295 K and 3.66 GPa; (b) three single crystals–liquid equilibrium at 295 K and 3.65 GPa; (c) one crystal seed at 298 K and 3.65 GPa; (d-i) the single crystal growth during increasing pressure and simultaneous decrease in the volume of high-pressure chamber and (j) the single crystal filling the DAC chamber at 295 K and 4.40 GPa. The ruby chip, for pressure calibration, is located in the central part of the DAC.

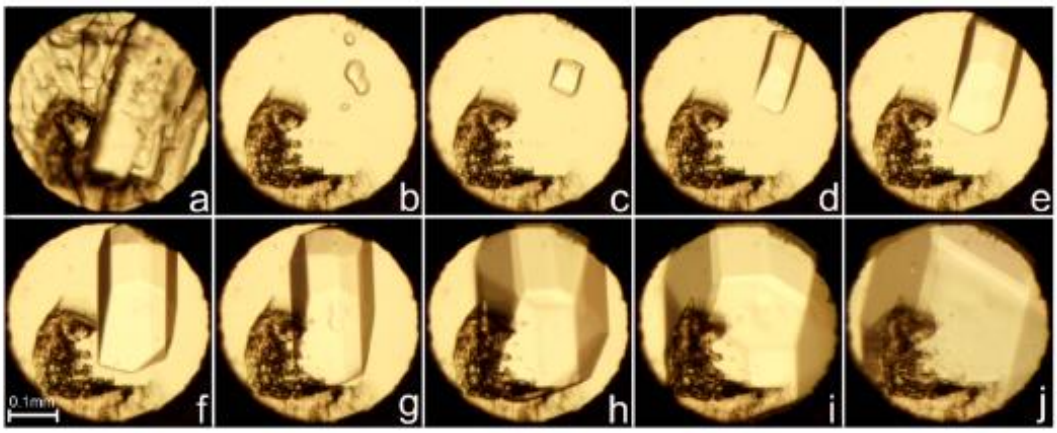

Figure S2. Stages of the **CB** single-crystal growth inside the DAC chamber: (a) polycrystalline mass grown isothermally at 303 K; (b) three single crystals–liquid equilibrium at 329 K; (c) one crystal seed at 329 K; (d-i) the single crystal cooled to 296 K and (j) the single crystal filling the DAC chamber at 295 K and 1.75 GPa. The ruby chips, for pressure calibration, are located in the lower part of the DAC.

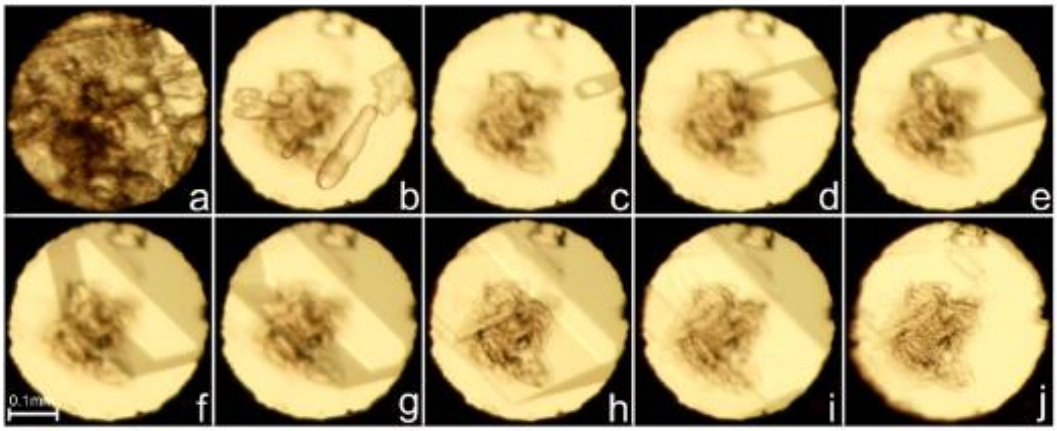

Figure S3. Stages of the **CB** single-crystal growth inside the DAC chamber: (a) polycrystalline mass grown isothermally at 298 K; (b) single crystals–liquid equilibrium at 366 K; (c) one crystal seed at 370 K; (d-i) the single crystal cooled to 325 K and (j) the single crystal filling the DAC chamber at 295 K and 2.25 GPa. The ruby chips, for pressure calibration, are located in the upper and central part of the DAC.

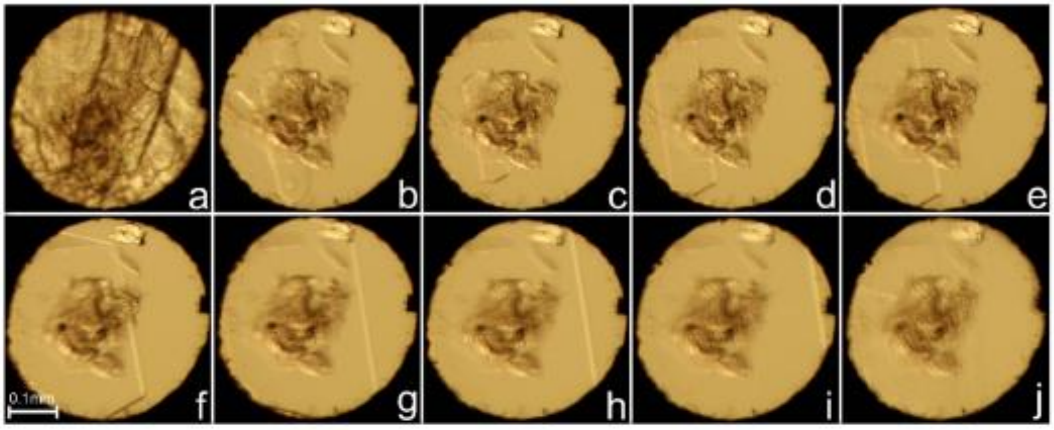

Figure S4. Stages of the **CB** single-crystal growth inside the DAC chamber: (a) polycrystalline mass grown isothermally at 298 K; (b) single crystals–liquid equilibrium at 401 K; (c) one crystal seed at 404 K; (d-i) the single crystal cooled to 363 K and (j) the single crystal filling the DAC chamber at 295 K and 3.05 GPa. The ruby chips, for pressure calibration, are located in the upper and central part of the DAC.

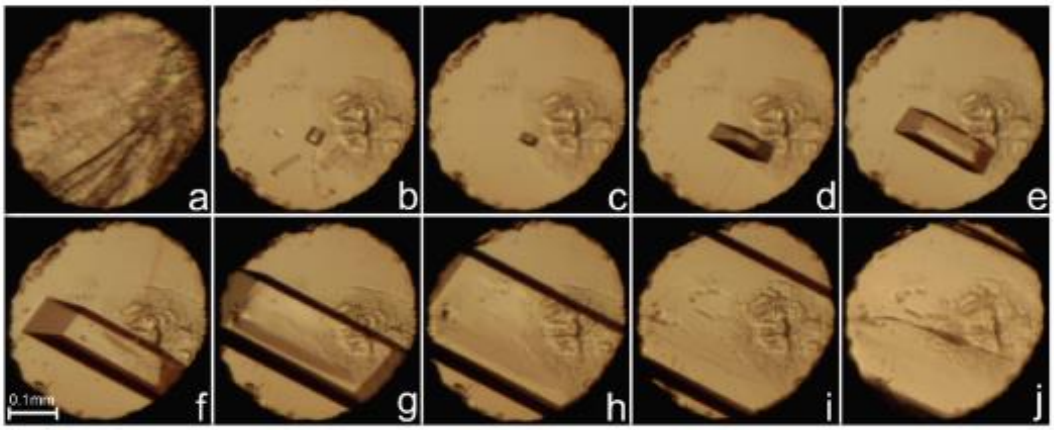

Figure S5. Stages of the **CB** single-crystal growth inside the DAC chamber: (a) polycrystalline mass grown isothermally at 298 K; (b) single crystals–liquid equilibrium at 453 K; (c) one crystal seed at 454 K; (d-i) the single crystal cooled to 372 K and (j) the single crystal filling the DAC chamber at 295 K and 3.70 GPa. The ruby chips, for pressure calibration, are located in the right part of the DAC.

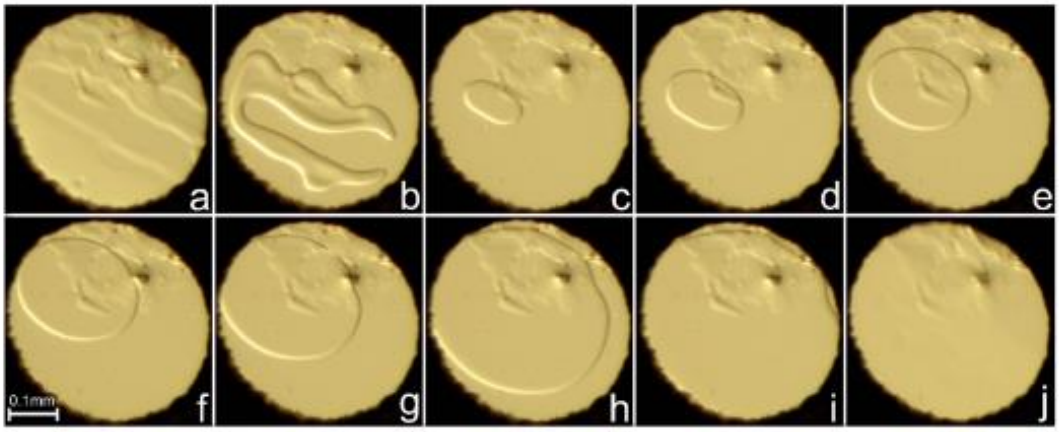

Figure S6. Stages of the **TB** single-crystal growth inside the DAC chamber: (a) single-crystal–liquid equilibrium at 308 K; (b) single-crystal–liquid equilibrium at 370 K; (c) one crystal seed at 375 K; (d-i) the single crystal cooled to 358 K and (j) the single crystal filling the DAC chamber at 295 K and 0.75 GPa. The ruby chip, for pressure calibration, lies in the central part of the DAC.

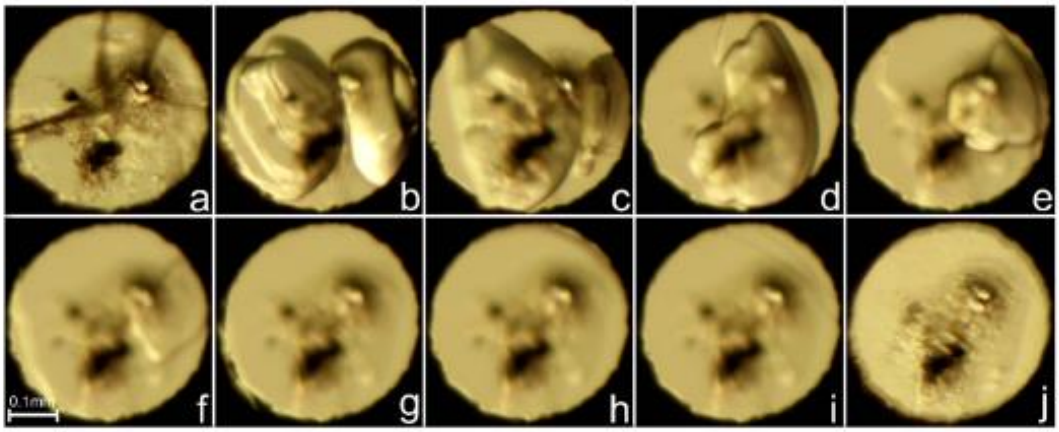

Figure S7. Stages of the **TB** single-crystal growth inside the DAC chamber: (a) single-crystals–liquid equilibrium at 298 K; (b) two single-crystals–liquid equilibrium at 445 K; (c) one crystal seed at 450 K; (d-i) the single crystal cooled to 430 K and (j) the single crystal filling the DAC chamber at 295 K and 1.10 GPa. The ruby chip, for pressure calibration, lies in the central part of the DAC.

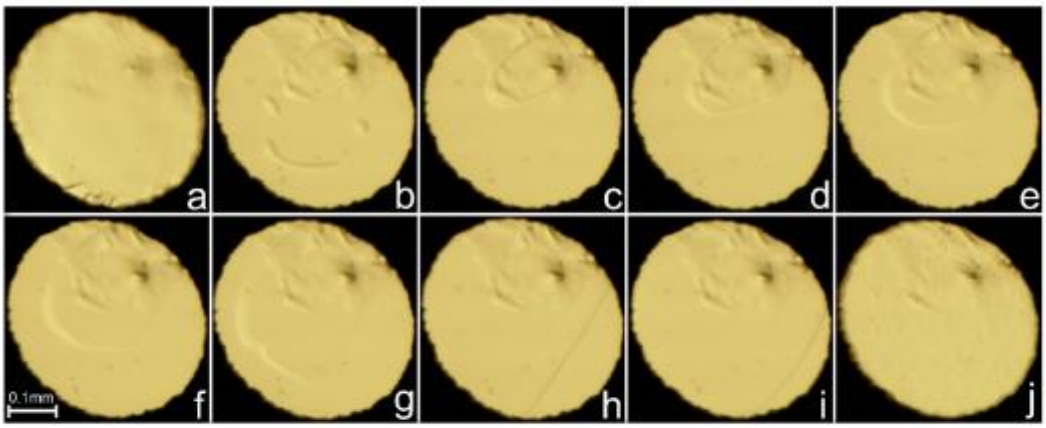

Figure S8. Stages of the **TB** single-crystal growth inside the DAC chamber: (a) single-crystal–liquid equilibrium at 343 K; (b) single-crystals–liquid equilibrium at 506 K; (c) one crystal seed at 507 K; (d-i) the single crystal cooled to 473 K and (j) the single crystal filling the DAC chamber at 295 K and 1.50 GPa. The ruby chip, for pressure calibration, lies in the central part of the DAC.

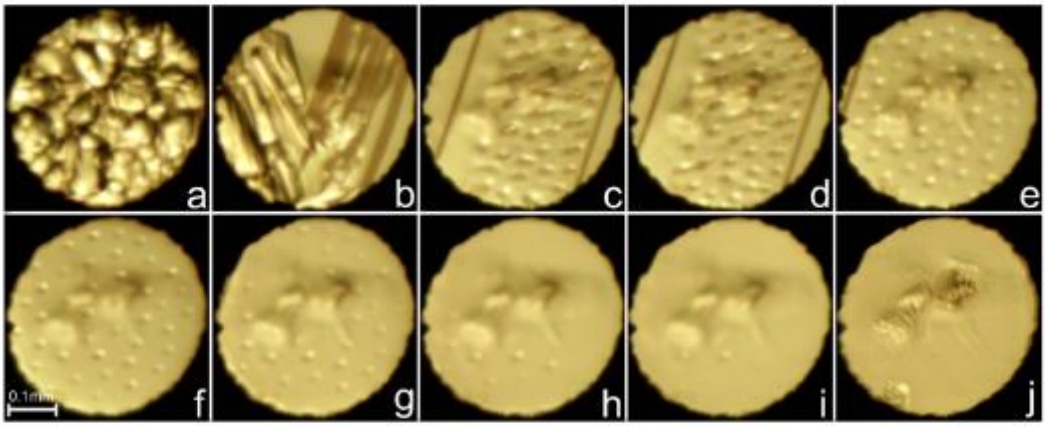

Figure S9. Stages of the **TB** single-crystal growth inside the DAC chamber: (a) polycrystalline mass grown isothermally at 298 K; (b) polycrystal–liquid equilibrium at 505 K; (c) one crystal seed at 510 K; (d-i) the single crystal cooled to 403 K and (j) the single crystal filling the DAC chamber at 295 K and 1.85 GPa. Three ruby chips, for pressure calibration, are located in the central part of the DAC.

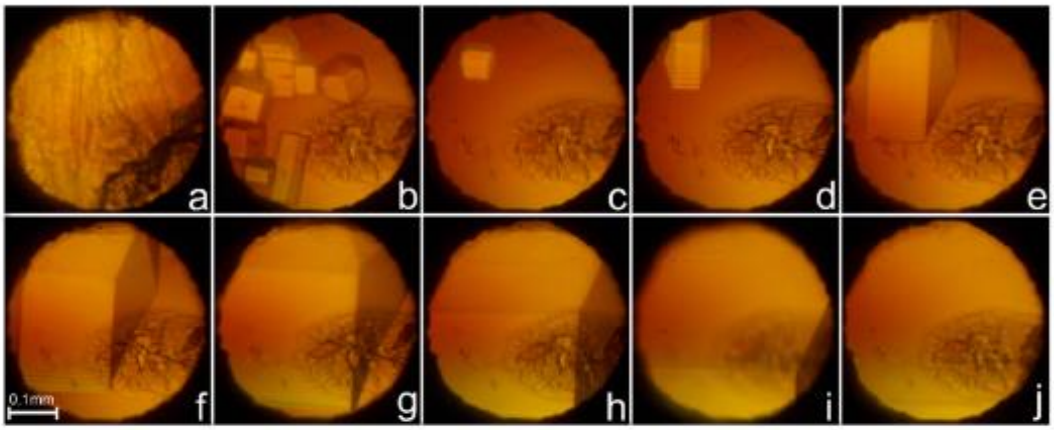

Figure S10. Stages of the **IB** single-crystal growth inside the DAC chamber (polarized-light mode): (a) polycrystalline mass grown isothermally at 298 K; (b) polycrystal–liquid equilibrium at 346 K; (c) one crystal seed at 347 K; (d-i) the single crystal cooled to 308 K and (j) the single crystal filling the DAC chamber at 295 K and 1.60 GPa. The ruby chip, for pressure calibration, is located in the central part of the DAC.

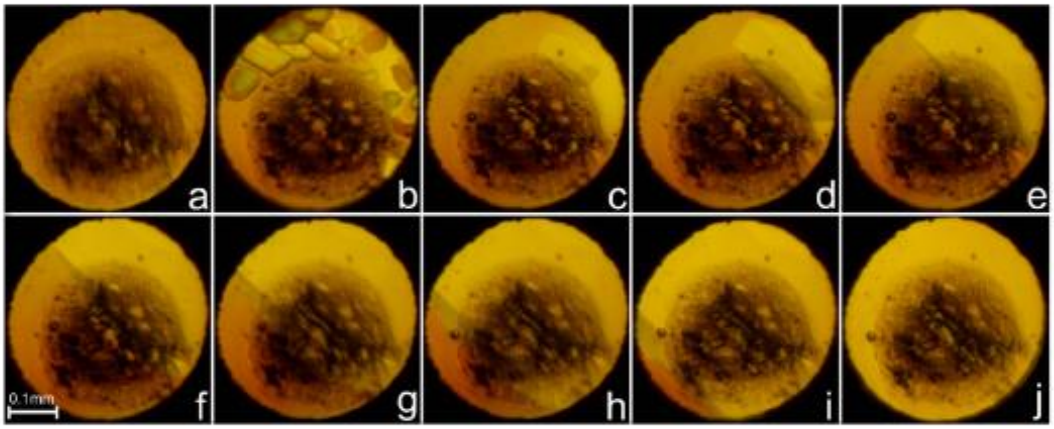

Figure S11. Stages of the **IB** single-crystal growth inside the DAC chamber (polarized-light mode): (a) polycrystalline mass grown isothermally at 298 K; (b) polycrystal–liquid equilibrium at 384 K; (c) one crystal seed at 385 K; (d-i) the single crystal cooled to 353 K and (j) the single crystal filling the DAC chamber at 295 K and 1.90 GPa. The ruby chip, for pressure calibration, is located in the central part of the DAC.

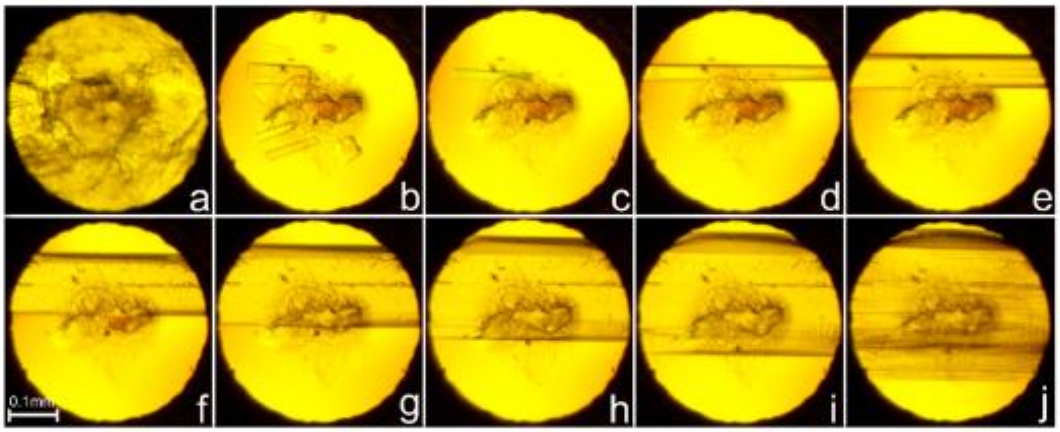

Figure S12. Stages of the **IB** single-crystal growth inside the DAC chamber (polarized-light mode): (a) polycrystalline mass grown isothermally at 298 K; (b) polycrystal–liquid equilibrium at 368 K; (c) one crystal seed at 369 K; (d-i) the single crystal cooled to 358 K and (j) the single crystal filling the DAC chamber at 295 K and 2.45 GPa. The ruby chip, for pressure calibration, is located in the central part of the DAC.

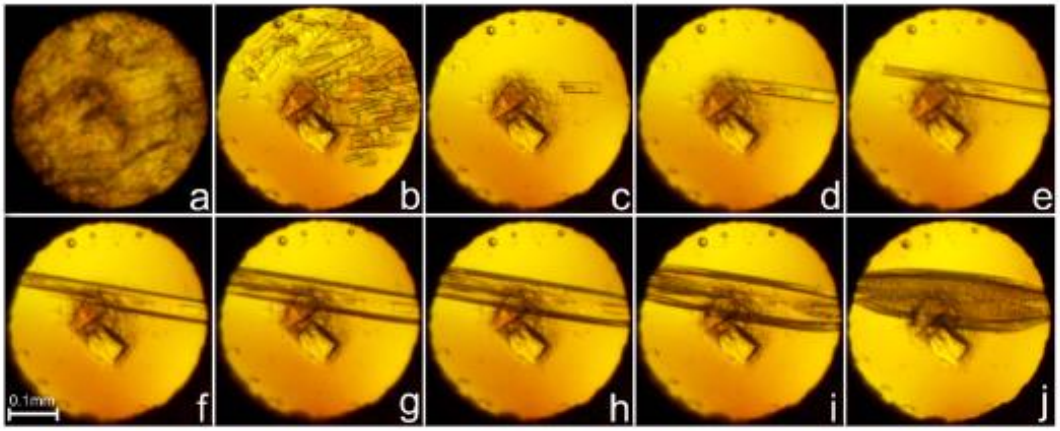

Figure S13. Stages of the **IB** single-crystal growth inside the DAC chamber (polarized-light mode): (a) polycrystalline mass grown isothermally at 298 K; (b) polycrystal–liquid equilibrium at 432 K; (c) one crystal seed at 433 K; (d-i) the single crystal cooled to 388 K and (j) the single crystal filling the DAC chamber at 295 K and 3.05 GPa. The ruby chip, for pressure calibration, is located in the central part of the DAC.

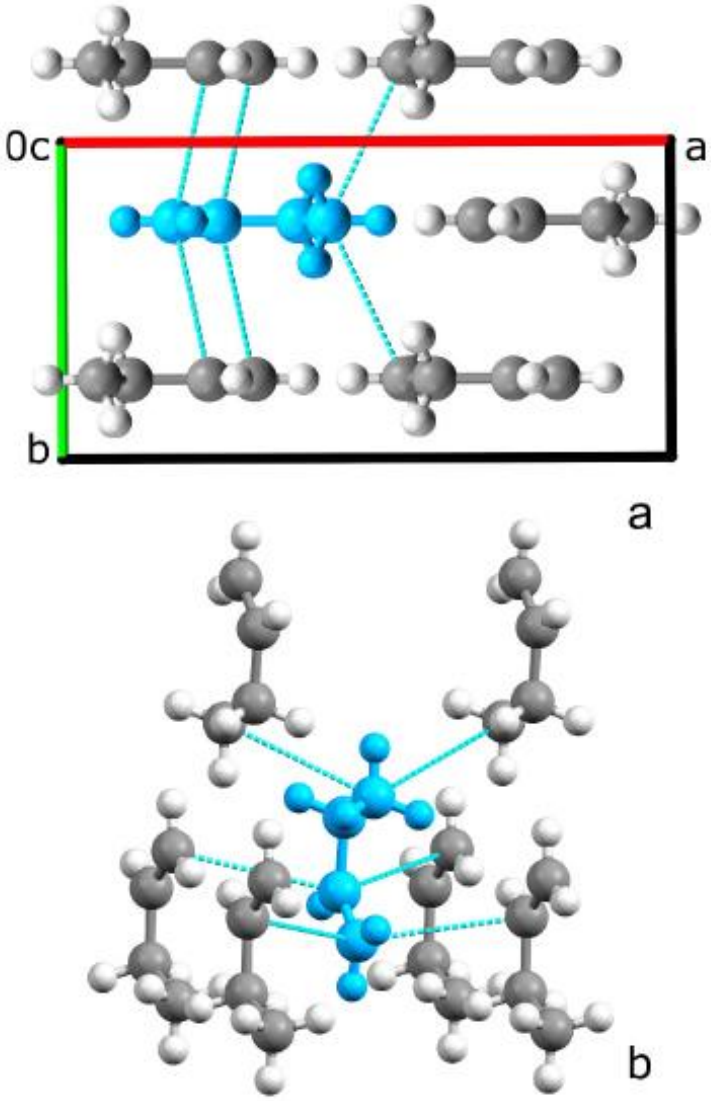

Figure S14. Crystal structure of **B** at 4.40 GPa/295 K viewed along ***c*** (a) and intermolecular C···C pattern (b). The shortest intermolecular C···C distances are indicated with blue dashed lines.

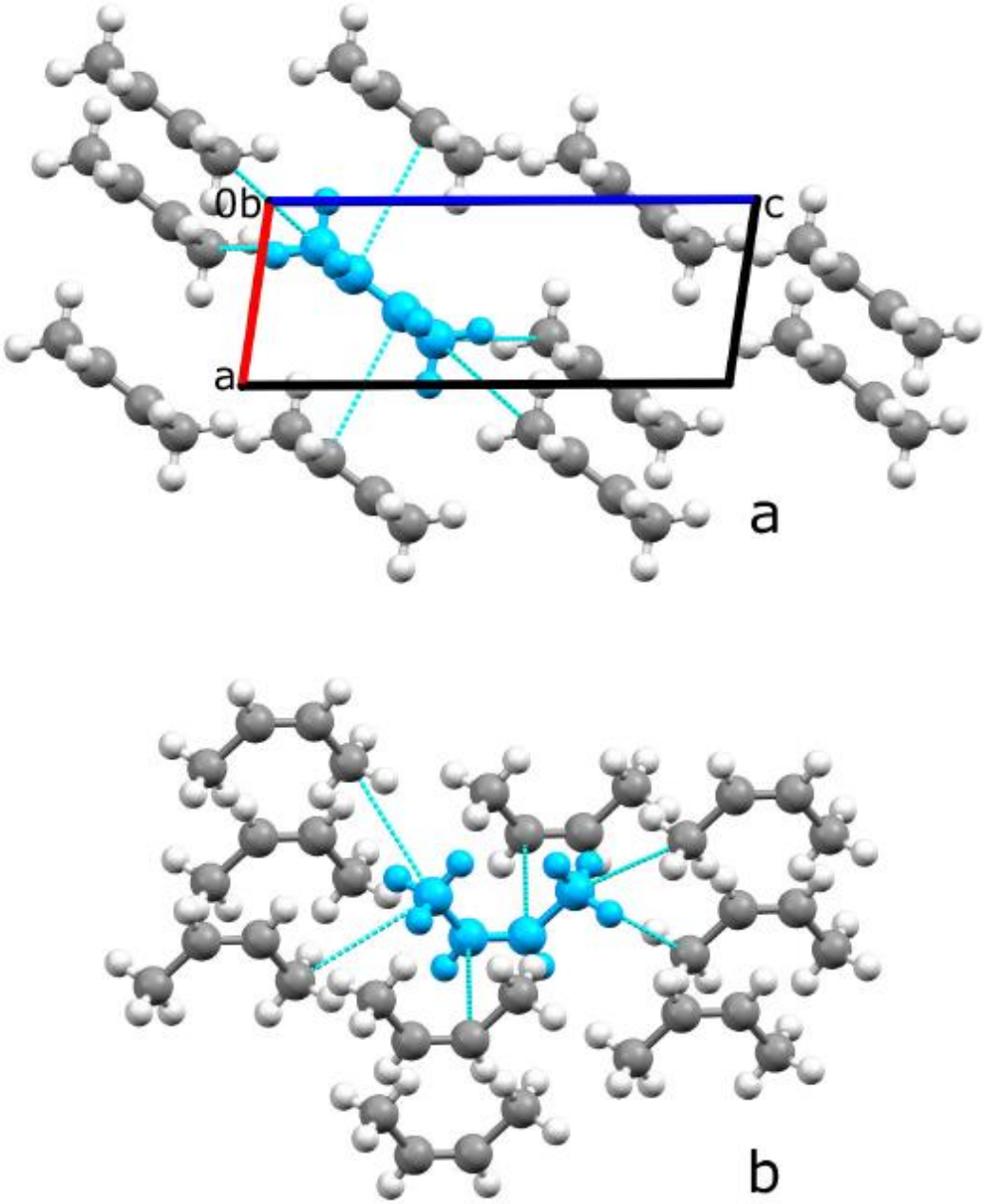

Figure S15. Crystal structure of **CB** at 1.75 GPa/295 K viewed along ***b*** (a) and intermolecular C···C pattern (b). The shortest intermolecular C···C distances are indicated with blue dashed lines.

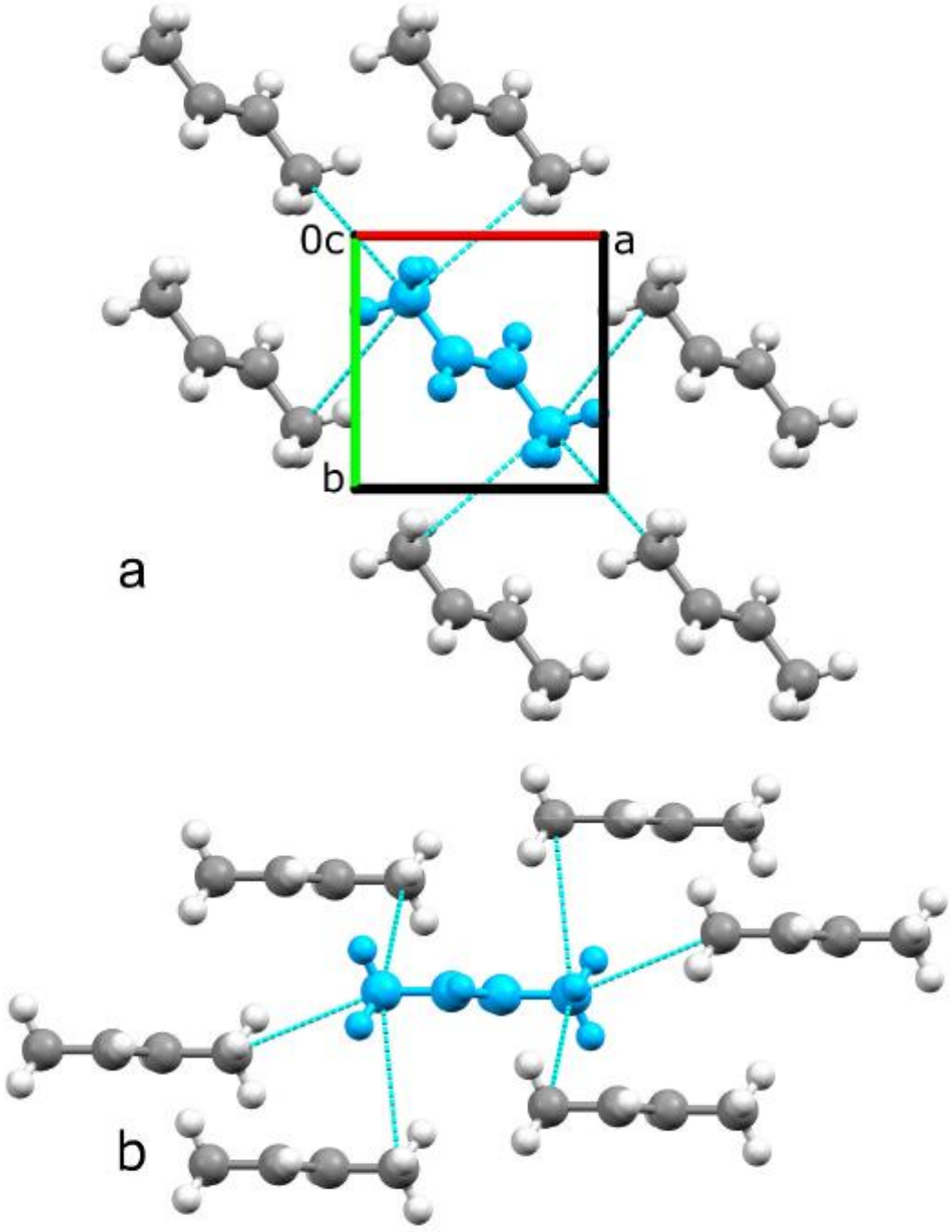

Figure S16. Crystal structure of **TB** at 0.75 GPa/295 K viewed along ***c*** (a) and intermolecular C···C pattern (b). The shortest intermolecular C···C distances are indicated with blue dashed lines.

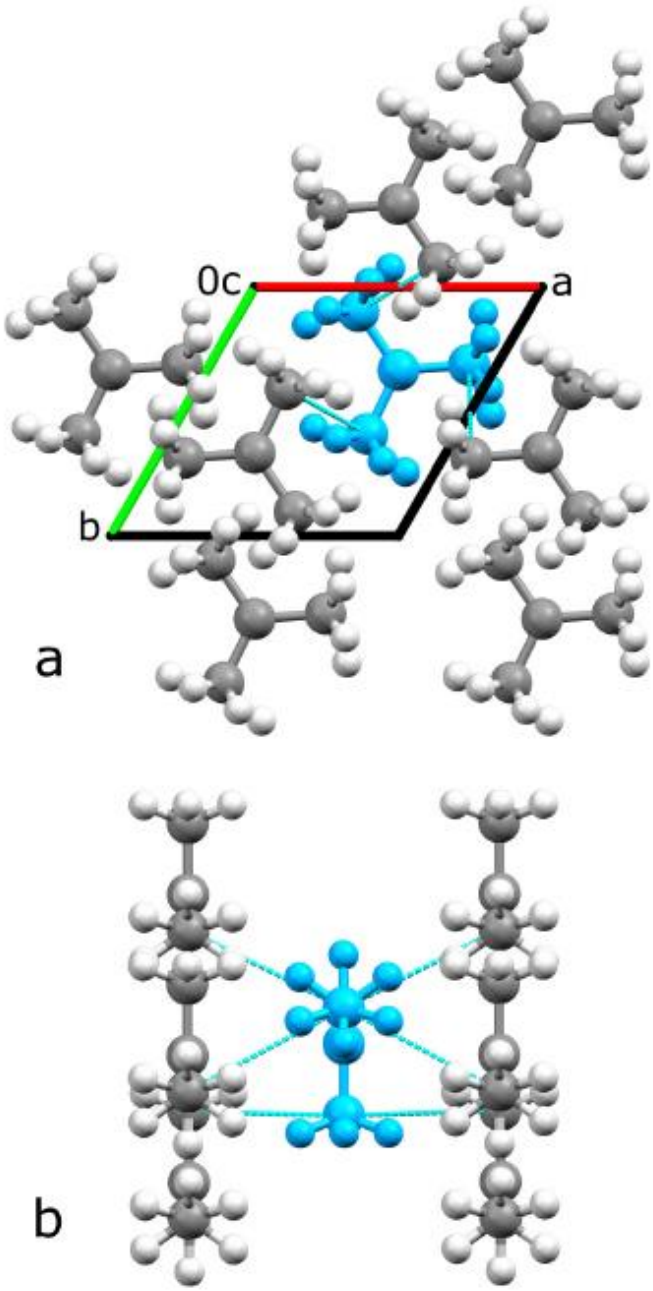

Figure S17. Crystal structure of **IB** at 1.90 GPa/295 K viewed along ***c*** (a) and intermolecular C···C pattern (b). The shortest intermolecular C···C distances are indicated with blue dashed lines.

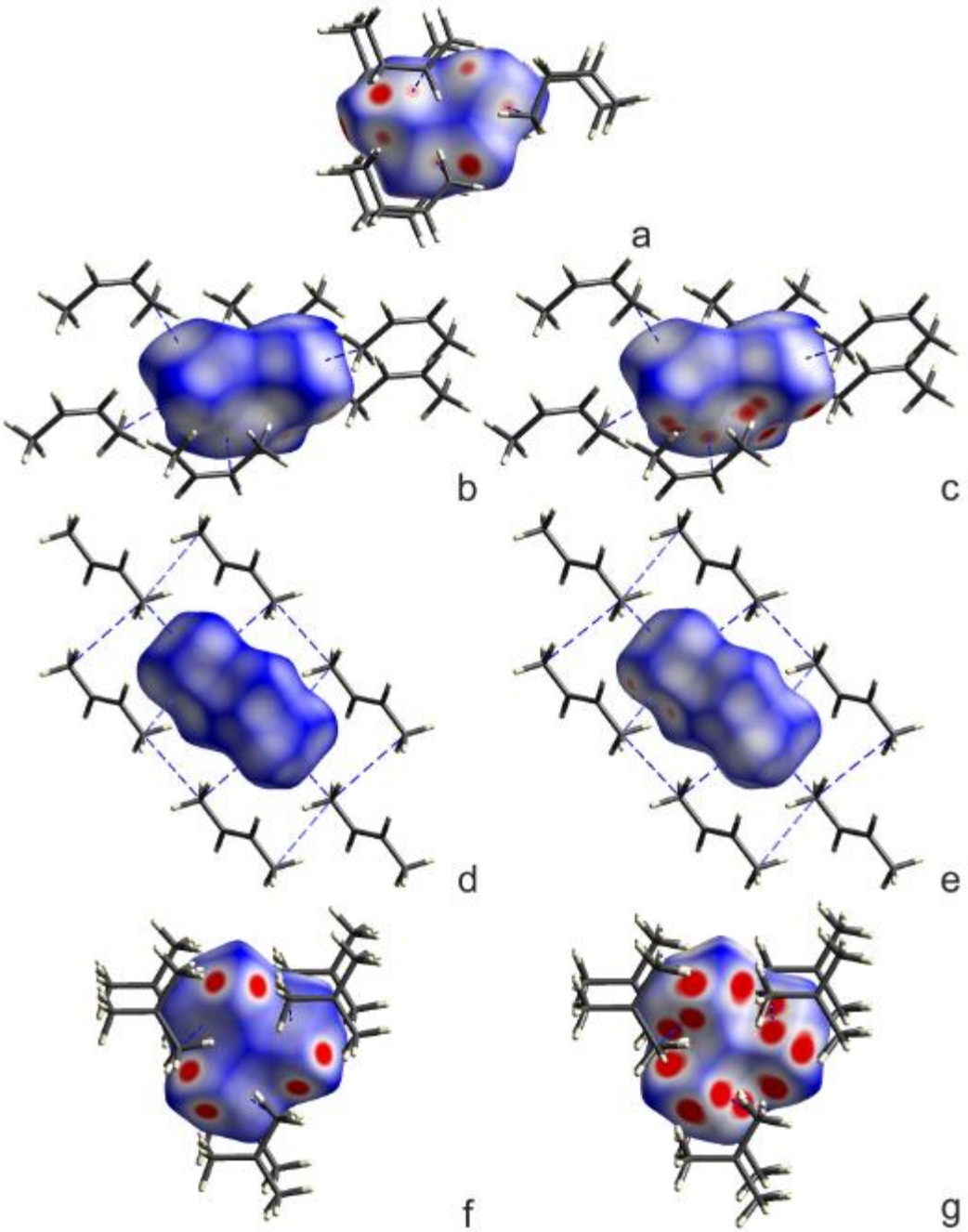

Figure S18. Hirshfeld surfaces (Spackman, P. R.; Turner, M. J.; McKinnon, J. J.; Wolff, S. K.; Grimwood, D. J.; Jayatilaka, D.; Spackman, M. A. *CrystalExplorer21*: a program for Hirshfeld surface analysis, visualization and quantitative analysis of molecular crystals, *J. Appl. Cryst.*, **2021**, *54*, 1006-1011) mapped with d_{norm} (from −0.1 to 0.7) of the butene isomers: **B** at 4.40 GPa/295 K (a), **CB** at 1.75 GPa/295 K (b), **CB** at 3.70 GPa/295 K (c), **TB** at 0.75 GPa/295 K (d), **TB** at 1.85 GPa/295 K (e), **IB** at 1.60 GPa/295 K (f), and **IB** at 3.05 GPa/295 K (g). The white, red and blue colors indicate contacts that are equal, shorter and longer, respectively, than the sums of the van der Waals radii of respective atoms.

Table S1. Crystal data and details of the refinement of **B** at 4.40 GPa/295 K.

	C_4H_8, **B**
Pressure (GPa)	4.40(2)
Formula weight	56.10
Crystal color	colorless
Crystal size (mm)	0.37x0.36x0.23
Crystal system	orthorhombic
Space group	*Pnma*
Unit cell dimensions	
a (Å)	11.364(4)
b (Å)	5.9132(10)
c (Å)	4.8370(7)
Volume (Å^3)	325.04(13)
Z, Z'	4, 1/2
D_x (g·cm^{-3})	1.146
Wavelength MoKα, λ (Å)	0.71073
Absorption coefficient (mm^{-1})	0.063
F(000) (e)	128
2Θ max (°)	53.34
Min./Max. indices h, k, l	-9/9, -6/7, -5/5
Reflections collected/unique	1749/245
R_{int} (all data)	0.0532
Observed reflections (I>2σ(I))	174
Data/restraints/parameters	245/0/25
Goodness of fit on F^2	1.120
Final R_1 indices (I>2σ(I))	0.0486
R_1/wR_2 indices (all data)	0.0793/0.1331
$\Delta\sigma_{max}$, $\Delta\sigma_{min}$ (e·Å^{-3})	0.17/-0.15
Weighting scheme: x; y[a]	0.0642/0.04

[a] $w=1/(\sigma^2(Fo^2)+x^2P^2+yP)$, where $P=(Fo^2+2Fc^2)/3$

Table S2. Crystal data and details of the refinements of **CB** at 1.75, 2.25, 3.05 and 3.70 GPa (all at 295 K).

	C_4H_8, CB	C_4H_8, CB	C_4H_8, CB	C_4H_8, CB
Pressure (GPa)	1.75(2)	2.25(2)	3.05(2)	3.70(2)
Formula weight	56.10	56.10	56.10	56.10
Crystal color	colorless	colorless	colorless	colorless
Crystal size (mm)	0.34x0.34x0.27	0.30x0.28x0.26	0.34x0.30x0.25	0.32x0.29x0.24
Crystal system	monoclinic	monoclinic	monoclinic	monoclinic
Space group	*C*2/*c*	*C*2/*c*	*C*2/*c*	*C*2/*c*
Unit cell dimensions				
a (Å)	3.9161(13)	3.8656(7)	3.8094(2)	3.7608(11)
b (Å)	9.174(3)	9.0946(5)	9.0023(3)	8.9308(9)
c (Å)	10.2411(12)	10.126(3)	9.932(5)	9.9392(6)
β (°)	98.87(2)	98.85(3)	98.474(16)	98.579(12)
Volume (Å^3)	363.51(18)	351.74(13)	336.88(17)	330.09(10)
Z, *Z'*	4, 1/2	4, 1/2	4, 1/2	4, 1/2
D_x (g·cm^{-3})	1.025	1.059	1.106	1.129
Wavelength MoKα, λ (Å)	0.71073	0.71073	0.71073	0.71073
Absorption coefficient (mm^{-1})	0.056	0.058	0.061	0.062
F(000) (e)	128	128	128	128
2Θ max (°)	51.33	52.86	53.10	52.55
Min./Max. indices *h*, *k*, *l*	-3/3, -7/7, -12/12	-3/3, -11/11, -8/8	-4/4, -11/10, -4/4	-2/2, -10/10, -12/12
Reflections collected/unique	597/104	1023/144	955/119	860/151
R_{int} (all data)	0.0576	0.0261	0.0193	0.0197
Observed reflections (I>2σ(I))	94	131	108	136
Data/restraints/parameters	104/0/20	144/0/20	119/0/20	151/0/20
Goodness of fit on F^2	1.205	1.114	1.192	1.117
Final R_1 indices (I>2σ(I))	0.0686	0.0412	0.0323	0.0396
R_1/wR_2 indices (all data)	0.0733/0.1867	0.0449/0.1161	0.0365/0.0904	0.0450/0.1137
$\Delta\sigma_{max}$, $\Delta\sigma_{min}$ (e·Å^{-3})	0.11/-0.13	0.10/-0.09	0.07/-0.06	0.09/-0.11
Weighting scheme: x; y[a]	0.1193/0.23	0.0768/0.11	0.0539/0.10	0.0719/0.11

[a] $w=1/(\sigma^2(Fo^2)+x^2P^2+yP)$, where $P=(Fo^2+2Fc^2)/3$

Table S3. Crystal data and details of the refinements of **TB** at 0.75, 1.10, 1.50 and 1.85 GPa (all at 295 K).

	C_4H_8, TB	C_4H_8, TB	C_4H_8, TB	C_4H_8, TB
Pressure (GPa)	0.75(2)	1.10(2)	1.50(2)	1.85(2)
Formula weight	56.10	56.10	56.10	56.10
Crystal color	colorless	colorless	colorless	colorless
Crystal size (mm)	0.31x0.29x0.27	0.26x0.24x0.24	0.32x0.30x0.25	0.27x0.26x0.24
Crystal system	monoclinic	monoclinic	monoclinic	monoclinic
Space group	$P2_1/c$	$P2_1/c$	$P2_1/c$	$P2_1/c$
Unit cell dimensions				
a (Å)	5.150(6)	5.121(4)	5.076(4)	5.0525(11)
b (Å)	5.0833(4)	4.9631(2)	4.9040(2)	4.864(6)
c (Å)	7.7661(12)	7.5648(8)	7.4399(10)	7.374(4)
β (°)	104.24(5)	102.57(3)	102.04(4)	101.84(3)
Volume (Å^3)	197.1(2)	187.67(14)	181.12(14)	177.4(2)
Z, Z'	2, 1/2	2, 1/2	2, 1/2	2, 1/2
D_x (g·cm^{-3})	0.945	0.993	1.029	1.050
Wavelength MoKα, λ (Å)	0.71073	0.71073	0.71073	0.71073
Absorption coefficient (mm^{-1})	0.052	0.054	0.056	0.057
F(000) (e)	64	64	64	64
2Θ max (°)	56.62	51.80	53.27	54.31
Min./Max. indices h, k, l	-2/2, -6/6, -10/10	-2/2, -6/6, -9/9	-2/2, -6/6, -9/9	-6/6, -3/3, -8/8
Reflections collected/unique	1340/159	1042/106	971/114	640/107
R_{int} (all data)	0.0357	0.0228	0.0167	0.0490
Observed reflections (I>2σ(I))	107	98	105	79
Data/restraints/parameters	159/0/20	106/0/20	114/0/20	107/0/20
Goodness of fit on F^2	1.113	1.156	1.250	1.179
Final R_1 indices (I>2σ(I))	0.0773	0.0444	0.0317	0.0582
R_1/wR_2 indices (all data)	0.1184/0.1632	0.0468/0.1342	0.0371/0.0918	0.0780/0.1139
$\Delta\sigma_{max}$, $\Delta\sigma_{min}$ (e·Å^{-3})	0.16/-0.11	0.09/-0.05	0.06/-0.06	0.08/-0.09
Weighting scheme: x; y[a]	0.0318/0.18	0.0727/0.05	0.0404/0.03	0.0134/0.14

[a] $w=1/(\sigma^2(Fo^2)+x^2P^2+yP)$, where $P=(Fo^2+2Fc^2)/3$

Table S4. Crystal data and details of the refinements of **IB** at 1.60, 1.90, 2.45 and 3.05 GPa (all at 295 K).

	C_4H_8, IB	C_4H_8, IB	C_4H_8, IB	C_4H_8, IB
Pressure (GPa)	1.60(2)	1.90(2)	2.45(2)	3.05(2)
Formula weight	56.10	56.10	56.10	56.10
Crystal color	colorless	colorless	colorless	colorless
Crystal size (mm)	0.34x0.33x0.27	0.40x0.38x0.26	0.37x0.27x0.25	0.33x0.24x0.09
Crystal system	hexagonal	hexagonal	hexagonal	hexagonal
Space group	$P6_3/m$	$P6_3/m$	$P6_3/m$	$P6_3/m$
Unit cell dimensions				
a (Å)	5.845(6)	5.819(2)	5.7701(9)	5.75(3)
c (Å)	6.344(8)	6.281(3)	6.2055(10)	6.131(4)
Volume (Å^3)	187.7(4)	184.20(17)	178.93(6)	175.4(18)
Z, Z'	2, 1/6	2, 1/6	2, 1/6	2, 1/6
D_x (g·cm^{-3})	0.993	1.012	1.041	1.062
Wavelength MoKα, λ (Å)	0.71073	0.71073	0.71073	0.71073
Absorption coefficient (mm^{-1})	0.054	0.055	0.057	0.058
F(000) (e)	64	64	64	64
2Θ max (°)	51.02	52.67	55.13	53.42
Min./Max. indices h, k, l	-4/4, -7/7, -3/3	-5/5, -7/7, -5/5	-6/6, -3/3, -7/7	-4/4, -7/7, -7/7
Reflections collected/unique	117/43	663/82	736/66	562/61
R_{int} (all data)	0.0946	0.0617	0.0334	0.0676
Observed reflections (I>2σ(I))	14	71	58	38
Data/restraints/parameters	43/0/10	82/0/10	66/0/10	61/0/10
Goodness of fit on F^2	1.127	1.224	1.199	1.179
Final R_1 indices (I>2σ(I))	0.0984	0.0648	0.0479	0.0466
R_1/wR_2 indices (all data)	0.1940/0.2571	0.0776/0.1857	0.0533/0.1393	0.0915/0.0837
$\Delta\sigma_{max}$, $\Delta\sigma_{min}$ (e·Å^{-3})	0.05/-0.06	0.13/-0.14	0.11/-0.14	0.14/-0.08
Weighting scheme: x; y[a]	0.1063/0.01	0.0754/0.10	0.0684/0.04	0/0.09

[a] $w=1/(\sigma^2(Fo^2)+x^2P^2+yP)$, where $P=(Fo^2+2Fc^2)/3$

Paper P5

Mechanism of Isostructural Phase Transition in Isobutane

Sacharczuk, N.; Kuleczka, B.; Olejniczak, A.; Katrusiak, A.; Podsiadło, M.

J. Phys. Chem. C **2025**, 129, 31, 14196−14203

THE JOURNAL OF PHYSICAL CHEMISTRY C
A JOURNAL OF THE AMERICAN CHEMICAL SOCIETY
pubs.acs.org/JPCC

Article

Mechanism of Isostructural Phase Transition in Isobutane

Natalia Sacharczuk, Bernadetta Kuleczka, Anna Olejniczak, Andrzej Katrusiak, and Marcin Podsiadło*

Cite This: J. Phys. Chem. C 2025, 129, 14196−14203

ABSTRACT: Gaseous isobutane, when isothermally compressed at 295 K, condenses into a liquid at 0.32 MPa and freezes either at 1.41 GPa into the crystalline phase α or at 1.55 GPa into phase β. Their structures are similar, and an isostructural transition has been observed, preserving the space-group symmetry *Pnma*, while displaying considerable hysteresis and reversed relation of the crystal volumes. The compression of the two new phases has been analyzed through *in situ* isothermal and isochoric crystallizations, X-ray diffraction structural determinations, and a description of subtle differences in the molecular arrangement. The implications of this phase transition have been discussed in the context of molecular dynamics, emphasizing the interplay between pressure, temperature, and structural changes. The volume relations have rationalized the exemption of isobutane and *n*-butane isomers from Carnelley's rule, reflecting molecular close packing and interactions. However, the isothermal crystallization of isobutane and *n*-butane proceeds according to Carnelley's rule; i.e., the higher-symmetric isomer, isobutane, requires lower pressure than the lower-symmetric *n*-butane, despite its markedly higher density.

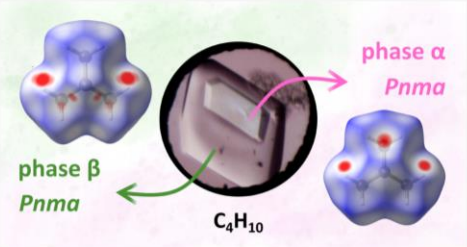

INTRODUCTION

Isobutane (2-methylpropane, C_4H_{10}) is a gaseous, saturated, branched-chain hydrocarbon and one of the two isomers of butane. It is the smallest hydrocarbon displaying isomorphism. The structural differences between isobutane and *n*-butane strongly influence their physical and chemical properties, significantly affecting their practical applications and behavior under various conditions. Isobutane and *n*-butane defy Carnelley's rule,[1] which states that the isomers of higher molecular symmetry melt at higher temperatures.[2] The isobutane molecule is C_{3v}-symmetric, and the predominant conformer, trans of *n*-butane, is C_{2h}-symmetric; the staggered conformers, gauche+/gauche-, are C_2-symmetric. The ideal position of the terminal methyl rotors was assumed for assigning these symmetries. Nonetheless, isobutane freezes at 113.56 K and boils at 261.45 K;[3] these temperatures are significantly lower than those for *n*-butane: 133−139 and 272.65 K, respectively.[3] It is plausible that the unexpectedly low melting point of isobutane originates from a weaker aggregation of molecules, which has not yet been verified due to the lack of information about its crystal structure.

Both butane isomers play important roles in petrochemical industries and are widely found in natural gas deposits[4] and Earth's atmosphere.[5,6] Interest in hydrocarbons such as isobutane has grown due to their potential presence on outer planets and their moons. Isobutane is an important raw material in the petrochemical industry, and it is commonly used in the production of propylene glycols,[7] oxides, polyurethane foams,[8] and resins.[9] Furthermore, isobutane is widely used as an aerosol propellant, aviation fluid additive, household and industrial fuel, solvent, and refrigerant.[10] It is the main substitute for refrigerant Freon gases, which endanger the Earth's ozone layer.

Despite its many applications, high-pressure studies of isobutane remain scarce. High-quality thermodynamic data are relatively limited for butanes, especially at higher pressures. So far, there have been only a few high-pressure studies of isobutane[11] and *n*-butane,[12] in contrast to extensive research on lighter and heavier alkanes such as methane,[13−15] ethane,[15−17] propane,[12,18] *n*-pentane,[19−21] *n*-hexane,[5,22,23] and *n*-heptane.[24,25] The lack of high-pressure data for isobutane represents a significant gap, especially given the increasing scientific interest in the properties of hydrocarbons relevant to extreme geological and astrophysical environments. Moreover, insights from high-pressure studies of other molecular solids demonstrate that pressure can reveal unexpected polymorphism and structural behaviors, often governed by kinetic factors.[26] Here, we present a high-pressure investigation of isobutane aimed at measuring its compressibility and determining its crystal structure, phase transitions, and the

Received: May 8, 2025
Revised: July 8, 2025
Accepted: July 14, 2025
Published: July 25, 2025

https://doi.org/10.1021/acs.jpcc.5c03155
J. Phys. Chem. C 2025, 129, 14196−14203

structural origins of differences between the properties of isomers.

EXPERIMENTAL SECTION

2-Methylpropane, a gas under ambient conditions (99%), purchased from Linde Gaz Polska, was used as received. All high-pressure crystallizations and single-crystal X-ray diffraction (SCXRD) measurements were conducted in a modified Merrill-Bassett diamond-anvil cell (DAC).[27] The DACs included a steel gasket 0.3 mm thick with a hole 0.4 mm in diameter, and the diamond culet sizes in the DACs were 0.75 mm.

The high-pressure *in situ* crystallizations were performed in DACs under both isothermal and isochoric conditions. When the polycrystalline mass appeared, a single crystal was grown isothermally. This process involves melting the polycrystalline mass, except for one crystallite, by increasing the volume of the high-pressure chamber. Then, the volume of the pressure chamber was reduced, allowing a single crystal to grow and eventually fill the entire volume of the chamber. Afterward, the pressure was increased to ensure crystal stability during the diffraction measurement.

For the isochoric conditions, the DAC and the polycrystalline mass inside the chamber were heated by using a hot-air gun until all but one grain melted. Then, the DAC was slowly cooled to room temperature, and the single crystal samples grew, eventually filling the entire volume of the chamber. The morphology of the crystals obtained through isothermal and isochoric crystallization, which indicates the presence of the two polymorphic forms referred to hereafter as phase α and β, is illustrated in Figure 1. We examined phase α from 1.86 GPa, the lowest pressure at which the sample crystals were securely fixed in the DAC chamber at room temperature (295 K), up to 3.10 GPa, and phase β from 1.83 up to 4.10 GPa (Tables 1).

The infrared laser thermometer was used to measure the temperature inside the DAC chamber. At each pressure point, single crystals were grown *in situ*. The pressure was calibrated by the ruby fluorescence method[28,29] using a Photon Control spectrometer with an accuracy of 0.02 GPa. The calibration was performed before and after the diffraction measurements.

Diffractometers Xcalibur EOS and ATLAS were used for high-pressure SCXRD studies. The DAC was centered by the gasket-shadow method.[30] The *CrysAlisPro*[31] program suite was used for data collection, determination of the *UB* matrices, and data reduction. All data were corrected for Lorentz, polarization, and absorption effects. Programs *OLEX2-1.5*,[32] *SHELXT*,[33] and *SHELXL*[34] were used to solve the structures by direct methods and to perform full-matrix least-squares refinement of the models. Anisotropic temperature factors were applied to carbon atoms. The H atoms were positioned based on molecular geometry, with C−H distances set to 0.98 Å for the −CH group and 0.96 Å for the $-CH_3$ group, and their U_{iso} factors were constrained to 1.2 and 1.5 times U_{eq} of their carriers, respectively. The experimental and crystal data refinement details are summarized in Table 1 and Tables S1 and S2.

RESULTS AND DISCUSSION

Under high pressure, isobutane crystallizes into two distinct phases, labeled α and β, freezing at 1.41 and 1.55 GPa, respectively. Both phases adopt the orthorhombic symmetry of the space group *Pnma*. Phases α and β coexist in the pressure range from 1.55 to 3.10 GPa at least. The nucleation of phase α is favored by a temperature around 273 K, while even at room temperature, the crystal growth of phase α is more favored than that of phase β, and the latter slowly disappears as all the compound is "consumed" by phase α (Figure 1). This indicates that close to the crystallization pressure, phase α is more stable than phase β. This conclusion is consistent with the lower melting pressure of phase α compared to phase β, 1.41 and 1.55 GPa, respectively, and with the higher density of phase α than that of phase β below 1.64 GPa. A schematic diagram illustrating the distinct crystalline phases α and β obtained under different crystallization protocols is presented in Figure 2. Based on experimental evidence, e.g., 6-azido-8-methyl[1,2,4]triazolo[4,3-*b*]pyridazine[35] and ruthenocene,[36] it is often assumed that denser phases are more stable both under ambient and high-pressure conditions. However, there are numerous exceptions to this rule under ambient pressure. For example, the stable low-pressure phases of paracetamol,[37,38] imidazole,[39] benzimidazole,[40] 2-methylbenzimidazole,[41] osmocene,[42] sodium tartrate monohydrate,[43] and others are less dense than the coexisting metastable high-pressure phases. In the pressure range of the high-pressure phase stability, the high-density phases of all of these compounds become more stable. A unique case of recently revealed pressure dependence of DL-menthol shows that low-density phases can be more stable, equally under ambient-pressure and high-pressure conditions.[44] The extensive hysteresis between the isobutane phases α and β hampers the exact determination of the stability

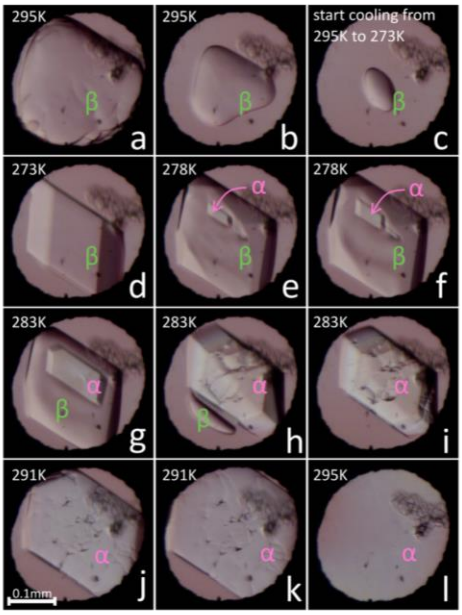

Figure 1. Isobutane, β phase in equilibrium with the liquid (a). Pressure was reduced until one small crystal of the β phase remained (a−c). The DAC rapidly cooled to 273 K. The β-phase crystal grew slightly at this time (d), and then, the α-phase crystal appeared (e). The temperature inside the DAC was about 278 K (e−f) and then about 283 K; at that time, the α-phase crystal was growing (e−j), while the β phase was melting (e−h). Then, the pressure was slowly increased to 1.99 GPa, allowing the single crystal of phase α to grow and fill the entire volume of the DAC chamber (k−l).

https://doi.org/10.1021/acs.jpcc.5c03155
J. Phys. Chem. C 2025, 129, 14196−14203

Table 1. Selected Crystal Data for the Lowest and Highest Pressures of Phases α and β at 295 K

	phase α	phase α	phase β	phase β
p (GPa)	1.86(2)	3.10(2)	1.83(2)	4.10(2)
crystal system	orthorhombic	orthorhombic	orthorhombic	orthorhombic
space group	*Pnma*	*Pnma*	*Pnma*	*Pnma*
a (Å)	7.5484(3)	7.329(4)	7.8584(16)	7.4745(3)
b (Å)	9.041(7)	8.8578(14)	8.9564(4)	8.6798(10)
c (Å)	5.8341(2)	5.7315(8)	5.6557(2)	5.4895(5)
V (Å^3)	398.2(3)	372.1(2)	398.06(8)	356.14(5)
Z, Z'	4, 0.5	4, 0.5	4, 0.5	4, 0.5
D_x (g·cm^{-3})	0.970	1.038	0.970	1.084
R_1 ($F^2 > 2\sigma(F^2)$)	0.0476	0.0651	0.0477	0.0435
R_{int} (all data)	0.0364	0.0669	0.0366	0.0346

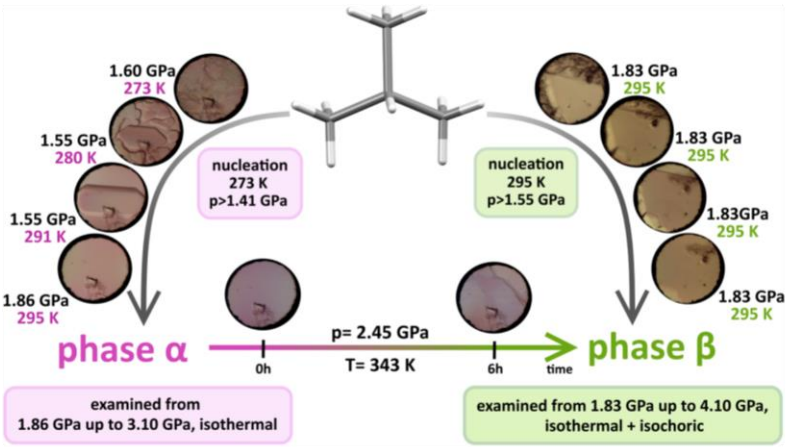

Figure 2. Schematic representation of isobutane phases α and β formed via high-pressure nucleation and thermal transformation, depending on the applied temperature−pressure conditions.

regions, but the 'parasitic' growth of phase α below 1.55 GPa, the contributions of both phases to the Gibbs free energy and the thermally induced transition gives insights into the thermodynamic landscape of this compound. Finally, we managed to compress phase α to 3.10 GPa, while phase β could be compressed to at least 4.10 GPa, indicating that phase β is the high-pressure form, most likely stable above 1.64 GPa when it becomes denser than phase α (Figure 3).

Previous Raman spectroscopy studies at ambient temperature on isobutane, by Kudryavtsev et al.,[11] identified two separate phase transitions, one occurring between 1.6(5) GPa and 2.7(5) GPa and a subsequent one between 2.7(5) GPa and 3.5(5) GPa. The freezing pressure points, determined by us at 295 K, for phase α at 1.41(2) GPa and phase β at 1.56(2) GPa both correspond, within experimental errors, to the pressure-induced freezing observed by Raman spectroscopy in the 1.6−2.7(5) GPa range. According to the Raman study,[11] another solid−solid phase transition at ambient temperature is reported between 2.7(5) and 3.5(5) GPa. However, in our experiments, the isothermal compression of phase α to 3.10(2) GPa and phase β to 4.10(2) GPa revealed no phase transition involving symmetry changes. We only observed the transition from phase α to phase β, caused by temperature, when the crystal of phase α at 2.45 GPa was heated for 6 h at 343 K. X-ray diffraction data confirmed that phase α fully transformed to phase β during this period (Figures 2 and S7).

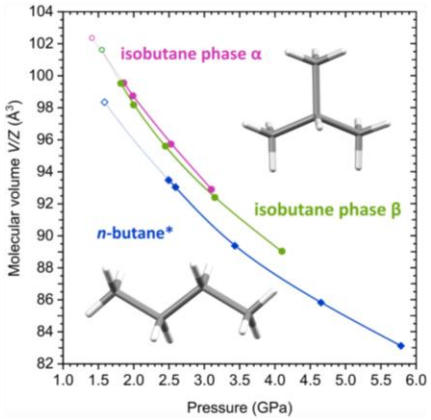

Figure 3. Molecular volume (V/Z) of isobutane phases α (pink), β (green) and *n*-butane* (blue)[12] plotted as a function of pressure. Open circles and diamonds indicate the extrapolated volume values at the observed freezing-pressure points. The estimated standard deviations (ESDs) are smaller than the plotted symbols.

It is remarkable that despite strong intermolecular interactions in this classical molecular compound, its polymorphs α and β coexist over a wide pressure range,

https://doi.org/10.1021/acs.jpcc.5c03155
J. Phys. Chem. C 2025, 129, 14196−14203

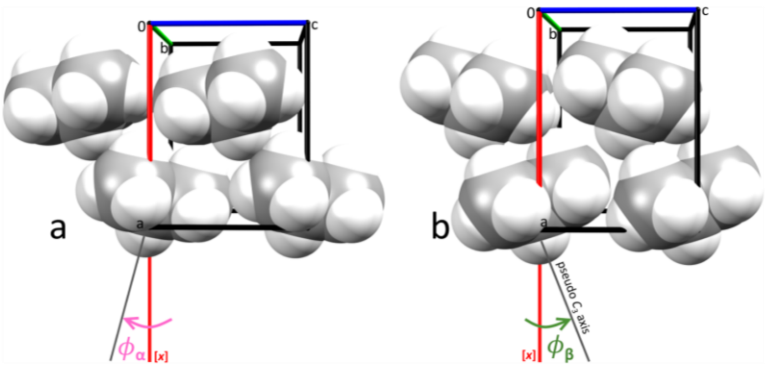

Figure 4. Autostereographic projections of isobutane corresponding structural portions of four molecules in phases (a) α at 1.99 GPa and (b) β at 2.00 GPa.

Table 2. Tilt Angle ϕ between the Crystal Axis $[x]$ and Molecular Pseudo-C_3 Axis in Phases α and β, Order Parameter η (eq 1), the Volume Differences δV_m, and the Work Contributions $p\delta V_m$ to the Free Energy Changes $\delta G = p\delta V_m$[a]

phase	p (GPa)	tilt ϕ (°)	η	V (Å^3)	V_m (Å^3)	δV_m (Å^3)	$p\delta V_m$ (kJ mol^{-1})
α	**1.41**	12.45	0.956	409.00	102.25	0	0
	1.86	12.94	0.993	398.20	99.55	−2.70	3.049
	1.99	13.27	1.019	395.00	98.75	−3.50	4.215
	2.53	13.15	1.009	382.90	95.73	−6.52	9.996
	3.10	13.33	1.023	372.10	93.03	−9.22	17.251
β	**1.55**	−15.48	−0.980	406.20	101.55	−0.70	0.662
	1.83	−15.49	−0.980	398.06	99.52	−2.73	3.024
	2.00	−15.74	−0.996	392.69	98.17	−4.08	4.924
	2.45	−15.67	−0.992	382.40	95.60	−6.65	9.839
	3.15	−16.14	−1.021	369.47	92.37	−9.88	18.769
	4.10	−16.30	−1.031	356.14	89.04	−13.21	32.656

[a]Values for 1.41 and 1.55 GPa are extrapolated.

starting from their formation at about 1.5 GPa to at least 3.1 GPa. Both phases adopt the same space group type and exhibit similar unit-cell parameters (Table 1). Our SCXRD measurements show that initially, the unit-cell volume of phase α is lower until 1.64 GPa, at which point it becomes higher than that of phase β (Figure 3). The other isomer of butane, *n*-butane, crystallizes at 1.60 GPa.[12] Across the entire range of studied pressures, *n*-butane is denser than phases α and β of isobutane (Figure 3).

The structures of phases α and β are clearly related, as marked by the same space-group type, similar unit-cell dimensions (Table 1), and similar molecular arrangements (Figure 4). Moreover, we have observed a transition between phases α and β, which was nondestructive for the single crystals, testifying that the structural changes are displacive rather than reconstructive. Phase transitions preserving the space-group type, lattice translations, and positions of molecules are termed isostructural transitions. These transitions are discontinuous (1st order according to Ehrenfest)[45] and display hysteresis, consistent with our observations (Figure 3).

The mechanism of the isostructural phase transition in isobutane can be classified as a pressure-induced collapse caused by molecular reorientation and a shift toward tighter space-filling. The transition order parameter can be associated, at the molecular level, with the reorientation of molecules, leading to tighter packing. In both phases, α and β, the isolated-molecule symmetry of the crystal structure, represented by point group C_{3v}, aligns with the mirror plane perpendicular to $[y]$. Therefore, the molecular orientation can be conveniently described by the angle between the molecular pseudo-C_3 axis and the lattice direction $[x]$. The sense of reorientation is important for the description of the phase transition. Hence, we precisely define it here: (i) for a given molecule, the molecular pseudo-C_3 axis is collinear with the methylidyne C−H group; (ii) the positive rotations of the methylidyne vector C−H are in the right direction (clockwise) when looking from the origin up the $[y]$ axis; (iii) the rotation angle $\phi = 0°$ when the methylidyne C−H vector is parallel to and points up the $[x]$ axis; and (iv) the sign of angle ϕ is associated with a specific molecule, as the structure is centrosymmetric, and the signs will change for the molecules transformed through the inversion center or glide plane perpendicular to $[x]$. Based on the molecular tilts, the transition-order parameter η is defined as

$$\eta = \frac{\phi}{|\overline{\phi_i}|} \tag{1}$$

where $\overline{\phi_i}$ denotes the average ϕ tilt for the phase indicated by subscript i, either $\overline{\phi_\alpha}$ or $\overline{\phi_\beta}$.

In phase α, the molecule is tilted along the mirror plane by an angle ϕ_α of *ca.* 13°, and in phase β, the molecular tilt ϕ_β is reversed to *ca.* −15.4° (Table 2 and Figure 4). It is noteworthy that the intermediate position for the molecular pseudo-C_3 axis

https://doi.org/10.1021/acs.jpcc.5c03155
J. Phys. Chem. C 2025, 129, 14196−14203

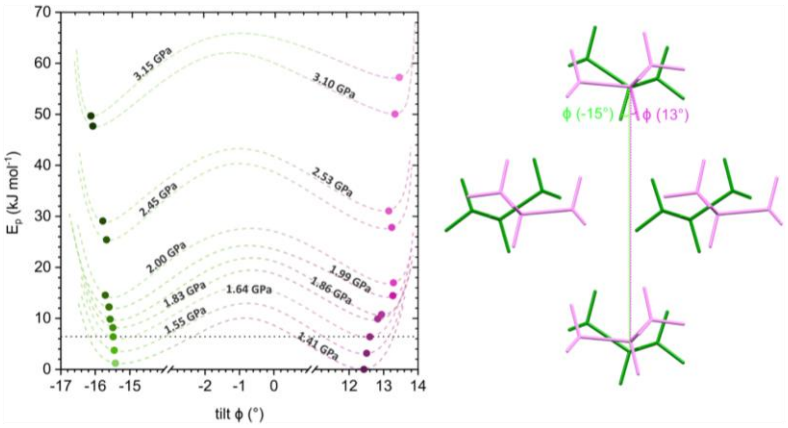

Figure 5. Double-well potential energy (E_p) of phase $\boldsymbol{\alpha}$ (pink curves and circles) and phase $\boldsymbol{\beta}$ (green curves and circles). Dashed lines represent the rotational barriers at the indicated pressure. Below 1.64 GPa, the E_p of phase $\boldsymbol{\alpha}$ is lower; at 1.64 GPa, phases $\boldsymbol{\alpha}$ and $\boldsymbol{\beta}$ are at equilibrium (black dashed line), and at still higher pressure, phase $\boldsymbol{\beta}$ becomes more stable.

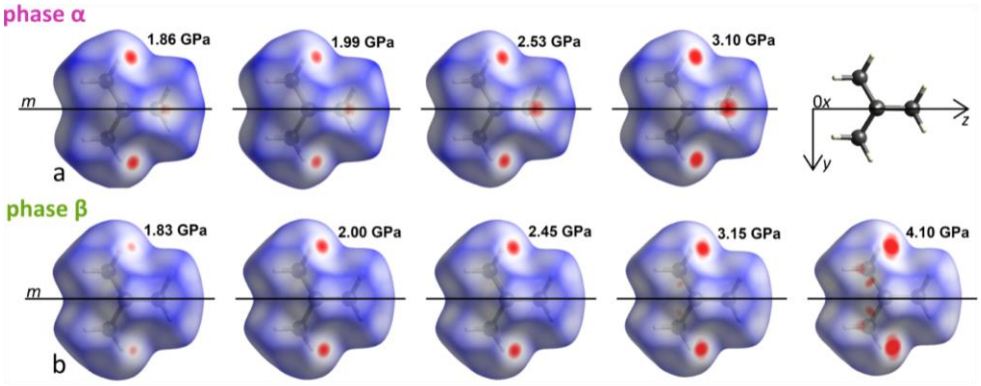

Figure 6. Hirshfeld surfaces[46] decorated with the color scale (from −0.12 to 0.90) depicting the normalized intermolecular distances: (a) in $\boldsymbol{\alpha}$ and (b) in $\boldsymbol{\beta}$ phase. The surface regions showing intermolecular distances equal to the sum of the van der Waals radii[47] are white, shorter red, and longer blue (Figure S11 shows the molecules from its methylidyne side).

aligned along [$\boldsymbol{x}$] would (very roughly) resemble a trigonal arrangement for one layer of molecules; however, their shifts along [$\boldsymbol{x}$] and the position of neighboring layers significantly disrupt the trigonal symmetry (Figure S10). The intermediate $\phi = -1°$ position can be associated with the barrier for the rotation (Figure 5), separating the minima of phases $\boldsymbol{\alpha}$ and $\boldsymbol{\beta}$. The potential energy difference between the minima can be derived from the volume compression, which can be assessed from the thermal energy, whereas the height of the barrier between the minima can be obtained by the Boltzmann formula.

The transition from phase $\boldsymbol{\alpha}$ to phase $\boldsymbol{\beta}$ is associated with a strong deformation, which reduces the crystal dimensions along [$\boldsymbol{y,z}$] but lengthens the crystal along [$\boldsymbol{x}$] by 3.8% for the measurements at 3.10 and 3.15 GPa (Figure S15). The effect of elongated crystal dimensions, despite the transition to the more dense phase $\boldsymbol{\beta}$, is both intriguing and interesting from the point of view of understanding the phase-transition mechanism. The geometric relations between molecular positions and the lattice dimensions show that the elongation along [$\boldsymbol{x}$] is consistent with the increased tilt ϕ of the molecules to the [$\boldsymbol{x}$] axis. At the same time, the shortening along [$\boldsymbol{z}$] is consistent with the reduced tilt angles $(90 - \phi)°$, as illustrated in Figure 4 and Tables 2. These relations of tilt angles ϕ_α and ϕ_β with the unit-cell deformations δa *and* δc can be approximated by equations:

$$\delta a = 2L \times (\sin(\phi_\beta) - \sin(\phi_\alpha)) \quad (2)$$

$$\delta c = L \times (\cos(\phi_\beta) - \cos(\phi_\alpha)) \quad (3)$$

where L is the longest molecular dimension ($L \approx 6$ Å for isobutane) and ϕ_α and ϕ_β are the tilt angles in phases $\boldsymbol{\alpha}$ and $\boldsymbol{\beta}$ listed in Table 2. The mechanism of this transformation and the derivation of eqs 2 and 3 are schematically shown in Figure S14. The crystal deformations calculated in this way along [$\boldsymbol{x}$] and [$\boldsymbol{z}$] for the structures of phase $\boldsymbol{\alpha}$ at 3.10 GPa and phase $\boldsymbol{\beta}$ at 3.15 GPa (Table 2) are $\delta a = 0.569$ Å and $\delta c = -0.075$ Å.

These changes alone would increase the crystal volume, but the molecular packing becomes tighter in phase $\boldsymbol{\beta}$, reducing the volume of small voids. This effect of tighter packing is not included in eqs 2 and 3, but if we account for the unit-cell volume reduction based on the crystal deformation along [$\boldsymbol{y}$],

https://doi.org/10.1021/acs.jpcc.5c03155
J. Phys. Chem. C 2025, 129, 14196−14203

$\delta b \approx -0.1$ Å, the calculated deformations $\delta a'$ and $\delta b'$ are as follows:

$\delta a' = \delta a - 2\delta b = 0.369$ Å and $\delta c' = \delta c - \delta b = -0.175$ Å, which become much closer to the experimentally measured values:

$\delta a = 0.278(4)$ Å and $\delta c = -0.187(1)$ Å.

The increased volume calculated in this way indicates that the molecular tilts are not the primary reason for the transition, but rather the change in tilt is a consequence of the pressure-induced molecular rearrangement, leading to tighter packing.

The different packing of molecules in phases $\boldsymbol{\alpha}$ and $\boldsymbol{\beta}$ is reflected in intermolecular distances mapped on the Hirshfeld surfaces[46] (Figure 6). The shortest contacts of C···H (two per molecule on each side), approximately along [x] in phase $\boldsymbol{\alpha}$, link the molecules into sheets perpendicular to [z]. On the Hirshfeld surface, these shortest C···H contacts are marked as the most intense red spots in phase $\boldsymbol{\alpha}$ (Figure 6a), and they persist in phase $\boldsymbol{\beta}$ (Figure 6b). Thus, at the transition, the molecule tilts on these C···H contacts like on hinges. The third methyl group, lying on the mirror plane, gradually builds up its short contact through the compression of phase $\boldsymbol{\alpha}$ (Figure 6a), which is released at the transition to phase $\boldsymbol{\beta}$ (Figure 6b). The shortest distance in the $\boldsymbol{\alpha}$ phase is unique, forming an infinite chain stabilizing the structure (Figures 7 and S12). Both

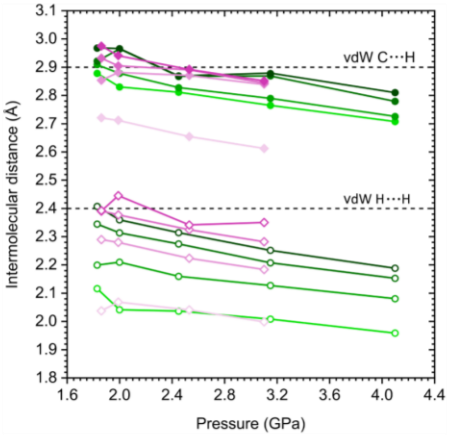

Figure 7. Shortest intermolecular distances as a function of pressure for phase $\boldsymbol{\alpha}$ (pink diamonds) and $\boldsymbol{\beta}$ (green circles). The four shortest distances for the two types of intermolecular distances are presented: filled shapes represent C···H, and empty shapes represent H···H intermolecular distances. The dashed horizontal lines show the sum of the van der Waals radii[47] of C···H (2.90 Å) and H···H (2.40 Å). The ESDs are smaller than the plotted symbols.

phases exhibit a region of initial adjustment between 1.8 and 2.0 GPa, after which the compression of C···H and H···H distances is monotonic (Figure 7). The shortest distances C···H and H···H plotted in Figure 7 show that in phase $\boldsymbol{\alpha}$, there is only one C···H contact shorter than those in phase $\boldsymbol{\beta}$. It is about 0.2 Å shorter than the shortest in phase $\boldsymbol{\beta}$.

The exemption of isobutane and *n*-butane from Carnelley's rule[1] can be attributed to the high-pressure structures associated with their higher density, and hence, closer packing and stronger interactions of molecules in the crystal of *n*-butane. From 1.55 to 3.10 GPa, phases $\boldsymbol{\alpha}$ and $\boldsymbol{\beta}$ of isobutane are *ca.* 2% less dense than *n*-butane. The intermolecular void spaces are also several percent smaller in *n*-butane (Figure S13). This may originate from the easier tight packing of zigzag chains of *n*-butane compared to the pyramidal, disk-like isobutane molecules.

CONCLUSIONS

In this study, we have revealed two competing modes of freezing of isobutane under high-pressure conditions. We have determined the structures of two isobutane crystal phases and observed an isostructural phase transition, which does not change the crystal symmetry but significantly modifies the molecular packing, highlighting the intricate nature of phase transitions in small alkanes. By examining the effects of pressure on the molecular structure, we have provided a deeper understanding of how such transitions can occur without breaking symmetry, emphasizing the role of intermolecular interactions and packing efficiency. We have also rationalized the exemption of butane isomers from Carnelley's rule by the closer molecular packing of lower-symmetry *n*-butane molecules, as observed by the higher density of *n*-butane compared to isobutane phases $\boldsymbol{\alpha}$ and $\boldsymbol{\beta}$. However, unlike at ambient pressure, the higher-symmetry isobutane isomer more easily crystallizes as a function of pressure, which is consistent with Carnelley's rule: isobutane phase $\boldsymbol{\alpha}$ at 1.41 GPa and phase $\boldsymbol{\beta}$ at 1.55 GPa compared to *n*-butane at 1.60 GPa, all at 295 K. This shows that the effect of molecular symmetry in isomers can be reversed or strongly changed by the crystallization method under different thermodynamic conditions. To our knowledge, this is the first report of the reversed sequence of isobaric and isothermal crystallizations: when thermodynamic conditions change, compliance with Carnelley's rule also changes.

ASSOCIATED CONTENT

Supporting Information

The Supporting Information is available free of charge at https://pubs.acs.org/doi/10.1021/acs.jpcc.5c03155.

Details of the experiments for obtaining single crystals of phases $\boldsymbol{\alpha}$ and $\boldsymbol{\beta}$, additional structural and Hirshfeld surfaces drawings mentioned in the text, additional plots showing the dependence of voids space and lattice parameters on pressure, tables with crystallographic data, and refinement details for the structures of phases $\boldsymbol{\alpha}$ and $\boldsymbol{\beta}$ (PDF) The single-crystal X-ray diffraction images of all experiments are available on request from authors.

Crystallographic Information Files of phase $\boldsymbol{\alpha}$ (CIF)

Crystallographic Information Files of phase $\boldsymbol{\beta}$ (CIF)

Accession Codes

Deposition Numbers for phase $\boldsymbol{\alpha}$: 2449253-2449256 and for phase $\boldsymbol{\beta}$: 2449257-2449261 contain the supplementary crystallographic data for this paper. These data can be obtained free of charge via the joint Cambridge Crystallographic Data Centre (CCDC) and Fachinformationszentrum Karlsruhe.

AUTHOR INFORMATION

Corresponding Author

Marcin Podsiadło − *Faculty of Chemistry, Adam Mickiewicz University, Poznań 61-614, Poland;* orcid.org/0000-0001-6702-1875; Email: marcinp@amu.edu.pl

Authors

Natalia Sacharczuk − *Faculty of Chemistry, Adam Mickiewicz University, Poznań 61-614, Poland;* orcid.org/0000-0001-6931-1059

Bernadetta Kuleczka − *Faculty of Chemistry, Adam Mickiewicz University, Poznań 61-614, Poland*

Anna Olejniczak − *Faculty of Chemistry, Adam Mickiewicz University, Poznań 61-614, Poland;* orcid.org/0000-0002-4460-4362

Andrzej Katrusiak − *Faculty of Chemistry, Adam Mickiewicz University, Poznań 61-614, Poland;* orcid.org/0000-0002-1439-7278

Complete contact information is available at: https://pubs.acs.org/10.1021/acs.jpcc.5c03155

Author Contributions

The manuscript was written through contributions of all authors. All authors have given approval to the final version of the manuscript.

Notes

The authors declare no competing financial interest.

■ ACKNOWLEDGMENTS

This study was supported by the National Science Centre (grant no. 2020/37/B/ST4/00982).

■ REFERENCES

(1) Carnelley, T., XIII Chemical Symmetry, or the Influence of Atomic Arrangement on the Physical Properties of Compounds. *London, Edinburgh Dublin Philos. Mag. J. Sci.* **1882**, *13* (79), 112−130.

(2) Bujak, M.; Podsiadlo, M.; Katrusiak, A. Properties and Interactions - Melting Point of Tribromobenzene Isomers. *Acta Crystallogr., Sect. B: struct. Sci., Cryst. Eng. Mater.* **2021**, *77*, 632−637.

(3) *CRC Handbook of Chemistry and Physics*; Haynes, W. M.; Lide, D. R.; Bruno, T. J., Eds.; CRC Press, 2016; Vol. *44*. .

(4) Judd, A. G. Geological Sources of Methane. *Atmos. Methane* **2000**, 280−303.

(5) Stephens, E. R.; Burleson, F. R. Analysis of the Atmosphere for Light Hydrocarbons. *J. Air Pollut. Control Assoc.* **1967**, *17* (3), 147−153.

(6) Helmig, D.; Bottenheim, J.; Galbally, I. E.; Lewis, A.; Milton, M. J. T.; Penkett, S.; Plass-Duelmer, C.; Reimann, S.; Tans, P.; Thiel, S. Volatile Organic Compounds in the Global Atmosphere. *Eos (washington DC)* **2009**, *90* (52), 513−514.

(7) Coker, A. K. Process Planning, Scheduling, and Flowsheet Design. *Ludwig's Appl. Process Des. Chem. Petrochem. Plants* **2007**, *1*, 10−13.

(8) Silano, V.; Bolognesi, C.; Chipman, K.; Cravedi, J. P.; Engel, K. H.; Fowler, P.; Franz, R.; Grob, K.; Gürtler, R.; Husøy, T.; et al. Safety Assessment of the Substance Isobutane, for Use in Food Contact Materials. *EFSA J.* **2018**, *16* (1), 1−7.

(9) Casanave, D.; Fiaty, K.; Dalmon, J. A.; Forissier, M. Kinetics and Mechanism Studies of the Catalytic Dehydrogenation of Isobutane on Platinum-Indium Catalyst. *Stud. Surf. Sci. Catal.* **1999**, *122*, 367−374.

(10) Palm, B. Hydrocarbons as Refrigerants in Small Heat Pump and Refrigeration Systems - A Review. *Int. J. Refrig* **2008**, *31* (4), 552−563.

(11) Kudryavtsev, D. A.; Kutcherov, V. G.; Dubrovinsky, L. S. Raman High-Pressure Study of Butane Isomers up to 40 GPa. *AIP Adv.* **2018**, *8* (11), 115104−1.

(12) Podsiadło, M.; Olejniczak, A.; Katrusiak, A. Why Propane? *J. Phys. Chem. C* **2013**, *117* (9), 4759−4763.

(13) Hirai, H.; Konagai, K.; Kawamura, T.; Yamamoto, Y.; Yagi, T. Solid Methane Behaviours under High Pressure at Room Temperature. *J. Phys.: Conf. Ser.* **2008**, *121* (10), 102001.

(14) Sun, L.; Yi, W.; Wang, L.; Shu, J.; Sinogeikin, S.; Meng, Y.; Shen, G.; Bai, L.; Li, Y.; Liu, J.; et al. X-Ray Diffraction Studies and Equation of State of Methane at 202 GPa. *Chem. Phys. Lett.* **2009**, *473* (1−3), 72−74.

(15) Kolesnikov, A. Y.; Saul, J. M.; Kutcherov, V. G. Chemistry of Hydrocarbons Under Extreme Thermobaric Conditions. *Chemistry-Select* **2017**, *2* (4), 1336−1352.

(16) Shimizu, H.; Shimazaki, I.; Sasaki, S. High-Pressure Raman Study of Liquid and Molecular Crystal Ethane up to 8 GPa. *Jpn. J. Appl. Phys.* **1989**, *28* (9R), 1632−1635.

(17) Podsiadło, M.; Olejniczak, A.; Katrusiak, A. A New Ethane Polymorph. *Cryst. Growth Des.* **2017**, *17* (1), 228−232.

(18) Kudryavtsev, D.; Serovaiskii, A.; Mukhina, E.; Kolesnikov, A.; Gasharova, B.; Kutcherov, V.; Dubrovinsky, L. Raman and IR Spectroscopy Studies on Propane at Pressures of Up to 40 GPa. *J. Phys. Chem. A* **2017**, *121* (32), 6004−6011.

(19) Kavitha, G.; Narayana, C. Pressure-Induced Structural Transition in n-Pentane: A Raman Study. *J. Phys. Chem. B* **2007**, *111* (25), 7003−7008.

(20) Kato, M.; Taniguchi, Y. High Pressure Study on Molecular Conformational Equilibria of N-Pentane. *J. Chem. Phys.* **1991**, *94* (6), 4440−4445.

(21) Qiao, E.; Zheng, H. Raman Scattering Spectroscopic Study of N-Pentane under High Pressure. *Appl. Spectrosc.* **2005**, *59* (5), 650−653.

(22) Safin, D. A.; Babashkina, M. G.; Robeyns, K.; Mitoraj, M. P.; Kubisiak, P.; Garcia, Y. Influence of the Homopolar Dihydrogen Bonding C-H···H-C on Coordination Geometry: Experimental and Theoretical Studies. *Chem. - A Eur. J.* **2015**, *21* (46), 16679−16687.

(23) Kavitha, G.; Narayana, C. Raman Spectroscopic Investigations of Pressure-Induced Phase Transitions in n-Hexane. *J. Phys. Chem. B* **2007**, *111* (51), 14130−14135.

(24) Kavitha, G.; Narayana, C. Raman Scattering Studies on N-Heptane under High Pressure. *J. Phys. Chem. B* **2006**, *110* (17), 8777−8781.

(25) Yamaguchi, M.; Serafin, S. V.; Hellman, T.; Chronister, E. L. Infrared Absorption Studies of N-Heptane under High Pressure. *J. Phys. Chem. B* **2003**, *107* (12), 2815−2821.

(26) Boldyreva, E. High-Pressure Polymorphs of Molecular Solids: When Are They Formed, and When Are They Not? Some Examples of the Role of Kinetic Control. *Cryst. Growth Des.* **2007**, *7* (9), 1662−1668.

(27) Bassett, W. A. Diamond Anvil Cell, 50th Birthday. *High. Press. Res.* **2009**, *29* (2), 163−186.

(28) Mao, H. K.; Xu, J.; Bell, P. M. Calibration of the Ruby Pressure Gauge to 800 Kbar under Quasi-Hydrostatic Conditions. *J. Geophys. Res.* **1986**, *91* (B5), 4673.

(29) Piermarini, G. J.; Block, S.; Barnett, J. D.; Forman, R. A. Calibration of the Pressure Dependence of the R1 Ruby Fluorescence Line to 195 Kbar. *J. Appl. Phys.* **1975**, *46* (6), 2774−2780.

(30) Budzianowski, A.; Katrusiak, A. High-Pressure Crystallographic Experiments with a CCD-Detector. *High-Pressure Crystallogr.* **2004**, 101−112.

(31) CrysAlisPro Software System *Rigaku Oxford Diffraction*; Oxford Diffraction Ltd., 2019.

(32) Dolomanov, O. V.; Bourhis, L. J.; Gildea, R. J.; Howard, J. A. K.; Puschmann, H. OLEX2: A Complete Structure Solution, Refinement and Analysis Program. *J. Appl. Crystallogr.* **2009**, *42* (2), 339−341.

(33) Sheldrick, G. M. SHELXT - Integrated Space-Group and Crystal-Structure Determination. *Acta Crystallogr., Sect. A: Found. Crystallogr.* **2015**, *71* (1), 3−8.

(34) Sheldrick, G. M. Crystal Structure Refinement with SHELXL. *Acta Crystallogr., Sect. C: Struct. Chem.* **2015**, *71* (Md), 3−8.

(35) Olejniczak, A.; Katrusiak, A.; Podsiadło, M.; Katrusiak, A. Preference of High-Nitrogen-Content Compounds to Form Hydrates and the Tandem Contacts of Azide Groups. *Cryst. Growth Des.* **2022**, *22* (10), 5996−6003.

(36) Moszczyńska, I.; Katrusiak, A. Competition between Hydrogen and Anagostic Bonds in Ruthenocene Phases under High Pressure. *J. Phys. Chem. C* **2022**, *126* (10), 5028−5035.
(37) Boldyreva, E. V.; Shakhtshneider, T. P.; Ahsbahs, H.; Sowa, H.; Uchtmann, H. Effect of High Pressure on the Polymorphs of Paracetamol. *J. Therm. Anal. Calorim.* **2002**, *68* (2), 437−452.
(38) Nelyubina, Y. V.; Glukhov, I. V.; Antipin, M. Y.; Lyssenko, K. A. "Higher Density Does Not Mean Higher Stability" Mystery of Paracetamol Finally Unraveled. *Chem. Commun.* **2010**, *46* (20), 3469−3471.
(39) Paliwoda, D.; Dziubek, K. F.; Katrusiak, A. Imidazole Hidden Polar Phase. *Cryst. Growth Des.* **2012**, *12* (9), 4302−4305.
(40) Zieliński, W.; Katrusiak, A. Hydrogen Bonds NH···N in Compressed Benzimidazole Polymorphs. *Cryst. Growth Des.* **2013**, *13* (2), 696−700.
(41) Zieliński, W.; Katrusiak, A. Colossal Monotonic Response to Hydrostatic Pressure in Molecular Crystal Induced by a Chemical Modification. *Cryst. Growth Des.* **2014**, *14* (9), 4247−4253.
(42) Moszczyńska, I.; Gulaczyk, I.; Katrusiak, A. Giant Deformation between Osmocene Phases Induced by Anagostic Bonds Promoted under High Pressure. *J. Phys. Chem. C* **2023**, *127* (38), 19250−19257.
(43) Roszak, K.; Katrusiak, A. High-Pressure Crystallization and Thermodynamic Stability Study on the Resolution of High-Density Enantiomers from Low-Density Racemates. *Org. Lett.* **2023**, *25* (1), 37−41.
(44) Roszak, K.; Katrusiak, A. Low-Density Preference of the Ambient and High-Pressure Polymorphs of DL-Menthol. *IUCrJ* **2023**, *10* (3), 341−351.
(45) Jaeger, G. The Ehrenfest Classification of Phase Transitions: Introduction and Evolution. *Arch. Hist. Exact Sci.* **1998**, *53* (1), 51−81.
(46) Spackman, P. R.; Turner, M. J.; McKinnon, J. J.; Wolff, S. K.; Grimwood, D. J.; Jayatilaka, D.; Spackman, M. A. CrystalExplorer: A Program for Hirshfeld Surface Analysis, Visualization and Quantitative Analysis of Molecular Crystals. *J. Appl. Crystallogr.* **2021**, *54*, 1006−1011.
(47) Bondi, A. Van Der Waals Volumes and Radii. *J. Phys. Chem.* **1964**, *68* (3), 441−451.

https://doi.org/10.1021/acs.jpcc.5c03155
J. Phys. Chem. C 2025, 129, 14196−14203

Supporting Information

Mechanism of Isostructural Phase Transition in Isobutane

Natalia Sacharczuk, Bernadetta Kuleczka, Anna Olejniczak, Andrzej Katrusiak and Marcin Podsiadło*

Faculty of Chemistry, Adam Mickiewicz University, Uniwersytetu Poznańskiego 8, Poznań, 61-614, Poland

*E-mail: marcinp@amu.edu.pl

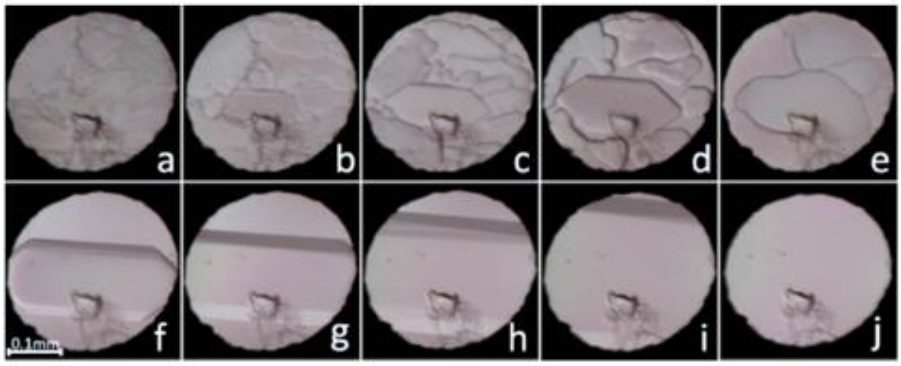

Figure S1. Stages of the isobutane α phase single-crystal growth inside the DAC chamber: (a) polycrystal obtained from the liquid by increasing the pressure up to 1.60 GPa; (b-d) the DAC chamber rapidly cooled to 273 K; (e-f) the DAC chamber left overnight at 291 K, only one crystalline left; (g-i) the pressure increased from 1.55 GPa to 1.86 GPa and (j) the single crystal filling the DAC chamber at 295 K and 1.86 GPa. The ruby chip for pressure calibration lies in the central part of the DAC chamber.

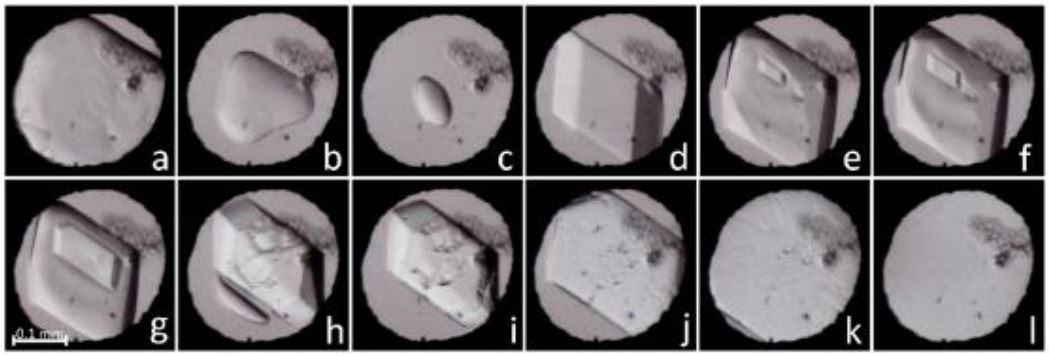

Figure S2. Stages of the isobutane α phase single-crystal growth inside the DAC chamber: (a-b) decreasing the pressure at 295 K; (c) one crystal seed at 295 K; (d) the DAC chamber cooled to 273 K, and the crystal of the β phase grew slightly; (e) crystal of the α phase appeared; (f-h) melting of the β phase crystal, and growing of the α phase crystal; (i) one crystal of the α phase left and (j-l) pressure inside the DAC increased slowly to 1.99 GPa. The ruby chip for pressure calibration lies in the right part of the DAC chamber.

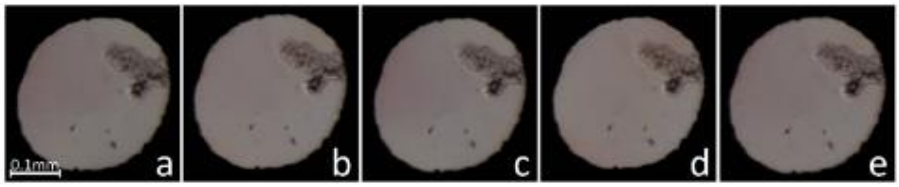

Figure S3. Stages of slowly increasing the pressure inside the DAC, with the single crystal of α phase: (a) 1.99 GPa; (b) 2.08 GPa; (c) 2.17 GPa; (d) 2.24 GPa; (e) 2.53GPa.

Figure S4. Single crystal of the α phase at 3.10 GPa and 295 K. The single crystal was obtained by increasing the pressure from 2.53 GPa to 3.10 GPa.

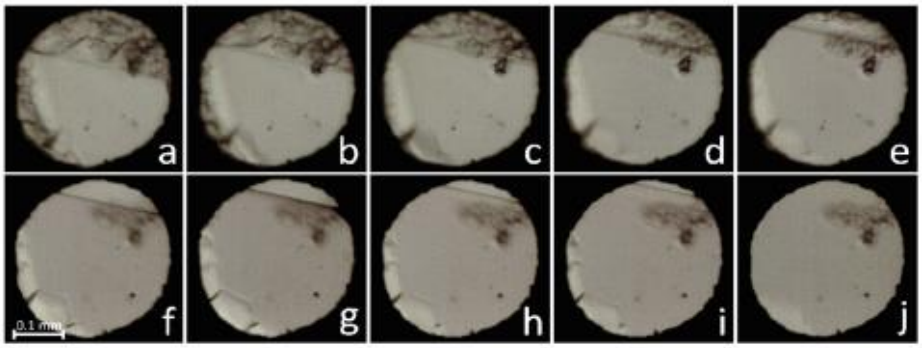

Figure S5. Stages of the isobutane β phase single-crystal growth inside the DAC chamber: (a) polycrystalline mass with one bigger crystallite grown isothermally at 295 K and 1.83 GPa; (b-e) melting of the polycrystalline mass, growing of the single crystal; (f-i) the single crystal growth while decreasing the volume of the high-pressure chamber and (j) the single crystal filling the DAC chamber at 295 K and 1.83 GPa. The ruby chip for pressure calibration lies in the right part of the DAC chamber.

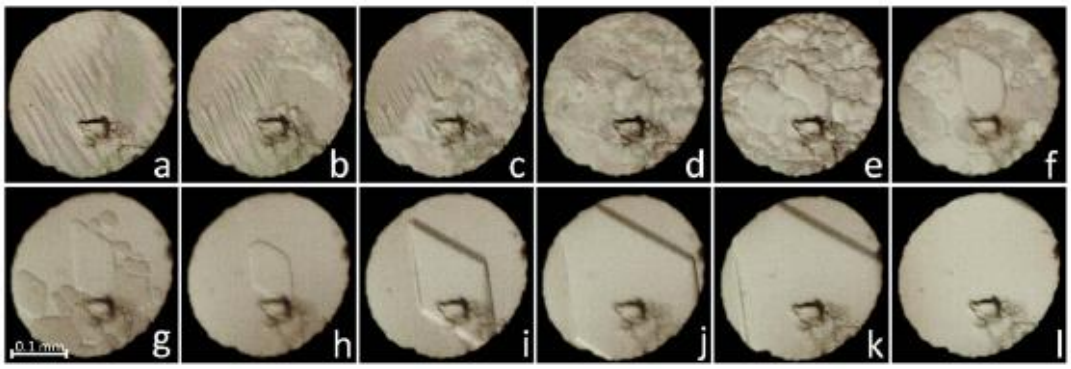

Figure S6. Stages of the isobutane β phase single-crystal growth inside the DAC chamber: (a-c) slowly decreasing the pressure from 3.15 GPa to 1.77 GPa, melting of the crystals; (d) the pressure increased to 2.00 GPa; (e-g) melting of the polycrystalline mass, the DAC chamber heated to 379 K; (h-k) the single crystal growth while cooling the DAC chamber to room temperature and (l) the single crystal filling the DAC chamber at 295 K. The ruby chip for pressure calibration lies in the central part of the DAC chamber.

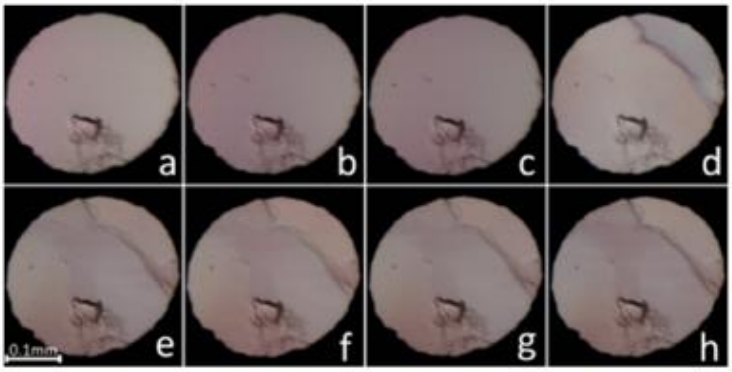

Figure S7. Stages of the isobutane β phase single-crystal growth inside the DAC chamber: (a-c) slowly increasing the pressure to 2.45 GPa; (d-g) the crystal heated for 6 hours up to 343 K, and (h) the DAC chamber cooled to 295 K. The ruby chip for pressure calibration lies in the central part of the DAC chamber.

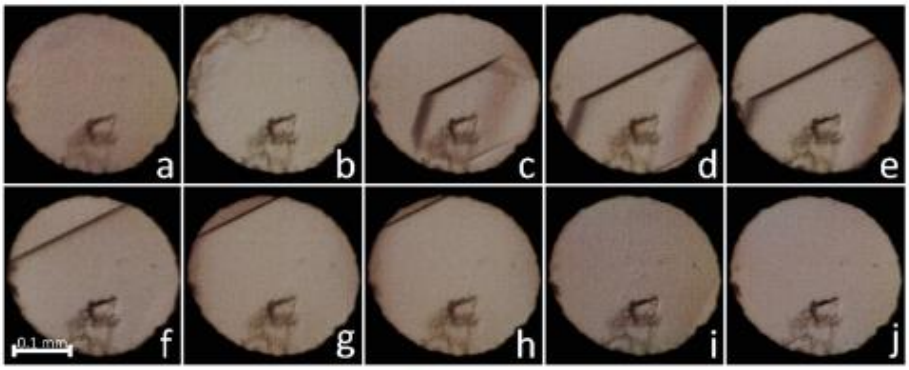

Figure S8. Stages of the isobutane β phase single-crystal growth inside the DAC chamber: (a-b) the DAC chamber heated up to 471 K; melting of the polycrystalline mass; (c) one crystallite left; (d-h) the DAC chamber slowly cooled to room temperature, allowing the single crystal to grow and (i-j) the single crystal filling the DAC chamber at 295 K. The ruby chip for pressure calibration lies in the central part of the DAC chamber.

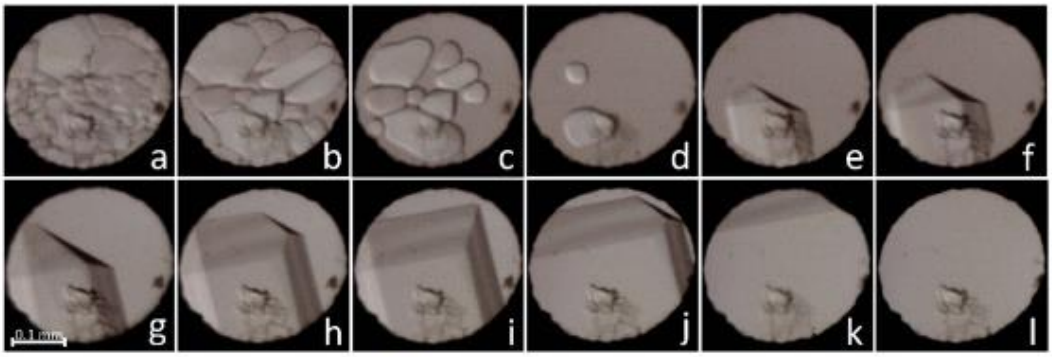

Figure S9. Stages of the isobutane β phase single-crystal growth inside the DAC chamber: (a-d) the DAC chamber heated up to 504 K, melting of the polycrystalline mass; (e) one crystallite left; (f-k) the DAC chamber slowly cooled to room temperature, allowing the single crystal to grow and (l) the single crystal filling the DAC chamber at 295 K. The ruby chip for pressure calibration lies in the central part of the DAC chamber.

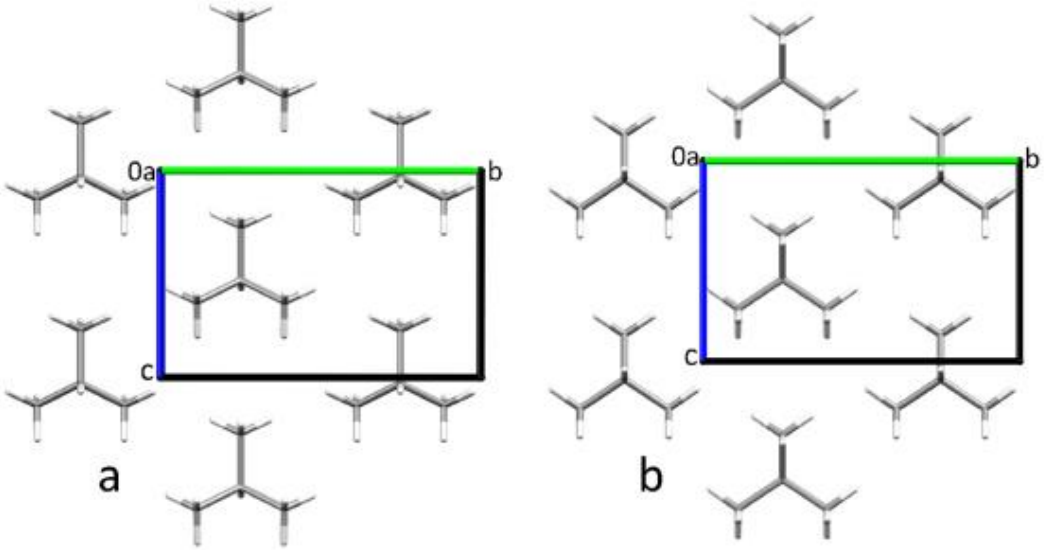

Figure S10. Strongly distorted trigonal arrangements (note the methylidyne H directions in the surrounding molecules) of one layer of isobutane molecules in (a) phase α at 1.99 GPa and (b) phase β at 2.00 GPa.

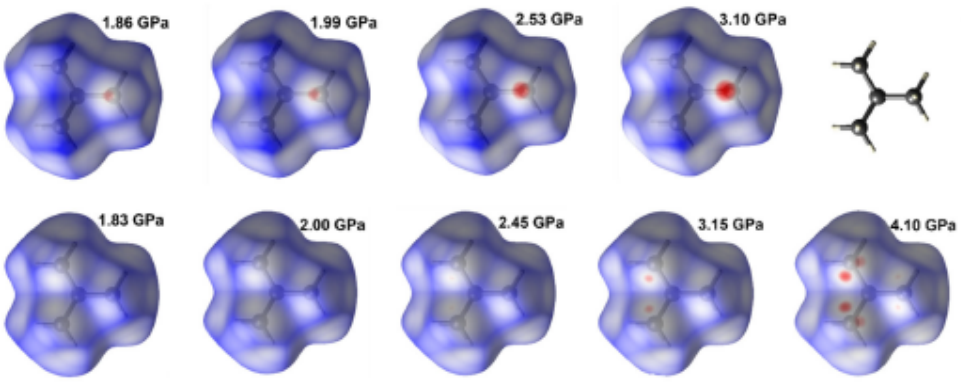

Figure S11. The Hirshfeld surfaces (Spackman, P. R.; Turner, M. J.; McKinnon, J. J.; Wolff, S. K.; Grimwood, D. J.; Jayatilaka, D.; Spackman, M. A. CrystalExplorer21: a program for Hirshfeld surface analysis, visualization and quantitative analysis of molecular crystals, *J. Appl. Crystallogr*. **2021**, *54*, 1006–1011) decorated with the colour scale (from -0.12 to 0.90) depicting the normalised intermolecular distances: (a) in α phase and (b) in β phase (reversed side of the molecules compared to those shown in the main text in Figure 5). The surface regions showing intermolecular distances equal to the sum of the van der Waals radii (Bondi, A. van der Waals Volumes and Radii, *J. Phys. Chem*. **1964**, *68*, 441–451) are white, shorter red, and longer blue.

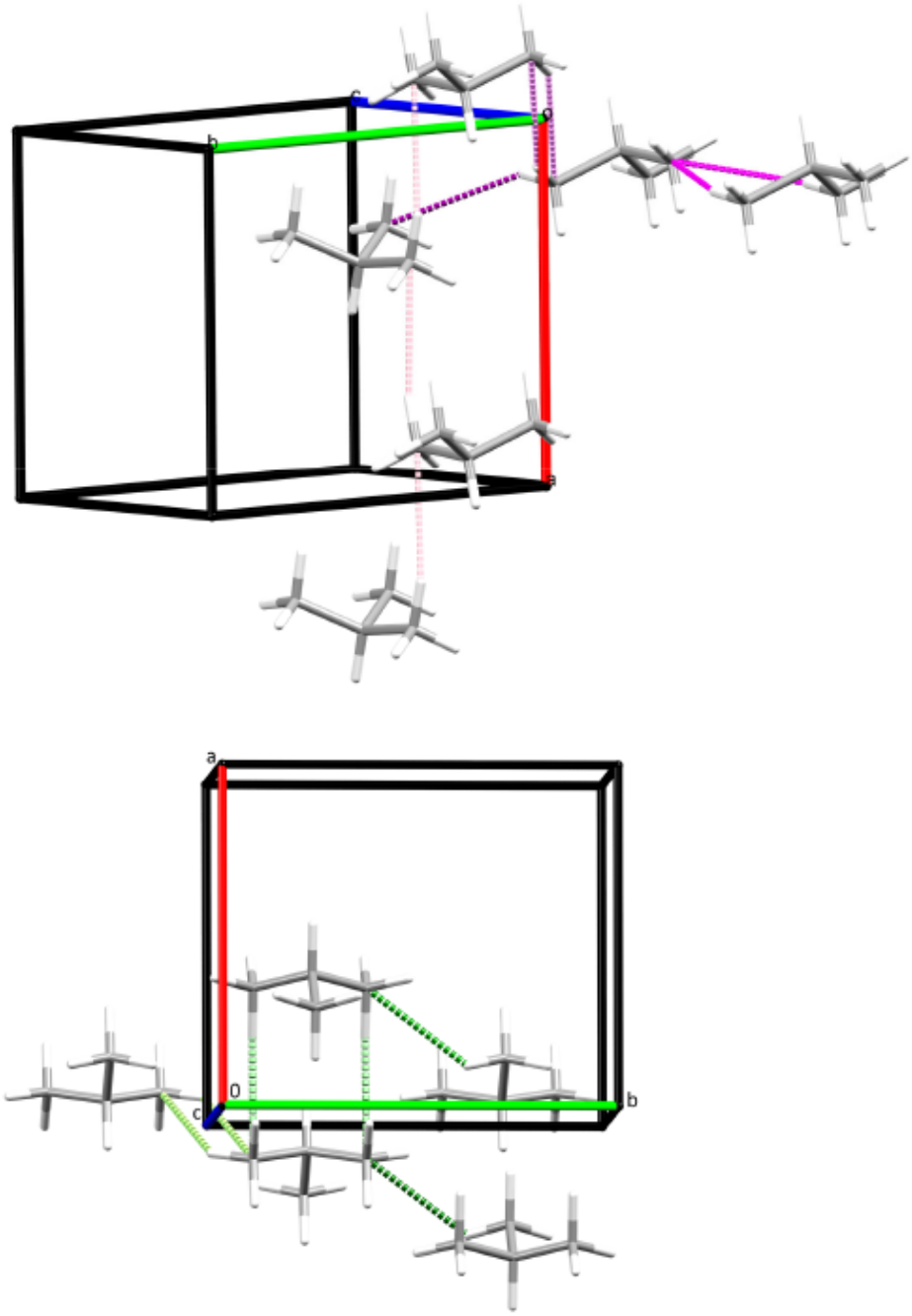

Figure S12. Different C···H intermolecular distances characterised each shade of pink (phase α) and green (phase β) (the lightest is the shortest). In phase α, the shortest C···H intermolecular distances create an infinite chain, stabilising the structure in a range of investigated pressures. In phase β, different distributions of the shortest intermolecular C···H distances are observed.

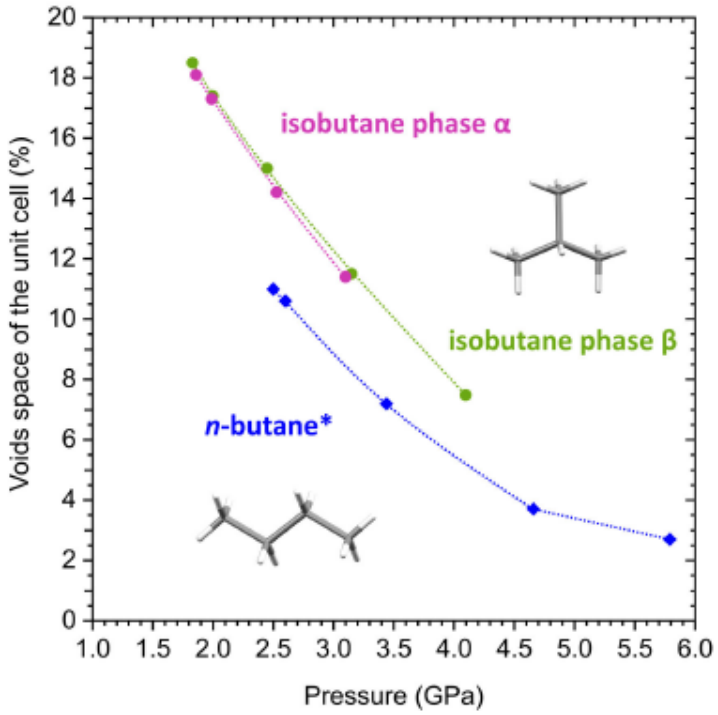

Figure S13. Voids space calculated with a probe radius of 0.3 Å and grid spacing of 0.1 Å for isobutane phase α (pink circles), isobutane phase β (green circles), and *n*-butane*(blue diamonds) (Podsiadło, M.; Olejniczak, A.; Katrusiak, A. Why Propane? *J. Phys. Chem. C* **2013**, *117*, 4759–4763) by the program Mercury (Macrae, C. F.; Edgington, P. R.; McCabe, P.; Pidcock, E.; Shield,s G. P.; Taylor, R.; Towler, M.; van de Streek, J. Mercury: visualization and analysis of crystal structures, *J. Appl. Cryst*. **2006**, *39*, 453–457).

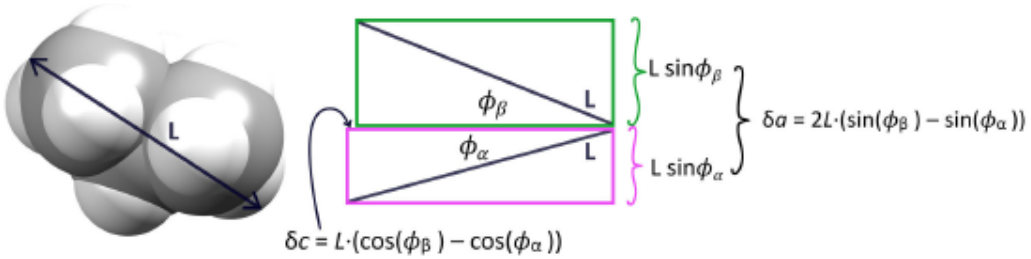

Figure S14. Schematic illustration of the mechanism of elongation of the unit-cell parameter *a* by δa at the transition from phase α to phase β, accompanied by the shrinking of the parameter *c* by δc, depending on the changed tilt angle ϕ from ϕ_α in phase α to ϕ_β in phase β, for the molecule of length L (the magnitude of ϕ_α and ϕ_β have been increased for clarity).

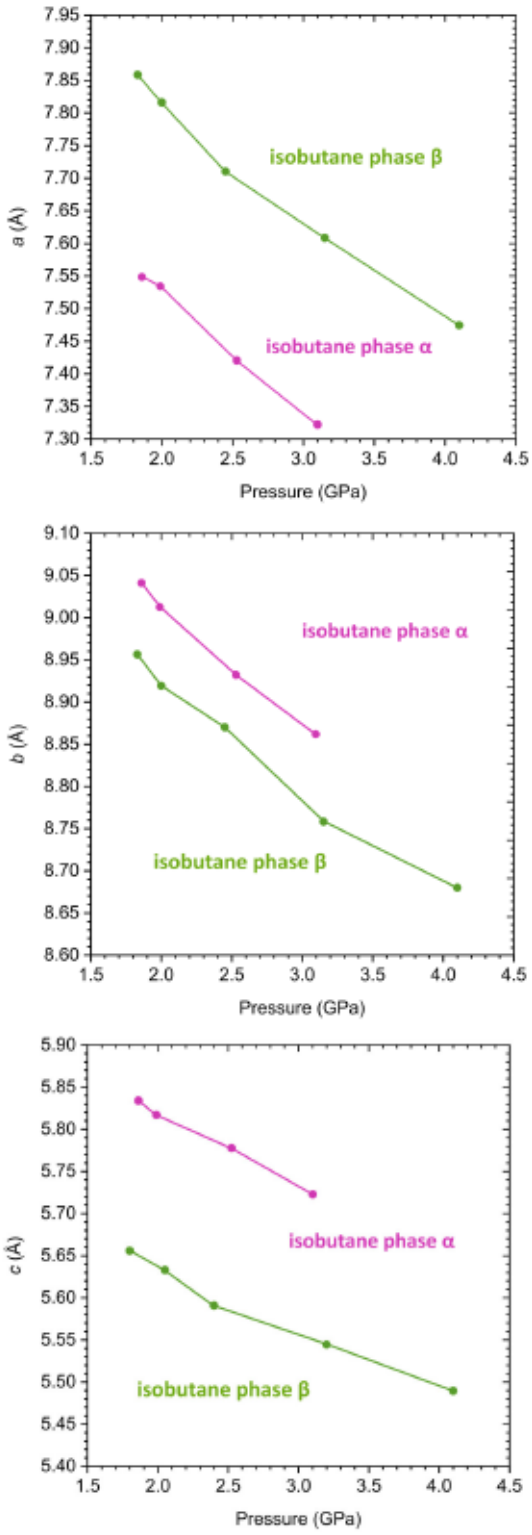

Figure S15. Unit-cell parameters of isobutane for phases α and β.

Table S1. Crystal data and details of the refinements of isobutane phase α at 1.86, 1.99, 2.53 and 3.10 GPa (all at 295 K).

	C_4H_{10} phase α	C_4H_{10} phase α	C_4H_{10} phase α	C_4H_{10} phase α
Pressure (GPa)	1.86(2)	1.99(2)	2.53(2)	3.10(2)
Formula weight	58.12	58.12	58.12	58.12
Crystal colour	colourless	colourless	colourless	colourless
Crystal size (mm)	0.37x0.34x0.30	0.31x0.31x0.30	0.31x0.31x0.29	0.32x0.30x0.28
Crystal system	orthorhombic	orthorhombic	orthorhombic	orthorhombic
Space group	*Pnma*	*Pnma*	*Pnma*	*Pnma*
Unit cell dimensions				
a (Å)	7.5484(3)	7.534(4)	7.420(5)	7.329(4)
b (Å)	9.041(7)	9.0125(14)	8.9323(16)	8.8578(14)
c (Å)	5.8341(2)	5.8169(5)	5.7767(8)	5.7315(8)
Volume (Å^3)	398.2(3)	395.0(2)	382.9(3)	372.1(2)
Z, *Z'*	4, 0.5	4, 0.5	4, 0.5	4, 0.5
D_x (g·cm^{-3})	0.970	0.977	1.008	1.038
Wavelength MoKα, λ (Å)	0.71073	0.71073	0.71073	0.71073
Absorption coefficient (mm^{-1})	0.052	0.053	0.055	0.056
F(000) (e)	136	136	136	136
2Θ max (°)	63.31	62.718	62.59	63.146
Min./Max. indices *h*, *k*, *l*	-11/11, -2/2, -8/8	-5/5, -12/12, -8/8	-5/5, -12/12, -8/8	-5/5, -12/12, -8/8
Reflections collected/unique	3416/204	3031/346	2920/330	2810/319
R_{int} (all data)	0.0364	0.0688	0.0555	0.0669
Data/restraints/parameters	204/0/23	346/0/23	330/0/23	319/0/23
Observed reflections (I>2σ(I))	167	201	199	194
Goodness of fit on F^2	1.105	1.030	1.078	1.062
Final R_1 indices (I>2σ(I))	0.0476	0.0671	0.0737	0.0651
R_1/wR_2 indices (all data)	0.0592/0.1435	0.1190/ 0.1965	0.1178/0.2043	0.1186/0.1403
$\Delta\sigma_{max}$, $\Delta\sigma_{min}$ (e·Å^{-3})	0.12/-0.09	0.15/-0.13	0.18/-0.12	0.12/-0.11
Weighting scheme: *x*; *y*[a]	0.0720/0.1101	0.1073/0.0320	0.0962/0.1024	0.0357/0.1915

[a] $w=1/(\sigma^2(Fo^2)+x^2P^2+yP)$, where $P=(\mathrm{Max}(Fo^2,0)+2Fc^2)/3$

Table S2. Crystal data and details of the refinements of isobutane phase β at 1.83, 2.00, 2.45, 3.10 and 4.10 GPa (all at 295 K).

	C_4H_{10} phase β	C_4H_{10} phase β	C_4H_{10} phase β	C_4H_{10} phase β	C_4H_{10} phase β
Pressure (GPa)	1.83(2)	2.00(2)	2.45(2)	3.15(2)	4.10(2)
Formula weight	58.12	58.12	58.12	58.12	58.12
Crystal colour	colourless	colourless	colourless	colourless	colourless
Crystal size (mm)	0.32x0.31x0.30	0.39x0.36x0.30	0.37x0.34x0.29	0.38x0.36x0.30	0.38x0.36x0.30
Crystal system	orthorhombic	orthorhombic	orthorhombic	orthorhombic	orthorhombic
Space group	*Pnma*	*Pnma*	*Pnma*	*Pnma*	*Pnma*
Unit cell dimensions					
a (Å)	7.8584(16)	7.8162(6)	7.710(4)	7.6085(5)	7.4745(3)
b (Å)	8.9564(4)	8.9193(5)	8.8702(13)	8.7582(14)	8.6798(10)
c (Å)	5.6557(2)	5.6328(2)	5.5908(4)	5.5445(7)	5.4895(5)
Volume (Å^3)	398.06(8)	392.69(4)	382.4(2)	369.47(8)	356.14(5)
Z, *Z'*	4, 0.5	4, 0.5	4, 0.5	4, 0.5	4, 0.5
D_x (g·cm^{-3})	0.970	0.983	1.010	1.045	1.084
Wavelength MoKα, λ (Å)	0.71073	0.71073	0.71073	0.71073	0.71073
Absorption coefficient (mm^{-1})	0.052	0.053	0.055	0.057	0.059
F(000) (e)	136	136	136	136	136
2Θ max (°)	62.83	62.528	62.504	62.44	62.318
Min./Max. indices *h*, *k*, *l*	-5/5, -12/12, -8/8	-8/8, -10/10, -8/7	-5/5, -11/12, -8/8	-10/10, -8/9, -6/6	-10/10, -8/9, -6/6
Reflections collected/unique	3261/344	3336/365	3079/254	3062/353	2896/344
Observed reflections ($I>2\sigma(I)$)	266	294	172	264	274
R_{int} (all data)	0.0366	0.0381	0.0829	0.0361	0.0346
Data/restraints/parameters	344/0/23	365/0/23	254/0/23	353/0/23	344/0/23
Goodness of fit on F^2	1.066	1.101	1.061	1.056	1.148
Final R_1 indices ($I>2\sigma(I)$)	0.0477	0.0455	0.0547	0.0429	0.0435
R_1/wR_2 indices (all data)	0.0676/0.1448	0.0571/0.1340	0.0911/0.1441	0.0646/0.1179	0.0583/0.1241
$\Delta\sigma_{max}$, $\Delta\sigma_{min}$ (e·Å^{-3})	0.11/-0.11	0.13/-0.12	0.12/-0.10	0.14/-0.11	0.18/-0.12
Weighting scheme: *x*; *y*[a]	0.0797/0.0506	0.0675/0.0702	0.0675/0.0734	0.0599/0.0596	0.0589/0.0650

[a] $w=1/(\sigma^2(Fo^2)+x^2P^2+yP)$, where $P=(\mathrm{Max}(Fo^2,0)+2Fc^2)/3$

Oświadczenia współautorów

Poznań, 4.05.2026

Natalia Sacharczuk
Adam Mickiewicz University
Faculty of Chemistry
Uniwersytetu Poznańskiego 8
61-614 Poznań, Polska

Declaration of PhD Candidate Contributions

I declare that I am a co-author of the following publications:

- N. Sacharczuk, B. Kuleczka, A. Olejniczak, A. Katrusiak, M. Podsiadło, Mechanism of Isostructural Phase Transition in Isobutane, *The Journal of Physical Chemistry C*, **2025**, 129(31), 14196-14203. DOI: 10.1021/acs.jpcc.5c03155

  My contribution to this paper included project conceptualization, conducting high-pressure in situ crystallizations in diamond anvil cells, performing high-pressure single-crystal X-ray diffraction experiments, analysis and interpretation of experimental data, preparing figures and tables for the manuscript and Supporting Information, and writing and editing the manuscript and its Supporting Information.

- B. Kuleczka, N. Sacharczuk, A. Olejniczak, M. Podsiadło, High-pressure crystal structure of n-hexylamine, *Acta Cryst. C*, **2025**, 81, 346-350. DOI: 10.1107/S2053229625004504

  My contribution to this paper included project conceptualization, performing high-pressure single-crystal X-ray diffraction experiments, analysis and interpretation of experimental data, preparing figures and tables for the manuscript and Supporting Information, and writing and editing the manuscript and its Supporting Information.

- N. Sacharczuk, A. Olejniczak, M. Bujak, M. Podsiadło, Molecular Aggregations in Crystals of Butene Isomers Determined at High Pressure, *Crystal Growth & Design*, **2024**, 24, 9909-9913. DOI: 10.1021/acs.cgd.4c00983

  My contribution to this paper included project conceptualization, carrying out high-pressure in situ crystallizations in a DAC, performing high-pressure single-crystal X-ray diffraction experiments, analysis and interpretation of experimental

data, preparing figures and tables for the manuscript and Supporting Information, as well as writing and editing the manuscript and its Supporting Information.

- N. Sacharczuk, A. Olejniczak, M. Bujak, K. F. Dziubek, A. Katrusiak, M. Podsiadło, Conformation-aggregation interplay in the simplest aliphatic ethers probed under high pressure, *IUCrJ*, **2024**, 11, 57-61. DOI: 10.1107/S2052252523009995

  My contribution to this paper included project conceptualization, carrying out high-pressure in situ crystallizations in a DAC, performing high-pressure single-crystal X-ray diffraction experiments, analysis and interpretation of experimental data, performing quantum-mechanical computations, preparing figures and tables for the manuscript and Supporting Information, as well as writing and editing the manuscript and its Supporting Information.

- N. Sacharczuk, A. Olejniczak, M. Bujak, M. Podsiadło, Polymorphism, Intermolecular Interactions, and Properties of Primary Amines at High Pressure, *Crystal Growth & Design*. **2023**, 23, 10, 7119–7125. DOI: 10.1021/acs.cgd.3c00456

  My contribution to this paper included project conceptualization, conducting high-pressure in situ crystallizations in a DAC, performing high-pressure single-crystal X-ray diffraction experiments, analysis and interpretation of experimental data, preparing figures and tables for the manuscript and Supporting Information, and writing and editing the manuscript and its Supporting Information.

Natalia Sacharczuk

Mgr Podsiadło

Poznań, 4.05.2026

Prof. UAM dr hab. Marcin Podsiadło
Adam Mickiewicz University
Faculty of Chemistry
Uniwersytetu Poznańskiego 8
61-614 Poznań, Poland

Co-author declaration

With reference to Natalia Sacharczuk's application for the Doctoral degree in Chemical Sciences at Adam Mickiewicz University in Poznań, I declare that I am a co-author of the following publications:

- N. Sacharczuk, B. Kuleczka, A. Olejniczak, A. Katrusiak, M. Podsiadło, Mechanism of Isostructural Phase Transition in Isobutane, *The Journal of Physical Chemistry C*, **2025**, 129(31), 14196-14203. DOI: 10.1021/acs.jpcc.5c03155

- B. Kuleczka, N. Sacharczuk, A. Olejniczak, M. Podsiadło, High-pressure crystal structure of n-hexylamine, *Acta Cryst. C*, **2025**, 81, 346-350. DOI: 10.1107/S2053229625004504

- N. Sacharczuk, A. Olejniczak, M. Bujak, M. Podsiadło, Molecular Aggregations in Crystals of Butene Isomers Determined at High Pressure, *Crystal Growth & Design*, **2024**, 24, 9909-9913. DOI: 10.1021/acs.cgd.4c00983

- N. Sacharczuk, A. Olejniczak, M. Bujak, K. F. Dziubek, A. Katrusiak, M. Podsiadło, Conformation-aggregation interplay in the simplest aliphatic ethers probed under high pressure, *IUCrJ*, **2024**, 11, 57-61. DOI: 10.1107/S2052252523009995

- N. Sacharczuk, A. Olejniczak, M. Bujak, M. Podsiadło, Polymorphism, Intermolecular Interactions, and Properties of Primary Amines at High Pressure, *Crystal Growth & Design*. **2023**, 23, 10, 7119–7125. DOI: 10.1021/acs.cgd.3c00456

My contributions to these papers included conceptualization and supervision of the research, as well as manuscript writing, editing, and review.

Poznań, 4.05.2026

Prof. UAM dr hab. Anna Olejniczak
Adam Mickiewicz University
Faculty of Chemistry
Uniwersytetu Poznańskiego 8
61-614 Poznań, Poland

Co-author declaration

With reference to Natalia Sacharczuk's application for the Doctoral degree in Chemical Sciences at Adam Mickiewicz University in Poznań, I declare that I am a co-author of the following publications:

- N. Sacharczuk, B. Kuleczka, A. Olejniczak, A. Katrusiak, M. Podsiadło, Mechanism of Isostructural Phase Transition in Isobutane, *The Journal of Physical Chemistry C*, **2025**, 129(31), 14196-14203. DOI: 10.1021/acs.jpcc.5c03155
- B. Kuleczka, N. Sacharczuk, A. Olejniczak, M. Podsiadło, High-pressure crystal structure of n-hexylamine, *Acta Cryst. C*, **2025**, 81, 346-350. DOI: 10.1107/S2053229625004504
- N. Sacharczuk, A. Olejniczak, M. Bujak, M. Podsiadło, Molecular Aggregations in Crystals of Butene Isomers Determined at High Pressure, *Crystal Growth & Design*, **2024**, 24, 9909-9913. DOI: 10.1021/acs.cgd.4c00983
- N. Sacharczuk, A. Olejniczak, M. Bujak, K. F. Dziubek, A. Katrusiak, M. Podsiadło, Conformation-aggregation interplay in the simplest aliphatic ethers probed under high pressure, *IUCrJ*, **2024**, 11, 57-61. DOI: 10.1107/S2052252523009995
- N. Sacharczuk, A. Olejniczak, M. Bujak, M. Podsiadło, Polymorphism, Intermolecular Interactions, and Properties of Primary Amines at High Pressure, *Crystal Growth & Design*. **2023**, 23, 10, 7119–7125. DOI: 10.1021/acs.cgd.3c00456

My contributions to these papers included preparing Hirshfeld surface projections, part of structural drawings, as well as writing and editing the manuscripts.

Anna Olejniczak

Opole, 7 May 2026

Maciej Bujak
Institute of Chemistry
Faculty of Chemistry and Pharmacy
University of Opole
Oleska 48, 45-052 Opole, Poland

Declaration of co-authorship

With reference to Natalia Sacharczuk's application for the degree of Doctor of Philosophy in Chemical Sciences at Adam Mickiewicz University in Poznań, I declare that I am a co-author of the following publications:

- N. Sacharczuk, A. Olejniczak, M. Bujak, M. Podsiadło, Polymorphism, Intermolecular Interactions, and Properties of Primary Amines at High Pressure, *Crystal Growth & Design*. **2023**, 23, 10, 7119–7125. DOI: 10.1021/acs.cgd.3c00456

- N. Sacharczuk, A. Olejniczak, M. Bujak, K. F. Dziubek, A. Katrusiak, M. Podsiadło, Conformation-aggregation interplay in the simplest aliphatic ethers probed under high pressure, *IUCrJ*, **2024**, 11, 57-61. DOI: 10.1107/S2052252523009995

- N. Sacharczuk, A. Olejniczak, M. Bujak, M. Podsiadło, Molecular Aggregations in Crystals of Butene Isomers Determined at High Pressure, *Crystal Growth & Design*, **2024**, 24, 9909-9913. DOI: 10.1021/acs.cgd.4c00983

My contribution to these three papers included assistance with the preparation of structural models, participation in manuscript preparation, and involvement in manuscript editing and responding to reviewers' comments.

Poznań, 4.05.2026

Bernadetta Kuleczka,

Adam Mickiewicz University

Faculty of Chemistry

Uniwersytetu Poznańskiego 8,

61-614 Poznań, Polska

Co-author declaration

With reference to Natalia Sacharczuk's application for the Doctoral degree in Chemical Sciences at Adam Mickiewicz University in Poznań, I declare that I am a co-author of the following publications:

- N. Sacharczuk, B. Kuleczka, A. Olejniczak, A. Katrusiak, M. Podsiadło, Mechanism of Isostructural Phase Transition in Isobutane, *The Journal of Physical Chemistry C*, **2025**, 129(31), 14196-14203. DOI: 10.1021/acs.jpcc.5c03155

- B. Kuleczka, N. Sacharczuk, A. Olejniczak, M. Podsiadło, High-pressure crystal structure of n-hexylamine, *Acta Cryst. C*, **2025**, 81, 346-350. DOI: 10.1107/S2053229625004504

My contributions to these papers included assisting with the preparation of figures and tables, as well as conducting selected high-pressure experiments.

Kuleczka

Poznań, 4.05.2026

Prof. dr hab. Andrzej Katrusiak

Adam Mickiewicz University

Faculty of Chemistry

Uniwersytetu Poznańskiego 8

61-614 Poznań, Polska

Co-author declaration

With reference to Natalia Sacharczuk's application for the Doctoral degree in Chemical Sciences at Adam Mickiewicz University in Poznań, I declare that I am a co-author of the following publications:

- N. Sacharczuk, B. Kuleczka, A. Olejniczak, A. Katrusiak, M. Podsiadło, Mechanism of Isostructural Phase Transition in Isobutane, *The Journal of Physical Chemistry C*, **2025**, 129(31), 14196-14203. DOI: 10.1021/acs.jpcc.5c03155

- N. Sacharczuk, A. Olejniczak, M. Bujak, K. F. Dziubek, A. Katrusiak, M. Podsiadło, Conformation-aggregation interplay in the simplest aliphatic ethers probed under high pressure, *IUCrJ*, **2024**, 11, 57-61. DOI: 10.1107/S2052252523009995

My contributions to these papers included manuscript writing, editing, and review.

Prof. dr hab. Andrzej Katrusiak

Poznań, 01.09.2025

Dr Kamil Filip Dziubek

University of Vienna,

Josef-Holaubek Platz 2

1090 Vienna

Austria

Oświadczenie o współautorstwie

Potwierdzam swój wkład w następującą publikację:

- Sacharczuk, N.; Olejniczak, A.; Bujak, M.; Dziubek, K.F.; Katrusiak, A.; Podsiadło, M. Conformation–Aggregation Interplay in the Simplest Aliphatic Ethers Probed under High Pressure. *IUCrJ* **2024**, *11*, 57–61, doi:10.1107/S2052252523009995.

Mój wkład w powstanie wyżej wymienionej pracy dotyczył dostarczenia danych eksperymentalnych. Uczestniczyłem również w recenzowaniu szkicu manuskryptu.

Życiorys naukowy

Education

October 2021-present	***PhD student:*** *"The effect of high pressure on crystal structures, polymorphism, and intermolecular interactions in the simplest aliphatic hydrocarbons and their derivatives,* Adam Mickiewicz University, supervisor: prof. Marcin Podsiadło
June 28, 2021	***Master of Science****: "Synthesis of TiO_2 with defective crystal structure for dye-sensitized solar cells applications",* Adam Mickiewicz University, Faculty of Chemistry, Poznań, Poland
June 28, 2019	***Bachelor of Science****: "Synthesis of spherical black titania for dye sensitized solar cells applications",* Adam Mickiewicz University, Faculty of Chemistry, Poznań, Poland

Research projects

January 1, 2026 – *December* 31, 2027	***Investigator***, NAWA Polish National Agency for Academic Exchange Joint research projects 2025 Poland – China, (Grant No. BPN/BCH/2025/1/00018/U/00001), "*Structural evolution and electrical transport properties of Cu(I) coordination polymers under pressure"*
October 1, 2021 – *April* 1, 2026	***Investigator:*** *National Science Centre of Poland grant: OPUS 19 (No. 2020/37/B/ST4/00982) "Simplest aliphatic hydrocarbons and their derivatives in extreme conditions"*
April 1, 2018 – May 1, 2021	***Investigator:*** *National Science Centre of Poland grant: OPUS 13, (2017/25/B/ST8/01864), "Photoactive hybrid structures for photovoltaic applications"*

Internships and Workshops

In Academy	
April 13-27, 2026	University of Electronic Science and Technology of China, Chengdu, Sichuan, China
February 26-March 18, 2025	University of La Laguna**,** Tenerife, Spain, under the supervision of prof. Victor Lavin della Ventura
September 16-20, 2024	International Summer School "Ab initio Modeling in Solid State Chemistry - MSSC2024", London, UK
July 21-27, 2024	High-pressure Single Crystal X-Ray Diffraction Summer School, Edinburgh, Scotland
August 19-20, 2023	Olex2 Workshop, Melbourne, Australia

Teaching Experience		
Academic at Adam Mickiewicz University	*X*, 2024 – *II*, 2025	*The materials in extreme conditions*: Laboratory, 30h
	X, 2023 – *II*, 2024	*Fundamentals of physical chemistry:* Laboratory, 60h
	X, 2022 – *II*, 2023	*Fundamentals of physical chemistry:* Laboratory, 60h

Awards and prizes

2024	**Initiative of Excellence - Research University Funding Award**, Adam Mickiewicz University, Poznań — financial support for participation in prestigious scientific conferences in Europe
2024	Small conference grant from the International Union of Crystallography: 34th European Crystallographic Meeting Padwa, Italy
2024	IUCr Young Scientist Award, Edinburgh, Scotland, 2024
2023	Small conference grant from the IUCr: 26th Congress and General Assembly of the International Union of Crystallography, Melbourne, Australia
2023	**Initiative of Excellence - Research University Funding Award, Adam Mickiewicz University, Poznań — financial support for the internationalization of research conducted within the AMU Doctoral School**
2022	Small conference grant from the IUCr: 33rd European Crystallographic Meeting (ECM), Versaille, France
X, 2019 –*VI*, 2020	Adam Mickiewicz University Rector's scholarship, the second degree

List of conferences

24-29. 08. 2025	N. Sacharczuk, A. Olejniczak, A. Katrusiak, M. Podsiadło, "Structural and conformational analysis of dimethyl, diethyl, and dipropyl sulfides under high pressure" –35th European Crystallographic Meeting, Lviv-Poznan (*poster*)
23-27.08.2024	N. Sacharczuk, A. Olejniczak, M. Bujak, M. Podsiadło "Molecular aggregations in crystals of butene isomers determined at high-pressure", 34th European Crystallographic Meeting, Padwa, Italy (*poster*)

5-8.08.2023	N. Sacharczuk, A. Olejniczak, M. Bujak, M. Podsiadło, "High pressure studies of the simplest primary amines", 64 Konwersatorium Krystalograficzne, Wrocław, Poland (*poster*)
22-27.08.2022	N. Sacharczuk, A. Olejniczak, M. Bujak, M. Podsiadło, "Intermolecular Interactions, Polymorphism and Properties of Primary Amines at High Pressure", 33rd European Crystallographic Meeting (ECM), Wersal, France (*poster*)
10-14.04.2019	N. Sacharczuk, M. Zalas, „Synthesis of spherical black TiO_2 for applications in dye-sensitized solar cells", Spring Meeting of the Student Section of the Polish Chemical Society, Ustroń, Poland, (poster)
23-25.03.2018	N. Sacharczuk, "Bitter-sweet chemistry, or what is the story with sugar?", 21st Symposium of the AMU Student Scientific Society of Chemists, Jeziory, Poland, (oral presentation)
22.03.2018	N. Sacharczuk, „Application of black titanium(IV) oxide in dye-sensitized solar cells (DSSCs)", "Student Volunteering" Conference, Poznań, Poland, (oral presentation)

Publications record

1.	N. Sacharczuk, A. Olejniczak, U. R. Rodríguez-Mendoza, A. Katrusiak, M. Podsiadło *Aggregation and Conformations in Dimethyl, Diethyl, and Dipropyl Sulfides at Low Temperature and High Pressure* Crystal Growth & Design, **2026**, 9, 3290–3299 DOI: 10.1021/acs.cgd.5c01554
2.	N. Sacharczuk, B. Kuleczka, A. Olejniczak, A. Katrusiak, M. Podsiadło *Mechanism of Isostructural Phase Transition in Isobutane* The Journal of Physical Chemistry Part C, **2025**, 129(31), 14196-14203 DOI: 10.1021/acs.jpcc.5c03155
3.	M. Bujak, N. Sacharczuk, A. Olejniczak, M. Podsiadło *Halogen Bonding at High-Pressure- the Case of C_2F_5I and C_3F_7I* Crystal Growth & Design, **2025**, 25, 10087-10093 DOI: 10.1021/acs.cgd.5c00761
4.	N. Sacharczuk, A.Olejniczak, M. Bujak, M. Podsiadło *Molecular Aggregations in Crystals of Butene Isomers Determined at High Pressure* Crystal Growth & Design, **2024**, 24, 9909-9913 DOI: 10.1021/acs.cgd.4c00983

6.	N. Sacharczuk, A. Olejniczak, M. Bujak, K. F. Dziubek, A. Katrusiak, M. Podsiadło *Conformation-aggregation interplay in the simplest aliphatic ethers probed under high pressur*e IUCrJ, **2024**, 11, 57-61 DOI: 10.1107/S2052252523009995
7.	Sacharczuk, N.; Olejniczak, A.; Bujak, M.; Podsiadło, M.; Polymorphism, *Intermolecular Interactions, and Properties of Primary Amines at High Pressure,* Cryst. Growth Des. **2023**, 23, 10, 7119–7125 https://doi.org/10.1021/acs.cgd.3c00456
8.	Kubiak, A.; Żółtowska, S.; Bartkowiak, A.; Gabała, E.; Sacharczuk, N.; Zalas, M.; Siwińska-Ciesielczyk, K.; Jesionowski, T. *The TiO2-ZnO Systems with Multifunctional Applications in Photoactive Processes-Efficient Photocatalyst under UV-LED Light and Electrode Materials in DSSCs. Materials* **2021**, 14, 6063 DOI: 10.3390/ma14206063